Role of defects on the growth mechanism and on the structural, optical, electrical and electronic properties of GaN nanostructures

A Thesis
Submitted For The Degree of
Doctor of Philosophy
in The Faculty of Science

by
Abhijit Chatterjee

Chemistry and Physics of Materials Unit
Jawaharlal Nehru Centre for Advanced Scientific Research
Bangalore - 560 064, India

August 2021

Dedication

Dedicated to my family

DECLARATION

I hereby declare that the matter embodied in the thesis entitled "**Role of defects on the growth mechanism and on the structural, optical, electrical and electronic properties of GaN nanostructures**" is the result of investigations carried out by me at the Chemistry and Physics of Materials Unit, Jawaharlal Nehru Centre for Advanced Scientific Research, Bangalore, India under the supervision of **Prof. S. M. Shivaprasad** and that it has not been submitted elsewhere for the award of any degree or diploma.

In keeping with the general practice in reporting scientific observations, due acknowledgement has been made whenever the work described is based on the findings of other investigators. Any omission that might have occurred by oversight or error of judgement is regretted.

AChatterjee

Abhijit Chatterjee

Date:
Place: Bangalore, India

CERTIFICATE

I hereby certify that the matter embodied in this thesis entitled "**Role of defects on the growth mechanism and on the structural, optical, electrical and electronic properties of GaN nanostructures**" has been carried out by Mr. **Abhijit Chatterjee** at the Chemistry and Physics of Materials Unit, Jawaharlal Nehru Centre for Advanced Scientific Research, Bangalore, India under my supervision and that it has not been submitted elsewhere for the award of any degree or diploma.

Prof. S. M. Shivaprasad
(Research Supervisor)

Date:
Place: Bangalore, India

Acknowledgement

First and foremost I wish to thank my supervisor Prof. S.M. Shivaprasad for his guidance and support, both academic and non-academic, during the course of my stay here. I am thankful for the freedom he provided me to try out my own ideas.

I wish to thank Prof. C.N.R. Rao for the immense inspiration I derived from his talks and activities. It has been a privilege to witness his work.

I thank past and present CPMU chairpersons – Prof. Balasubramanian, Prof. Chandrayabhas Narayana, and Prof. Sundaresan for their support in various ways. I thank my JNCASR course instructors Prof. Umesh Waghmare, Prof. S.M. Shivaprasad, Prof. Sundaresan and Prof. Balasubramanian. They helped me understand different aspects of material science.

I am thankful for my teachers in schools and colleges who taught and guided me along the way. I specially thank my teachers Sukanta Bhattacharya, Pradeep Roychowdhury and Meena Sarkar in high school who implored me to choose research as a career.

I acknowledge the huge help provided by technical staff who helped us run and fix the instruments, especially Srinath sir, Mr. Mahesh and Mr. Vinayak Pattar. Several people helped in characterisation of samples and deserve special thanks - Prajwal, Jagadish, Mr. Kannan, Ms. Meenakshi, and Dr. Jay Ghatak.

I am thankful to my past and present labmates who helped in the work and also provided a cheerful and colourful atmosphere. I thank Dr. Satish Shetty, Dr. Malli Tangi, Dr. Varun Thakur, Dr. K K Nagaraja, Dr. Arpan De, Dr. Sanjay Nayak, Rajendra, Shivaram, Dr. Muthuvinayagam, Sachin, Dheemahi, Krishna, Bidesh, Sourjyadeep, Dr. Saraswati and Dr. Shashidhara. I especially thank Dr. Shashidhara for several collaborative projects. I thank my friends Badri, Akash, Srikant and others for making my stay here enjoyable.

All the help provided by academic section, administration, library and

hostel office is appreciated. I thank the mess, chandraya, and utility for providing sustenance.

I am grateful to CPMU and ICMS for providing the growth and characterisation facilities. I thank DST for junior and senior research fellowships.

Finally, I would like to thank my family for raising me and always supporting me. I would not be here without them. I dedicate this thesis to them.

Synopsis

The fundamental and technological importance of the group III-nitride materials can not be overstated, due to their exciting structural and band-structure properties. These materials have been used widely in applications such as optoelectronics, high-frequency and high-power electronics, photovoltaics and sensing, to name a few. Because of thermodynamic constraints, it is not easy or cheap to produce large scale good quality single crystals of AlN, GaN and InN, and due to unavailability of native substrates one is forced to grow them on foreign substrates. The mismatch of the lattice parameters and thermal expansion coefficients between the substrate and the overlayer leads to the generation of point and extended defects and residual strain in the films. Nanostructuring III-nitride films can help alleviate some of these issues and can also be used to enhance and tailor the properties of the material because of the novel properties that arise due to the low-dimensionality.

The systematic work in this thesis helps us understand the enhanced luminescence and superior transport properties of GaN nanowall network along with observation of room temperature ferromagnetic properties by correlating these with experimentally derived electronic band-structure, and quantum mechanical effects. Due to its unique morphology, polarisation induced spontaneous formation of 2DEG is possible and it determines many of the transport properties. To further understand how the unique structure of nanowall network influences its properties, comparative studies with low-dimensional nanorods, and flat or porous thin films have been carried out.

In this thesis, we carry out comparative studies of GaN thin films and one and two-dimensional nanostructures to understand the effect of defects and low-dimensionality on the properties of the material. The work has been divided into seven chapters described as follows.

Chapter 1 gives a brief introduction to the III-nitride semiconductor family focussing on GaN and its intrinsic properties, which makes it technologically important. An understanding of how defects affect structural, optical, electrical and electronic properties and can affect the growth process itself is reviewed. The role of the enhanced surface area and quantum size effects in the nanostructured films in determining the properties are discussed in this chapter and sets the stage for discussing the experimental results.

Chapter 2 provides the details of the experimental facilities used in this work for the growth and characterisation of the samples. It begins with basic information regarding nitride plasma-assisted molecular beam epitaxy (PAMBE SVTA) system along with its various components such as radio-frequency nitrogen plasma source, k-cells as metal source, the vacuum pumps which help maintain an ultra-high vacuum up to low 10^{-11} Torr and in situ characterisation tools such as reflection high energy electron diffraction (RHEED) for monitoring of growth and residual gas analyser (RGA) for checking the ambient. Ex situ characterisation techniques include field emission scanning electron microscopy (FESEM FEI quanta 3D) for studying sample morphology, high resolution X-ray diffraction (Bruker D8 discover), high resolution transmission electron microscopy (FEI Titan), Raman spectroscopy (Horiba Jovin Yvon) for structural characterisation, and photoluminescence spectroscopy (Edinburgh customised PL system), UV-visible-NIR spectrometer (Perkin Elmer) for optical studies and are briefly described. X-ray photoelectron spectroscopy (Omicron) has been used to obtain information regarding the electronic structure and the electrical and magneto-transport properties of the samples were measured using Quantum Design (QD) Versalab for resistivity and Hall measurements and QD SQUID for magnetic measurements. Electrochemical studies using Keithley 2450 SMU and Keysight E4980A precision LCR meter were used to complement the electrical studies to understand the electronic properties of the materials. Basic concepts underlying the growth and characterisation techniques used in this work have been briefly discussed in this chapter.

Chapter 3 deals with the MBE growth of the GaN thin films and nanostructures. The conditions inside MBE being far from equilibrium, the growth is tuned by controlling the kinetics of the atomistic processes of impingement, diffusion, nucleation and desorption of the adatoms. By changing the source fluxes and substrate temperature the growth kinetics can be modified to facilitate the formation of one-dimensional nanorods, quasi-two-dimensional nanowalls and porous or compact thin films. The nanorods are found to grow by a step-flow mechanism and variation of metal flux and shadowing effects are exploited to change the nanorod shapes from tapering to widening, as it grows. Unintentional partial nitridation of the substrate has been used to explain appearance of a bottom compact layer along with long thin nanorods during growth on sapphire. The effect of nitrogen flux and temperature on the growth rates of the one dimensional structures are studied. The models explaining the mechanism of self-induced growth of a nanowall network (NwN) are reviewed.

Chapter 4 provides structural information on the low-dimensional structures described in the previous chapter. The non-uniform distribution of residual strain and dislocations in the nanorods and nanowalls are studied and correlated with the growth process. By controlling the growth conditions NwNs of varying morphology are obtained, which are found to have residual strain varying from compressive to tensile (for growth on sapphire), which is attributed to island coalescence induced microstructure dependent strain. By fitting the X-ray diffraction profile with strain field dependent intensity from dislocated regions, information regarding dislocation distribution is obtained. The morphology of NwN is found to correlate with tilt and twist (out-of-plane and in-plane misorientation among individual nanowalls) determined from XRD Williamson-Hall and Lee analysis and reciprocal space maps. These observations are discussed in terms of generation of boundary dislocations to accommodate misorientations.

Chapter 5 is devoted to the study of optical properties observed in the nanorods, NwN and porous GaN samples. We start with the reproducible observation, that compared to a compact GaN thin film the NwN has higher luminescence intensity (at least by two orders of magnitude), wide featureless near band-edge emission which is blue shifted, and the absence of defect-related UV, blue or yellow emission. By a comparative study of the morphology and carrier concentration dependent optical properties, we explain quantitatively the observed PL peak position and width and absorption edge position on the basis of quantum size effect, residual strain, and excess carrier concentration (up to 10^{20} cm^{-3} in some NwN samples) related band filling, bandgap renormalisation and band tailing. A screening of electron-phonon interaction was used to explain the observation of relatively small temperature-induced bandgap shrinkage (BGS) and information regarding phonon dispersion was found by analysis of measured data with Passler theory of BGS. In an experimental study, NwNs with low carrier concentration were found to exhibit yellow and UV luminescence - absent in NwN with higher carrier concentration. The non-band-edge emissions were explained on the basis of donor-acceptor pair transition among shallow donors and the shallow and deep acceptors. Compensation of the acceptor defects in the unintentionally doped (UID) NwN quenches the defect-related emission. Quantum effects, strain relaxation and morphology related enhancement of light extraction efficiency are used to explain the increase in luminescence intensity for NwN.

Chapter 6 is related to electrical transport and electronic properties of GaN nanostructures. As mentioned in the previous section, UID NwN samples have a high carrier concentration. Despite this, they exhibit a high conductivity including a very high electron mobility of up to 10^4 cm^2/Vs. In our previous work, the superior transport properties have been attributed to a novel way of formation of polarisation induced two-dimensional electron gas (2DEG) inside the nanowalls without any need for fabrication of heterostructures. Building up from that understanding, we further explored electrical and magneto-transport properties. The NwN with high carrier concentration exhibit a shallow minimum in the temperature variation of resistivity graph. While exploring the possible explanations, we discounted the magnetic impurity scattering related Kondo effect and infer it as being due to quantum interference phenomena such as weak localisation and electron-electron interaction. Based on analyses of the temperature and magnetic field dependent conductivity, we attribute our observations to localisation effects that persisted up to high temperatures and high magnetic fields up to 3 T. The morphological peculiarity in this configuration does not enable the application of magnetic fields completely perpendicular to the 2DEG inside the nanowalls and a particular distribution profile of defects have been discussed as the plausible reasons behind the persistence of the localisation.

Encouraged by literature reports of observation of magnetic properties in nanostructures of normally non-magnetic (in bulk) materials, and the interesting magneto-transport phenomenon of this system led us to probe if the GaN NwN shows any magnetic properties and we found that indeed the NwN shows morphology dependent magnetic properties. A comparative study of a compact GaN film, a highly rough and porous NwN and a sample with intermediate roughness and porosity, showed that a weak ferromagnetic nature with a high Curie temperature ($T_C > 370$ K) for the sharp NwN, ferromagnetism with lower T_C for the intermediate sample and the expected diamagnetic behaviour for the compact GaN sample. Apart from the morphology dependence of the T_C, the saturation magnetisation was found to be anisotropic, being higher when the magnetic field is applied perpendicular to the substrate compared to when it is parallel. The observation of the high value of T_C motivated us to carry out magnetic force microscopy (MFM) studies of the NwN samples. We found that the magnetic moments are concentrated in the tip of the nanowalls and clear magnetisation reversals are seen when an external magnetic field is applied during MFM studies. A spontaneous spin polarisation of the 2DEG of the nanowalls induced by quantum effects has been put forward as a plausible explanation of the observed unprecedented phenomena.

From X-ray photoelectron spectroscopy (XPS) studies, we have observed a morphology dependent surface chemistry and electronic structure of the NwN. Based on bandgap determined from luminescence studies and position of core levels and surface Fermi levels from XPS, the band structure of the NwN, showing the amount of band bending has been elucidated. Based on that, and by comparing with density functional theory calculations, the NwN has been found to have a Ga bilayer on its surface, whereas the compact GaN samples had a Ga deficient surface. Further studies of surface electronic structure, through capacitance-voltage measurements, are plagued by issues related to peculiar morphology and high carrier concentration of the NwN samples. The high carrier concentration makes it difficult to form Schottky contacts. In addition, the geometry of electrical contacts to NwN and NR samples being non-conformal, makes a straightforward extraction of electrical parameters complicated. As a possible solution to these issues, we use electrolytic solution as contacts instead of metallic ones to ensure conformity. Electrochemical cyclic voltammetry and impedance spectroscopy studies help us study properties of the porous GaN NwN and flat GaN epilayer. Additional surface states are found in the bandgap of NwN, which are not present in the epilayer. By studying the effects of various surface treatments on these two types of samples, the surface states were correlated with surface non-stoichiometric oxides and dangling bonds and the nature of the surface for different GaN samples was understood.

Chapter 7 summarises the results and the conclusions drawn from each of the preceding work chapters. The role of morphology of the nanostructured film and its growth-related defects on the properties are restated. A list of highlights of these investigations that can generate interest in fundamental and applied studies are listed. Limitations of the current scope of work and prospects of future work are mentioned briefly. Overall, the work has addressed several less understood aspects of the unprecedented observations of properties of nanostructures, and arrived at very interesting and plausible inferences.

List of Publications

Publications included in the thesis.

Chatterjee, A., Acharya, S., & Shivaprasad, S. M. (2020). Morphology-Related Functionality in Nanoarchitectured GaN. **Annual Review of Materials Research**, 50, 179-206.

Amaladass, E. P., **Chatterjee, A.**, Sharma, S., Mani, A., & Shivaprasad, S. M. (2017). Weak localization and electron–electron interaction in GaN nanowalls. **Materials Research Express**, 4(9), 095014.

Chakraborti, H., Deb, S., Schott, R., Thakur, V., **Chatterjee, A.**, Yadav, S., ... & Dhar, S. (2018). Coherent transmission of superconducting carriers through a $\sim 2\mu$m polar semiconductor. **Superconductor Science and Technology**, 31(8), 085007.

Chatterjee, A., Swathi, S. P., & Shivaprasad, S. M. (2018). Morphology dependent surface properties of nanostructured GaN films grown by molecular beam epitaxy. arXiv preprint arXiv:1801.02374.

Chatterjee, A., & Shivaprasad, S. M. Role of interface in GaN nanorod growth mechanism on sapphire.
Manuscript prepared.

Chatterjee, A., & Shivaprasad, S. M. Effect of carrier concentration on photoluminescence properties of GaN nanowall network.
Manuscript communicated.

Chatterjee, A., & Shivaprasad, S. M. Effect of carrier concentration on photoluminescence properties of GaN nanowall network.
Manuscript communicated.

Chatterjee, A., Acharya, S., & Shivaprasad, S. M. Electrochemical investigation of electronic band structure of self induced GaN nanowall

network.
Manuscript communicated.

Chatterjee, A., Acharya, S., & Shivaprasad, S. M. Weak localization and electron-phonon interaction in GaN nanowall network.
Manuscript prepared.

Publications not included in the thesis.

Acharya, S., **Chatterjee, A.**, Gupta, M., & Saha, B. (2020). Influence of AlN buffer layer on molecular beam epitaxy growth of wurtzite Al 1-x Sc x N thin films. **Bulletin of Materials Science**, 43(1), 1-6.

Rao, D., Biswas, B., Flores, E., **Chatterjee, A.**, Garbrecht, M., Koh, Y. R., ... & Saha, B. (2020). High mobility and high thermoelectric power factor in epitaxial ScN thin films deposited with plasma-assisted molecular beam epitaxy. **Applied Physics Letters**, 116(15), 152103.

Acharya, S., **Chatterjee, A.**, Bhatia, V., Pillai, A. I. K., Garbrecht, M., & Saha, B. (2021). Twinned growth of ScN thin films on lattice-matched GaN substrates. **Materials Research Bulletin**, 111443.

Ghatak, J., **Chatterjee, A.**, & Shivaprasad, S. M. (2021). Site-specific angular dependent determination of inelastic mean free path of 300 keV electrons in GaN nanorods. **Journal of Microscopy**, 282(3), 250-257.

Kumar, R., **Chatterjee, A.**, & Shivaprasad, S. M. (2021). Impact of doping on the morphology, structure and optical properties of c-oriented GaN nanorods. **Materials Research Bulletin**, 142, 111390.

Contents

Acknowledgements v

Synopsis vii

List of publications xiii

Contents xv

List of Figures xix

List of Tables xxix

Acronyms xxxi

1 Introduction 1
- 1.1 Introduction 1
- 1.2 History of GaN devices 2
- 1.3 Material properties of GaN 4
- 1.4 Substrates for GaN 5
- 1.5 Defects in GaN films 7
  - 1.5.1 Stress and strain 11
  - 1.5.2 Dislocations 14
- 1.6 Properties of GaN nanostructures and effect of defects . . 15
- 1.7 Organisation of thesis 18

2 Growth and characterisation techniques 21
- 2.1 Growth techniques 21
  - 2.1.1 Plasma Assisted Molecular Beam Epitaxy 21
  - 2.1.2 Physical Vapour Deposition 29
- 2.2 characterisation techniques 30
  - 2.2.1 Reflection high energy electron diffraction 31

2.2.2 Scanning electron microscopy 34
2.2.3 Transmission electron microscopy 36
2.2.4 High resolution X-ray diffraction 39
2.2.5 Raman spectroscopy 43
2.2.6 Ultraviolet-visible-near infrared spectroscopy 45
2.2.7 Photoluminescence spectroscopy 47
2.2.8 X-ray photoelectron spectroscopy 49
2.2.9 Hall and resistivity measurement 52

3 Growth mechanism of GaN films, nanorods and nanowalls 55
3.1 Introduction 55
3.2 MBE growth process 56
3.3 Controlling sample morphology through kinetics 61
3.3.1 Experimental details 62
3.3.2 Results 63
3.3.3 Inferences 66
3.4 Growth of nanorods 67
3.4.1 Experimental details 67
3.4.2 Results 68
3.4.3 Inferences 75
3.5 Growth of porous films and nanowall network 76
3.5.1 Experimental details 77
3.5.2 Results 78
3.5.3 Discussion 79
3.5.4 Experimental details 80
3.5.5 Results 81
3.5.6 Inferences 84
3.6 Conclusion 84

4 Study of structural properties of nanostructures 87
4.1 Introduction 87
4.2 Microstructural properties of nanorods 88
4.3 Residual strain in porous films 96
4.3.1 Experimental details 96
4.3.2 Results 97
4.4 Microstructural properties of NwN 99
4.4.1 Experimental details 99
4.4.2 Results 100

4.5 Conclusion 112

5 Study of optical properties 115
5.1 Introduction 115
5.2 Luminescence properties of nanorods: effect of size 116
5.3 Luminescence properties of porous samples 121
5.4 Luminescence properties of nanowalls 124
  5.4.1 Experiment 124
  5.4.2 Results 125
5.5 Conclusion 137

6 Study of electronic, electrical transport and magnetic properties 139
6.1 Introduction 139
6.2 Electronic properties 140
  6.2.1 Photoelectron spectroscopy study 140
  6.2.2 Electrochemical studies 150
6.3 Electrical transport properties 164
  6.3.1 Experimental details 165
  6.3.2 Results 167
  6.3.3 Conclusions 173
6.4 Magnetic properties 174
  6.4.1 Experimental details 175
  6.4.2 Results 176
  6.4.3 Conclusions 182
6.5 Conclusion 182

7 Summary and future directions 185
7.1 Summary of results 185
7.2 Limitations and future directions 188

Bibliography 191

List of Figures

1.1 (a) Atomic positions of wurtzite unit cell viewed along $[11\bar{2}0]$ direction. (b) Atomic positions of wurtzite unit cell viewed along [0002] direction. (c) Schematic diagram of hexagonal GaN unit cell showing orientations of common crystallographic planes. 6
1.2 Silicon unit cell viewed along [111] direction. 8
1.3 Rhombohedral structure of sapphire unit cell. 9
1.4 Schematic representation of point defects: vacancy,self interstitial defects, and impurities in substitutional and interstitial positions. 10
1.5 (a) Dissimilar sized film and substrate unit cells. (b) Strained film during lattice matched growth (c) Plastic strain relaxation by forming dislocations. (d) Elastic strain relaxation for low-dimensional nanostructure. 13
1.6 A schematic diagram showing misfit dislocation at the interface between film and substrate evolving as threading dislocation as the film grows. 15
1.7 Schematic diagram showing (a) edge dislocation and (b) screw dislocation. 16

2.1 A phtograph of the SVTA nitride MBE system used in this work. 23
2.2 A schematic diagram of the PAMBE system showing its various components. 23
2.3 Schematic diagram of nitrogen plasma source. 24
2.4 A typical spectrum of nitrogen plasma produced by the RF plasma source. 25
2.5 (a) Photograph of a k-cell. (b) Schematic diagram of the k-cell showing crucible, heater and thermocouple. 26

2.6 Residual gas analyser schematic diagram showing the main components. 28
2.7 (a) Photo of SVTA PVD used in this work. (b) Schematic diagram of PVD showing electron gun, crucible and sample holder. 30
2.8 Schematic diagram of the reflection high energy electron diffraction (RHEED) depicting the basic components. . . . 32
2.9 1(a) A flat surface with domains smaller than electron coherence length. 1(b) Broadened reciprocal space rods. 1(c) Experimental RHEED pattern of a flat GaN sample.2(a) Rough surface with three dimensional islands. 2(b) Expected arrangement of reciprocal lattice points. 2(c) Experimental RHEED pattern of a columnar GaN sample. . . 33
2.10 Schematic diagram of field emission scanning electron microscope (FESEM). 35
2.11 A schematic diagram of diffraction pattern and image formation in transmission electron microscope. 37
2.12 (a) A schematic diagram of the HRXRD set-up. (b) Definition of some commonly used angles. 39
2.13 Schematic diagram showing reciprocal lattice points and XRD scan geometry. 40
2.14 Wurtzite structure and its Raman active modes. 44
2.15 Examples of radiative recombination transitions in semiconductors: (a) band to band transition, (b) recombination between free electron and hole bound to acceptor, (c) donor acceptor pair recombination, and (d) donor bound electron and free hole recombination. 48
2.16 Photoluminescence set-up showing the laser source, sample holder, monochromator, PMT detector, and associated optics. 48
2.17 Photoelectron emission process 49
2.18 Schematic diagram showing (a) four probe resistivity measurement and (b) Hall measurement. 53

3.1 Schematic diagram of atomistic processes involved in the growth in molecular beam epitaxy. 57

3.2 Top panel: Dependence of various growth modes on supersaturation and film-substrate misfit. Bottom panel: epitaxial growth modes in successive stages in cross sectional schematic. 59

3.3 Experimentally determined relationship between Ga k-cell temperature and beam equivalent pressure of Ga flux. The exponential nature of the dependence is evident. 61

3.4 Plan view FESEM images of samples A1,B1 and C1. The scale bar corresponds to 1 μm. The insets are higher magnification images clearly showing a change in morphology from well aligned nanorods in sample A1 to nanorods emanating out of a faceted matrix layer in sample B1 to a compact layer in sample C1. 62

3.5 Plan view FESEM images of samples A2,B2 and C2. The scale bar corresponds to 2 μm. 64

3.6 Plan view FESEM images of samples A3, B3 and C3. The insets show the corresponding cross-sectional image. The scale bar corresponds to 1 μm. A reduction in volume of matrix layer is seen in samples B2 and C2 compared to sample A2. 65

3.7 Graphs showing dependence of microstructural parameters on the deposition temperature. Variation of (left) nanorod diameter, (middle) nanorod height, and (right) base layer thickness with deposition temperature. 65

3.8 Plan view FESEM images of samples (a)A4 and (b)B4. The scale bar corresponds to 500 nm. 67

3.9 Plan view FESEM images of samples A5, B5 and C5. Inset shows higher magnification images. Scale bar corresponds to 500 nm. 68

3.10 Low magnification TEM images of samples (a) A5, (b) B5 and (c) C5. Arrows mark the positions of bunched steps on the nanorod sidewall. 69

3.11 High magnification TEM images of samples (a) A5 and (b) B5. The growth direction along c axis is marked. The bunched steps on the sidewalls marked with arrows. 71

3.12 Low resolution TEM two-beam bright field image of the nanorod from sample A5 with zone axis [10-10] and g vector (a) (0002) and (b) (11-20). (c) shows the image taken with a 10° tilt from (0002) g vector. In (d) a low resolution bright field image of a nanorod from sample B5. (e) shows a high resolution image of a nanorod top from sample C5 with the facets indexed. Inset shows the diffraction pattern of the image. (f) shows an FESEM image of a nanorod of sample C5 showing spiral nature of growth. 73

3.13 A schematic digram showing impingement and diffusion of adatoms leading to axial and radial growth. 76

3.14 FESEM images of porous samples (a) A6 (b) B6 (c) C6. The scale bar corresponds to 1μm 78

3.15 Graphs of variation of microstructural parameters of porous GaN samples with flux. (Left) pore density, (middle) mean pore size, and (right) sample thickness as a function of ratio of beam equivalent pressure of nitrogen and gallium flux. . 79

3.16 FESEM images of sample B6 focussing on different regions. The scale bar corresponds t0 100 nm. (a) shows a large area region. (b) shows merger of two pores to form an elongated slit-like pore. (c) shows three pores merging to form an extended triangular void. (d) shows a wedge shaped nanowall forming between two elongated voids. (e) shows that the nanowalls around voids can join to form a network, as indicated by dashed lines. 80

3.17 FESEM images of samples (a)A7, (b) B7 and (c) C7. The scale bar corresponds to 1 μm. 81

3.18 Schematic diagram of evolution of film morphology with time due to shape transition and edge enhanced growth. Last image shows FESEM image of a nanowall network sample. Adapted from ref 49. 83

4.1 Typical plan-view FESEM image of (a) GaN nanorods grown on sapphire (0001) and (b) silicon (111). The inset shows the 30 ° tilted-view images. The scale bar corresponds to 1 μm. 88

4.2 Plan-view FESEM image of sample A2 showing the nanorods emerging out of base matrix layer. Right-top inset shows a 75° tilted-view image and right-bottom inset shows a cross-sectional view of the sample. The scale bar corresponds to 500 nm. 90

4.3 HRXRD $2\theta - \omega$ scans of sample A2. (Top) 002 reflection and (bottom) 101 reflection. 2θ positions corresponding to relaxed GaN lattice parameters are marked with arrows. . 91

4.4 Raman spectra of sample A2 showing sapphire substrate peak and GaN $E_2{}^H$ peak. 92

4.5 (Left) low resolution TEM image of a nanorod and matrix layer from sample A2. (Right) electron diffraction patterns corresponding to regions marked as A and B in the micrograph. 93

4.6 Schematic diagram showing in-plane epitaxial relationship between GaN grown directly on c-sapphire and GaN grown on AlN. 93

4.7 Schematic diagram demonstrating atomic geometry of Ga-polar and N-polar GaN. Accumulation of induced charges and direction of polarisation vector P are also shown. . . . 94

4.8 Schematic diagram of GaN nanorod and matrix layer grown on partially nitrided sapphire. 95

4.9 Plan-view FESEM images of sample (a)A3 (b)B3, and (c)C3. The scale bar corresponds to 1 μm. 97

4.10 Left column: plan view FESEM images of the samples (a) A4, (b) B4, and (c) C4. Middle column: cross-sectional view of the samples. The scale bars correspond to 1 μm. Right column: the average width of the nanowalls obtained from image analysis. 100

4.11 (a) Symmetric $2\theta - \omega$ scan and (b) azimuthal ϕ scans of GaN 101 and sapphire 1010 reflection. 101

4.12 Raman spectra of samples A4, B4, and C4 showing the $E_2{}^H$ peak. 102

4.13 A comparison of out-of-plane biaxial strain calculated from XRD and in-plane biaxial strain calculated from XRD and Raman data for samples A4, B4, and C4. 103

4.14 Sample A4 (a) 002 omega scan and (b) 101 omega scan, fitted by equation (11). (c) The central portion of the XDP of 002 omega scan fitted with Gaussian function. (d) The tail portion of 002 omega scan fitted with inverse cubic asymptotic function. 106

4.15 (a) Plan-view FESEM image of sample C4. (b) Panchromatic cathodoluminescence mapping of the same region of sample C4. Circled regions show high brightness in cathodoluminescence map compared to other regions. The scale bar corresponds to 1 μm. 107

4.16 Normalized 002, 004 and 006 $2\theta - \omega$ scans of sample A4. X axis is the deviation of scattering vector from Bragg position, divided by reflection order. 109

4.17 Williamson-Hall plot of samples A4, B4, and C4. The extracted parameters are given in Table 4.7. 109

4.18 The FWHM of omega scans of symmetric and asymmetric reflections 105, 204 and 101 of samples A4, B4, and C4 as a function of the inclination angle of the reflections. The solid line is a fit using equation (16). The extracted parameters are given in Table 4.7. 110

5.1 Plan-view FESEM images of samples (a) A1 (b) B1 (c) C1 and (d) D1. the scale bar corresponds to 1000 nm. 117

5.2 Normalized room temperature PL spectra of samples A1 to D1 showing near band-edge emission and defect related luminescence. 118

5.3 Room temperature PL spectra of samples A1 to D1 showing the near band-edge emission. 118

5.4 Room temperature PL spectra for samples A1 to D1 showing defect related luminescence. The spectra has been fitted with Gaussian peaks corresponding to red, yellow and green luminescence with peaks at 1.8, 2.1 and 2.35 eV. 119

5.5 Plan-view FESEM images of samples A2, B2, and C2. The scale bar corresponds to 1 μm. 122

5.6 PL spectra of samples A2, B2, and C2 taken at 11 K temperature. 123

5.7 Plan-view FESEM images of NwN samples (a)A3, (b)B3, (c)C3, (d)D3, and (e)E3. The scale bar corresponds to 500 nm. 126
5.8 PL spectra of samples A3, B3, C3, D3, and E3 taken at (left) 11 K and (right) 300 K. 127
5.9 PL spectra of sample A3 taken at 11 K showing the deconvoluted defect related peaks. 128
5.10 PL intensity as a function of excitation power density for samples A3 and E3. The solid line fit corresponds to a power law fit with the extracted exponent depicted. 129
5.11 Intensity of NBE and UV luminescence peaks as a function of inverse temperature for samples (left) A3 and (right) B3. 131
5.12 Positions of band edge for samples A3, B3, C3, D3, and E3 as a function of temperature. Also shown is data from ref[1]. 131
5.13 Schematic diagram of band structure showing band gap renormalisation (BGR) and Burstein-Moss shift (BMS). Right panel shows donor band overlapping with conduction band tail. 132
5.14 Square of absorption coefficient versus energy plot for samples A3, B3, C3, D3 and E3. 132
5.15 PL spectrum and absorption coefficient for sample E3. Lower energy tail of PL peak fitted with Gaussian function and higher energy tail fitted with density of occupied states. . . 133

6.1 FESEM images of samples A1, B1, C1, and D1. The scale bar corresponds to 1 μm. 142
6.2 Deconvoluted XPS Ga 3d core level peak of samples A1, B1, C1, and D1. 143
6.3 Plot of bulk carrier concentration n versus the calculated stoichiometry of the sample surface. 144
6.4 Cathodoluminescence spectra of samples A1, B1, C1, and D1 showing the NBE emission. 145
6.5 Schematic representation of band structure of samples A1 and B1 showing the degree of band bending and position of Fermi level. 146
6.6 Deconvoluted XPS Ga 3d core level spectrum of sample A1 for different sputtering durations of 0, 10, and 20 minutes. 147

6.7 Deconvoluted XPS valence band spectra of sample A1 for different sputtering durations of 0, 10, and 20 minutes. The arrow marks the position of surface Fermi level at zero binding energy where a build-up of intensity indicates metallisation. 149

6.8 Current-voltage characteristics of different metal/GaN nanowall network contacts. (a) Al/GaN (b) Au/GaN, and (c) Pt/GaN. 151

6.9 Schematic diagram of a metal-insulator-semiconductor (MIS) device. 152

6.10 Capacitance-voltage characteristics of an MIS device with polymethyl methacrylate (PMMA) insulating layer and Al metal contact. 152

6.11 Schematic diagram of electrochemical measurement set-up with a three electrode configuration. 153

6.12 FESEM images of samples A2, B2, and C2. The scale bar corresponds to 1 μm. 154

6.13 Cyclic voltammogram data for samples (a) A2, (b) B2, and (c) C2. The insets show a close-up view of the cathodic current. 154

6.14 Cyclic voltammogram of sample B2 with and without illumination. 155

6.15 Representative frequency dependent impedance spectra of samples (a) A2, (b) B2, and (c) C2 plotted in Nyquist form. The solid lines are a fit to experimental data using an equivalent circuit shown in inset of (b). 157

6.16 Bias dependent parameter values extracted from equivalent circuit fitting. (a) Exponent of constant phase element α and (b) charge transfer resistance R_2. 157

6.17 Capacitance of the electrochemical system of sample (a) A2 and (b) C2 depicted in Mott-Schottky plot. The solid squares represent the total capacitance and the solid circles represent the capacitance after removal of the Helmholtz layer contribution. The linear fits are according to Mott-Schottky equation. 159

6.18 (Left) schematic band structure depicted alongside (right) cyclic voltammogram for sample A2. The positions of conduction and valence band edges are determined by a linear fit of the rising cathodic and anodic currents beyond the onset potential. The degree of band bending is determined from value of flat band potential. 161

6.19 Low temperature photoluminescence spectrum of sample A2 at 12 K showing NBE and defect related peaks. The inset shows the defect related peak deconvoluted into red and yellow luminescence bands. 162

6.20 FESEM images of samples (a) A3, (b) B3, (c) C3, (d) D3, and (e) E3. The scale bar corresponds to 1 μm. 166

6.21 Temperature variation of longitudinal resistance for samples A3, B3, C3, D3, and E3. 167

6.22 Temperature variation of resistivity for samples (a)A3, (b)B3, (c)C3, (d)D3, and (e)E3. The solid line fits to the experimental data are according to equation (6.12). 168

6.23 Temperature variation of longitudinal resistance for sample A3 with different magnetic fields of magnitude 0, 0.01, 0.1, and 1 T. 169

6.24 Calculated charge density distribution inside wedge shaped nanowall network depicting formation of 2DEG inside the nanowall[2]. Reprinted with permission. 172

6.25 AFM image topographic data plotted in 3D to depict the orientation of applied magnetic field with respect to individual nanowalls. 173

6.26 The longitudinal conductivity of sample A3 at (a) 50 K and (b) 300 K. The solid line represents a fit of equation (6.12) to the experimental data. 174

6.27 FESEM images of samples (a)A4, (b)B4, and (c)C4. The scale bar corresponds to 1 μm. 176

6.28 Field dependence of magnetisation for samples (a)A4, (b)B4, and (c)C4 at 2 K and 300 K temperature. 176

6.29 Field dependence of magnetisation for samples A4 in low magnetic field regime showing the magnitude of remanent magnetisation and coercivity at 2 K and 300 K. 177

6.30 Temperature dependence of field cooled (FC) and zero field cooled (ZFC) magnetisation for samples (a)B4 and (b)C4. Applied magnetic field for FC measurements is 1000 Oe. . 177
6.31 Field dependence of magnetisation for sample C4 at 370 K temperature. 178
6.32 (A) Atomic force microscopy image of sample C4 showing the topography. (B) Cross-sectional transmission electron microscopy image of an individual nanowall showing the tapered geometry of the wall. The inset shows the high resolution image of the tip region. (C) Magnetic force microscopy image of sample C4 showing the non-uniform strength of magnetisation in different parts of the nanowall network. (D) Zoomed view of magnetisation distribution for an individual nanowall with a line scan for estimating size of the region with comparatively high magnetisation. 180
6.33 Field dependence of magnetisation with magnetic field applied parallel or perpendicular to the substrate. 180
6.34 Magnetic force microscopy image of sample C4 with an external magnetic field applied perpendicular to the substrate with field direction (a) into and (b) coming out of the substrate plane. 181

List of Tables

1.1 Substrates for GaN 7
1.2 Dislocation types 15

4.1 Growth conditions of porous GaN samples 97
4.2 Microstructural parameters of porous GaN samples 98
4.3 Lattice parameters and strain of porous GaN samples . . . 98
4.4 Growth conditions of GaN samples 99
4.5 Lattice parameters and strain of GaN NwN samples 102
4.6 Dislocation correlation parameters for NwN samples. . . . 107
4.7 Parameters extracted from Williamson-Hall plots 110

5.1 Sample growth parameters and results of Hall measurement, and Raman spectroscopy: carrier concentration n and the E_2^H peak position 125
5.2 Summary of calculated energy shifts and characteristic energies.ΔE_{BGR}, ΔE_{BMS} and ΔE_{strain} are shifts due to band-gap renormalization, Burstein-Moss effect and strain, respectively. E_g^* and E_{abs}^* are calculated values of modified band-gap and absorption edge. E_{PL} and E_{abs} experimentally observed positions of PL NBE peak and absorption edge. All energies are in eV. 135

6.1 Typical metal contacts to n-GaN 151
6.2 Growth parameters and carrier concentration n 165
6.3 Phase coherence length of samples at 50 K and 300 K calculated using eqn. 6.12 172

Acronyms

LED	Light Emitting Diode
MOCVD	Metal Organic Chemical Vapour Deposition
PAMBE	Plasma Assisted Molecular Beam Epitaxy
TD	Threading Dislocation
NR	Nanorod
NWN	Nanowall Network
2DEG	Two Dimensional Electron Gas
BEP	Beam Equivalent Pressure
RGA	Residual Gas Analyser
FESEM	Field Emission Scanning Electron Microscope
HRTEM	High Resolution Transmission Electron Microscope
XRD	X-Ray Diffraction
XPS	X-Ray Photoelectron Spectroscopy
SAED	Selected Area Electron Diffraction
RHEED	Reflection High Energy Electron Diffraction
DP	Diffraction Pattern
CL	Cathodoluminescence
PL	Photoluminescence
RSM	Reciprocal Space Map
SAGB	Small Angle Grain Boundary
XDP	X-Ray Diffraction Profile
NBE	Near Band Edge
BMS	Burstein-Moss
BGR	Band Gap Renormalisation
SCR	Space Charge Region
CV	Cyclic Voltammetry
EIS	Electrochemical Impedance Spectroscopy
QCC	Quantum Correction to Conductivity
WL	Weak Localisation

Chapter 1

Introduction

This chapter deals with the technological importance of GaN semiconductor and the materials issues limiting the realisation of its full potential. Nanostructuring can solve some of these issues, and along with defect engineering, can be used to enhance and tune various properties. Defects are unavoidably present in a semiconductor and can affect all aspects of a semiconductor, from electrical to optical and structural and even the growth itself. Understanding the effect of defects is of paramount importance to increase the efficiency of GaN-based devices. We review the current understanding of these subjects in this chapter.

1.1 Introduction

Semiconductor materials and devices have played a prominent role in shaping the technology of modern society. Beginning with silicon, which started the microelectronics field, we have had second-generation compound semiconductors such as GaAs, AlAs, InP, which led to immense advances in mobile and optical communication, digital infrastructure, light-emitting diodes (LED), to name a few. For further advancement, the focus shifted in the third generation to wide bandgap semiconductors such as ZnO, SiC, GaN. Some of the most important materials in this third-generation are the III-nitrides.

The III-nitride material system, composed of gallium nitride and its alloys with aluminium and indium have excellent properties and a mature growth technology which propelled them to a broad range of applications[3 4]. They have a direct and tunable bandgap - ranging from 0.65 eV for InN, to 3.4 eV for GaN, and finally to 6.2 eV for AlN, covering the entire solar spectrum, promising various applications such as LEDs, laser diodes, solar cells and photo-detectors. The electron transport properties of III-nitrides are magnificent; they have high carrier mobility, saturated drift velocity and break-down strength - leading to myriad device applications, where operating speed or high-power handling capability is essential. High stability of III-nitrides at harsh conditions provide an added advantage.

Among III-nitrides, GaN is the most widely studied material and therefore its growth, and device fabrication technology is the most mature. InN has specific growth-related challenges owing to its low dissociation temperature and high nitrogen vapour pressure, forcing its growth temperature to be low and thereby impacting the quality of the grown crystal, which has limited its wide-scale adoption till now although work in this regard continues[5]. The work in this thesis involves the growth and characterisation of GaN nanostructured films to understand its morphology related properties and the effect of defects. In this chapter, we present a brief discussion on the properties of GaN material, beginning with a historical perspective of GaN devices to set the context of the experimental work as discussed in the later chapters.

1.2 History of GaN devices

Polycrystalline gallium nitride was first synthesised in 1932 by W. C. Johnson and co-workers by flowing ammonia gas over gallium metal heated to temperatures around 900-1000°C in a furnace[6]. Using hydride vapour phase epitaxy (HVPE), GaN crystalline films were first grown by Maruska and Tietjen in the laboratories of the radio corporation of America in the winter of 1968[7]. These films allowed electrical characterisation for the first time as previous powdered forms were not amenable to such measurements. In the 1960s, visible and infra-red LEDs had been fabricated using compound semiconductors. In 1962, Jacques Pankove had reported infra-red emission from GaAs and in 1964 Hermann Grimmeiss and H Scholz prepared green-emitting GaP LEDs with an efficiency of 0.6%[8 9]. Blue LEDs had been fabricated using SiC, but they had an electrical to optical conversion efficiency of only up to 0.03%[10]. The indirect nature of the bandgap of SiC and GaP means electron-hole pair recombination needs phonons for momentum conservation, making the probability for this three-body collision low and thereby reducing the efficiency. Due to its wide and direct bandgap, GaN was perceived to be a good candidate to make blue LEDs, and this started a worldwide effort to achieve that. A conventional LED needs a junction of p-type and n-type material; since as-prepared GaN always came to be of n-type, therefore effort was put on growing p-type GaN. In 1969, Maruska and co-workers tried to dope GaN with Zn, Mg, Cd and Hg, to make it p-type conducting but failed. By 1971, blue electroluminescence was observed by Pankove in a Zn doped GaN, and by next year he had fabricated blue GaN LED, which had an MIS (metal-insulator-semiconductor) structure[11]. Separately, ultraviolet emitting LEDs were fabricated by Maruska with a similar MIS structure using undoped n-type GaN and thin Mg-doped GaN for the insulating layer[12]. No significant progress was made in the next decade, and the blue and ultra-violet emitting LEDs continued to be of low efficiency. The main reason for this was the low crystalline quality and high defect concentration of the GaN samples prepared by HVPE. In 1984, Toshiharu Kawabata at Matsushita Research Institute, Tokyo fabricated blue GaN LED by similar Zn doping, with a metal-organic chemical vapour deposition (MOCVD) reactor[13]. MOCVD grown samples were better in crystal quality compared to HVPE ones. In 1986, Hiroshi Amano of Nagoya University in Japan introduced the technique of using a buffer layer of AlN preceding GaN growth for the improvement of structural quality[14]. In 1988, Amano reported improved luminescence from Zn:GaN after the samples were irradiated with a low energy electron beam (e-beam). Next year, Isamu Akasaki's group in Nagoya university demonstrated for the first time low resistivity p-type GaN sample using Mg as the dopant and low energy e-beam irradiation for activation of the dopants. This was an important breakthrough, as now onwards, proper p-n junctions could be fabricated. In typical GaN growth in HVPE or MOCVD reactors, the acceptors (such as Zn and Mg) form complexes with hydrogen, which is always present as an impurity. E-beam irradiation breaks the acceptor-hydrogen bond, and the hydrogen can be released as molecules from the sample. The next development came from Shuji Nakamura, working in Nichia Corporation in Japan, who found that thermal annealing of Mg-doped GaN films led to the creation of highly conducting p-type GaN films. Unlike e-beam irradiation, thermal annealing is a uniform process. Whereas in 1989 first p-n junction blue LED was demonstrated, it took till 1994 to create a truly bright blue LED combining the latest efforts[15]. Bright blue or UV LED combined with phosphors are used to make white solid-state lighting devices. Around 2001, Sumitomo used a dislocation elimination method to grow low defect GaN single crystals on GaAs for the fabrication of laser diodes. Nichia began commercial production of laser diodes, and in 2003, Sony introduced blue-ray DVDs based on these 405 nm blue laser diodes.

In 1991, Asif Khan et al. reported MOCVD growth of GaN/AlGaN heterostructures which exhibited mobilities of more than 600 cm^2/Vs at room temperature[16]. Based on these heterostructures, a high electron mobility transistor (HEMT) was fabricated in 1993 by the same group, paving the way for the application of GaN in high-frequency and high-power electronics[17]. Work by Bernardini in 1997 helped understand the polarisation related properties of III-nitrides[18]. In 1999, Ambacher and co-workers presented an analytical model to describe the properties of 2D electron gas (2DEG) in GaN/AlGaN structures that are still in use[19]. In a conventional HEMT, the current flowing through the 2DEG channel from the source to the drain Ohmic contacts can be tuned by the application of a negative potential on a Schottky contact which acts as a gate electrode. Such a device is referred to as normally-on, as the current can flow with zero gate voltage. In 1999, Sheppard demonstrated a high power microwave HEMT based on GaN/AlGaN heterostructures grown on SiC[20]. Several important proof of concept devices were fabricated in the following years, such as the creation of normally-off AlGaN/GaN HEMT in 2006, which was commercialised in 2009[21][22]. Normally-off transistors are essential for high-power applications to minimise current leakage and power loss. In 2012, a milestone was reached when AlGaN/GaN heterostructures could be fabricated in a large scale on 200 mm silicon wafers, making way for the integration of GaN technology with the pre-existing mature silicon fabrication technologies[23]. Further progress in high-frequency and high-power applications has continued; in 2013, high-frequency GaN HEMT of cut-off frequency more than 450 GHz was achieved, and in 2015, 600 V normally-off GaN HEMTs were commercialised by transphorm. Today, GaN is at the cusp of replacing silicon based technologies in several fields of application such as high-current (≈100 Å) high-voltage (600-900 V) power amplifiers for vehicles, intelligent grids in local power distribution, microwave amplifiers in mobile phone base stations[24][25].

1.3 Material properties of GaN

GaN is a group III-V semiconductor, which has mixed covalent-ionic type inter-atomic bonding. It can exist in three crystal structures: hexagonal wurtzite, cubic zinc blende, and cubic rock salt. The rock salt structure has only been observed under very high pressures, and the zinc-blende structure can only be grown under particular experimental conditions on a cubic substrate. The wurtzite structure is the stable structure of GaN and is the one most commonly observed. The wurtzite unit cell is shown in Figure 1.1 and contains two Ga atoms and two nitrogen atoms per unit cell. The unit cell is characterised by 'c' and 'a' lattice parameters: c is the distance between bilayers of Ga (or N) atoms, and a is the side-length of the regular hexagon of the conventional unit cell. The lattice parameters of unstrained GaN are taken from literature to be a=3.1891 Åand c=5.1855 Å[26]. Each atom in the wurtzite unit cell is bonded tetrahedrally to four atoms of the other species, and since the bond is semi-ionic, partial charge separation occurs between the electropositive Ga atom and the electronegative N atom. This polar nature of the bond manifests as a charge separation across the unit cell in the c direction and an associated spontaneous internal electric field of the order of a MV/cm. Application of stress or temperature variation can distort the unit cell and change the internal electric field, giving GaN a piezoelectric and pyroelectric nature. The majority of GaN sample growth is done along [0001] axis yielding c-plane samples, although non-polar $(10\bar{1}0)$ m-plane, $(11\bar{2}0)$ a-plane and semi-polar $(10\bar{1}1)$ r-plane are also grown, especially if the internal electric field is undesirable for some particular application.

GaN has a wide direct bandgap of about 3.4 eV at room temperature. The melting point of GaN is more than 2500 °C, and it does not decompose till at least 900 °C, thus ensuring stability at any standard device operating temperatures. GaN is reasonably chemically inert and has strong radiation hardness. The atomic displacement energy is defined as the energy required to permanently move the atom from its lattice position and is valued as 20.8 eV for Ga atom in GaN and 10.8 eV for N atom[27]. These values are higher compared to silicon and GaAs, meaning that GaN is more resistant to the creation of point defects during irradiation. This remarkable stability of GaN makes it suitable for applications in harsh environments.

1.4 Substrates for GaN

Due to the inability to grow large size defect-free single crystals of GaN affordably, homoepitaxial growth of GaN is not feasible, and it must be grown heteroepitaxially on a dissimilar substrate with the choice of substrate depending on the intended application. The degree of mismatch between the film and substrate in the lattice parameters and thermal ex-

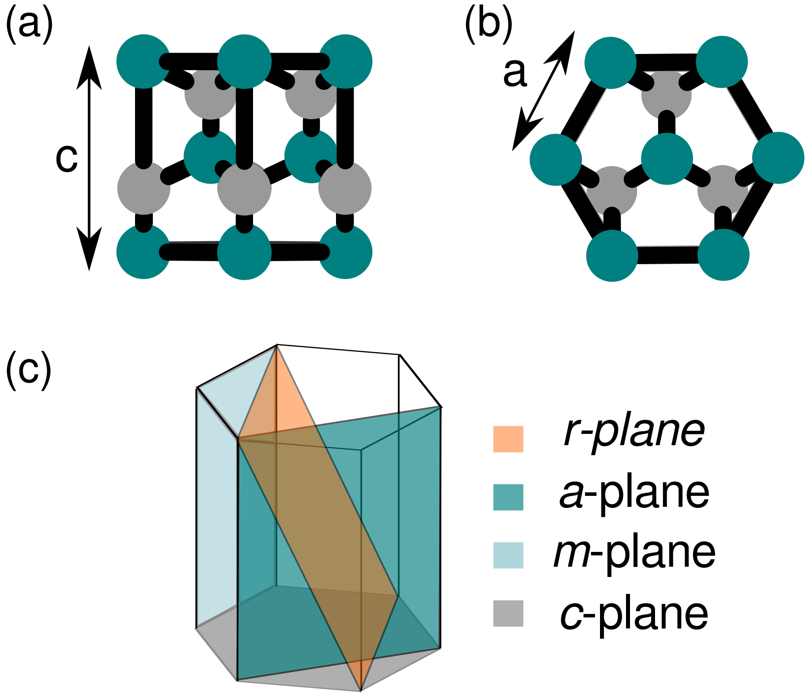
(a)
c
(b)
a
(c)
r-plane
a-plane
m-plane
c-plane

Figure 1.1: (a) Atomic positions of wurtzite unit cell viewed along $[11\bar{2}0]$ direction. (b) Atomic positions of wurtzite unit cell viewed along [0002] direction. (c) Schematic diagram of hexagonal GaN unit cell showing orientations of common crystallographic planes.

pansion coefficient is usually the primary deciding factor along with the cost.

Although a number of materials can be used for GaN heteroepitaxy, the three most common ones are sapphire ($\alpha - Al_2O_3$), silicon and silicon carbide. The last material exists in several polytypes and the hexagonal 6H-SiC is used widely. The structural parameters of these substrates are shown in Table 1.1.

Table 1.1: Substrates for GaN

Material	Crystal structure	Lattice parameters (Å)		Lattice mismatch (%)
GaN	wurtzite	3.1891	5.1855	0
Al_2O_3	rhombohedral	4.765	12.982	16
Si	diamond	a=c=5.431		21
SiC	wurtizte	3.0806	15.1173	-3.1

The choice of the substrate determines polarity, surface morphology, strain and concentration of structural defects. Silicon carbide has the lowest mismatch, followed by Al_2O_3 and then by silicon, whereas the substrates' cost has the opposite trend.

With the least mismatch of lattice parameters and thermal expansion coefficient, and good thermal conductivity, SiC is suitable for those high power applications in which cost is not a priority. Due to its transparency over a large spectral region, comparatively lower cost and availability, sapphire is the substrate of choice for optoelectronic applications such as LEDs and laser diodes. Silicon is simultaneously the cheapest substrate among the three, as well as the one available in the highest crystal quality and largest wafer size. The growth of GaN on silicon opens the possibility of integrating GaN with mature silicon technology. The quality of GaN on silicon suffers from a large concentration of defects and cracks due to the large mismatch between the two[28].

1.5 Defects in GaN films

The mismatch of lattice parameters and thermal expansion coefficients between substrates and the GaN overlayer leads to a high density of defects. Additionally, impurities may be present in the source materials, or the ambient and can get incorporated into the grown material. Defects exist in all semiconductors, whether unintentionally or by design. Defects can

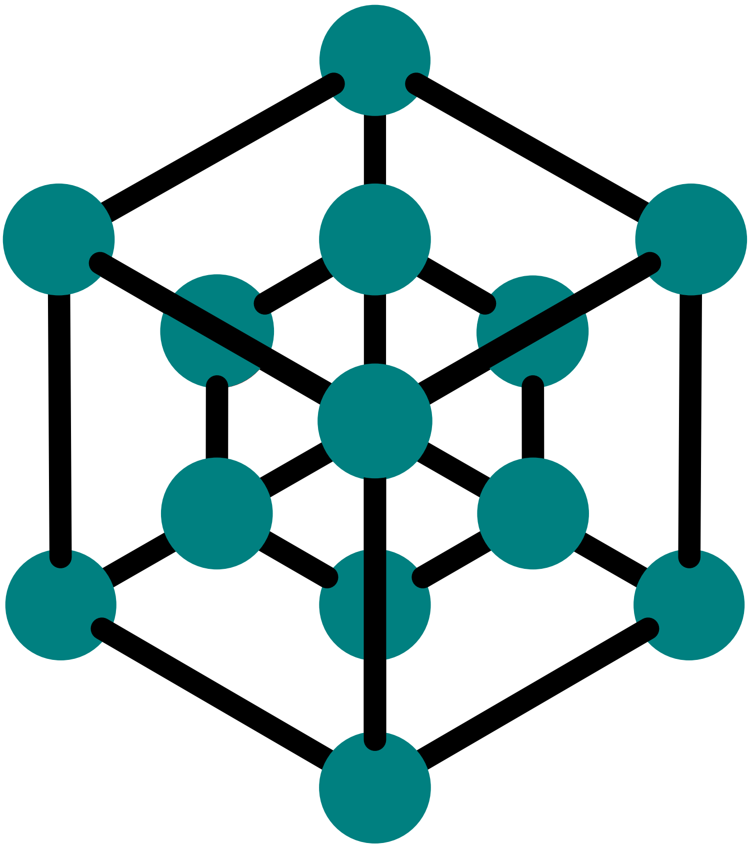

Figure 1.2: Silicon unit cell viewed along [111] direction.

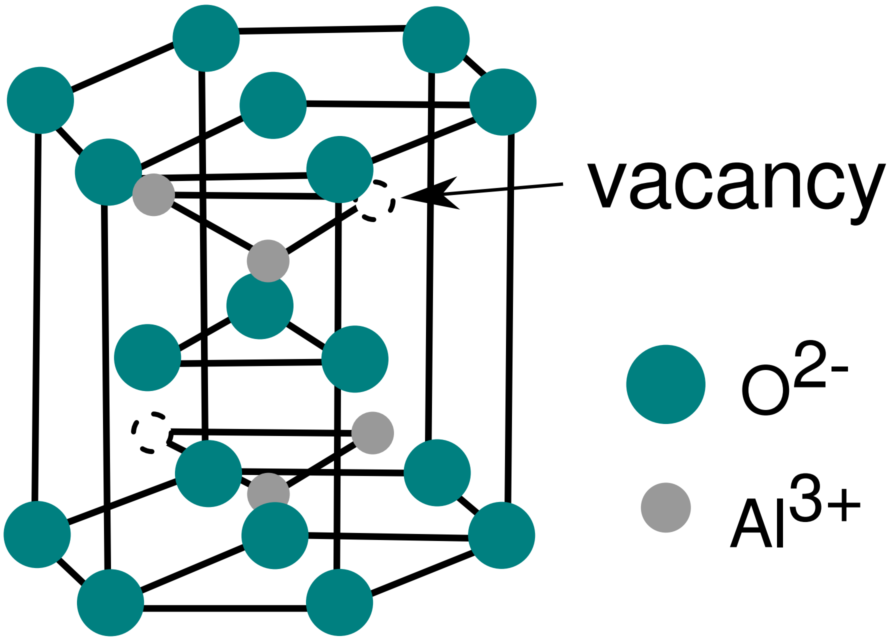
vacancy
O2-
Al3+

Figure 1.3: Rhombohedral structure of sapphire unit cell.

affect all semiconductor material properties: structural, electrical, optical, magnetic, etc. Defects may be point defects - an imperfection at a single lattice position or extended - along one, two or three dimensions. The point defects include vacancies which are missing atoms, interstitials - atoms in between regular lattice sites, antisites - atoms occupying wrong lattice sites (e.g.: A sites occupied by B atoms in an AB type crystal) and impurity atoms. Due to thermodynamic reasons, some concentration of native defects is unavoidable. Figure 1.4 schematically shows some common types of point defects. In GaN, vacancies are quite common, along with the inclusion of ambient impurities (such as oxygen, silicon) in substitutional sites. It is more likely for small-sized impurities such as hydrogen to exist in interstitial sites rather than larger atoms such as gallium. Apart from point defects, extended defects are also common in GaN, including linear dislocations, two-dimensional stacking faults and three-dimensional voids and inclusions.

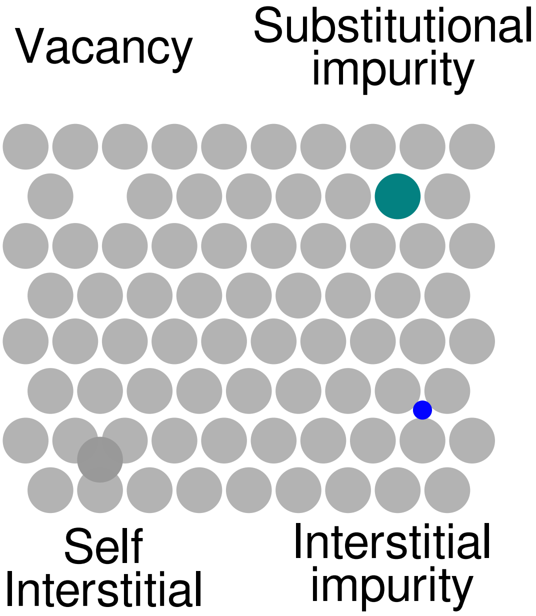

Figure 1.4: Schematic representation of point defects: vacancy,self interstitial defects, and impurities in substitutional and interstitial positions.

1.5.1 Stress and strain

The growth of a semiconductor on a dissimilar substrate results in strain in the film, which is thickness dependent. For a particular degree of mismatch, there exists a critical film thickness $\mathrm{h_c}$, such that for thickness $\mathrm{h}<\mathrm{h_c}$, the film grows pseudomorphically, forcing its lattice parameter to be equal to that of the substrate. For higher thickness, strain is relaxed either elastically or plastically. The strain is classified as either tensile or compressive depending on relative values of the film and substrate lattice parameters (respectively $\mathrm{a_f}$ and $\mathrm{a_s}$). For a partially relaxed layer there exists a tensile stress acting on the film for $\mathrm{a_f} < \mathrm{a_s}$ and compressive stress for $\mathrm{a_f} > \mathrm{a_s}$. The stress and strain acting on a hexagonal wurtzite crystal can be described by tensors.

$$\sigma_i = \sum_j C_{ij}\epsilon_j \tag{1.1}$$

Where σ are the stress components, ϵ are the strain components, and C are the stiffness coefficients. Heteroepitaxial growth of GaN usually leads to hydrostatic and biaxial stresses explained as follows.

Hydrostatic and biaxial strain

As the name suggests, biaxial stress acts along two directions, which in the case of GaN growth, acts in the (0001) basal plane, whereas the film is free to relax along the perpendicular [0001] direction. The strain in the film unit cell are calculated as:

$$\epsilon_{xx} = \epsilon_{yy} = \frac{a_f - a_s}{a_s} \tag{1.2}$$

$$\epsilon_{zz} = \frac{c_f - c_s}{c_s} \tag{1.3}$$

The in-plane and out-of-plane strains are related as:

$$\epsilon_{zz} = \frac{-2C_{13}}{C_{33}}\epsilon_{xx} = \frac{-2\nu}{1-\nu}\epsilon_{xx} \tag{1.4}$$

Here, ν is the Poisson ratio of the material, which for GaN is usually taken as 0.2, although the experimentally measured values range from 0.15 to 0.23[26]. The lattice mismatch causes biaxial stress on GaN, it is compressive for GaN growth and silicon and tensile for GaN on sapphire.

Hydrostatic stress is isotropic, its value is same along all directions and therefore does not change the shape of the unit cell.

$$\epsilon_h = \frac{\Delta a}{a_s} = \frac{\Delta c}{c_s} \tag{1.5}$$

Point defects induce hydrostatic stress in the material - whereas stress due to vacancies is compressive, for interstitial defects, it is tensile. Stress due to antisites and impurities depend on relative sizes of the atoms. It is usual for biaxial and hydrostatic stresses to coexist in a heteroepitaxial GaN film[29]. The resulting strains can be resolved as follows:

$$\epsilon_{zz} = \epsilon_{zz}^{bi} + \epsilon_h \tag{1.6}$$

$$\epsilon_{xx} = \epsilon_{xx}^{bi} + \epsilon_h \tag{1.7}$$

The hydrostatic component can be evaluated as:

$$\epsilon_h = \frac{1-\nu}{1+\nu}(\epsilon_{zz} + \frac{2\nu}{1+\nu}\epsilon_{xx}) \tag{1.8}$$

From measured strain values, the stresses can be computed from knowledge of stiffness coefficients.

$$\sigma_{xx} = (\frac{C_{11} + C_{12} - 2C_{13}^2/C_{33}}{C_{33}})\epsilon_{xx} \tag{1.9}$$

For biaxial stress, $\epsilon_{xx} = \epsilon_{yy}$, all off-diagonal components are zero and σ_{zz} can be calculated using equations (4) and (9). And for hydrostatic stress, $\sigma_{yy} = \sigma_{yy} = \sigma_{zz}$.

Strain relaxation

Lattice parameter mismatch between the substrate and the epitaxial overlayer (epilayer) impacts the growth and properties of the final grown material. Typically, the substrate thickness is much larger than film thickness, thus to a first approximation, we can consider that only the film is strained while the substrate is not; although sometimes a bowing of the substrate becomes non-negligible. The strained film tries to relax to its original lattice parameters to reduce its free energy. Relaxation can happen in two ways: either the strain is shared evenly among all unit cells, and the displacement of the film atoms from their unstrained positions is the same for all atoms on the interface or there can be a series of discontinuous atomic

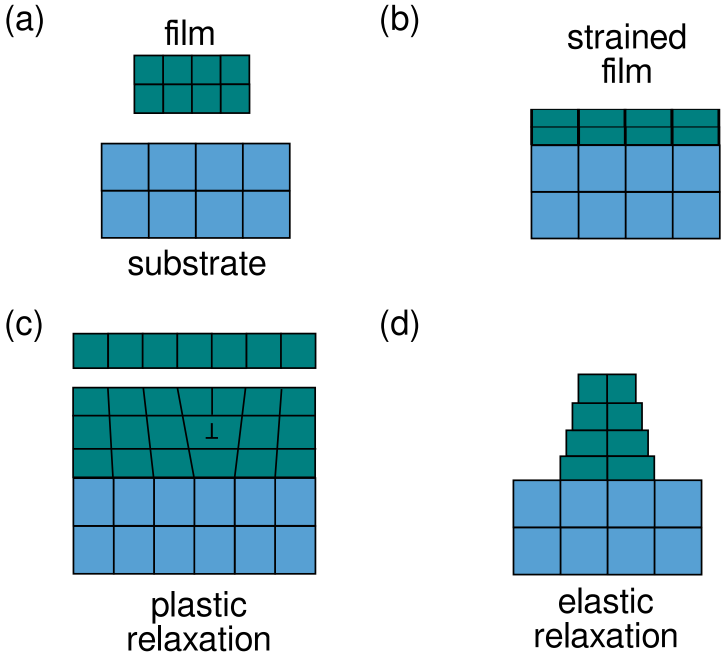

Figure 1.5: (a) Dissimilar sized film and substrate unit cells. (b) Strained film during lattice matched growth (c) Plastic strain relaxation by forming dislocations. (d) Elastic strain relaxation for low-dimensional nanostructure.

planes - called misfit dislocations (MD) to accommodate the strain. These two modes are referred to as elastic and plastic relaxation, respectively.

The elastic energy stored in the strained film per unit area is given as:

$$E^{el} = (2\mu\frac{1+\nu}{1-\nu})h\epsilon_{xx}^2 \tag{1.10}$$

Where, μ is the elastic shear modulus and h is film thickness. Thus, as the film grows, the stored elastic energy increases, and at critical thickness h_c, it is energetically cost effective to create dislocations rather than form another strained monolayer of film. To calculate the critical thickness, one has to solve the following transcendental equation[30]:

$$h_c = \frac{b}{4\pi(1+\nu)\epsilon_{xx}} ln(\frac{h_c}{b} + 1) \tag{1.11}$$

Here, b is the Burgers vector of the dislocation. It can be seen that the higher the strain due to mismatch, the lower the critical thickness. As an illustration, for GaN grown on sapphire with a thin AlN buffer layer h_c is about 3.2 nm[31]. Beyond the critical thickness, misfit and threading dislocations (TD) form. An MD is essentially a missing half atomic plane, and its two ends are connected to the film surface by two TDs. In the vicinity of a dislocation, the strain is high, but it decays quickly away from the dislocation core. If the density of MDs is insufficient, then the film still remains partially strained. Figure 1.5 shows schematic diagrams of the two modes of strain relaxation. In Figure 1.5(a), the dissimilar lattice parameters of the substrate are shown in their relaxed state. Figure 1.5(b) shows the pseudomorphic nature of the film growth for a thickness less than the critical thickness. Figure 1.5(c) shows plastic stress relaxation by the formation of MDs in a flat film, and (d) shows elastic stress relaxation in the case of a one-dimensional nanostructure.

The significant mismatch between GaN and the common substrates, 16% between GaN and sapphire, and 17% between GaN and silicon, leads to a high density of TDs and residual strain, forcing one to adopt different growth strategies. One such strategy is the introduction of intermediate layers (also called buffer layers), which have lattice parameters intermediate between GaN and the substrate, such as AlN, which reduce the mismatch and resulting dislocation density. Multiple buffer layers of different composition are often used for efficient reduction of dislocations and strain engineering.

1.5.2 Dislocations

Figure 1.6 shows a schematic diagram of a misfit dislocation at film-substrate interface giving way to threading dislocation. Dislocations can be viewed as the terminating line of an extra atomic plane. They are characterised by their Burgers vector, which specifies the magnitude and direction of lattice distortion caused by the dislocation. Figure 1.7 shows schematic diagrams depicting pure edge and screw dislocations. The Burgers vector is parallel to the dislocation line for a pure screw dislocation, perpendicular to it for a pure edge dislocation and for most dislocations, which are of intermediate nature (‘mixed type’), the angle is in between the two extreme cases. Table 1.2 shows the direction and magnitude of the Burgers vector of the three types of dislocations. The extent of lattice positions affected by the dislocation and the associated energy depends on the dislocation type. The dislocation energy per unit length has two components, core energy and elastic energy. Former is energy stored in the dislocation core, and latter is due to distorted bonds in its vicinity. For both screw and edge dislocations, the strain energy varies as the logarithm of the distance from the core.

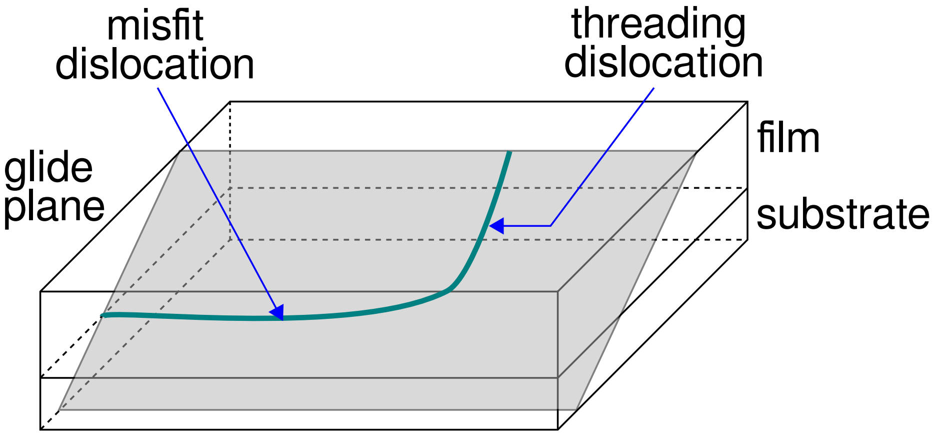

Figure 1.6: A schematic diagram showing misfit dislocation at the interface between film and substrate evolving as threading dislocation as the film grows.

Table 1.2: Dislocation types

Type	Burgers vector	Magnitude(nm)
Edge	$\frac{1}{3} < 11\bar{2}0 >$	0.319
Screw	$< 0001 >$	0.519
Mixed	$\frac{1}{3} < 11\bar{2}3 >$	0.608

In heteroepitaxy, some concentration of dislocations is unavoidable. Dislocations have been known to assist crystal growth by providing nucleation centres for adatoms and thereby reduce the energy cost of crystal growth even in low source fluxes. Dislocations have a number of properties that make them undesirable in device applications. They scatter charge carriers and hereby reduce the mobility in electronic devices. Dislocations act as non-radiative recombination centres for electrons and holes and reduce the luminescence efficiency of optoelectronic devices. In devices utilising a barrier for carriers, such as Schottky diodes, dislocations act as a path for leakage current and undermine the performance and device lifetime. Since dislocations can terminate on a free surface, it is clear that materials with a large free surface, such as nanostructures, can be used to reduce the density of dislocations and associated undesirable effects.

1.6 Properties of GaN nanostructures and effect of defects

Low-dimensional nanostructures of GaN help ameliorate several growth challenges of GaN heteroepitaxy on foreign substrates. They can relax strain efficiently and reduce the TD density owing to their large free sur-

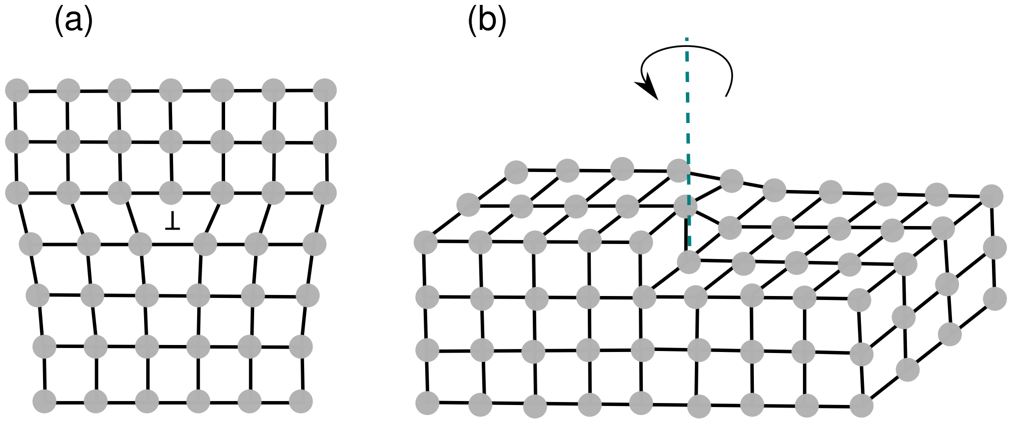

Figure 1.7: Schematic diagram showing (a) edge dislocation and (b) screw dislocation.

face to volume ratio. Additionally, low dimensional structures such as nanorods and nanowalls provide other advantages, such as the ability to tune electronic bandstructure and photonic properties by modifying their morphology and thereby inducing carrier and phonon confinement. Also, functionalisation of the nanostructures is possible by proper chemical treatment of the free surface.

Although device integration of GaN thin films is now an established technology, integration of nanostructures of GaN is less established. It is only recently that GaN nanorods have shown some promise in applications such as electronics, sensing, catalysis and lighting[12 32 33]. Compared to one-dimensional nanorods, two-dimensional nanowalls can be advantageous. Like nanorods, nanowalls also permit strain relief through lateral elastic relaxation, and dislocation filtering at free surfaces. A network of nanowalls (henceforth NwN) has a large surface to volume ratio, which is important for applications such as light detection, chemical sensing, catalysis etc. In contrast to nanorods, nanowall network provides lateral continuity of material which is important for integration into electronic devices.

Techniques used for the growth of GaN films can also be used for growth of both nanorods and nanowalls by controlling the conditions, including the use of catalysts. In MBE, a kinetic control of growth allows one to grow low dimensional structures. Specifically, a large nitrogen/gallium flux ratio suppresses lateral diffusion and changes growth mode from flat 2D to 3D. There are many reviews of nanorod growth available[34 35]. As for nanowall network, two pathways can be used: either a top-down approach to etch away bulk GaN or a bottom-up approach. Through the latter approach, Kesaria grew GaN nanowall network using plasma-assisted MBE for the first time in a self-assembled manner by kinetic control of growth[36]. The resulting GaN nanowall network growth was epitaxial, single-phase and had a number of interesting properties[37].

Defects, whether point or extended, determine the majority of functional properties of a semiconductor. They can affect the growth process itself by providing nucleation centres or by changing the energetics of growth through strain-related energy. Structural properties such as residual stress, hardness and elastic properties are determined through the type and concentration of defects. Defects introduce energy levels in the forbidden bandgap of the host semiconductor and thereby modify optical, electrical and magnetic properties.

In GaN, the most common defects are dislocations, stacking faults, and point defects, mostly vacancies and substitutional foreign atoms.The energy required to create defects is different for nanostructures than bulk crystals and can have a size dependence[38]. The formation energy of defects in the nanostructures is strongly dependent on the growth conditions. The growth parameters determine the position of the Fermi level, which has a direct effect on defect formation energy. For example, the calculated formation energies for gallium vacancy changes from more than 9 eV to around 2 eV as the position of Fermi level changes from near the valence band maximum to near the conduction band minimum[39]. For a Fermi level position at the top of the valence band, the formation energy of gallium interstitial defect calculated using density functional theory is found to be 0.58 eV in Ga-rich conditions and 1.02 eV in N-rich conditions[40]. The most energetically favourable native defect in most conditions in GaN is the nitrogen vacancy, which has a donor nature. Although there has been some debate in the past about the exact value of its formation energy, it has been used to explain the propensity of undoped GaN to be of n-type[41]. The nitrogen vacancy mostly exists in the +3 and +1 charge states, with the +2 state having high formation energy. The formation energy for +3 V_N is negative for Fermi energy close to valence band maximum, which indicates that acceptors would be readily compensated by the V_N - demonstrating the difficulty of p-doping of GaN. Silicon and oxygen atoms, which are typical contaminants during MBE and MOCVD growths of GaN, are shallow donors. Among the plausible native point defects, nitrogen vacancy, as mentioned, has a donor nature along with gallium interstitial, whereas gallium vacancy has an acceptor nature, and nitrogen interstitial is amphoteric along with the (both types of) anti-site defects[42].

These defects and their complexes form energy levels, transitions involving which have been used to explain the various defect-related luminescence properties of GaN[43]. Apart from atomic point defects, dislocations and stacking faults have also been implicated in the observation of certain types of luminescence, such as yellow luminescence[44][45][46]. As the electronic band-structure of the semiconductor is affected by carrier concentration, and they also affect the ionisation energies of the defects through the screening effect. Thus the luminescence properties may have a strong carrier concentration dependence.

While the doping effects of point defects are very well known, the defects can influence the transport properties in other ways also. The carrier mobility is determined by scattering from neutral and charged point defects, scattering from dislocations and from phonons. The electronic band-structure is affected by potential fluctuations around point defects and lead to band-tailing, which may influence optical and electrical properties. Lastly, point defects can have spin magnetic moments, which can make the semiconductor paramagnetic, or if some ordering phenomenon exists, whether by proximity or otherwise, cooperative magnetic effects such as ferromagnetism can occur. Defect related magnetic properties in non-magnetic semiconductor nanostructures are well reported[47][48][49].

In summary, changing the growth conditions can change the morphology including the dimensionality of the grown sample, which in-turn have an effect on the type and concentration of defects that are incorporated. These defects influence most of the observable properties of the semiconductor material and a clear understanding in this regard is necessary to tune the properties of these nanostructured materials.

1.7 Organisation of thesis

The work presented in this thesis is organised into chapters described as follows.

Chapter 1 provides an introduction to the GaN material. A brief historical description of GaN devices is presented to gain an understanding of the place occupied by this material in current technology. We discuss the intrinsic GaN material properties and impartation of size dependent properties for nanostructures of GaN. Defects typically formed during heteroepitaxy of GaN on different substrates are discussed along with how the defects affect the properties of the material, to set the stage for reporting of experimental results in the rest of the chapters.

Chapter 2 provides a description of the experimental techniques used in this work for growth and characterisation of the GaN samples along with the underlying principles.

In **Chapter 3**, we focus on the MBE growth of GaN thin films and nanostructures such as nanorods and nanowall network. The fundamental energetics and kinetics of growth are discussed and it is shown that by varying the kinetics the morphology of the GaN samples can be tuned. The mechanism underlying the growth of nanorods, porous films and nanowall network is studied.

In **Chapter 4**, we carry out experimental studies to investigate the micro-structural properties of GaN nanorods and nanowall network including residual stress and extended defects. We correlate the growth with the resultant structural properties.

Chapter 5 deals with optical properties of GaN nanorods and nanowall network. Band-edge and defect related emission from these low dimensional nanostructures are studied to gain an understanding of their defect structure and electronic properties.

In **Chapter 6** we study transport and electronic properties of GaN nanostructures. The observed superior transport properties of GaN nanowall network is understood in terms of polarisation induced 2DEG due to its unique morphology. Along with interesting magneto-transport properties, GaN nanowall network also shows morphology dependent magnetic properties. The electronic structure investigated through XPS measurements is also found to be morphology dependent. The difficulty in performing conventional electrical measurements of capacitance to study carrier distribution due to the peculiar morphology and high carrier concentration of nanowall network led us to carry out electrochemical studies to investigate the electronic properties.

Chapter 7 summarises the results of the thesis and provides an outlook for future work in this direction.

Chapter 2

Growth and characterisation techniques

To study the various properties of GaN thin films and nanostructures, we have used molecular beam epitaxy for sample growth and several in-situ and ex-situ characterisation techniques to study the samples. This chapter describes briefly the experimental methods.

2.1 Growth techniques

2.1.1 Plasma Assisted Molecular Beam Epitaxy

Molecular beam epitaxy (MBE) is a thin film growth technique that employs molecular beams of source elements that propagate in vacuum and condense on a heated crystalline substrate. MBE has been used to grow crystals of elemental or compound semiconductors, insulators and metals. In MBE, the source can be either be supplied in the gas phase or by heating a solid source which then sublimes. In MBE, high purity sources are used in low flux to reduce contamination and maintain a good vacuum. The lower flux of metals results in a slower growth rate compared to other vapour phase epitaxy (VPE) methods, such as metal-organic chemical vapour deposition (MOCVD) or halide vapour phase epitaxy (HVPE). The lower growth rate enables the fabrication of abrupt junctions or submonolayer growth, which allows for the creation of complex heterostructure devices. In this work, an SVTA - USA nitride MBE system has been used for sample growth, and Figure 2.1 shows a photograph of the installed system.

Epitaxy refers to a geometric relationship between the substrate and the overlayer crystal structure, i.e. that the film grows in an ordered orientation with respect to the substrate. The term molecular beam is understood to mean a low flux stream of atoms or molecules which travel in the same direction in a region of low pressure, such as an evacuated chamber. In order to ensure a significant growth rate, it is imperative that the collisions among the constituent particles (atoms, molecules, ions) before reaching the substrate surface is less probable. The mean free path between collisions is given by the well-known equation:

$$\lambda = \frac{K_B T}{\sqrt{2}\pi d^2 p} \tag{2.1}$$

Here, d is the particle diameter and p and T are the pressure and temperature respectively. Thus a low pressure leads to longer mean free path. As an illustration, a nitrogen molecule at zero degree Celsius travels travels about 60 nm on average in between collisions at atmospheric pressure whereas it could travel about 440 km at a pressure of 1×10^{-10} Torr! If the characteristic distance in the growth chamber is denoted as D, then the ratio λ/D, called Knudsen number, describes the probability of collisions. For λ/D $<<$ 1, most collisions are among the particles, whereas for λ/D $>>$ 1 particles travel in a straight beam with very few collisions among them. Additionally, the walls of MBE growth chamber are kept close to liquid nitrogen temperature using a cryo-shroud to trap the particles directed towards the walls.

In this discussion we shall limit ourselves to MBE growth of group III nitride semiconductors. The two common sources of nitrogen in MBE is nitrogen plasma and ammonia. The use of radio frequency plasma instead of ammonia is beneficial in several ways. Firstly, thermal decomposition (i.e. cracking) of ammonia is necessary to obtain active nitrogen species, which constraints the substrate temperature to be always kept high, in contrast to plasma assisted MBE (PAMBE) where the temperature is an independent parameter. Secondly, contamination of growth surface by hydrogen is a known issue, which does not arise in PAMBE. Finally, apart from changing the metal to active nitrogen flux ratio by changing the nitrogen flow rate, PAMBE allows for fine tuning of the ratio by controlling the applied power in the radio frequency generator. The next sections describe some components of MBE, viz. the nitrogen plasma source, effusion cells, residual gas analyser and the vacuum pumps used to achieve ultra high vacuum in the system. Figure 2.2 shows a schematic diagram of the parts of an MBE system.

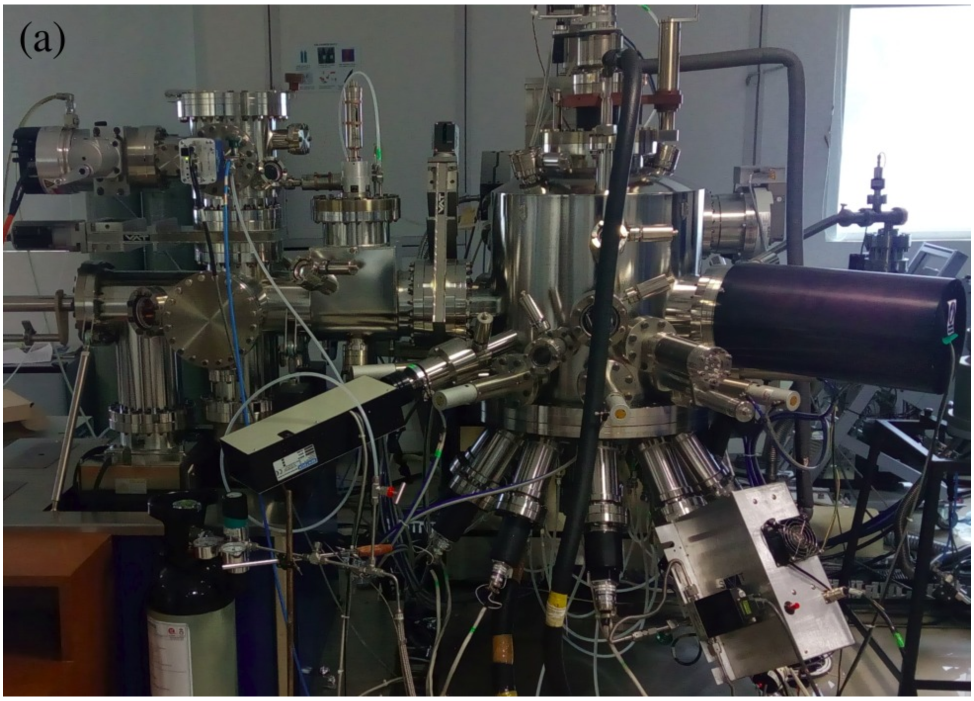

Figure 2.1: A phtograph of the SVTA nitride MBE system used in this work.

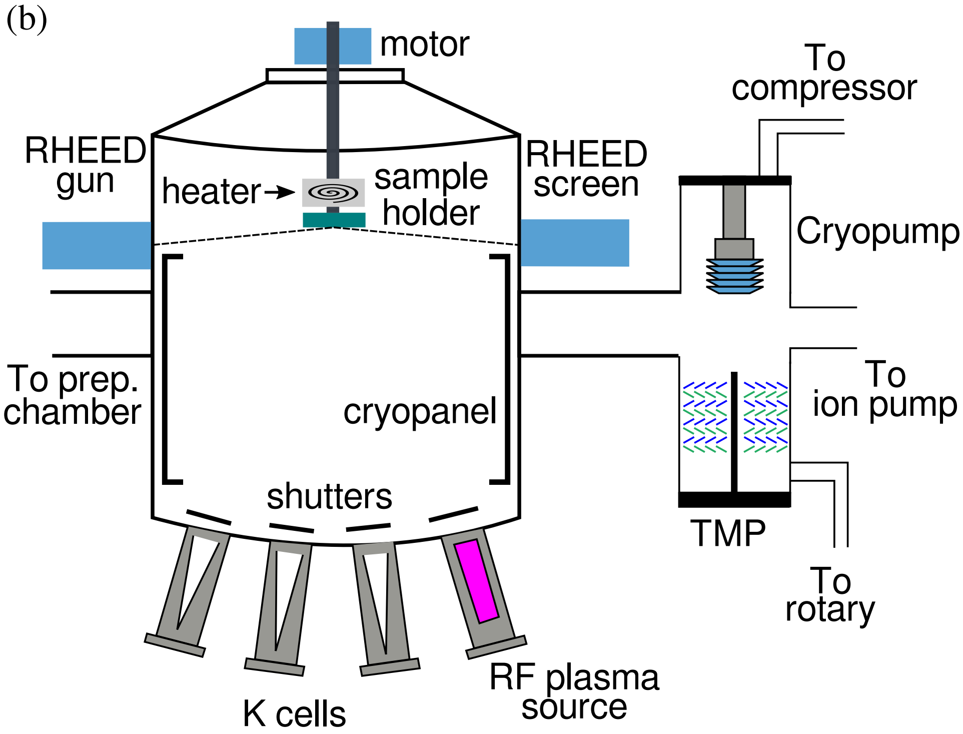
(b)
motor
To compressor
RHEED gun
heater
sample holder
RHEED screen
Cryopump
To prep. chamber
cryopanel
To ion pump
shutters
TMP
To rotary
RF plasma source
K cells

Figure 2.2: A schematic diagram of the PAMBE system showing its various components.

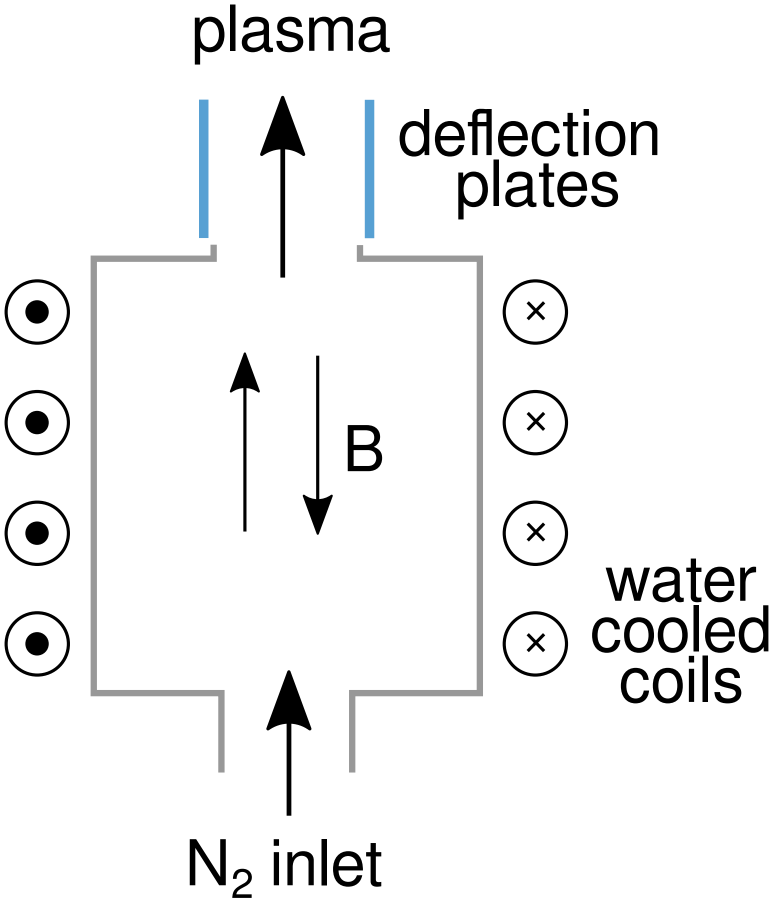

Figure 2.3: Schematic diagram of nitrogen plasma source.

2.1.1.1 Nitrogen plasma source

At typical III-nitride growth temperatures, nitrogen molecule is inert and cannot be used directly for growth. There are several techniques to obtain active nitrogen species such as using DC glow discharge plasma, electron cyclotron resonance (ECR) plasma and radio frequency (RF) plasma. The plasma sources produce a flux of neutral as well as charged molecules, and neutral and ionised nitrogen atoms, though the relative concentration of such species varies among the plasma generation methods. It has been found that apart from atomic nitrogen species, excited nitrogen molecule ($N_2{}^*$) can also contribute to GaN growth[50].

In this work, an SVTA RF 4.5 model plasma source has been employed, whose construction and working is described as follows. Figure 2.3 shows a schematic diagram of a RF plasma source and Figure 2.4 shows a typical emission spectrum of the nitrogen plasma recorded through an optical window. The central part of the plasma source contains a pyrolytic BN (PBN) tube positioned between RF coils for passing nitrogen gas through

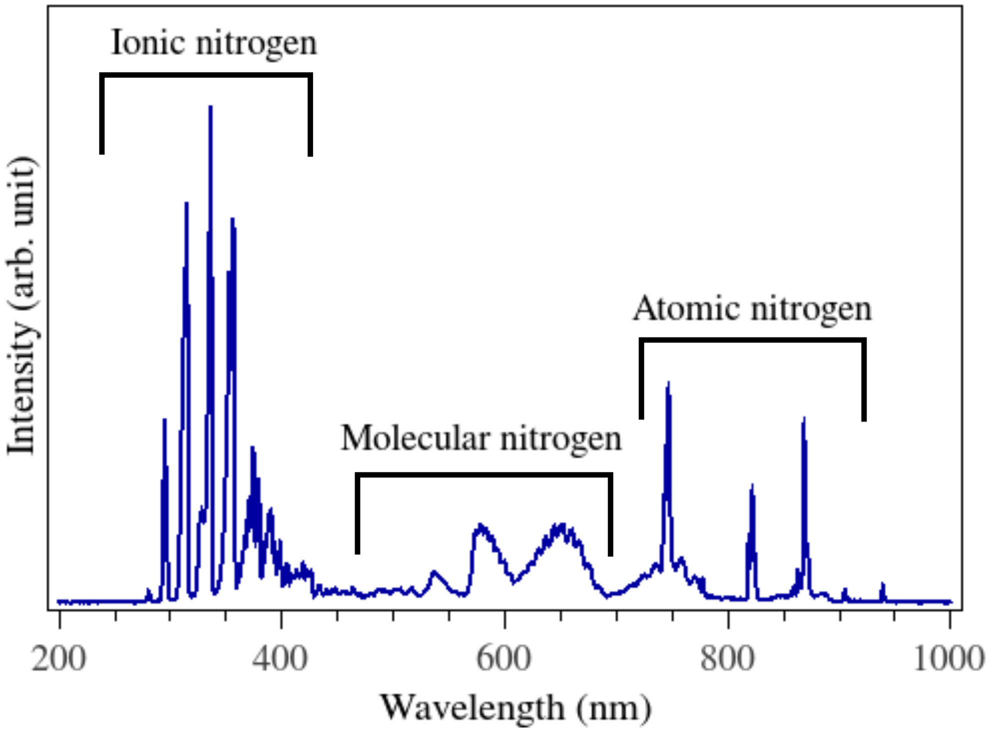

Figure 2.4: A typical spectrum of nitrogen plasma produced by the RF plasma source.

a leak valve, and a impedance matching network (also called ‘match box’). The RF coils are copper tubes wound several turns over the PBN tube. Chilled water, with a temperature of 16 °C flows through the copper tube to remove the heat. A mass flow controller is used to maintain a constant flow in the range of 0-10 standard cubic centimetre per minute (sccm) of 99.99999% pure nitrogen.

From the electrical power source, an alternating current applied to the RF coil generates an alternating magnetic field inside the coil. A changing magnetic field induces an electric field. The alternating field accelerates any charged particles present in the gas which then collide and ionise more gas molecules. This way a nitrogen plasma is generated rapidly. A pair of deflection plates positioned at the exit of the PBN tube are biased with DC voltages to create an electric field which acts upon the plasma. By changing the bias, the concentration of ions and neutral species reaching the substrate can be controlled.

2.1.1.2 Knudsen cells

Knudsen cells or k-cells are the source ovens which provide the group III metal flux. It mainly consist of a conical crucible for the storage of the metal evaporant, filaments for resistive heating, thermocouple for temper-

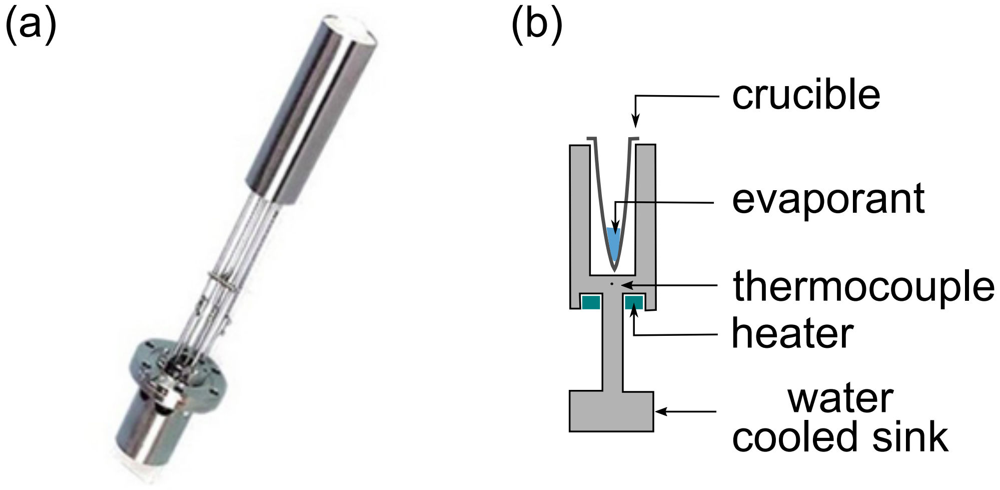

Figure 2.5: (a) Photograph of a k-cell. (b) Schematic diagram of the k-cell showing crucible, heater and thermocouple.

ature measurement and a water based cooling system. For growth of GaN, we use high purity (99.99999%) Ga as source material. For evaporating Ga, typically pyrolytic BN (PBN) crucibles are used. The conical shape of the crucible is used to compensate for the beam focussing, thereby providing a constant flux over an angular range, which is important for uniformity. Figure 2.5 shows photograph of a k-cell along with a schematic diagram showing its parts.

The metal flux is controlled by changing the k-cell temperature. The flux (in atoms per unit area per unit time) can be calculated by measuring the resulting beam equivalent pressure (BEP) using pressure gauges. The following expression can be used for such calculation.

$$\phi = \frac{1}{A}\frac{dN}{dt} = \frac{p}{2\pi m K_B T} \tag{2.2}$$

Here ϕ is the atomic flux, which depends on pressure p and k-cell temperature T, and m is the mass of one atom. Consistent system of units must be used, e.g. all in S.I. units. Since the metal flux is directly proportional to the k-cell temperature, the latter can be logged as a measure of flux, but this requires regular flux calibrations, i.e. measurement of flux BEP as a function of k-cell temperature.

A chilled water supply maintained at 16°C is provided to the k-cell to remove excess heat. The k-cells are equipped with pneumatically controlled shutters which can be operated through software to automate the process. In this way it is possible to grow complex multilayer structures without operator intervention.

2.1.1.3 Residual Gas analyser

A residual gas analyser (RGA) is a mass spectrometer which is used to determine the composition of gases present in a low pressure region. It can be used for checking contamination of a high vacuum chamber down to ppm levels or for leak detection in a system using helium or propanol. In this work, an SRS 200 model RGA has been used. The operating principle of RGA is ionization of gas molecules, separation of the ions according to their charge to mass ratio and finally, detection of those ions. The basic components of an RGA are depicted in Figure 2.8 and are: 1) an ionizer unit with electrostatic lenses, 2) a quadrupole mass filter, and 3) ion detectors.

The ioniser is made up of two thoria coated iridium (ThO_2/Ir) wire filaments to produce electrons by thermionic emission, a wire mesh anode to accelerate the electrons, which then hit the molecules and ionise them, and a focus plate kept at a negative potential to attract and guide the resulting positive ions. The next part is a quadrupole mass filter made up of four stainless steel (SS) rods positioned symmetrically between alumina spacers. A combination of DC and RF potential is applied to the rods to produce a quadrupole field. Specifically, a potential of ($V_{dc} + V_{rf}$ cosωt) is applied to the top and bottom rods and -($V_{dc} + V_{rf}$ cosωt) to the left and right rods. The trajectory of a charged particle in this electrodynamic field depends strongly on its charge to mass ratio (q/m). During an RGA scan probing different masses, the potentials are varied to select a particular charge/mass ratio ion to have a stable trajectory, with all other q/m ions getting accelerated onto the rods and becoming neutralised. The filtered ions are then detected, either directly by a Faraday cup (FC) or by an electron multiplier, called a channeltron. The FC is a SS metal bucket, placed on the quadrupole axis. The FC is kept at a negative potential to attract the positive ions, which then get neutralised, producing a current. The current signal is measured by a fast electrometer and is proportional to the number of ions. The FC detects all ions with equal sensitivity irrespective of its mass. Below a certain pressure, such as 10^{-9} Torr, it is preferable to use the channeltron as it has a very high sensitivity, and for the same reason the channeltron should not be used in low vacuum conditions. The channeltron consists of several tubes and a conical part made up of special resistive glass which has a high secondary electron emission yield. A high

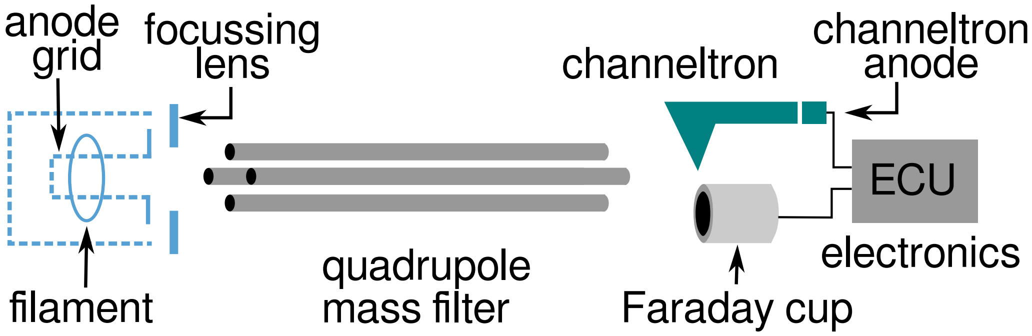

Figure 2.6: Residual gas analyser schematic diagram showing the main components.

negative voltage (upto ∼ -2500V) is applied to the front cone relative to the tube back-end, which accelerates the positive ions towards the cone. The ions which hit the cone, produce secondary electrons which are accelerated down the channels and produce more secondary electrons after hitting the special glass material. For each ion, there can be as many as 10^7 electrons, which is denoted as the gain of the channeltron and depends on the applied high voltage. The electrons are picked up by a grounded anode and produce electrical current, read by an electrometer.The high sensitivity of the channeltron makes RGA capable of detecting partial pressures down to 10^{-14} Torr, which is helpful in keeping the MBE system contamination free.

2.1.1.4 Vacuum pumps

In our PAMBE system, pumping of the growth chamber is done using turbomolecular pump, cryo-pump, and ion pump to achieve a base pressure of 2×10^{-11} Torr. The turbomolecular pump (TMP) consists of multiple pairs of high speed rotor blades and stationary stator blades. Gas molecules get hit by the angled blades of rotors and are directed towards holes in the stator unit. Subsequent stages transport the gas towards the backing rotary pump and thereafter through the outlet. The pumping rate depends on blade dimensions, their angle, and rotation frequency. A rate of 1000 litres/sec is typical in this case. Since the pump works on the basis of momentum transfer, light weight molecules such as hydrogen and helium are difficult to pump using TMP.

A cryopump achieves evacuation by condensing gas molecules on a cold surface. The pump has multiple stages. The first stage condensing array is maintained at 80 K and condenses water and hydrocarbon vapours. The second stage is maintained around 15 K and it condenses nitrogen, oxygen, argon etc. This stage also has a charcoal adsorber to trap hydrogen and helium. The condensation arrays are cooled by a closed cycle helium compressor. Compressed helium flows into a motor driven piston assembly, where displacement of the piston allows for expansion of helium and reduction in temperature. The returning piston pushes the helium back to the compressor and the cycle repeats. The pumping rate depends on the nature of the gas to be evacuated, especially its boiling and freezing temperature, and can range around several thousand litres/sec.

An ion pump operates by ionizing the gas molecules and using a strong electric potential of several kilovolts to trap them. It consists of a magnet and two electrodes - a cylindrical anode usually made of stainless steel and titanium cathode plates fixed on the sides. On application of a strong electric field, electrons are emitted from the cathode and are directed by the magnetic field to move in helical paths along the axis of the anode. The gas molecules suffer collisions with these electrons and get ionized and subsequently get attracted towards the cathode. The accelerated ions which hit the cathode, either get buried inside it or sputter out titanium. Sputtered titanium is active and it speeds up the pumping process by chemisorption of gas molecules, in a process called as gettering. The ion pump cannot operate in atmospheric pressure and needs another pump such as TMP to provide a base vacuum of the order of 10^{-4} Torr. The advantage of ion pump is that unlike TMP or cryopump, it lacks moving parts, thereby eliminating vibration, and unlike a rotary pump does not use oil, ruling out any contamination. The pumping rate of ion pump depends on the nature of the gas and is of the order of about 100 litres/sec or less.

2.1.2 Physical Vapour Deposition

Physical vapour deposition (PVD) is a class of thin film deposition techniques in which source material is converted into its vapour phase, and re-condensed onto a substrate for film growth. A number of methods are used to obtain the vapour phase such as evaporation, sputtering and laser ablation. In this work a PVD instrument from SVTA, USA has been used which has thermal evaporation and electron beam (e^- beam) evaporation modes for film deposition. Figure 2.7 shows a photograph of the PVD system used in this work along with its schematic diagram. E beam evaporation is a good technique to deposit high melting point materials such as

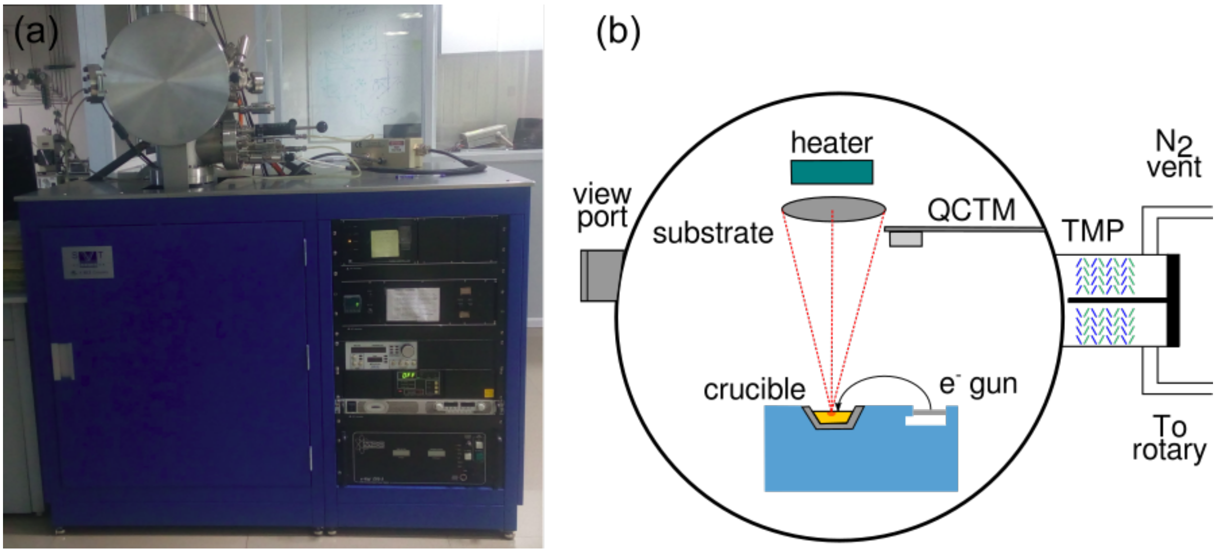

Figure 2.7: (a) Photo of SVTA PVD used in this work. (b) Schematic diagram of PVD showing electron gun, crucible and sample holder.

Pt or SiO_2. In this case the material is placed in a crucible, and the substrate is positioned above it in a line of sight direction facing the crucible. An electron gun produces a beam of electrons by heating a filament which are then accelerated to high energies by application of a 5.5 kV potential. A magnetic field is used to guide the electron beam onto the material placed inside the crucible. Different types of crucibles are available such as graphite, tungsten, molybdenum etc., and the choice depends on the material to be evaporated. In this work, PVD has been primarily used to deposit metal contacts onto the samples.

The chamber is kept at a vacuum of 10^{-8} Torr to maintain purity of the deposited film. The vacuum is achieved with the help of an ion pump and a TMP. A view-port allows observation of the process and especially to make sure that the electron beam falls at the centre of the source material. A quartz crystal thickness monitor (QCTM) is used to determine the thickness of the film being deposited in real time. It employs a piezoelectric quartz crystal which oscillates when an alternating voltage is applied to it. Deposition of film on the quartz crystal changes its resonance frequency which can be used for thickness measurement after calibration.

2.2 characterisation techniques

Several types of characterisation techniques have been used in this work to analyse the MBE grown GaN samples. These include observing the sample morphology using field emission scanning electron microscope (FESEM), investigating the crystal structure using X-ray diffraction (XRD), transmission electron microscope (TEM) and Raman spectroscopy, studying the sample's band structure and defect related properties through photoluminescence spectroscopy, UV visible NIR spectroscopy and X-ray photoelectron spectroscopy (XPS) and analysing its electrical properties by resistivity and Hall measurements. The techniques are described in the following sections in more detail.

2.2.1 Reflection high energy electron diffraction

Electron diffraction techniques are well established for analysis of structure of a crystalline or polycrystalline sample. Examples include selective area electron diffraction (SAED) in TEM, low energy electron diffraction (LEED) and reflection high energy electron diffraction (RHEED) etc. While the former is carried out in transmission mode and thus the information is from the whole thickness, the latter two are carried out in reflection mode and provide information from the sample surface. In this work, RHEED is used in-situ to monitor the MBE growth of samples. It can provide valuable insight regarding surface crystal structure, epitaxial relationship with substrate, sample roughness etc. It is also used to confirm atomic level cleanliness of the substrate by observation of characteristic diffraction patterns (DP) which are affected by presence of impurities. The RHEED system consists of an electron gun, focussing lens, deflection coils, phosphorescent screen to produce the DP and camera to capture the screen. Figure 2.8 shows a schematic diagram of the RHEED system.

The process of formation of diffraction patterns is explained as follows. The electron beam formed by the electron gun is accelerated and focussed by a magnetic lens. The X and Y deflection coils help direct the beam spot onto the sample. The beam hits the sample at a glancing angle of about 3°and thus the beam penetration is low and the information obtained comes from surface. Further due to the glancing angle, the region of the sample irradiated is about a mm long, meaning that the information is averaged over a macroscopic area.

The diffraction of electrons can be understood using the familiar 'Ewald construction' described as follows. Mathematically, the reciprocal space is the Fourier transform of real space. If the 2D lattice representing the crystal surface can be spanned by the lattice vectors $\overrightarrow{a_1}$ and $\overrightarrow{a_2}$, then the

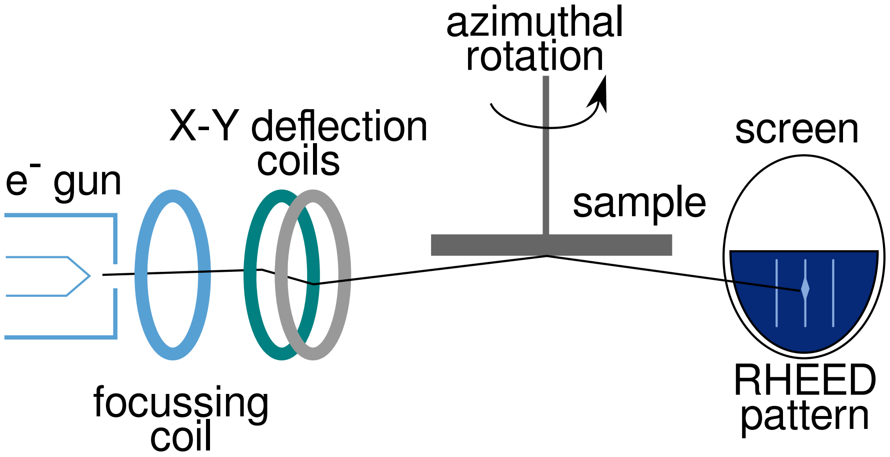

Figure 2.8: Schematic diagram of the reflection high energy electron diffraction (RHEED) depicting the basic components.

reciprocal vectors $\overrightarrow{b_1}, \overrightarrow{b_2}$ can be calculated using the formula: $\overrightarrow{a_i}.\overrightarrow{b_j} = 2\pi\delta_{ij}$ For example, if we consider a line of equidistant atoms in real space, the Fourier transform of it is a series of equidistant planes perpendicular to the line of atoms. A square lattice can be considered as a combination of rows of atoms and a second set of rows which are 90° rotated. Its reciprocal lattice would be intersections among the sets of equidistant planes which are 90° rotated, i.e. a set of rods arranged in squares, perpendicular to the sample surface. Considering only elastic scattering, the wave vector of electron would remain unchanged:

$$K_i = K_f = K_0 = 2\pi/\lambda_0$$

Where K_i and K_f correspond to incident and diffracted beams. A sphere drawn from common origin with radius K_0 is called Ewald sphere. The vectors drawn from origin to the intersection points of Ewald sphere and reciprocal lattice points correspond to allowed diffracted wave vectors. For the square lattice, the intersection between the reciprocal space rods and the Ewald sphere are points which appear a diffraction spots on the RHEED screen. An intersection of reciprocal space plane with Ewald sphere gives a circle, called Laue circle, which can often be observed in RHEED pattern in form of concentric semicircular arcs. Another feature often observed in RHEED pattern are Kikuchi lines or Kikuchi bands, which are straight lines or bands connecting bright diffraction spots and passing through the Laue circles. The Kikuchi lines arise from inelastically scattered electrons which penetrate the sample bulk and satisfy the Bragg diffraction conditions.

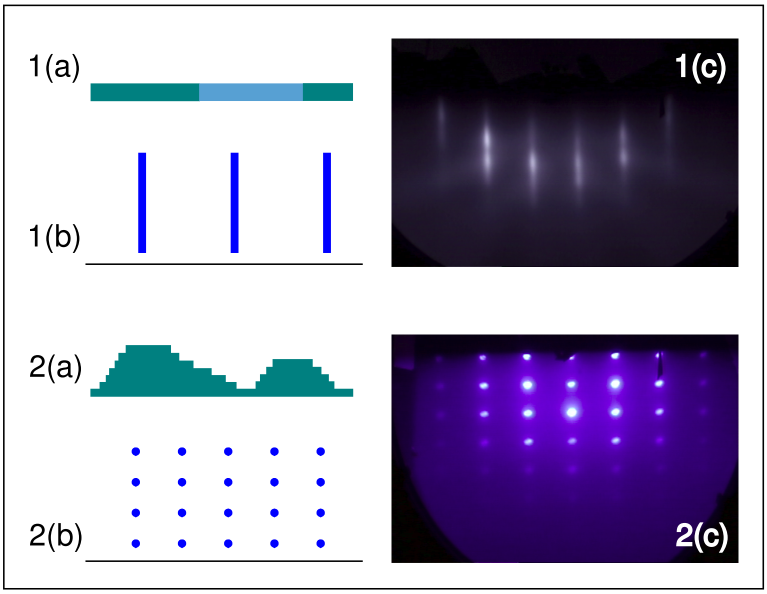

Figure 2.9: 1(a) A flat surface with domains smaller than electron coherence length. 1(b) Broadened reciprocal space rods. 1(c) Experimental RHEED pattern of a flat GaN sample.2(a) Rough surface with three dimensional islands. 2(b) Expected arrangement of reciprocal lattice points. 2(c) Experimental RHEED pattern of a columnar GaN sample.

Another concept which is important for practical RHEED pattern analysis is the coherence length of the electrons. Coherence length is the spatial dimension over which successive waves maintain a definite phase relationship and are able to interfere. For the electron beam, it depends on the degree of monochromaticity, taken as divergence ΔE among electron energies, and angular divergence of the beam, $\Delta\theta$. The coherence length l is given by:

$$l = \frac{\lambda}{\sqrt{2(\Delta\theta)^2 sin^2\alpha + (\frac{\Delta E}{E})^2 cos^2\alpha}}$$

Here, E is electron mean energy and λ is its wavelength and α equals 0° parallel to the beam and 90° perpendicular to it. For typical experimental conditions, l comes to about 100 nm. If the regions of sample irradiated by electron beam are made of coherently scattering domains which are smaller than electron beam coherence length, that will cause broadening of the RHEED spot or line feature. Finally, a few commonly observed RHEED patterns are presented here in Figure 2.9 where, subfigure 1 shows a flat sample surface composed of domains, each of which diffracts electrons coherently. The width of reciprocal lattice rods is inversely proportional to size of the domains, and thus domains smaller than electron beam coherence length broaden the reciprocal lattice rods significantly. The intersection of these rods and Ewald sphere are elongated ellipses which match with the experimental pattern shown in 1(c). Subfigure 2 shows a rough sample morphology with 3D islands. In this case, the electron beam transmits through top portions of the islands and forms a transmission diffraction pattern. For epitaxially grown islands, the arrangement of reciprocal space lattice points in three dimensions does not change and the intersection of those points with Ewald sphere form the observed pattern. For non-epitaxial growth, the islands may be oriented randomly and in this case, the spots are rotated about the electron beam and we obtain a Debye-Scherrer ring pattern.

2.2.2 Scanning electron microscopy

It is well known that the smallest feature size that can be resolved by a microscope depends on the wavelength of the light used for imaging. Since wavelength of electrons can be tuned electromagnetically to nanometre level or less, thus microscopes using accelerated electron beam for imaging can resolve sample feature size down to several nanometres. A scanning electron microscope (SEM) uses an electron gun to generate a beam of electrons which are then accelerated and focussed onto a sample. The scattering of the high energy electrons by the sample atoms can have different probable outcomes. The high energy electrons, called primary electrons, can ionize the atoms, and the electrons liberated in the process are called secondary electrons (SE). The primary electrons can cause the electrons of the atoms to get excited, and the relaxation of those electrons is accompanied by photon emission, in a process known as cathodoluminescence (CL). The primary electrons can also be backscattered (BSE - backscattered electrons) by the atoms, though with a smaller probability. By raster scanning the primary electron beam across the sample and detecting the signal - SE, BSE or CL photons, imaging can be carried out, though typically the low energy SE are used for this purpose.

In this work, a field emission scanning electron microscope (FESEM - quanta 3D, FEI, Netherlands) has been used to study the morphology of the samples. The instrument has SE as well as BSE detectors and a CL attachment.

Field emission (FE) is the method of extracting electrons from a material by applying large electric fields. A nanoscale sharp tip of the filament

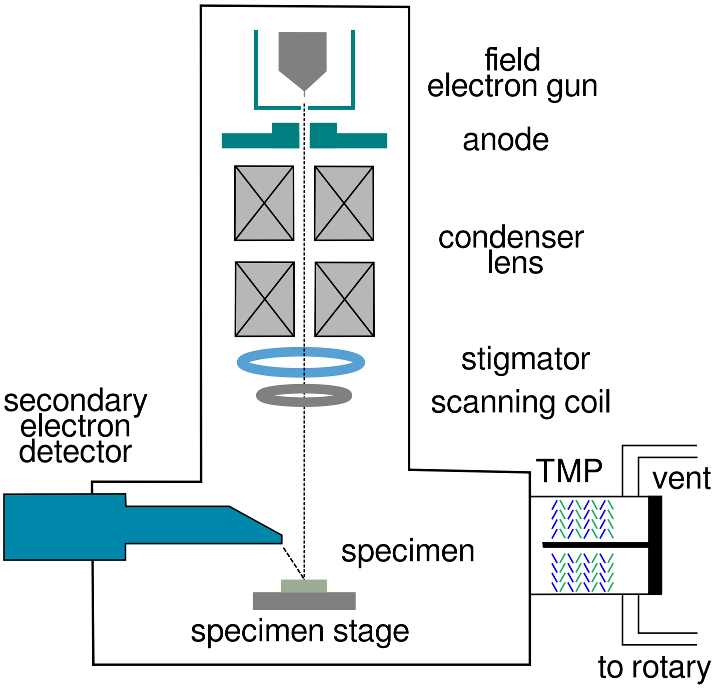

Figure 2.10: Schematic diagram of field emission scanning electron microscope (FESEM).

helps enhance the electric field experienced by the electrons for an applied potential difference. Thermionic emission uses heating for the electrons to overcome the work function of the material. Typically a Tungsten (W) filament is heated to more than 2000°C to obtain free electrons. Both type of electron sources can be used in SEM, although FESEM routinely provides better resolution than W-SEM.

Figure 2.10 shows a basic schematic diagram of an FESEM. The basic components and their functions are described as follows. The FE gun is made of tungsten and coated with zirconia (ZrO_2) to reduce work function. The anode positioned after the FE gun accelerates the electrons, from less than 1 kV to 30 kV. The whole column has to be kept in high vacuum (10^{-8} Torr or better) to reduce electron scattering. Turbomolecular pump and ion pump are used for this purpose. Apertures and electromagnetic lenses are used to obtain a tiny spot size of the electron beam. The condenser lens current is varied to vary the beam size; higher the current, more focussed the beam. Ideally the electron beam spot is perfectly circular, although errors in column alignment or electron gun can cause distortion in spot shape. This phenomenon is called astigmatism and results in uneven focus. A weak electric field or a quadrupole magnetic field is used in the stigmator component to correct for this aberration. Finally, the scanning coils are used to deflect the beam across the sample to create the image. As mentioned before, the SE originating from near surface are used typically for imaging. Although, BSE which originate deeper, are sensitive to atomic number of sample atoms and can be used for a phase contrast imaging.

2.2.3 Transmission electron microscopy

Similar to SEM, a transmission electron microscope (TEM) uses a focussed beam of high energy electrons for imaging a sample. It can also provide electron diffraction pattern from a selected region of the sample. An aberration corrected high resolution TEM (HRTEM) can provide images of sample with an atomic level resolution. TEM needs extensive sample preparation steps to obtain an thin slice of the sample which is transparent to electron beam.

In this work, FEI Titan and FEI Tecnai have been used for recording images and DPs of GaN nanostructures. The former is an aberration corrected 300 kV TEM with a resolution down to 0.8 Å. It has additional EELS detectors.

The basic operation of TEM is shown in Figure 2.11, and described as follows. The electron gun provides a beam of electrons which are accelerated by anode to several hundred kV of energy and made to pass through a hole in anode plate. Thereafter one or two condenser lenses focus the beam to a point some distance above the specimen. The electrons can interact with the specimen to produce a variety of secondary signals. The electrons might pass through without scattering, or it might scatter elastically or inelastically. The energy transfer from primary electrons to the atoms may lead to liberation of secondary electrons, Auger electrons or X-ray photons. For image and DP formation, only the scattered primary electrons are used. Several types of electromagnetic lenses are used such as objective lens, intermediate lens and projector lens. The objective lens placed after the specimen provides a small magnification of the order ×50. To record the DP from the sample, the lenses are adjusted so that the back focal plane of the objective lens becomes the object for the intermediate lens. This makes the entire DP to be projected onto the screen through the projector lens. It is possible to record DP from any chosen region of the sample by using a selective area diffraction (SAD) aperture in the image plane of the objective lens. By moving the aperture near to the chosen

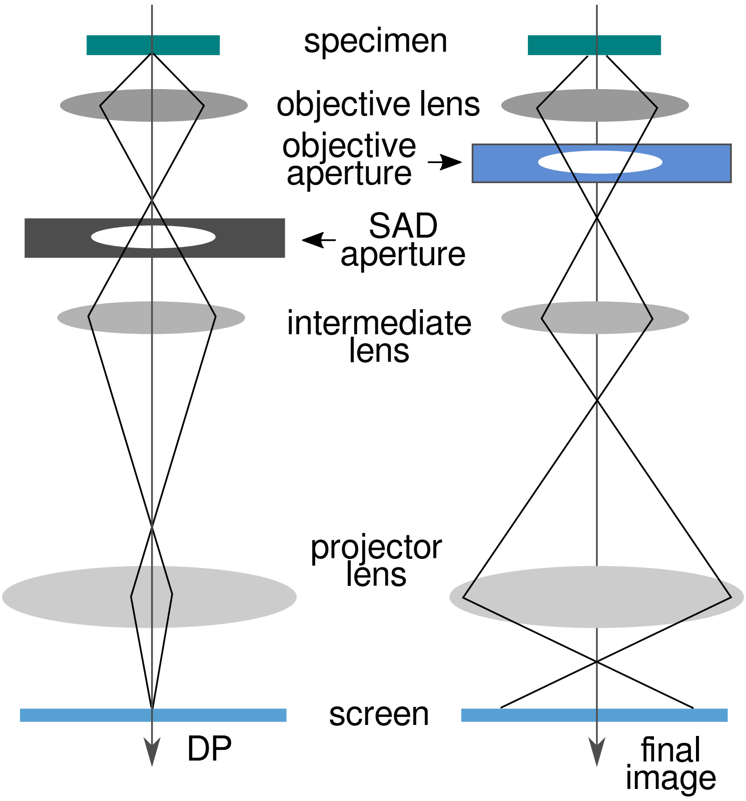
specimen
objective lens
objective aperture
SAD aperture
intermediate lens
projector lens
screen
DP
final image

Figure 2.11: A schematic diagram of diffraction pattern and image formation in transmission electron microscope.

section of sample, the electrons from other portions are blocked and do not take part in DP formation. For sample imaging operation, the SAD aperture is not used, but rather an objective aperture is placed into the back focal plane of the objective lens. The intermediate lens is adjusted such that the image plane of the objective lens becomes the object plane of the intermediate lens. If the direct beam is used for image formation, it forms bright field (BF) image. If the intermediate lens is adjusted so that scattered electrons which are not part of direct beam are used for image formation, then it forms dark field (DF) images.

TEM is an excellent instrument to study the crystal structure of the sample along with the defects present. Using an SADP pattern or a high resolution image, the sample phase can be identified, and the lattice parameter can be accurately measured, which can give information about any non-uniform strain in the film. When the sample is tilted inside the TEM, the reciprocal lattice space of the sample is also tilted accordingly and it is possible to choose which reciprocal lattice vector g takes part in the image or DP formation. As mentioned previously:

$$g(hkl) = \frac{1}{d_{hkl}}$$

and thus the interplanar spacings $\mathrm{d_{hkl}}$ can be calculated. In practice, one can calculate the d values from DP using the following equation:

$$Rd_{hkl} = L\lambda \tag{2.3}$$

Here, R is the distance of a particular diffraction spot from the bright central spot (corresponding to unscattered direct electron beam), and L and λ are constants denoting distance between sample and screen and the electron wavelength. Further, by tilting the sample (thereby choosing g vector), and observing the contrast, information about Burgers vector 'b' of a dislocation or index of planar defect can be obtained. For example, one can invoke the well known 'invisibility criterion', g.b=0 to calculate b. If this criterion is satisfied, the dislocation will either vanish ($g.b = 0$) or appear with a weak contrast ($g.b \approx 0$). In all, detailed defect characterisation is possible in TEM along with obtaining spectroscopic information such as plasmonic excitations, optical excitations etc. from electron energy loss spectra of the sample. However, since the region of sample explored in TEM is small, it is advisable to complement this technique with a larger area characterisation technique such as XRD to get statistically correct

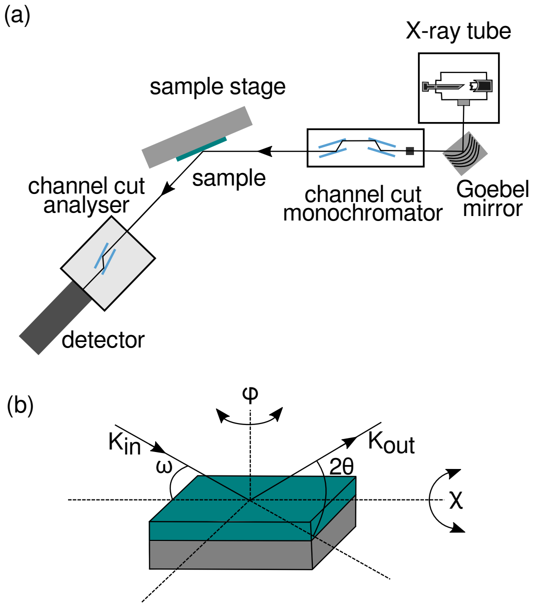

Figure 2.12: (a) A schematic diagram of the HRXRD set-up. (b) Definition of some commonly used angles.

information.

2.2.4 High resolution X-ray diffraction

Crystalline solids have their constituent atoms arranged in a periodic manner in three dimensions. This periodicity and the fact that typical interatomic distances are of same order as wavelength of lab X-ray sources, makes diffraction of X-ray photons a powerful non-destructive tool to study crystal structure. In this work, GaN thin films and nanostructures have been grown on non-native substrates. The lattice mismatch between the film and the substrate and also the difference in thermal expansion coefficient of the two leads to presence of strain, which is partially relaxed through formation of extended defects such as misfit and threading dislocations (MD and TD). X-ray diffraction (XRD) can be used to determine all these structural properties such as sample lattice parameters, strain, density of defects, epitaxial relationship between a epilayer and substrate etc. We have used a high resolution XRD (HRXRD), D8 discover - from Bruker, USA for studying the samples.

Figure 2.12(a) shows a schematic diagram of basic components of the instrument. These are discussed briefly here. The source part consists of a copper anode, Goebel mirror and a monochromator which has four Ge crystals and several removable width limiting slits. This produces a colli-

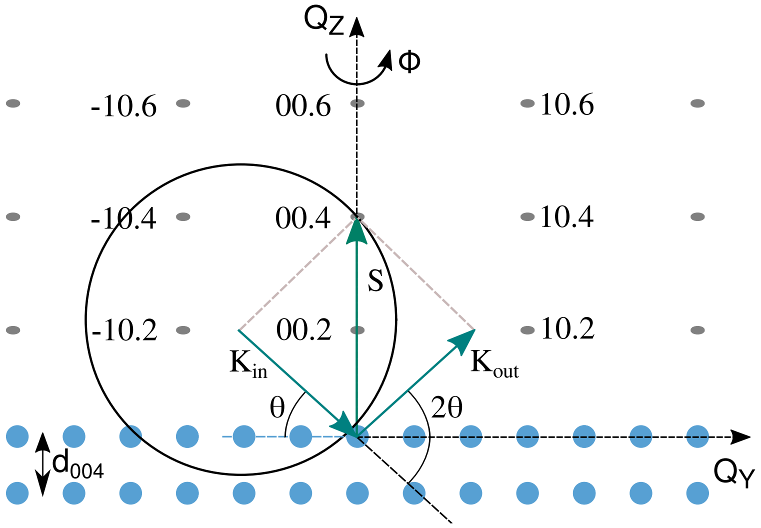

Figure 2.13: Schematic diagram showing reciprocal lattice points and XRD scan geometry.

mated parallel Cu K-α X-ray beam of wavelength 1.54056 Å, with the K-β component filtered out. The sample stage is fixed onto a four circle goniometer, which gives freedom to choose geometry between incident beam, sample and detector. A scintillation counter is used as a point detector for the X-ray. Additionally, there is a motorized slit and analyser Ge crystal, either of which can be used in front of the detector to choose what range of angles of the scattered X-ray is to be detected. While analyser crystal is used for high resolution work, an open detector (slits widened maximally) improves the signal-to-noise ratio of the XRD scans, and depending on the need, any option can be chosen.

Figure 2.12(b) depicts the angles that define the experiment geometry and are explained as follows. The angle ω is between the sample plane and the direction of the incident beam, not to be confused with θ, which is the angle between the atomic planes under study and the incident beam. For atomic planes which are parallel to film surface, ω equals θ, but for atomic planes which are at an angle χ with respect to film surface, the two are not equal. The angle 2θ is between the direction of the incident beam and the direction of scattered beam. Finally, ϕ angle is the in-plane azimuthal angle about an axis perpendicular to the sample.

It is well-known that for constructive interference the Bragg's condition is to be satisfied. If a set of atomic planes have interplanar distance d, then it will scatter X-ray of wavelength λ with the scattering angle 2θ if the following equation is satisfied:

$$2dsin\theta = n\lambda \tag{2.4}$$

For ease of visualization of the diffraction process, we again use the concept of reciprocal space. We begin by arbitrarily choosing a point as the common origin in real and reciprocal space. For every set of atomic planes of the crystal lattice, there exists a point in reciprocal space called reciprocal lattice point (RLP) such that, if a vector is drawn from the origin to the RLP, the length of the vector would be inverse of the interplanar distance of the set of atomic planes and the direction of the vector would be perpendicular to the atomic planes. Figure 2.13 shows some reciprocal lattice points for an wurtzite crystal such as GaN. If the wave vectors of the incident and scattered X-rays are $\mathrm{K_{in}}$ and $\mathrm{K_{out}}$ respectively, then their geometric difference, $\mathrm{K_{out}}$ - $\mathrm{K_{in}}$ is called scattering vector 'S'. By varying the angles, the directions of $\mathrm{K_{in}}$ and $\mathrm{K_{out}}$ can be changed, although their length ($K = 2\pi/\lambda$) must remain constant. This changes the scattering vector in the reciprocal space. An XRD scan involves changing the experimental geometry angles so that the scattering vector can scan over one or more RLPs.

The most common XRD scan is $2\theta - \omega$ coupled scan, in which the detector angle 2θ is varied twice as fast as ω. In reciprocal space, this only changes the length of S without changing its direction, and S scans RLPs radially outward. The $2\theta - \omega$ scan is used for material identification by measuring the lattice parameters of the material. Using equation (4), the d value corresponding to a particular $2\theta - \omega$ peak can be calculated and in case of hexagonal wurtzite structure, the d value is related to lattice parameters a and c as:

$$\frac{1}{d^2} = \frac{4}{3}\frac{h^2 + hk + k^2}{a^2} + \frac{l^2}{c^2} \tag{2.5}$$

Thus by recording at least one symmetric ($h = 0, k = 0, l \neq 0$) and one asymmetric (atleast one between h and k non-zero, $l \neq 0$) scan, the a and c parameters can be calculated, though for better accuracy, more scans should be recorded. Any change in the lattice parameters from its ideal value constitutes strain, which may be tensile or compressive. The error in measurement of d can be found by differentiating Bragg's law and is given below.

$$(\Delta d_{hkl})^2 = (\frac{cos\theta\lambda\Delta\theta}{2sin^2\theta})^2 + (\frac{\Delta\lambda}{2sin\theta})^2 \tag{2.6}$$

It can be seen that since the error Δd_{hkl} decreases with increasing 2θ, it is better to consider higher index reflections, for example 006 instead of 002. A caveat is that higher index reflections tend to have lower intensity (thus lower signal to noise ratio) and so a balance has to be found.

Another commonly used scan is the ω scan, also known as rocking curve measurement, in which only the sample stage is moved, changing ω angle, keeping detector position fixed. Rocking scan is used often to estimate crystal quality, as a pure single crystal would lead to a narrow peak, whereas a sample containing many extended defects or consisting of slightly misoriented blocks would lead to a broad peak. An expression, often indiscriminately used to compute the density of threading dislocations is given below:

$$\rho = \frac{\beta^2}{Kb^2} \tag{2.7}$$

Here, ρ is dislocation density (number per unit area), β is width of rocking scan peak (in radians) and b is the relevant Burgers vector (b equals c lattice parameter for screw dislocations and a for edge). K is a constant usually taken as 4.35 or 9[26]. Although this formula is very commonly used, in theory it only applies when the distribution of the dislocations is completely random (no dislocation bunching). If dislocations are located at grain boundaries, forming a mosaic structure, then the following expression holds:

$$\rho = \frac{\beta}{3bt} \tag{2.8}$$

Here, t is the average grain size and b is Burgers vector.

Although mathematically, the reciprocal lattice is occupied by points, in practice, strain, tilt, twist and finite coherence length broadens the point to an ellipsoid. In rocking scan, the direction of $\mathrm{K_{in}}$ changes, making the scattering vector trace out an arc in reciprocal space. The direction of tangent to the arc is perpendicular to the radial direction of the $2\theta-\omega$ scan. Thus a combination of $2\theta-\omega$ and ω scan can probe the broadened reciprocal lattice point in its entirety, and this procedure is called as reciprocal space mapping (RSM).

The other scans which are often used are detector scan - in which only the detector position is moved, and χ and ϕ scans in which only those respective angles are varied keeping other positions fixed. The χ scan is sensitive to out-of-plane tilt present in the film whereas ϕ scan is sensitive to in-plane twist. Combined broad range χ and ϕ scans constitute a ‘pole figure’ which represents preferred orientation in a polycrystalline sample and can be used to examine in-plane epitaxial relationships in an epilayer sample.

In all, HRXRD is a powerful technique for structural characterisation of samples non-destructively and provides averaged information from a macroscopic region of a sample - of the order of 10 mm^2, - a typical X-ray beam spot size.

2.2.5 Raman spectroscopy

Light-matter interaction can take many forms depending on the type of matter and the energy of light. Absorption and re-emission of photon either instantaneously (scattering) or after a time delay (fluorescence and phosphorescence) can be used to characterize the material. Light can be scattered either elastically without any change in wavelength, for example in case of Rayleigh scattering, or inelastically, such as in case of Raman or Brillouin scattering. In Raman scattering, the change in energy of photon typically corresponds to excitation of vibrational modes of the material, though in special cases, lower energy rotational energy levels or higher energy electronic energy levels may also be probed.The process of absorption and re-emission of photons takes place by creation of instantaneous dipole moments by distorting the electrons from their position. The ease of distorting electronic cloud from its equilibrium position is described by its polarisability. If the polarisability of the material system is anisotropic and changes during vibration, then the vibrational mode is said to be Raman active. Since the polarisability of a material depends on factors such as electron density of constituent atoms, bond length, bond strength etc., thus lattice vibrations (phonon), collective valence electron oscillations (plasmon) and similar excitations can be studied using Raman spectroscopy.

In a typical set-up of a Raman spectroscopy, a visible, near infrared (NIR) or near ultra-violet (NUV) laser is used for excitation, and a monochromator and a CCD camera is used for the spectrometer. This

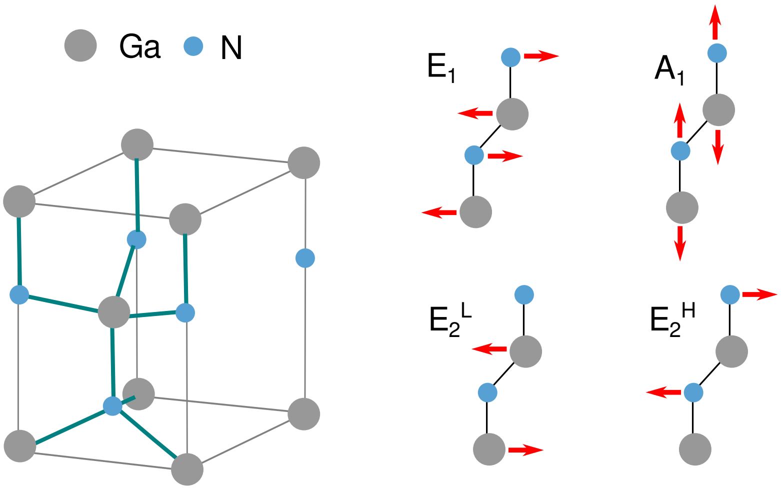

Figure 2.14: Wurtzite structure and its Raman active modes.

technique is non-contact and non-destructive, does not require special sample preparation and can provide a wealth of information. Especially in case of nitride semiconductors, the semi-covalent nature of the bonds mean that the electrons are less localised (compared to a purely ionic solid), and thus a larger modulation of the electronic polarisability is possible, giving rise to stronger scattering. Also, nitride semiconductors are highly stable against laser irradiation. In III-nitride semiconductors, the vibrational states are sensitive to alloy composition, crystalline quality, stress, electron concentration among others. Growth of GaN on non-native substrates such as silicon and sapphire gives rise to extended defects such as misfit and threading dislocations and residual stress, which has been characterized in this work using Raman spectroscopy.

Conservation laws dictate that both energy and momentum of the system be conserved. Thus, if a phonon of energy $\hbar\omega$ and momentum $\hbar$q is created (Stokes Raman shift) or annihilated (Antistokes Raman shift) during the photon scattering, then: $\omega = \omega_i - \omega_s$ and $q = K_i - K_s$ where, $\omega_i(\omega_s)$ and $K_i(K_s)$ are the frequency and wavevector of incident (scattered) photon. In a typical experiment involving visible, NIR or NUV photons, only zone center (q$\sim$0) phonons are probed. For the hexagonal wurtzite structure, group theory calculations predict that there are total 8 normal phonon modes at zone centre (Γ point): $2A_1+2E_1+2B_1+2E_2$. Among these, the A_1, E_1 and E_2 modes are Raman active. Figure 2.14 shows the stable phase wurtzite structure of GaN and the atomic vibrations which are associated with the allowed first order Raman modes. Different geometries, i.e. position of source and detector with respect to sample are required to observe different Raman modes. For example, in $z(x,x)\overline{z}$ geometry, A_1(LO) and E_2 modes can be observed and in $x(y,z)y$ geometry, E_1(TO) and E_1(LO) modes can be observed. The geometry notations are described as follows. The symbol $\alpha(\beta\gamma)\delta$ refers to direction of incident light α with polarization direction β and direction of scattered light δ with polarization direction γ.

The E_2 phonon mode has high Raman scattering cross section and is widely used to gauge the crystalline quality. The width of E_2 Raman peak is related to crystal quality, i.e. narrower the peak, better is the quality. The position of the $E_2{}^H$ peak in unstrained GaN is about 568 cm^{-1}, and the peak position shifts to higher (lower) values in case of presence of compressive (tensile) stress. A shift of 2.9 cm^{-1}GPa^{-1} is generally agreed upon for biaxial stress in GaN. To convert from stress σ_{xx} to strain ϵ_{xx} the following expression may be used:

$$\sigma_{xx} = [(C_{11} + C_{12}) - C_{13}^2/C_33]\epsilon_{xx} \tag{2.9}$$

Where C_{ij} are the elastic stiffness coefficients of GaN.

2.2.6 Ultraviolet-visible-near infrared spectroscopy

Absorption of light in ultraviolet-visible-near infrared (UV-vis-NIR) part of the electromagnetic spectrum by a material can lead to electronic transitions. Absorption studies are used to probe unoccupied energy levels of a material as photon can only be absorbed by an electron if the resulting final energy level is unoccupied. Thus factors such as doping, defects, stress etc. which affect the band structure of the material can be studied using UV-vis-NIR spectroscopy.

In this work a Perkin Elmer 750 UV-VIS-IR spectrometer was used to carry out absorption spectroscopy in transmission mode. Deuterium and tungsten-halogen lamps have been used as light sources along with photomultiplier tube (PMT) and thermoelectrically cooled PbS detectors.

The UV-vis-NIR spectroscopy can be carried out in transmission mode or reflection mode, depending on whether the substrate is transparent or opaque and in this work, mostly the former has been used. In transmission mode, the sample is placed between the source light monochromator and detector and the intensity of light passing through the sample is measured. If the energy of light photons are sufficient to excite the electrons across band gap, the light is absorbed and the intensity of light transmitting through is less than 100%. The absorption coefficient $\alpha(h\nu)$ is defined as relative rate of decrease of light intensity $I(h\nu)$ as it propagates in the material:

$$\alpha(h\nu) = \frac{1}{I(h\nu)}\frac{d}{dx}I(h\nu)$$

The preceding equation describes an exponential decrease in intensity as light propagates, and this behaviour is called as Beer-Lambert's law.

The energy dependence of the absorption coefficient is different for different processes such as direct band to band transition, indirect transition, free carrier absorption etc. and the transition rates can be calculated by Fermi golden rule. We omit the theory here and only note the final expressions of absorption coefficient. For direct transitions we have:

$$\alpha_{abs}(\hbar\omega) \propto |<v|p|c>|^2 \rho_{cv}(\hbar\omega)[f_{Ev} - f_{Ec}]$$

Here, v and c are initial and final states in the valence and conduction band respectively, ρ_{cv} is the joint density of states, f_E is Fermi function and p is electromagnetic momentum operator. Assuming two parabolic bands with an allowed inter band transition, the joint density of states becomes:

$$\rho_{cv}(\hbar\omega) = \frac{1}{2\pi^2}(\frac{2m_r}{\hbar^2})^{\frac{3}{2}}\sqrt{\hbar\omega - E_g}$$

Here, $\mathrm{m_r}$ is the reduced mass for valence and conduction bands ($1/\mathrm{m_r} = 1/\mathrm{m_e} + 1/\mathrm{m_h}$). Also, assuming very low temperatures, where valence band is nearly full, and conduction band is nearly empty, $f_{Ev} \approx 1$, $f_{Ec} \approx 0$ and the coupling matrix element becomes:

$$|<v|p|c>|^2 \approx \frac{m_0 E_g}{2}\frac{m_0}{m_*}$$

Here $\mathrm{m_0}$ is free electron mass. Combining these, and omitting constants, we get

$$\alpha_{abs}(\hbar\omega) \propto \frac{1}{\hbar\omega}\sqrt{\hbar\omega - E_g} \tag{2.10}$$

The final expression shows that if $(\alpha_{abs}(\hbar\omega)\hbar\omega)^2$ is plotted against $\hbar\omega$, the function will have an x-intercept at $\hbar\omega = E_g$, i.e., the band gap. This is the familiar Tauc plot and has been used in this work. For non-degenerately doped semiconductors, the absorption edge, i.e. where the absorption coefficient increases sharply, corresponds to the optical gap. However, for n(p) type degenerately doped semiconductors where the Fermi level has moved inside conduction (valence) band, the absorption edge corresponds to difference between valence band minimum (conduction band maximum) and Fermi level.

In the experiment, the transmittance is defined as: T = I_t/I_0. From Beer-Lambert's law: $I_t = I_0 e^{-\alpha d}$ where d is the sample thickness. This can be written as,

$$\alpha_{abs}(\hbar\omega) = \frac{ln(1/T)}{d} \tag{2.11}$$

This expression helps us experimentally determine the absorption coefficient, which embodies the optical properties of the semiconductor sample.

2.2.7 Photoluminescence spectroscopy

Photoluminescence (PL) is the phenomenon of emission of light from a material after absorption of photons. In case of semiconductors, if the incident photon energy is greater than the band gap, it creates an electron-hole pair by facilitating transition of an electron from valence band to conduction band. The relaxation can occur via a number of pathways such as band-to-band transition - where recombination happens between a free electron and free hole, free to bound transition where one of the carriers is bound to a dopant, or donor-acceptor pair (DAP) recombination between an electron bound to a donor and a hole bound to an acceptor. All these recombinations are accompanied by emission of a photon, and are therefore known as radiative recombinations, in contrast to non-radiative recombinations where the energy relaxation happens via generation of phonons.

Figure 2.15 depicts the above mentioned radiative recombination pathways involving free or bound carriers. The excitation of electrons might be followed by relaxation pathways (a), (b), (c) or (d) denoting band-to-band transition, free electron - acceptor bound hole recombination, donor - acceptor pair recombination or donor bound electron - free hole recombination respectively. The concentration of native defects and impurities present in the semiconductor affects the band structure in several ways, such as by introduction of defect related energy levels, band gap shrinkage or band filling effects. These factors determine the energies of the emitted photons, relative intensity of luminescence corresponding to different transitions, and their lifetimes. Because of this, photoluminescence spectroscopy or its variant, photoluminescence excitation (PLE) spectroscopy are important tools to probe the semiconductor band structure and pres-

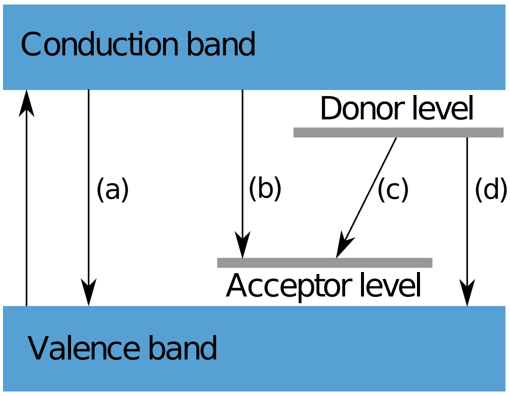

Figure 2.15: Examples of radiative recombination transitions in semiconductors: (a) band to band transition, (b) recombination between free electron and hole bound to acceptor, (c) donor acceptor pair recombination, and (d) donor bound electron and free hole recombination.

ence of defects in a non-contact and non-destructive manner. In a PLE experiment, the detector detects the intensity of light at a particular wavelength while the excitation wavelength is varied continuously. PL spectroscopy carried out as a function of temperature or incident light beam power contains a wealth of information. We have used a customized system from Edinburgh instruments in this work, and the set-up is described in the following.

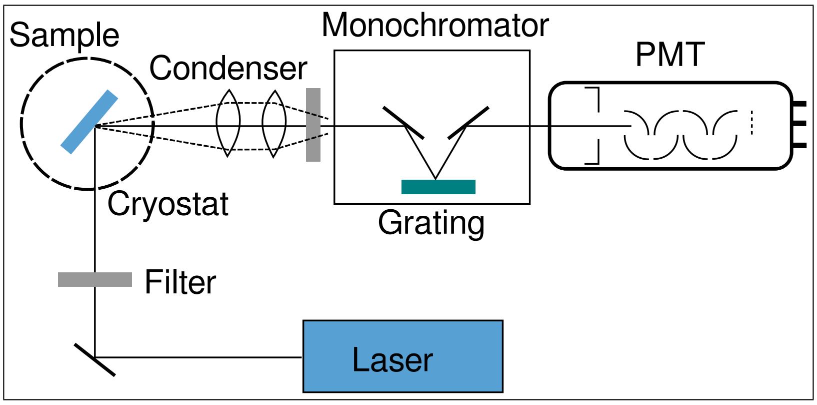

Figure 2.16: Photoluminescence set-up showing the laser source, sample holder, monochromator, PMT detector, and associated optics.

Figure 2.16 shows a schematic diagram of our PL spectroscopy system. As a source of excitation, He-Cd continuous wave laser, pulsed diode lasers of different wavelengths or a Tungsten lamp may be used. Neutral density (ND) filters are employed to tune the amount of incident source power if required. We have a choice of InAs detector, NIR photomultiplier

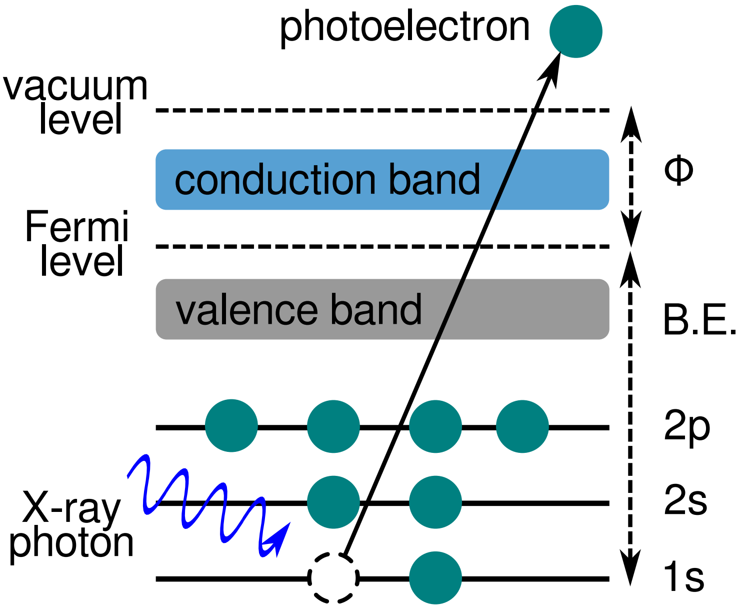

Figure 2.17: Photoelectron emission process

tube (PMT) and visible PMT, with the last option being used mostly. Monochromators, lenses and mirrors form part of the system. In this work, a typical solid state sample holder or a cryostat sample holder have been used. A closed cycle He cooled cryostat and heaters allow sample temperature to be varied between 10 K and 500 K.

2.2.8 X-ray photoelectron spectroscopy

Photoemission is a process in which electrons are emitted from a material after absorbing energy from photons. The energy of visible and UV light photons are of the order of binding energy of valence electrons of typical semiconductors, whereas X-ray photons have sufficient energy to liberate core level electrons from atoms. Since binding energies of core level electrons vary from one element to other, and are well known, X-ray photoemission can be used for elemental identification. X-ray photoelectron spectroscopy (XPS) is a surface sensitive technique for quantitative analysis of composition, and chemical and electronic state of surface of a material. In this work, an XPS instrument from Scienta Omicron, Germany has been used to analyse sample composition and surface states. The basic working of the technique is described briefly as follows.

An XPS instrument basically consists of an ultra-high vacuum (UHV) chamber - which reduces the contamination of sample surface, a source of X-ray and a detector which intercepts the emitted photoelectrons and measures their kinetic energies. We have aluminium and magnesium X-ray sources and a concentric hemispherical analyser (CHA) as detector. The detector system has two concentric hemispheres which are biased at certain negative and positive voltages. When the photoelectrons enter through an entrance slit, only electrons of a particular energy, called 'pass energy' (PE), can travel in a circular path towards the exit slit, and electrons with energies different from PE are deflected away. The PE depends on the voltage biases applied to the inner and outer hemispheres. After the exit slit, the photoelectrons arrive at electron multiplier tubes which strongly magnify the current due to impinging electrons and the signal is recorded. By varying the applied voltages, and thereby the PE, electrons of different kinetic energies can be detected. The kinetic energy of the photoelectrons equals the energy of the absorbed X-ray photons minus the energy required to overcome the potential barrier of atoms. This ignores energy loss by the photoelectrons due to inelastic scattering. Figure 2.17 shows the basic process of photoemission, and from this we can write the energy conservation equation as follows:

$$h\nu = B.E. + \phi + K.E. \tag{2.12}$$

Here, $h\nu$ is energy of X-ray photon, B.E is the binding energy, defined as the energy difference between core level and Fermi level, ϕ is the work function, defined as the energy difference between the vacuum level and Fermi level. Thus by measuring the K.E.of the electrons and knowing ϕ, their binding energies can be calculated. The instrument is set up so that the Fermi levels of the sample and that of spectrometer align. If the binding energy scale is calibrated with respect to the Fermi level, knowing the spectrometer work function is enough to calculate the photoelectron B.E. In practice this information is stored in the system, enabling users to directly obtain spectra showing number of detected photoelectrons (intensity) with particular binding energies.

Another important physical process to consider here is Auger electron emission. When X-ray photon is absorbed and photoelectron is emitted, this leads to creation of a core hole. Thereafter, an electron from higher (less negative) energy level recombines with the core hole leaving the atom with excess energy. The excess energy can be released by emission of a (X-ray) photon or by emitting another electron from the higher energy level, which are called as Auger electrons. In the XPS spectra both photoelectron peaks as well as Auger peaks can be observed.

As mentioned before, different elements have unique set of binding energies of core level electrons. This makes elemental identification possible and also the composition of the material down to a parts per thousand level. Inelastic scattering and resulting energy loss does not allow photoelectrons from deep inside the material to be ejected. Due to this, the information depth for XPS is typically a few monolayers of the top surface (less than 10 nm). Chemical shifts refer to the difference in position of an observed photoelectron or Auger peak and the ideal position expected for a pure elemental form. Bonding with a more (less) electronegative atom enhances (reduces) the B.E. The B.E. is also affected by the oxidation states of the atom. The valence electrons of semiconductors have low binding energy ($<$20 eV), and thus studying low binding energy portion of the XPS spectra can give insight into valence band structure. It is worth mentioning here that metallic sample is characterised by a peak or non zero intensity at the Fermi level, calibrated as zero of the biding energy scale.

The calculation of composition of surface of a sample is done as follows. First, the photoelectron or Auger peaks present in a long energy range (‘survey scan’) need to be identified with the help of handbook or database. Thereafter, the peak intensities, defined as area under the peak after subtraction of background intensity, have to be measured. Different elements have different atomic sensitivity factors ‘S’ which determines their peak intensity. Once again, the sensitivity factors of the elements identified from the survey scan have to be obtained from a handbook or a database. In this case, the relative concentration $\mathrm{C_i}$ of a particular element ‘i’ is given as follows:

$$C_i = \frac{I_i/S_i}{\sum_i I_i/S_i} \tag{2.13}$$

Here the numerator is a particular peak’s intensity scaled by sensitivity factor and denominator is sum of such scaled intensities for all elements present in the sample.

2.2.9 Hall and resistivity measurement

2.2.9.1 Resistivity

Electrical measurements have been carried out in this work to determine the carrier concentration, mobility and resistivity of the samples as a function of temperature and magnetic field. For determination of resistivity, four probe method has been used, which provides a more accurate value compared to a two probe method.

In four probe method, four ohmic contacts are deposited onto the sample in a collinear fashion maintaining an equal distance, ‘s’, between two contacts. The two outer contacts are the current leads whereas the inner ones are used for voltage measurement. Figure 2.18(a) shows a schematic diagram of the four probe method. The calculation of resistivity depends on sample dimensions and two extreme cases are of a bulk sample and a thin film. In bulk sample, the lateral sample dimensions are assumed semi-infinite and sample thickness ‘t’, is large compared to s, and in thin film, thickness is very small compared to s.

For a bulk sample the resistivity is given as:

$$\rho = 2\pi s \frac{V}{I}$$

In thin film samples, the sheet resistance is a readily measured and important quantity given as (in Ohms per square):

$$R_s = 4.532 \frac{V}{I}$$

which is related to the resistivity as $\rho = R_s t$. In our case, for a typical GaN sample grown on sapphire, the s parameter is of the order of 1 mm whereas the thickness is of the order of 1 μm, and thus the thin film formulae are well suited. However, for thin film grown on conducting substrates such as heavily doped silicon, the preferred path for current conduction would be through substrate, thus the extracted information would correspond to that of substrate, unless specifically taken care of by multilayer modelling.

2.2.9.2 Hall measurement

Hall measurement is a established technique which is used to measure carrier type (electron or hole majority carriers), carrier concentration, and Hall mobility of carriers. The technique is based on Hall effect, which is the

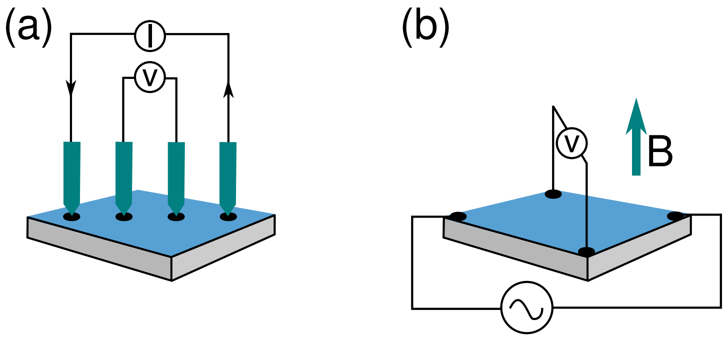

Figure 2.18: Schematic diagram showing (a) four probe resistivity measurement and (b) Hall measurement.

generation of a transverse voltage in conducting samples when a electric field is applied across the sample in presence of perpendicular magnetic field. Figure 2.18(b) shows a schematic diagram of measurement of Hall voltage. If a current 'i_x',flows along the sample along x direction in response to applied electric field, and a magnetic field 'B_z' has been applied along z direction, then there will be a voltage difference 'V_H' along y direction. If the length of the sample (along x axis) is 'l', width of the sample (along y axis) is 'w' and the thickness (along z axis) is 't', then the Hall voltage is given as:

$$V_H = \frac{i_x B_z}{ent}$$

Here, e is electronic charge and n is its concentration. The Hall coefficient is defined as:

$$R_H = \frac{E_y}{j_x B_z}$$

Here, j_x is the current density, $j_x = i_x/wt$ and E_y is induced Hall electric field $E_y = -V_H/w$. Thus for a sample of known dimensions, by applying a known voltage in a known magnetic field, a measurement of Hall voltage helps us calculate the carrier concentration.

Knowing the carrier concentration n and the conductivity σ, one can calculate the Hall mobility μ_H.

$$\sigma = \frac{1}{\rho} = ne\mu_H$$

It is important to differentiate between mobility of carriers in absence of magnetic field - called drift mobility and Hall mobility. The ratio of

Hall mobility to drift mobility is called Hall factor r_H (not to be confused with Hall coefficient R_H). For high carrier concentration samples, the Hall factor is assumed to be unity but for other cases, it might differ in value and has to be determined experimentally by measuring mobility by applying different magnetic fields. The basis for experimental determination is the fact that, Hall mobility measured in van der Pauw geometry in a very high magnetic field approaches the value of drift mobility[51].

Chapter 3

Growth mechanism of GaN films, nanorods and nanowalls

This chapter describes the molecular beam epitaxy growth of GaN nanostructures. The thermodynamic and kinetic factors underlying the growth of thin films and low dimensional nanostructures are discussed. Experimental studies elucidating the growth mechanism of low dimensional nanorods, nanowalls and porous films are discussed.

3.1 Introduction

Due to its high melting temperature and decomposition pressure, it is not affordable to grow large-sized good quality single crystals of GaN[52]. Thus for device fabrication one grows GaN epitaxially on foreign substrates. Several techniques are employed for epitaxial growth of semiconductors, such as liquid phase epitaxy, metal-organic chemical vapour deposition (MOCVD), hydride vapour phase epitaxy (HVPE), molecular beam epitaxy (MBE)[53]. Liquid phase epitaxy, in which one dips or slides the substrate through a heated saturated solution of the source material to deposit a thin film, has mostly given way to vapour phase techniques mentioned above which provide better control of thickness and composition. Vapour phase epitaxy, in which the source materials are in gaseous phase can provide good control over layer deposition and high throughput. HVPE uses hydrides, e.g. AsH_3, NH_3 and halides, e.g. $GaCl_3$, $InCl_3$ as sources which are transported using some carrier gas on to a heated region where chemical reactions takes place and final product is deposited onto a substrate. One can achieve growth rates up to several hundred μm/hr with this technique. For MOCVD growth of III-V semiconductors, one uses organometallic compounds for group III and hydrides for group V elements. MOCVD provides a greater degree of control over deposition and is the dominant growth technique in the semiconductor industry[54].

In contrast to the above-mentioned methods, MBE growth does not involve chemical reactions and takes place under a high vacuum. In this case, ultra-high pure metal is sublimated at high temperature along with gaseous group V element to form a molecular beam transported in a ballistic manner onto a heated substrate to form the thin film. Due to the application of high purity sources and ultra-high vacuum, the grown samples are highly pure with significantly reduced defect concentration. For the growth of nitride semiconductors, usually active species is generated out of nitrogen molecules using electron cyclotron resonance or radio-frequency plasma. Although the growth rate in MBE stands at about 1 Å/s, unprecedented monolayer control of growth and formation of abrupt heterojunctions can be achieved along with the added advantage of high sample purity[55].

3.2 MBE growth process

For MBE growth, the mass transport, kinetic and thermodynamic aspects are interwoven. Although the growth conditions inside MBE are far from equilibrium, nevertheless the basic growth process is driven by the thermodynamic free energy difference between source phases and solid film phase while also considering the energetics of surface and interface. It should be noted that thermodynamics in this case determines the maximum possible growth rate, whereas the actual nature and rate of growth can be understood through atomistic kinetic processes of the adsorbed atoms (adatoms).

In our MBE growth, pure Ga metal and plasma of high purity nitrogen gas are used as sources. After emanating from the hot k-cell and RF plasma source, the active species of gallium and nitrogen travel along straight paths in the form of a molecular beam and impinge on the substrate. After impingement, the atoms can diffuse over the substrate or film surface due to thermal non-equilibrium and collide with other atoms and form bonds to create a cluster of atoms. From energy considerations, there exists a critical size of such a cluster. A cluster of size larger than the critical size will grow over time by inducting new adatoms while subcritical clusters, after a while, will disintegrate and free up the constituent adatoms, which may then diffuse to join another cluster or re-evaporate. Figure 3.1 schematically shows these processes. The kinetics of adsorption, diffusion, condensation and re-evaporation of atoms can be controlled by changing the source fluxes and substrate temperature.

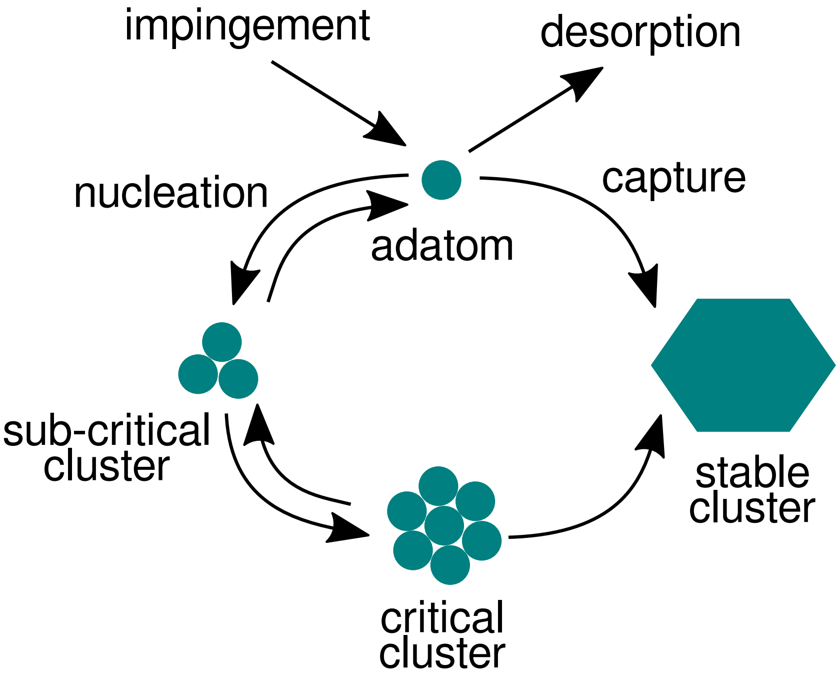

Figure 3.1: Schematic diagram of atomistic processes involved in the growth in molecular beam epitaxy.

Crystallisation is the formation of solid crystals from a homogeneous vapour or liquid phase. If the concentration of the homogeneous phase is more than equilibrium concentration ('supersaturation') and the temperature is lower than the melting temperature of the solid phase, the system can undergo a phase change to reduce the Gibbs free energy (G=H-TS). The formation of initial small crystallites ('nuclei') is termed nucleation which usually occurs on a foreign surface or around a seed crystal. Nucleation costs energy, mostly in the form of energy of the interface between the crystal and the liquid/vapour phase. Considering the case of a vapour phase condensing on a surface, if p and p_0 are the current pressure and equilibrium pressure of the vapour phase over the solid phase, the supersaturation σ is defined as $\sigma = \frac{p}{p_0} - 1$. The supersaturation is essentially the difference in chemical potential between the crystal and the vapour phase ($\Delta\mu = k_B T \ln \frac{p}{p_0}$) and is the thermodynamic driving force behind nucleation and further crystal growth. For our purpose of MBE growth, we can replace the pressure with the flux of atoms 'J' and write the supersaturation as: $\sigma = \frac{J}{J_0} - 1$.

The critical size of the stable nucleus can be found from free energy considerations. We consider the energy required to form the nucleus surface and the energy released by the formation of an ordered crystal. If γ is the energy required to form a unit area of the surface, then $4\pi r^2\gamma$ is the energy cost for a nucleus (assumed spherical) of radius r. The volume of the nucleus is $\frac{4\pi}{3}r^3$ and the number of atoms in the nucleus is $\frac{4\pi}{3}\frac{r^3}{\rho}$ where ρ is the density. This makes the energy released from forming nucleus as: $-\frac{4\pi}{3}\frac{r^3\Delta\mu}{\rho}$. The Gibbs free energy is given by $G = 4\pi r^2\gamma - \frac{4\pi}{3}\frac{r^3\Delta\mu}{\rho}$ and the stability criterion to be $\frac{\partial G}{\partial r} = 0$ which leads to the critical size being $r_{crit} = \frac{2\gamma\rho}{\Delta\mu}$. For GaN growth on silicon, the critical size is small, less than 10 nm[56].

For heteroepitaxial MBE growth of a film, several epitaxial growth modes can occur depending on the level of supersaturation and misfit between film and substrate. The growth mode characterises the nucleation and subsequent growth process and determines the final film morphology. Several of these epitaxial growth modes are depicted schematically in Figure 3.2, showing the time evolution of the growth. The three classical epitaxial growth modes are: Frank van-der Merwe (FM), Volmer-Weber (VW) and Stranski-Krastanov (SK)[57][58]. In FM mode, the film grows layer by layer, with a new layer nucleation happening only after the completion of the below layer. This growth mode is only observed when the degree of mismatch is very small. FM mode growth ideally can result in perfect flat films, albeit in practical cases, defects are always present. The VW mode is typical for a significant mismatch. In this mode, initially, a large number of nuclei form, which then grow laterally and vertically. This mode results in a 3D morphology of the final film. The SK case is typically observed when the film-substrate mismatch is intermediate. It proceeds by forming smooth complete layers up to a certain critical thickness and 3D islands after that.

One can understand the occurrence of these three modes by considering the surface and interface energies. Suppose γ_s,γ_f,γ_i are the energies per unit area of the bare substrate, film and the film-substrate interface, then $\Delta\gamma = \gamma_f + \gamma_i - \gamma_s$ is the energy per unit area of forming the film. If $\Delta\gamma < 0$, it is always energetically favourable to form a complete film and wet the substrate entirely; this corresponds to the FM mode. If $\Delta\gamma > 0$, complete

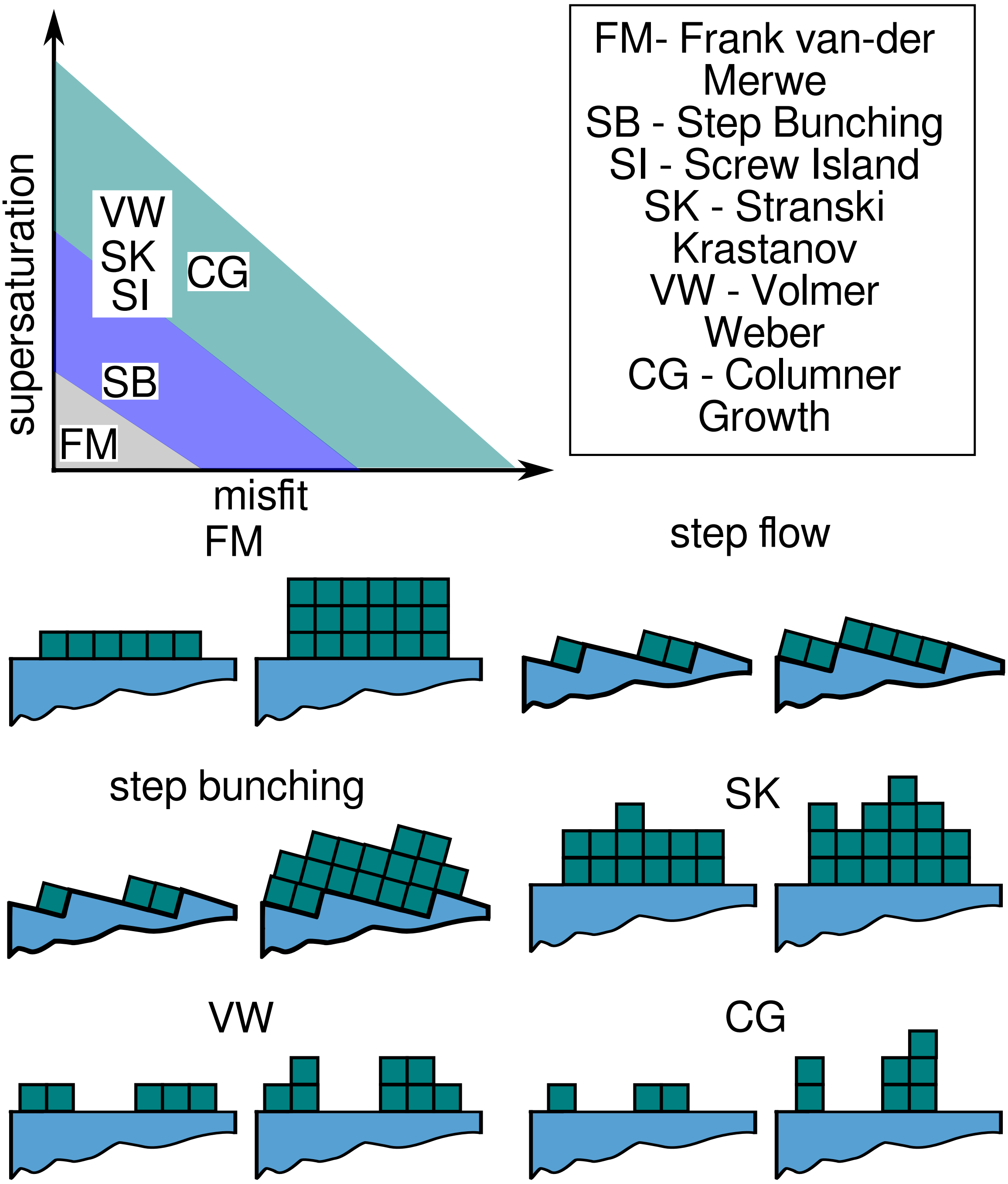
supersaturation
misfit
VW
SK
SI
CG
SB
FM
FM- Frank van-der Merwe
SB - Step Bunching
SI - Screw Island
SK - Stranski Krastanov
VW - Volmer Weber
CG - Columner Growth
FM
step flow
step bunching
SK
VW
CG

Figure 3.2: Top panel: Dependence of various growth modes on supersaturation and film-substrate misfit. Bottom panel: epitaxial growth modes in successive stages in cross sectional schematic.

wetting of substrate is energetically unfavourable, and growth proceeds via the formation of many islands in VW mode. The intermediate case, as mentioned before, is the SK mode - for the intermediate mismatch case. Here initially $\Delta\gamma < 0$, but as the film grows layer by layer, the strain energy increases, increasing the total energy cost of forming the 2D layers and after a critical thickness, $\Delta\gamma$ becomes positive, and the growth proceeds in 3D island mode.

Apart from these three well-known growth modes, there are four more experimentally observed growth modes: step-flow, step-bunching, screw island and columnar growth mode[59]. If we have a substrate with a miscut instead of a perfectly flat surface, then the substrate surface would have steps (see Figure 3.2). It is easier for adatoms to nucleate on the steps, which then grow row after row, in one direction, in a manner called 'step flow'. If many steps are growing at a time with high velocity, then one step can catch up with another and grow together as double, triple or n-tuple steps, which is called step bunching. While in step-flow growth, the height of a step is one film monolayer, in step-bunched growth, the height is multiples of monolayers, even as large as thousands-fold. Coalescence of a large number of islands can sometimes lead to screw-type dislocation formation, which continuously provides a spiral growth ledge for adatom attachment. This leads to a 'spiral island' or 'screw island' type of growth. Finally, in case the mismatch is high, but the supersaturation level is such that lateral growth is much lower than vertical growth; then the growth proceeds from initial VW to columnar manner forming nanorods or nanowires.

The diffusion rate of adatoms on substrate and film surface is one of the most important parameters determining growth mode (and thereby final morphology) along with mismatch and source flux. If an adatom can diffuse over a long distance, its probability of attaching to an existing island and contributing to island growth is more, compared to if the diffusion length is small. Longer diffusion lengths on the substrate surface can lead to a 2D layer by layer growth, whereas shorter ones tend to lead to 3D growth mode. In the simplest case, diffusion occurs by adatoms hopping from one available adsorption site to another. If the energy barrier to hopping is denoted as $\mathrm{E_d}$, then at temperature T the diffusion coefficient is given by $D = D_0 \exp{(-\frac{E_d}{k_B T})}$.[60] The relation between diffusion coefficient and diffusion length is given by: $\lambda = 2\sqrt{D\tau}$ where τ is the mean time spent by an adatom on the surface before it gets either incorporated or desorbed. The diffusion length depends on the atomic geometry of the surface, the concentration of adatoms, and temperature: the higher the temperature - the longer the diffusion length. The diffusion length of Ga adatom is longer than that of active N species[61]. Additionally, neutral N_2 molecules which do not take part in Ga-N bond formation can affect the diffusion length - a high N_2 concentration can reduce Ga adatom diffusion length.

3.3 Controlling sample morphology through kinetics

From the preceding discussion, it is clear that for a particular choice of film and substrate, which fixes the mismatch, by controlling the fluxes of the active source materials and growth temperature, the growth modes can be controlled. The Ga adatom flux is directly related to the Ga k-cell temperature and follows an exponential dependence as shown in Figure 3.3. The flux is a more fundamental parameter compared to k-cell temperature as the temperature required to achieve a particular flux varies with amount of material in the k-cell. It is typically recorded in terms of the beam equivalent pressure reading from the ion-gauge.

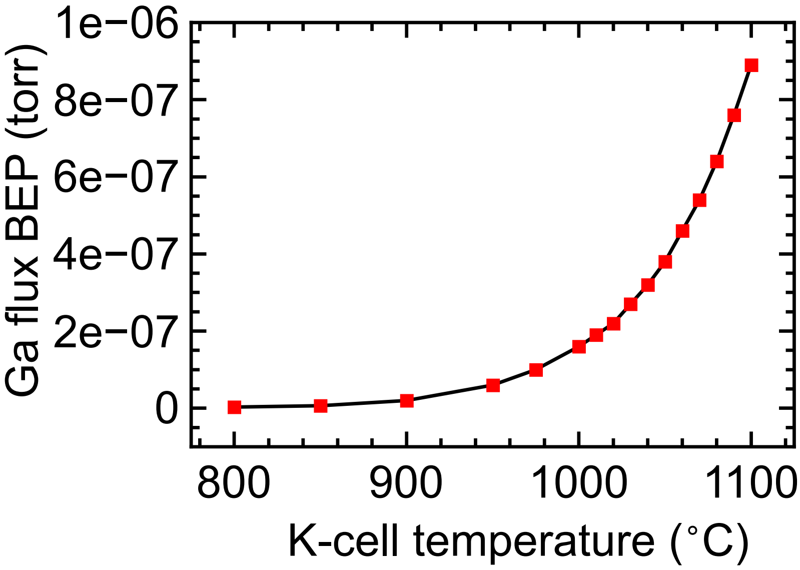

Figure 3.3: Experimentally determined relationship between Ga k-cell temperature and beam equivalent pressure of Ga flux. The exponential nature of the dependence is evident.

The active components in the nitrogen plasma are atomic nitrogen and excited (metastable) nitrogen molecules. The concentration of these species can be controlled by changing the flow rate of nitrogen into the plasma source or changing the RF forward power. The concentration of excited molecular nitrogen increases monotonically with both N_2 flow and plasma power, whereas the concentration of atomic nitrogen increases monotonically with RF power and is practically independent of nitrogen flow rate[50]. The substrate temperature determines the rate of desorption and the diffusion length. The substrate temperature is measured using a thermocouple and is regularly calibrated against pyrometry measurements.

3.3.1 Experimental details

A series of four experiments were done in this study to understand the effect of control parameters on the sample morphology. C-sapphire was used as substrate in all cases, which was degreased with organic solvents such as acetone, propanol and then rinsed with de-ionised water, blow-dried with nitrogen flow and then introduced in MBE chamber. Before deposition, the substrate was thermally degassed at 850°C in the preparation chamber for 60 minutes and then at 900 °C for 30 minutes in the growth chamber. The nitrogen plasma was generated with a forward power of 375 watts and stabilised for a few minutes before beginning growth.

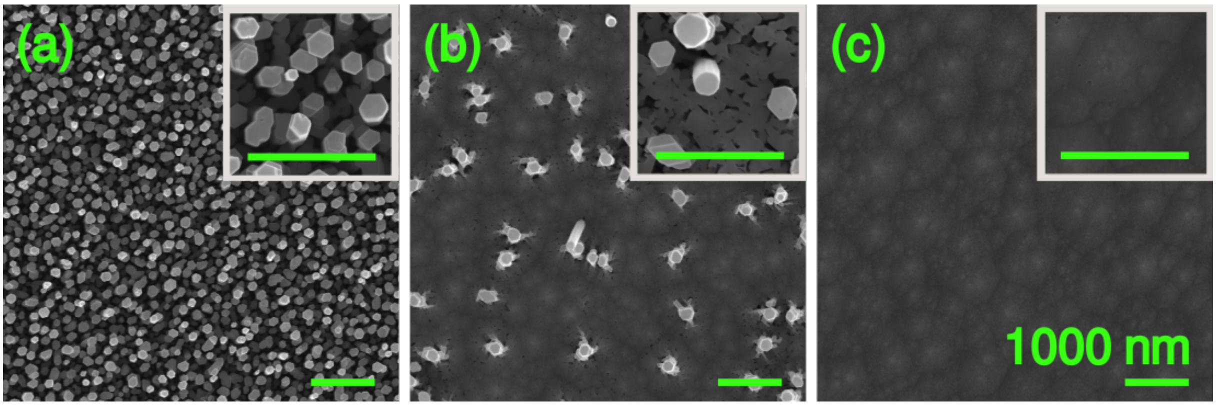

Figure 3.4: Plan view FESEM images of samples A1,B1 and C1. The scale bar corresponds to 1 μm. The insets are higher magnification images clearly showing a change in morphology from well aligned nanorods in sample A1 to nanorods emanating out of a faceted matrix layer in sample B1 to a compact layer in sample C1.

For the first experiment, we deposited a set of three samples, A1, B1 and C1, at a constant temperature of 630 °C and nitrogen flow of 6 sccm for 3 hours with different Ga fluxes. The Ga flux BEP corresponds to 3.2×10^{-7}, 5.0×10^{-7} and 6.5×10^{-7} torr, respectively.

For the second experiment, a set of three samples, A2, B2 and C2, were grown with different N_2 flows while keeping Ga flux BEP constant at 2.0×10^{-7} torr, the substrate temperature at 630 °C and for 3 hours duration. The N_2 flows were set at 4, 6 and 8 sccm for A2, B2 and C2, respectively.

In the third experiment, we varied the substrate temperature as 630 °C, 680 °C and 730 °C to deposit a set of three samples A3, B3 and C3, respectively. The Ga flux and N_2 were set at 2.0×10^{-7} torr and 4 sccm respectively and the growth was performed for 3 hours.

For the fourth experiment, the Ga flux, nitrogen flow and substrate temperature were kept fixed at 5.5×10^{-7} torr, 2.5 sccm and 630 °C. Two samples A4 and B4, were grown for a 2 hours duration with two different nitrogen sources. For A4, a nitrogen source of 7N purity (99.99999% pure) was used, whereas for B4, a source of 5N5 purity (99.9995% pure) was used. The morphology of the samples was studied using FESEM. The sample thicknesses were measured using cross-sectional FESEM imaging.

3.3.2 Results

Figure 3.4 shows the top-view FESEM images of samples A1, B1 and C1 grown by varying Ga flux. As we can see, A1 grown with the lowest Ga flux consists of a dense array of nanorods and C1 with the maximum Ga flux has a compact morphology formed from islands that have coalesced. Sample B1 with intermediate Ga flux shows an intermediate nature of nanorods emerging from a compact layer in the base. Clearly, low Ga flux, leading to a high N/Ga flux ratio is needed to form one-dimensional nanorods. The base layer of sample B1 is porous and faceted as seen in the inset, and presumably forms from the coalescence of faceted islands or nanorods.

Next, we vary the N/Ga flux ratio by varying the N_2 flow and keep the Ga flux constant. Figure 3.5 shows the plan-view FESEM image of samples A2, B2 and C2. Sample A2 consists of an array of nanorods emanating from a porous base layer. Sample B2 is a nanowall network, and sample C2 has a dimpled compact morphology with some emergent nanorods. The variation of morphology with nitrogen flow is not straightforward; we have found that a critical window exists for forming the nanowall network. As previously mentioned, the ratio of active atomic nitrogen to neutral N_2 molecules is nearly independent of nitrogen flow, whereas the fraction of meta-stable molecular species depends on it. The neutral N_2 molecules also hinder Ga adatoms' diffusion - affecting the growth mode and final morphology.

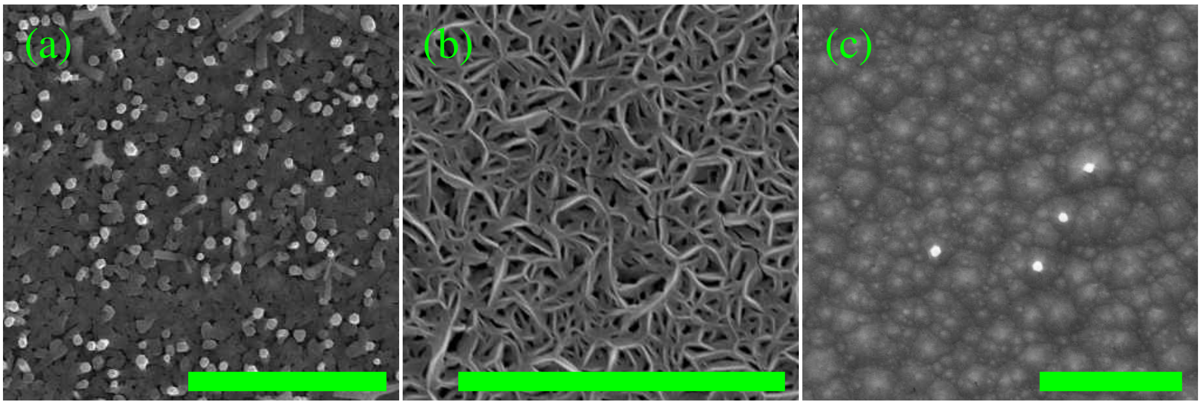

Figure 3.5: Plan view FESEM images of samples A2,B2 and C2. The scale bar corresponds to 2 μm.

To study the effect of substrate temperature, we consider samples A3, B3 and C3, whose plan-view FESEM images have been shown in Figure 3.6. We observe that a variation in this temperature range from 630 °C to 730 °C does not cause a significant qualitative change in morphology. All three samples consist of thin nanorods coming out of a faceted base layer ostensibly formed from the coalescence of nanorods of lower heights. We perform an analysis of the FESEM images using open-source ImageJ software to gain a quantitative understanding. We estimate the mean nanorod height and diameter, and thickness of the base layer for samples A3, B3 and C3. For calculating the nanorod mean dimensions, at least a hundred individual nanorods were considered to maintain statistical significance. The results are shown in Figure 3.7. We see that all three parameters decrease monotonically with increasing substrate temperature. As the temperature is increased from 630 °C to 730 °C, the mean diameter reduces from 90 to 62 nm, the mean height reduces from 1712 to 880 nm, and the thickness of the base layer decreases from 1110 to 438 nm. An increased substrate temperature enhances Ga adatoms' desorption, which reduces both lateral and vertical growth rate.

In the last part of this section, we study a comparatively less investigated topic - the effect of nitrogen purity on the final morphology of the sample. Figure 3.8 shows plan-view FESEM images of samples A4 and B4 grown with nitrogen gas of purity of 7N and 5N5, respectively. Both samples have a nanowall network morphology with the inclusion of very few nanorods. The cross-sectional thickness measured from FESEM shows the average nanowall height is about 1.0 μm for A4 and 0.6 μm for B4. The trace impurities present in nitrogen include carbon monoxide, car-

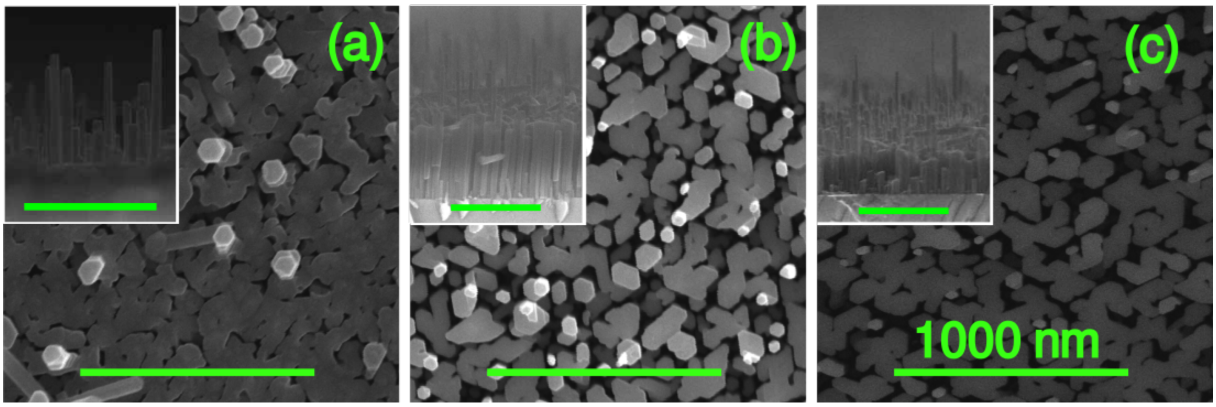

Figure 3.6: Plan view FESEM images of samples A3, B3 and C3. The insets show the corresponding cross-sectional image. The scale bar corresponds to 1 μm. A reduction in volume of matrix layer is seen in samples B2 and C2 compared to sample A2.

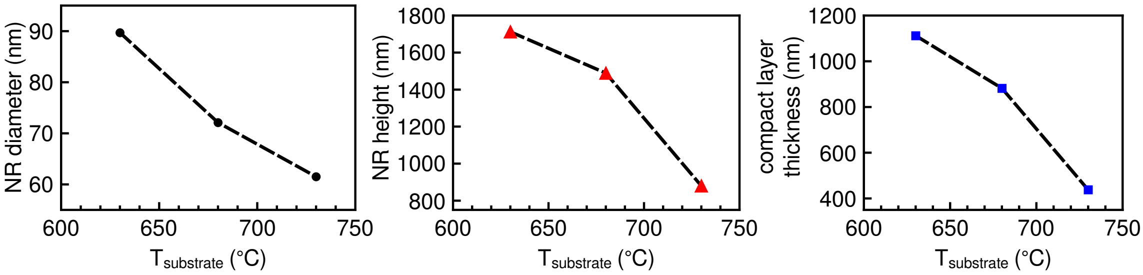

Figure 3.7: Graphs showing dependence of microstructural parameters on the deposition temperature. Variation of (left) nanorod diameter, (middle) nanorod height, and (right) base layer thickness with deposition temperature.

bon dioxide, oxygen, moisture, hydrocarbons, all of which are below 1.0 ppm level as per specifications. Some impurities, especially in the case of 5N5 nitrogen gas, has been observed using residual gas analysis of nitrogen plasma. Moisture and oxygen have been found to be below detection limits for high purity nitrogen. The samples' carrier concentration estimated from Hall effect measurements are 5×10^{19} cm^{-3} for sample A4 and 2.4×10^{20} cm^{-3} for sample B4. Since oxygen is known to be a shallow donor in GaN, trace oxygen impurities are expected to contribute to excess electron concentration in sample B4. Incorporation of oxygen in GaN depends on several factors - incorporation is more for nitrogen-rich condition than gallium-rich condition, and incorporation reduces with increasing substrate temperature[62]. Significant oxygen incorporation is known to cause tensile stress and even cracking, similar to excess Si doping of GaN[62 63]. Although in this case, no intentional oxygen doping has been performed, and indeed sample A4 has been grown with nitrogen which has negligible oxygen and moisture, the difference in vertical growth rates (0.5 μm/hr for A4 and 0.3 μm/hr for B4) may still be attributed to the difference in growth rates of GaN islands with varying strain. For an island with residual strain, an increase in height also increases the energy cost. Similar reports exist in the literature for heteroepitaxial GaN nanorod growth[64]. In addition to the variation of the strain state of the initial island nuclei which can lead to a difference in the incubation period for the nanorods and thereby alter the overall growth rate, another possible reason for the observed vertical growth rate difference is the modification of the adatom's kinetics by the presence of the unintentional dopants. Both the lateral and vertical growth rates of GaN nanostructures depend on the diffusion length and the nucleation of Ga adatoms on the sidewall surface. The presence of dopants such as silicon or magnesium have been known to alter the lateral and vertical growth rate and thereby modify the final morphology. We propose that the presence of unintended impurities plays a similar role here which leads to observed difference of heights of the two samples.

3.3.3 Inferences

Summarising the preceding results, we can see that the morphology of GaN samples grown on sapphire can be controlled by varying gallium and nitrogen flux and temperature, which in turn modify the atomistic kinetic processes. The thermodynamics of GaN growth in Ga-rich and N-rich

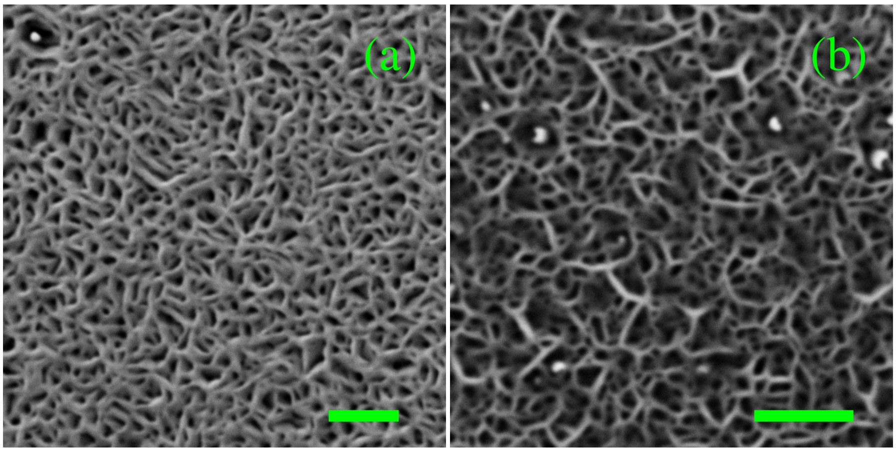

Figure 3.8: Plan view FESEM images of samples (a)A4 and (b)B4. The scale bar corresponds to 500 nm.

conditions are different - the former is known to lead to flat GaN layers, but even in nitrogen rich growth conditions, a variation in N/Ga flux ratio can tune the growth to form compact samples, to nanowall network to nanorod arrays. The growth rates can be tuned by changing the substrate temperature, which affects the Ga adatom desorption. Trace impurities were found to affect not only electrical properties but were also found to significantly change the growth rate, although not the sample morphology.

3.4 Growth of nanorods

We study the MBE growth of nanorods in detail to understand the underlying growth mechanism. Effect of adatom diffusion and dislocations, which have been used in literature to describe the nanorod growth are considered here. We change the growth parameters to grow a set on nanorod samples and carry out structural studies using FESEM and high resolution TEM to investigate their growth and structure.

3.4.1 Experimental details

GaN nanorods were grown on *c*-sapphire substrates by MBE. The active nitrogen species and Ga atoms were supplied by an RF plasma source fed with 7N purity N_2 gas and standard Ga k-cell. The substrate temperature was kept at 630 °C for all growths, the N_2 flow was fixed at 4.5 sccm, while the Ga flux had been varied. Samples A5, B5 and C5, had Ga k-cell temperature of 1012, 1040 and 1064 °C, corresponding to a Ga flux of 0.16, 0.37 and 0.63 $nm^{-2}s^{-1}$. The morphology of the samples was studied using

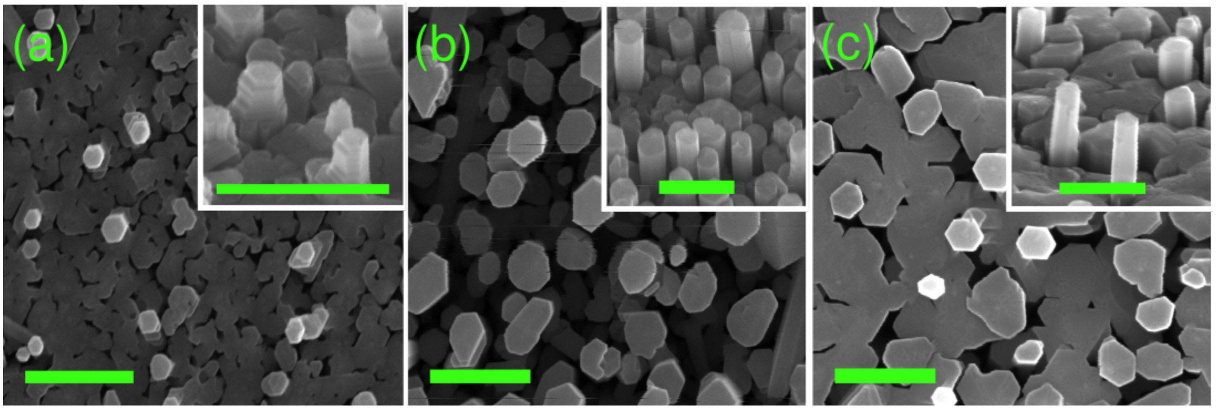

Figure 3.9: Plan view FESEM images of samples A5, B5 and C5. Inset shows higher magnification images. Scale bar corresponds to 500 nm.

FESEM and HRTEM. For TEM studies, nanorods were scratched off from the substrate, dissolved in ethanol and drop-casted onto a carbon-coated copper grid.

3.4.2 Results

Figure 3.9 shows plan and tilted view of FESEM images of samples A5, B5 and C5, all of which consist of an array of hexagonal nanorods. The nanorods are seen to emerge from a matrix layer, which is formed by coalescence of shorter nanorods, as evidenced by the faceted morphology of the matrix layer seen in sample C5.

From Figure 3.9, it can be seen that the nanorods of sample A5 have a tapered morphology, i.e. the diameter reduces as nanorods grow and additionally, the nanorod sidewalls have nanoscale steps, giving the nanorods a multi-section appearance. Similar nanorods with stepped sidewall shells have been reported in GaN growth by Galopin[65] and in ZnO growth by Hao Tang et al.[66]. Analyses of plan-view and cross-sectional view FESEM images were carried out to estimate mean nanorod heights and diameters for the samples. For each sample, 50-200 nanorods have been measured to achieve statistical significance. For samples A5, B5 and C5, in order of increasing applied Ga flux, the mean diameters are calculated to be 90 ± 24, 129 ± 26 and 174 ± 39 nm and the mean heights to be 1435 ± 183, 1601 ± 264 and 1963 ± 251 nm, respectively. Here, the error limits mentioned are the standard deviation of the measured data. Thus, increasing the Ga flux increases both the axial and radial growth rate of the nanorods.

For a more detailed examination, we have carried out TEM studies of nanorods mechanically removed from the samples and placed on a TEM

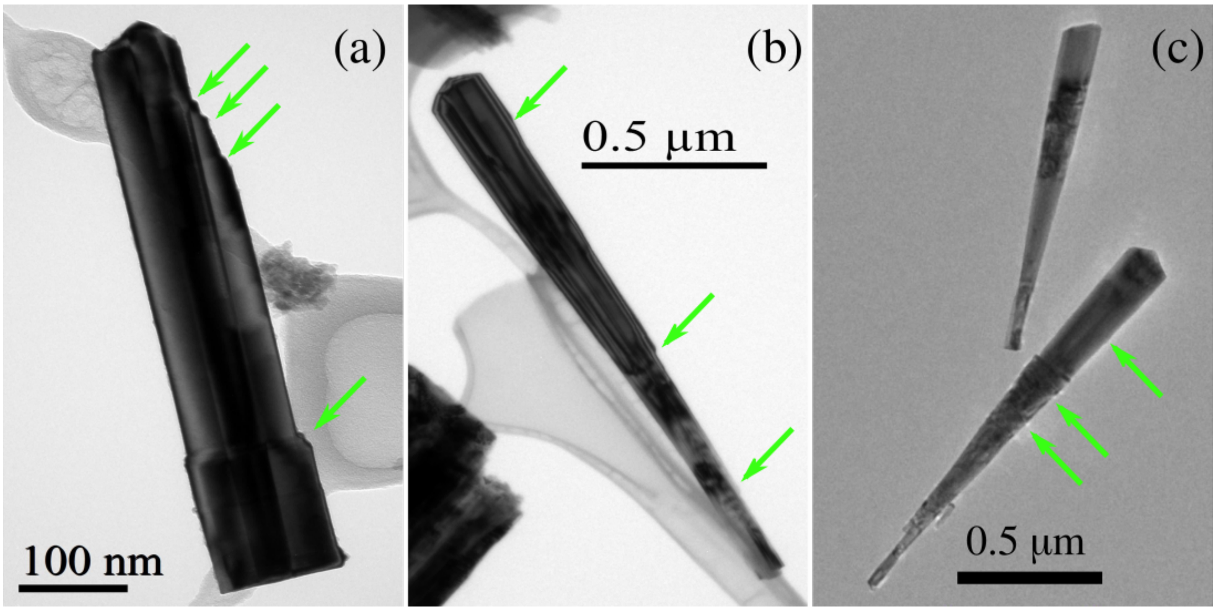

Figure 3.10: Low magnification TEM images of samples (a) A5, (b) B5 and (c) C5. Arrows mark the positions of bunched steps on the nanorod sidewall.

grid. Figure 3.10 shows low-resolution TEM images of a few nanorods from samples A5, B5 and C5 as representatives of the many nanorods studied for each sample. It is clear that from sample to sample, the mean size as well as the shape changes. In the case of sample A5, the nanorod diameter becomes thinner as it grows, as also seen in FESEM images, whereas the nanorods in samples B and C (grown with higher Ga fluxes) become wider as they grow. The steps on the sidewall have been marked with arrows in Figure 3.10. The angle of tapering or widening of the nanorods range from less than 0.5° to about 2.5°. The axial and radial growth rate, which determine the aspect ratio of the nanorod and the shape, can be calculated by considering the rate of impingement of adatoms and their diffusion. Since the MBE growth of GaN nanorod in nitrogen-rich conditions is Ga limited; it suffices to study the kinetics of the Ga adatoms. A nanorod (here assumed to be cylindrical) grows in height due to direct impingement of Ga adatoms on top and due to diffusion of adatoms from sidewalls towards the top. Similarly, the radial growth takes place due to the adatoms which impinge on the sidewalls and diffuse until getting either incorporated or desorbed. The volume increase of the nanorod of height H and radius R, due to axial growth can be written as[67] 2012 scaling]:

$$\frac{\pi R^2}{\Omega}\frac{dH}{dT} = (\pi R^2)\chi_1 J cos\theta + (2R\lambda)\chi_2 J sin\theta - (\pi R^2) J_{des1} \tag{3.1}$$

Here, J is the Ga flux incident at an angle θ with the substrate normal and the coefficients χ are related to the incorporation probability of the adatom on nanorod top. The first term on the right describes direct impingement of adatoms on nanorod top, and the second term is the contribution of adatoms impinging on the sidewall up to a distance λ diffusion length of adatoms) from the top and then diffusing to the top. Finally, the third term represents adatoms either desorbing from nanorod top or diffusing from top onto sidewalls. The inclusion of Ω, the elementary volume of a GaN pair (half the volume of primitive GaN unit cell, which has 4 atoms), makes each term independent of length dimension. The adatoms impinging on sidewalls below a distance λ from the top can contribute to radial growth:

$$\frac{2\pi R(L-\lambda)}{\Omega}\frac{dR}{dt} = (2R(L-\lambda))\chi_3 J sin\theta - J_{des2}2\pi RL \tag{3.2}$$

The first term on the right represents the direct impingement of adatoms on sidewall and second, the desorption from sidewalls. Factor χ_3 is again the incorporation probability, which typically has lower value compared with incorporation on top facet[35]. By making the approximation $L-\lambda \approx L$ and combining some constants, we can rewrite equations (1) and (2) as:

$$\frac{dH}{dt} = (a+\frac{b}{R})J - J'_{des1} \tag{3.3}$$

$$\frac{dR}{dt} = cJ - J'_{des2} \tag{3.4}$$

From eqn. (3) we see the familiar 1/R dependence of the length of nanorod, which is the signature of diffusion mediated growth, where the thinner nanorods grow faster. From eqn. (4), on the nanorod sidewall, whenever the rate of adatom incorporation exceeds the desorption rate, we have a radial growth. Integrating eqn. (4), we get a linear relationship of the radius with time. However, a uniform increase of radius of nanorod is only possible for a sparse nanorod array. For a crowded nanorod array, direct impingement of adatom on the lower portions of nanorod is hindered due to a shadowing effect due to neighbouring nanorods, which can lead to enhanced radial growth and wider diameters in the upper regions.

The radial growth rate, which varies with vertical position along the nanorod height, determines the nanorod shape, and to study the nanorod shapes further, we carry out a high-resolution TEM study of the nanorods,

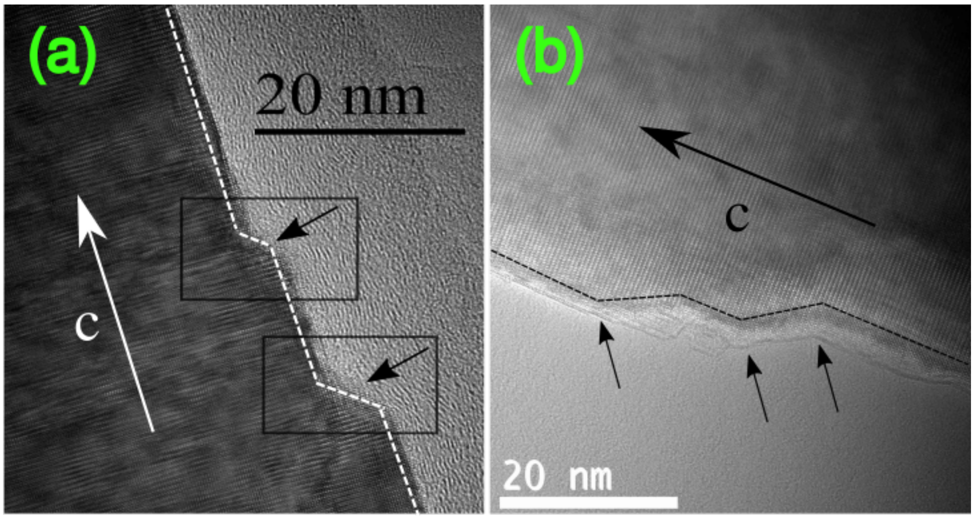

Figure 3.11: High magnification TEM images of samples (a) A5 and (b) B5. The growth direction along c axis is marked. The bunched steps on the sidewalls marked with arrows.

focussing on the sidewall steps. Figure 3.11 shows high magnification images of nanorods shown in Figure 3.10(a) and 3.10(b) acquired along the [11-20] zone axis. The flat sidewalls were confirmed to be (10-10) (m-facets) and the slant step portions as (10-11) (r-facets), from angle measurements. For higher step-flow velocities, it is common for the atomic steps to 'catch-up', near defects or fluctuations and grow in a bunched manner. The bunched sidewall steps of Figure 3.11 have a typical step-height of 5 nm, though the inter-step distances vary widely, resulting in a change in angle of tapering. The step-heights and step separations determine the tapering angle of the nanorod. It is clear from the figure that in the case of tapering nanorods, the step-flow radial growth must initiate near the bottom, whereas for widening nanorods, the step-flow growth must originate near the top of the nanorod. Since the Ga adatom density on the sidewalls is usually not high enough for island nucleation and layer by layer growth (owing to N-rich conditions), the sidewall growth occurs by step-flow. The two probable places of nucleation of atomic steps are the boundary between the nanorod top and the sidewall and the boundary between the nanorod sidewalls and the substrate. Galopin et al. and Dubrovskii et al. have reported that the latter is the more likely site[65][67]. Here, we propose that at lower adatom flux J, the sidewall step nucleation is likely to occur at the substrate-nanorod boundary, and with increasing flux, the combined density of directly impinging adatoms and those diffusing from the top facet increases, which beyond a critical value, make it more probable for the nucleation of new sidewall step to take place near the top of the nanorod.

Also, for higher flux, the axial growth rate is also higher, enhancing the shadowing effect for the taller nanorods and hindering nucleation of new steps at the nanorod substrate interface. In all, for a particular nanorod density, there must exist a critical value of adatom flux J_0 below which the nanorods primarily grow with a tapered shape and above which they are likely to grow with an inverse tapered shape.

The step-flow growth on the sidewall m-facets is fundamentally anisotropic owing to a directional energy barrier for diffusion of Ga adatoms. Lymperakis et al., from DFT calculations, found that the value of the energy barrier changes from 930 meV for diffusing along c axis to 210 meV for diffusion perpendicular to the c axis[68]. Since the diffusion lengths are related to the barrier as:

$$\lambda_{diff} \approx \sqrt{D\tau} \sim \sqrt{exp(-E_{diff}/k_B T)}$$

where D is the diffusion coefficient, and τ is the average adatom lifetime before it either gets incorporated or desorbed. Assuming that $\lambda_{||}$ and $\lambda_{\perp}$ are the Ga adatom diffusion lengths on the sidewall m-plane along the c axis and perpendicular to the c axis, respectively, then at a given temperature of 900 K (similar to experimental growth temperature), the ratio $\lambda_{||}/\lambda_{\perp}$ comes to be about 0.0096, which is almost a factor of 100 different. If we use a commonly quoted value of diffusion length $\lambda_{||}$ of GaN as 40 nm, the value of $\lambda_{\perp}$ will be approximately 4 μm.

We consider the continued radial growth, post initial nucleation of steps, to be similar to homoepitaxial growth of GaN m-plane on a miscut substrate, which also occurs by a step-flow route. Sawicka et al. observed that with increasing miscut angle, the step height increases, the number of steps decreases and bunching of steps occurs[69]. For a miscut towards c (similar to sample A5 in our case), it was found that the step flow growth results in rectangular 'tiles' which grow along [0001] and [11-20] directions, with the latter growth being faster. A miscut towards -c, (similar to sample B5 and C5 in our case) led to step flows in a direction 17° away from -c. In both cases, a component of the growth is directed perpendicular to the c direction, and based on previously mentioned diffusion length values, is likely to be more sustained compared to radial growth parallel (or antiparallel) to c direction. In this scenario, the radial growth may take place in a spiralling manner in the form of successive shells.

A spiralling growth of nanorods and nanotubes have been reported

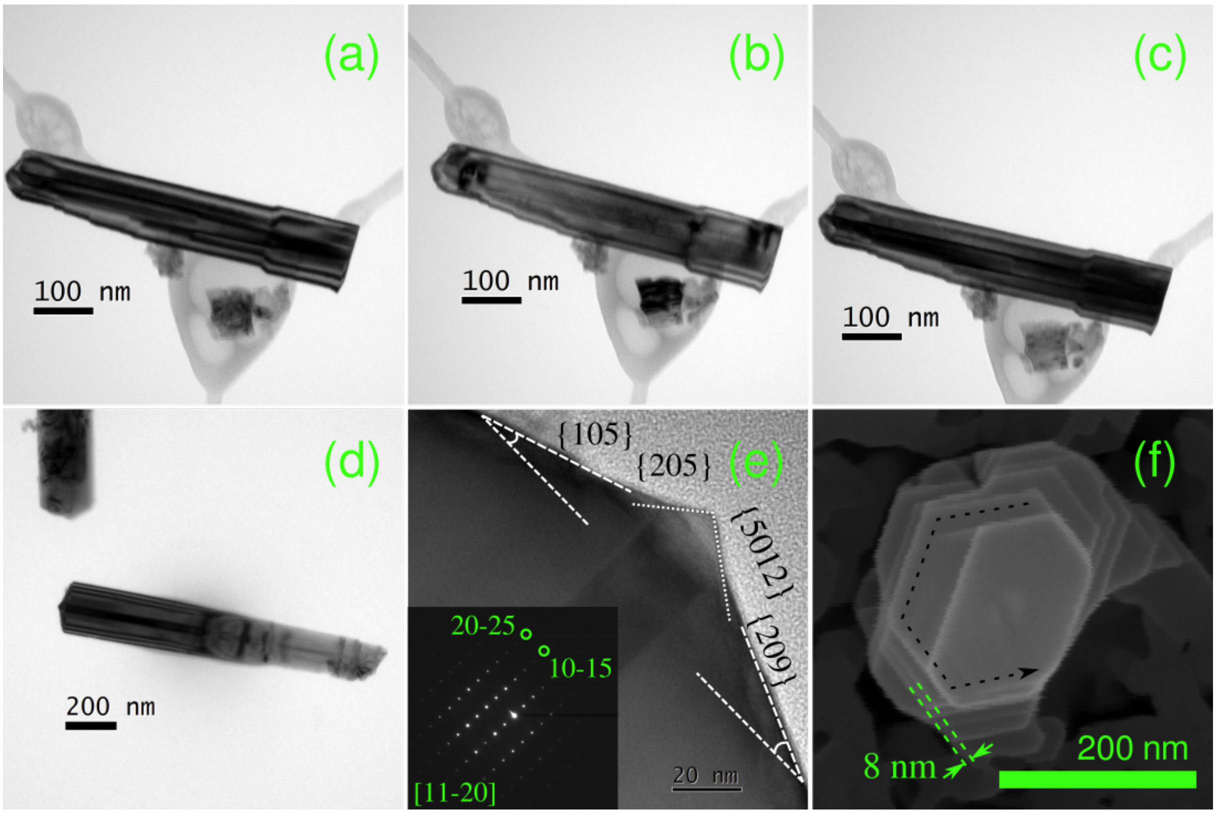
(a)
100 nm
(b)
100 nm
(c)
100 nm
(d)
200 nm
{105}
{205}
(e)
{5012}
{209}
20-25
10-15
[11-20]
20 nm
(f)
8 nm
200 nm

Figure 3.12: Low resolution TEM two-beam bright field image of the nanorod from sample A5 with zone axis [10-10] and g vector (a) (0002) and (b) (11-20). (c) shows the image taken with a 10° tilt from (0002) g vector. In (d) a low resolution bright field image of a nanorod from sample B5. (e) shows a high resolution image of a nanorod top from sample C5 with the facets indexed. Inset shows the diffraction pattern of the image. (f) shows an FESEM image of a nanorod of sample C5 showing spiral nature of growth.

by Jin et al. and Meng et al., who proposed screw dislocations as the primary driving factor behind the growth of such one-dimensional nanostructures[70 71]. Since the seminal work of Burton, Cabrera and Frank (BCF theory), screw dislocations are known to drive crystal growth even in low supersaturation conditions by continuously providing a growth ledge for adatom attachment. Previously we have reported the presence of screw threading dislocations (TD) inside nanorods and nanotubes grown on silicon[72]. Cherns et al. studied the growth of GaN nanorods on sapphire and found the presence of prismatic stacking faults inside the nanorods, which serve the same purpose of providing spiralling step edges for continued growth[73]. We have examined many nanorods in this study for such defects and found that extended defects are present in most nanorods, which extend throughout the length of the nanorod. In Figure 3.10(a), a dark band can be seen along the nanorod axis, about 30 nm wide, spanning its length. To characterize further, the same nanorod was imaged along different zone axes and by choosing different g vectors, and some of these images are shown in Figure 3.12. Figures 3.12(a) and 3.12(b) show two-beam bright-field images of the nanorod shown in 3.10(a), from sample A5, taken along [10-10] zone axis with g vectors (0002) and (11-20), respectively. The aforementioned dark band is present in both images, though it is much weaker in 3.12(b). Figure 3.12(c) is imaged at 10° tilt angle from [10-10] zone axis and it can be seen that the band is most clear in this case. We assign this defect to be a threading dislocation (TD) of mixed type with mostly screw character from the invisibility criterion. Such mixed TDs have been observed in both tapering and widening nanorods. Figure 3.12(d) and 3.12(e) depict nanorods from sample B5 and C5, respectively, containing central TDs.

Figure 3.12(e) shows a bright-field image of the top portion of a nanorod of sample C5, taken along [11-20] zone axis, with high resolution and its inset shows the corresponding diffraction pattern (DP). The BF image shows the dark contrast of the TD ending precisely at the nanorod tip. The majority of the nanorods studied here do not have (0001) plane at the top but instead have different semi-polar GaN facets. The figure shows that the nanorod top can be distinguished into two portions, a central tip making a higher angle with (0002) planes and the rest of the top portion with a lower angle. Additionally, both the central and remaining regions of the nanorod top have different bounding facets on the left and right sides. Angle measurements in the image and DP helped determine the bounding facets of the nanorod top. Facets {205} and {5012} (angle 36.9° and 38.0°) bound the central tip, whereas {105} and {209} (angle 20.6° and 22.6°) bound the remaining nanorod top. The appearance of such high index vicinal surfaces bounding nanorod tip have been reported by Azuelle et al. for GaN nanorods and Yin et al. for ZnO nanorods and are explained to be driven by kinetics as much as thermodynamic energy considerations[74][75]. The presence of different facets on nanorod tips was also reported by Cherns et al. and explained by unidirectional step-flow growth towards or away from spiralling central defect on the nanorod top[73]. In view of these observations, it can be inferred that for the nanorods examined in the present work; step flow defines both the axial as well as the radial growth. Finally, Figure 3.12(f) shows an FESEM image of a nanorod from the sample C5. Some well defined as well as incomplete hexagonal layers are seen, which originate due to a spiral growth of sidewall shells, defining the radial growth. The minimum step height (along radial direction) is found to be about 8 nm, comparable to the 5 nm height of the bunched steps as seen in TEM. Although the presence of dislocation can help both during the initial nucleation phase and at the growth stage, we do not observe the central TD in the case of every nanorod, suggesting that TD may not always be essential for nanorod growth. The initial nucleation may take place around any substrate defect or be purely driven by energetics.

Figure 3.13 summarises this study in the form of a schematic diagram, showing the step-flow radial growth of nanorods due to impingement and diffusion. When the adatom flux is less than a critical value, the step nucleations occur at the boundary of sidewalls with the substrate with higher probability and lead to a tapered growth, and for flux exceeding the critical value, the step nucleations are likely to occur at the sidewall-top boundary leading to an inverse tapered shape of the nanorod.

3.4.3 Inferences

We have examined the axial and radial growth in GaN nanorods fabricated by PAMBE on sapphire by varying Ga flux. We found that growth by step flow occurs in both the axial and radial directions. For low Ga flux, the steps nucleate from the nanorod-substrate boundary, and nanorod acquires a tapered shape as it grows, whereas for high Ga flux, the step nucleation is found to occur near the boundary between nanorod top and sidewall,

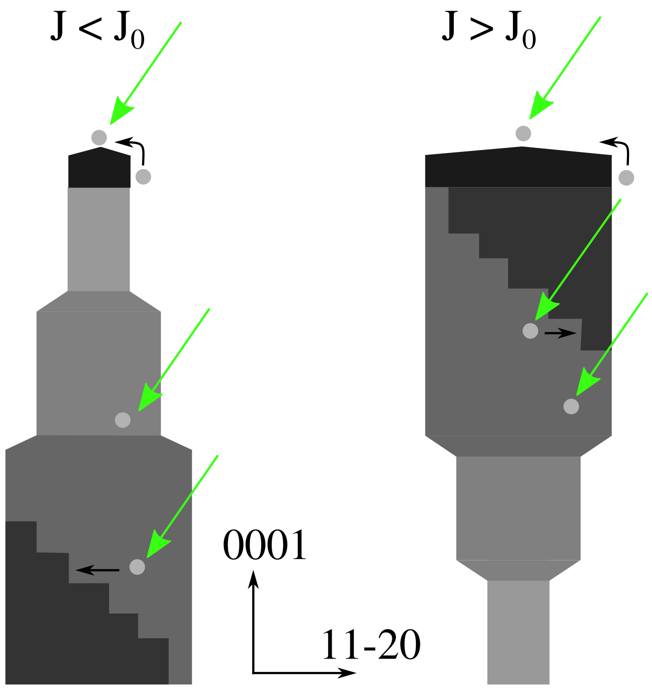

Figure 3.13: A schematic digram showing impingement and diffusion of adatoms leading to axial and radial growth.

and nanorod widens as it grows. The shadowing effect plays a role in determining nanorod shape by limiting adatom flux in lower regions of the nanorods. The radial growth is observed to occur in a spiral manner due to a higher diffusion length of adatoms perpendicular to the growth direction. Step bunching is observed in nanorods grown with both low and high Ga flux cases. Mixed threading dislocations were observed for many nanorods of each sample, which leads to dissimilar vicinal semi-polar facets at the top. Overall, a control over nanorod size and shape can be achieved spontaneously by varying the Ga flux and nanorod density, which can enable a minimal use of lithographic interventions to obtain desired properties of the nanorod assembly.

3.5 Growth of porous films and nanowall network

Porous films

It is well known that for several area-specific semiconductors applications, such as catalysis, energy storage and conversion, sensing, etc., it is very beneficial to use porous forms[76]. Porous semiconductors are predominantly created by electrochemical or photo-electrochemical etching of compact semiconductors[77]. Porosification of GaN is driven by holes - photogenerated or otherwise. The holes assist the oxidation Ga, forming a non-stoichiometric or in some cases, stoichiometric (Ga_2O_3) oxide then dissolves in the electrolyte[78].

$$2GaN + 6h^+ \rightarrow 2Ga^+ + N_2$$

In the case of photo-electrochemical etching, the electron-hole pairs are generated, and holes can be driven towards the electrolyte interface by the applied electric field. In the case of a highly n-doped GaN in the dark, though there are no photo-generated holes, free holes can still be created by Zenner tunnelling. If the band-bending resulting from applied potential is large enough, then the valence band at the surface may become energetically higher than the conduction band in the bulk. In this case, electrons can tunnel from electrolyte interface valence band to bulk conduction band and leave a free hole behind. By varying the electrolyte, applied potential and intensity of light, the density and size of pores can be controlled[78 79].

Porous semiconductors can also be formed by using sacrificial templates in which the template is removed chemically or by annealing and remaining overgrown material has a porous framework[80 81]. Glancing angle deposition from vapour phase has also been used to finely tune morphology of film from nanowires to porous films to flat films[82 83]. A reduced diffusion length, along with self-shadowing effect, has been used to explain direct deposition of porous films by glancing angle sputter deposition onto a rotating substrate[84].

We carry out PAMBE growth of porous GaN film on c-sapphire. As we show, by tuning the growth parameters, the microstructural parameters of the porous GaN film can be tuned. Compared to a top-down etching method, which may involve some damage and contamination, this self-induced bottom-up synthesis results in high purity porous samples.

3.5.1 Experimental details

A set of three samples were deposited by MBE on c-sapphire substrate at a substrate temperature of 630 °C and for a duration of 4 hours. Ga k-cell temperature and N_2 flow were varied to tune the N/Ga flux ratio from sample to sample. Sample A6, B6 and C6, had Ga k-cell temperatures of 1020°, 1040°, and 1064°C and had N_2 flow of 6.5, 6.5 and 4.5, respectively.

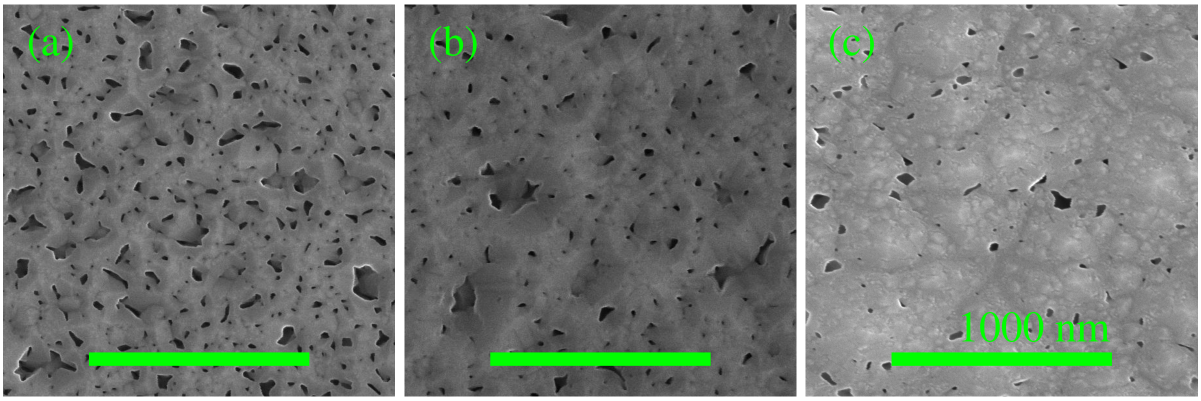

Figure 3.14: FESEM images of porous samples (a) A6 (b) B6 (c) C6. The scale bar corresponds to 1μm

The N/Ga flux BEP ratio is estimated to be 216, 148 and 50 for samples A6, B6 and C6. Sample morphology was studied using FESEM and image analysis was carried out using ImageJ software.

3.5.2 Results

Figure 5.5 shows plan-view FESEM images of samples A6, B6 and C6. All samples are porous. The smallest size of pores among these samples are a few nm in lateral size, while the largest ones are more than 100 nm. According to the IUPAC convention, samples are classified as nanoporous, mesoporous and macroporous if the pore sizes are less than 2 nm, between 2-50 nm, and more than 50 nm[85]. Thus these samples straddle the boundary between mesoporous and macroporous materials.

To quantify the microstructural parameters, we carry out image analyses of the FESEM micrographs. The pore density, mean pore size and average thickness for the samples are plotted in Figure 3.15. The pore density varies as 160 μm^{-2} for sample A6, 66 μm^{-2} for B6 and 49 μm^{-2} for C6. The mean size of the pores are found to be 60±22, 40±17, and 30±15 nm for A6, B6 and C6, respectively. The errors represent the standard deviation in the measured values. The sample thickness is 0.55 μm for A6, 0.8 μm for B6 and 2.26 μm for C6. All these growths have been performed at nitrogen-rich conditions. As we move towards more nitrogen-rich condition, the vertical growth rate decreases and the pores become bigger in size and more numerous. Thus the sample porosity, defined as volume fraction occupied by voids compared to the total volume of sample, can be tuned solely by changing flux ratio in the MBE growth.

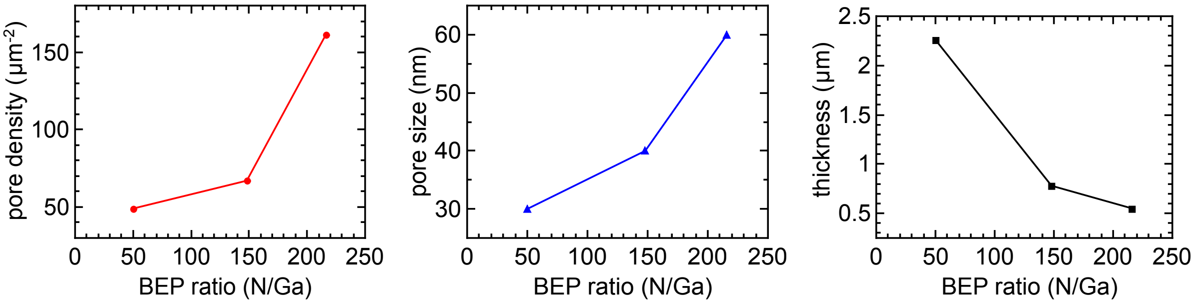

Figure 3.15: Graphs of variation of microstructural parameters of porous GaN samples with flux. (Left) pore density, (middle) mean pore size, and (right) sample thickness as a function of ratio of beam equivalent pressure of nitrogen and gallium flux.

3.5.3 Discussion

Looking at the pores in samples A6 - C6, some are a few nm wide and point-shaped, some are extended. We take a closer look at the pore morphology for sample B6, as shown in Figure 3.16. Figure 3.16(a) shows the overview, while the rest figures focus on specific regions of the sample. If two pores are close, they appear to merge to form an elongated line-like void as shown in 3.16(b). Multiple nearby pores can merge to form polygon or star-shaped voids, and 3.16(c) shows an example.

The smallest pores appear to be nanopipes which have been frequently reported for epitaxial growth of GaN[86][87]. The nanopipes are known to originate from open core screw dislocations. From F. C. Frank's work in 1951 we know that a dislocation with a large enough Burgers vector (> 1 nm), can only exist in equilibrium with an open core. The hollow core of the dislocation is formed by the removal of material from the strained region near the core to reduce strain energy and thereby form an internal surface[88]. The screw dislocation of the nanopipe have been found to lead to a spiral-type growth[89]. For GaN growth on sapphire in nitrogen-rich conditions, the tendency is to form 3D islands rather than a flat film. Due to the significant mismatch, screw dislocations form and thread upwards. Additional dislocations can form due to island coalescence to accommodate the mismatch in orientation[90]. It is known that screw dislocations can also form due to interactions between edge and mixed type threading dislocations[87]. When the islands coalesce, the spiralling growth from the individual nanopipes can interact to form a complex morphology such as that of the shown samples. Work by W.K. Burton, Frank and Cabrera analysed in detail the interactions of two or more growth spirals of the same or opposite Burgers vectors[91]. Two nearby screw-dislocation growth

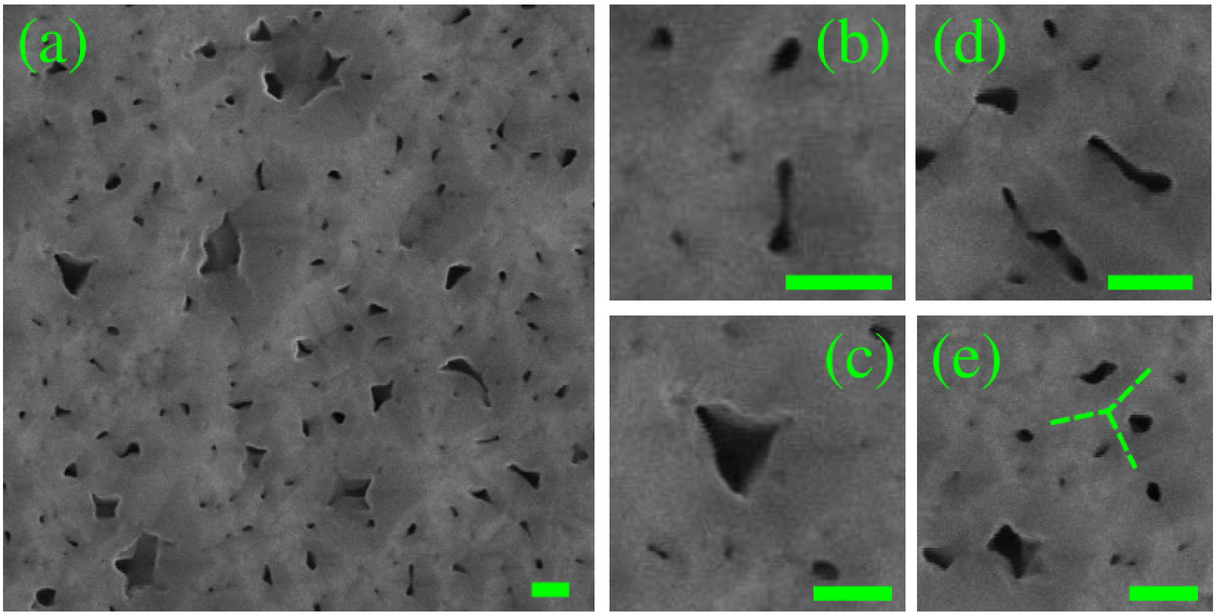

Figure 3.16: FESEM images of sample B6 focussing on different regions. The scale bar corresponds t0 100 nm. (a) shows a large area region. (b) shows merger of two pores to form an elongated slit-like pore. (c) shows three pores merging to form an extended triangular void. (d) shows a wedge shaped nanowall forming between two elongated voids. (e) shows that the nanowalls around voids can join to form a network, as indicated by dashed lines.

spirals can become synchronised and enhance the growth rate. During growth, the nanopipes can open up and indeed, pipes with widths of several tens of nm have been observed[89]. A valley-like formation, with a screw-dislocation at the centre, can interact with nearby valleys to result in various morphologies. Figure 3.16(d) shows the formation of a wedge-shaped nanowall bounded by two elongated voids. Such walls can form a network - interspersed by the voids as shown in Figure 3.16(e) and marked with dashed lines.

Tuning growth from porous film to nanowall network

3.5.4 Experimental details

Three samples were grown by MBE on c-sapphire substrate at a deposition temperature of 630°C and for 4 hours. The N/Ga flux ratio was varied from sample to sample by changing both Ga k-cell temperature and N_2 flow rate. Sample A7, B7 and C7, had Ga k-cell temperatures of 1040°, 1040°, and 1080°C and had N_2 flow of 6.5, 4.5 and 4.5, respectively. Sample morphology was studied using FESEM along with measurement of cross-sectional thickness.

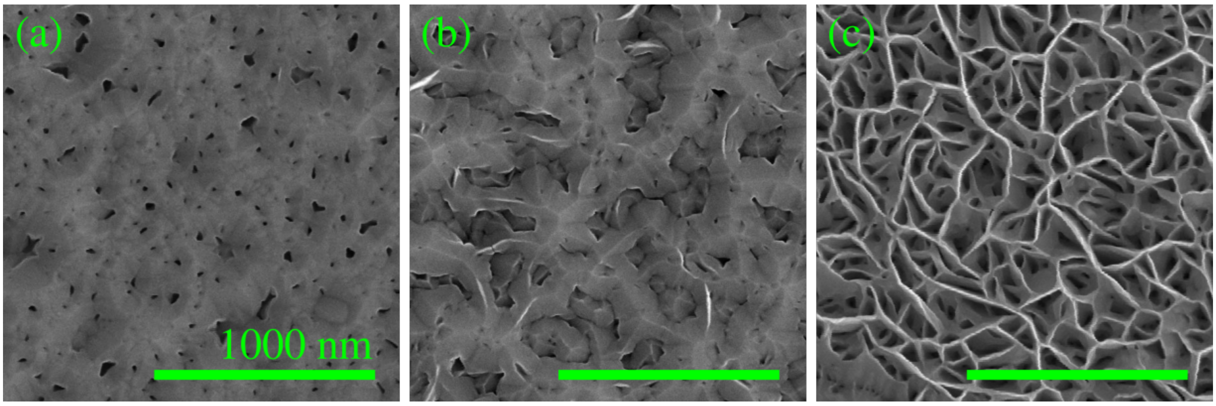

Figure 3.17: FESEM images of samples (a)A7, (b) B7 and (c) C7. The scale bar corresponds to 1 μm.

3.5.5 Results

Figure 3.17 shows the FESEM images of samples A7, B7 and C7. From A7 to C7, the N/Ga flux ratio reduces - i.e. C7 is grown at most metal-rich environment, albeit for all three samples N/Ga>>1. It can be seen that sample A7 has a porous morphology; for sample B7, wedge-shaped sharp-tipped nanowalls can be seen, and for C7, the sample has an interconnected sharp nanowall network morphology. The sample thicknesses are 0.74 μm for A7, 0.85 μm for B7, and about 2 μm for C7. Enhanced growth rate due to an increase in metal flux is found to help the formation of nanowall network.

Nanowall network growth mechanism

Self-induced plasma-assisted MBE growth of GaN nanowall network was first reported by Kesaria et al. in 2011[36]. This was followed by reports of MBE growth of nanowall network using laser MBE, plasma-assisted MBE, and ion beam assisted MBE on sapphire, silicon and SiC[92 93]. There have been several studies purporting to understand the growth mechanism of interconnected and in-plane randomly oriented nanowall network by varying growth conditions such as metal flux, nitrogen flux, substrate temperature, growth duration and by the introduction of an intermediate layer such as Al droplet, AlN thin film or GaN buffer layer[36 92 94].

As we have seen previously, a nitrogen-rich condition is essential for the growth of nanowall network. A high nitrogen flux suppresses Ga adatoms' diffusion and forces them to nucleate closer to their point of impingement. In a study by Poppitz et al., the importance of lateral growth for the formation of nanowall network was emphasised[93]. He carried out GaN growth on SiC using ion beam assisted MBE, which uses a standard Ga effusion cell and a hollow anode N ion beam source providing N^+ and N^{2+} ions. The morphology of the film was studied using SEM from substrate centre towards the edge such that the film thickness progressively falls due to reduction in source flux away from substrate centre. Thus this study provides a thickness-dependent morphology study. It was observed that the initial growth took place in the form of islands, and later on, the islands elongated laterally while also increasing in density. Finally, these elongated islands coalesce, forming the typical interconnected nanowall network morphology.

The importance of Ga adatom's surface diffusion in the growth of GaN nanowall network was stressed by Zhong et al. in his study of growth of GaN nanostructures on Si(111)[94]. By varying Ga flux and pre-depositing Al droplets on the substrate before GaN growth, the morphology of GaN could be tuned from nanocolumns to nanowall network to compact film. When GaN was deposited on bare silicon, it formed nanocolumns. Keeping other growth parameters same, an Al droplet layer was deposited on Si, following which the deposited GaN had nanowall network morphology. Finally, by keeping other parameters same, including the Al droplets, and only increasing the Ga flux, a compact film could be formed. SEM and AFM studies of the samples showed that the size of the voids of the nanowall network is similar to the size of the Al droplets. It was also found that the Ga diffusion length, estimated from the lateral size of nanocolumns, is also similar to the inter-droplet distance. The authors concluded that the growth of GaN is hindered on top of Al droplet, and adatoms diffuse in the bare regions forming the nanowall network.

Nayak et al. carried out a comprehensive study of the growth of GaN nanowall network, combining experiments and first-principles density functional theory (DFT) study, which involved the growth of nanowall network samples for different time durations, from 10 minutes to 80 minutes, which were then studied using AFM and SEM[95]. It was found that in earliest stages, the growth proceeds by formation of tetrahedral islands bounded by (20-21) planes, as determined by inter-planar angles. Later, the tetrahedral islands evolve into 'Y' shaped structures and their density increases. An edge-enhanced growth takes place, and the arms of the 'Y' shaped structure elongate. With time, those structures merge, at which point the edge enhanced growth stops, and is taken over by vertical growth of the connected structure. The time evolution of the morphology is shown

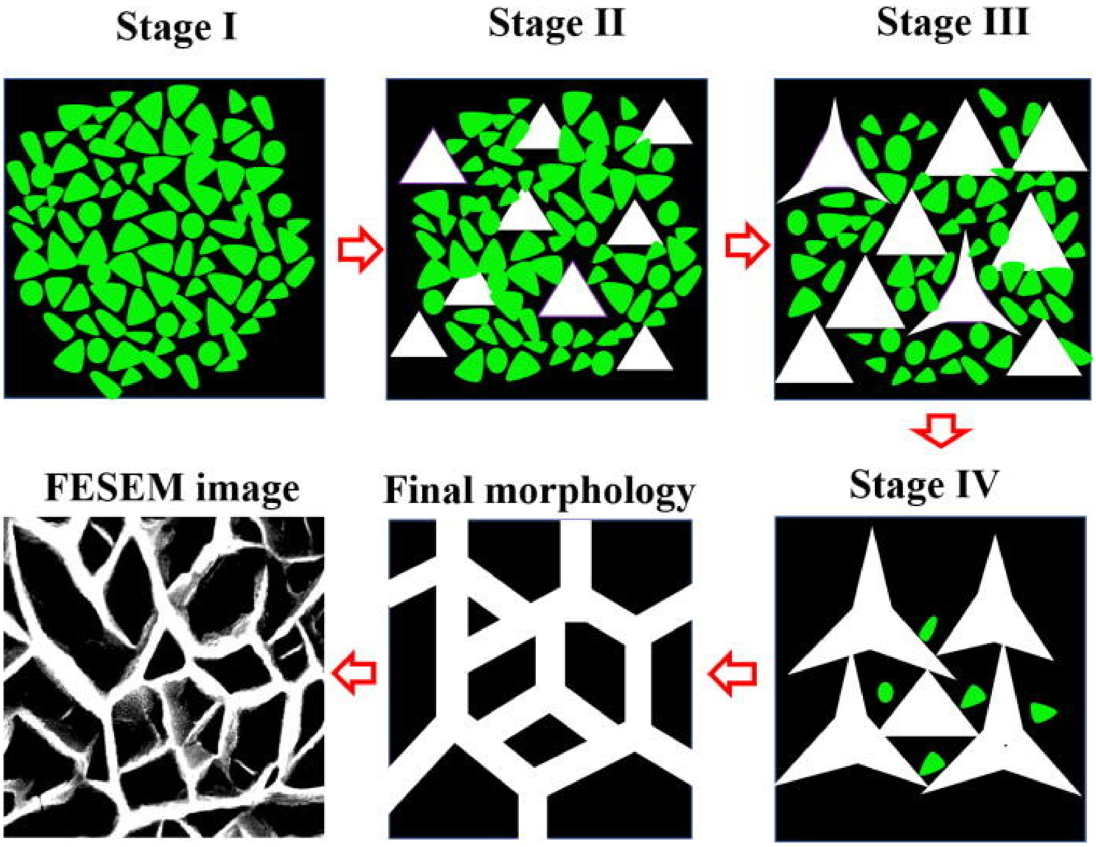

Figure 3.18: Schematic diagram of evolution of film morphology with time due to shape transition and edge enhanced growth. Last image shows FESEM image of a nanowall network sample. Adapted from ref 49.

schematically in Figure 3.18.

The initial formation of the tetrahedral islands was understood in terms of strain, surface and edge energies. The strain energy originating from the misfit of the heteroepitaxy can be relaxed elastically by the island by forming facets and changing its surface area or plastically by forming dislocations. It is known that lateral and vertical growth rate is more for dislocated and relaxed island compared to non-dislocated one – for which growth is accompanied by an increase in strain energy. It is possible that the tetrahedron shape originates from a difference in adatom attachment rates and site exchange between atomic steps. From literature, an energetics driven shape transition is also known to occur during the formation of GaN nanorods[64].

The mechanism of the edge-enhanced growth is studied using DFT calculations in which the islands are modelled as wedges bound by (20-21) atomic planes, which are N terminated. There exist two types of nitrogen atoms based on atomic positions; the ones on the surface have two dangling bonds, and the ones on edge have three. These nitrogen atoms form dimers and trimers accordingly. This means that the adsorption energy of the Ga atoms depends on their position, as that determines the number of neighbouring N atoms. Calculations revealed that the energetically favourable position for a Ga adatom is in the centre of the (20-21) facet. The adsorption energy was seen to decrease from -1.75 eV to -2.37 eV as the wedge width was changed from 6.35 $\AA$ to 3.14 $\AA$. A significant energy barrier exists for adatoms diffusion from one facet to another crossing the edge, and the barrier strengthens as the wedge width decreases. The implication is that Ga adatoms would move towards the thinner part of the wedge near the edge from the thicker part to reduce energy. This edge-enhanced diffusion mediated growth leads to the formation of nanowall network.

3.5.6 Inferences

A common theme among the mechanisms discussed so far for the growth of GaN nanowall network is that all of them start with the growth of 3D islands and later coalesce. In the model by Nayak et al. and Poppitz et al. elongated islands merge to form the network, and the bare substrate acts as the base of the voids. In the work by Zhong et al., the regions covered by Al droplets hinder the growth of GaN, and the bare substrate regions allow growth of GaN islands which join to form nanowall network.

In our experiment, we could tune the morphology smoothly from a porous film to a nanowall network just by changing the N/Ga flux ratio. Since formation screw dislocation related nanopipes can explain the porous morphology, the same can also be used to offer an alternative explanation of the formation of nanowall network. Growth around open core screw dislocations can lead to forming walls around a void. The high density of screw threading dislocations in the heteroepitaxial growth of GaN on sapphire ensure that there are a large number of voids in the islands that initially form. Coalescence of such islands and interaction among the spiralling growths lead to a merger of the walls and finally to the nanowall network morphology.

3.6 Conclusion

To summarise, this chapter discussed the heteroepitaxial growth of GaN, beginning with a comparison of different growth techniques and a discussion of the energetics and kinetics underlying the growth. Different epitaxial growth modes and their tuning by the degree of film-substrate mismatch and source flux was discussed. Focussing on the diffusion of adatoms, which can be controlled by changing growth parameters, it was experimentally shown that by tuning the parameters, the sample morphology could be changed from nanorods to porous films and nanowall networks to compact films. The microstructure of the sample can be tuned effectively by finely varying Ga flux, N_2 flow and substrate temperature.

Later in the chapter, we focus on the growth mechanism of nanorods. We were able to change the shape of the nanorods from tapering to widening by varying the Ga flux alone. We found that step-flow growth is crucial for both radial and axial growth of the nanorod. For low Ga flux, atomic steps on the nanorod sidewall originate from nanorod-substrate boundary leading to a tapered shape, and for high Ga flux, the steps originate from nanorod top-sidewall boundary resulting in a widening shape as nanorod grows. In several nanorods, mixed-type threading dislocations were observed starting at the interface and ending at nanorod top and forming dissimilar vicinal semi-polar facets there. But such were not observed in all nanorods, thereby discounting them as an essential requirement for nanorod formation.

In the final portion of the chapter, we study growth of porous films and nanowall network. In particular nitrogen-rich conditions, porous GaN have been grown by MBE and their microstructural parameters such as pore size and density tuned by changing the MBE parameters. By changing the N/Ga flux ratio the morphology could be tuned from porous film to interconnected nanowall network. Screw-dislocation related nanopipes can explain formation of pores. A number of reported growth mechanisms to explain formation of nanowall network were discussed. Formation of 3D islands in the nitrogen-rich growth regime and their subsequent coalescence underlies the growth of nanowall network. Edge enhanced growth and screw-dislocation related growth spirals may play an important role in this regard.

Chapter 4

Study of structural properties of nanostructures

This chapter describes the structural properties of molecular beam epitaxy grown GaN nanostructures. By varying the growth conditions a number of nanostructures such as nanorods, nanowall network and porous films are grown which are then studied using a number of ex-situ characterisation techniques such as high-resolution XRD, Raman spectroscopy and TEM to understand the morphology dependent structural properties.

4.1 Introduction

Defects and residual stress play a crucial role in determining the properties of semiconductor materials, and thus a control over them is necessary to optimise the material for specific applications. The heteroepitaxial growth of GaN on dissimilar substrates leads to well known material issues which can be ameliorated to a certain extent through nanostructuring. The relatively large free surface area of nanostructures allows it to relax the growth related stress. The low foot-print of one-dimensional nanostructures such as nanowires reduces the effect of film-substrate mismatch. The defects such as impurities, native defects, dislocations and stress can affect the optical and carrier transport properties of the material, which makes it important to understand the correlation between growth conditions, morphology and resulting structural properties. In this chapter, we look into three different types of samples - nanorod array, porous thin films, and nanowall network to understand their structural properties.

4.2 Microstructural properties of nanorods

GaN nanorods can be grown directly on common substrates without any special steps such as substrate patterning, use of catalysts, or deposition of metal droplets to act as nucleation centres. By tuning the growth parameters to suppress two-dimensional growth mode, nanorods can be grown in a self-induced manner. In this work, we have grown vertically aligned, well separated epitaxial GaN nanorods on sapphire and silicon substrates using MBE. A general observation made during the work is that, for GaN nanorods grown on sapphire, a 'matrix' layer also forms on the substrate, whereas for growth on silicon, such basal matrix layers are absent. Matrix layers have been reported in the literature previously for nanorod growth on both sapphire and silicon[96 97 35 98]. The shape of the matrix layer has been found to range from rough and irregular, to faceted, to quasi-columnar morphologies.

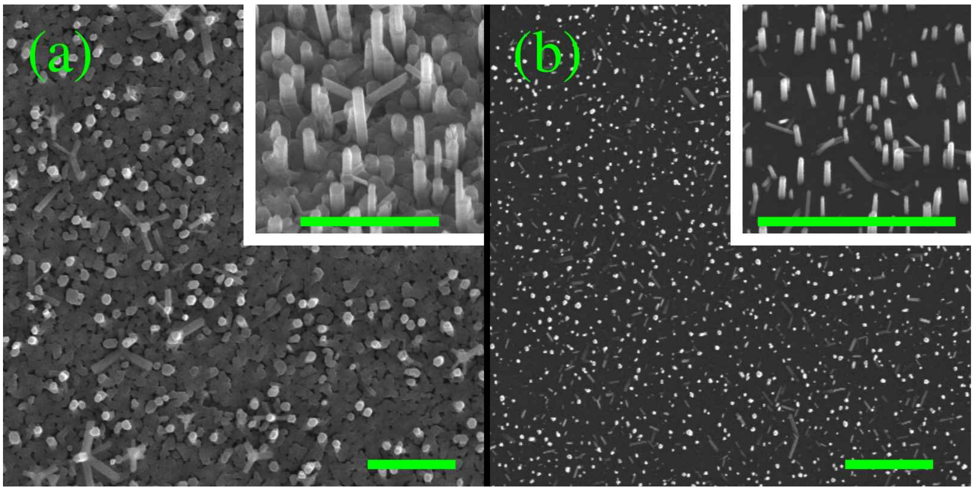

Figure 4.1: Typical plan-view FESEM image of (a) GaN nanorods grown on sapphire (0001) and (b) silicon (111). The inset shows the 30 ° tilted-view images. The scale bar corresponds to 1 μm.

As an example, we choose two GaN nanorod samples A1 and B1, with A1 grown on c-sapphire and B1 grown on Si(111). Both samples are grown at 630 °C temperature in similar nitrogen rich conditions. Figure 4.1 shows plan-view and tilted-view FESEM images of the samples. As we can see from the plan-view and tilted view images, in sample A1, the nanorods emerge from a faceted basal matrix layer which includes cavities. Sample B1 in Figure 4.1(b) consists of well separated GaN nanorods on bare silicon without any basal compact layer. It is known, that during growth of GaN on silicon, exposure to active nitrogen plasma may lead to formation of amorphous SiN_x layer on the silicon surface. Gallium flux on bare silicon can also form SiGa alloy layer, which makes subsequent GaN growth problematic. Often an intermediate layer (interlayer) such as AlN is used to prevent reaction between gallium and nitrogen, increase substrate wetting and accelerate GaN nanostructure formation on silicon[35 99].

The presence of a basal matrix layer can modify the properties of the nanorod array, and thus it is important to study the formation of the matrix layer and its effect on structural properties. Since we observe the formation of the matrix layer only during growth on sapphire, we choose the sample A2, which is also grown on c-sapphire, to study its growth related structural properties.

4.2.0.1 Experimental details

Sample A2 was grown using PAMBE on c-plane sapphire. The substrate was degreased using organic solvents, rinsed in de-ionised water, dried with N_2 gas, and thermally degassed inside MBE chamber at 850 °C for an hour. During the growth, the Ga flux was kept at a BEP of 5.5×10^{-7} Torr while the nitrogen flux had a BEP of 2.5×10^{-5} Torr, making the growth condition nitrogen rich. The forward plasma power was kept at 375 W and reflected power was kept low, at about 10 W, to stabilize the plasma. The plasma was allowed to stabilise for a few minutes before the commencement of growth. The substrate temperature was held at 630 °C and the growth duration was 120 minutes.

The sample morphology was studied using FESEM. Structural characterization was carried out using TEM, Raman spectroscopy and high resolution XRD. For TEM sample preparation, material was scratched off from the grown sample and subsequently dissolved in ethanol and drop-casted on carbon coated copper TEM grid. For Raman spectroscopy, a Horiba Jovin Yvon system with an Argon laser source of wavelength 514 nm was used with the sample positioned in backscattering geometry.

4.2.0.2 Results

Figure 4.2 shows the FESEM images of the sample in plan-view, cross-section and a 75° tilted-view. The sample consists of thin nanorods emerging out of a matrix layer. From these images it is clear that shorter and wider nanorods coalesce to form the basal matrix layer.

Next, we perform HRXRD studies to measure lattice parameters and

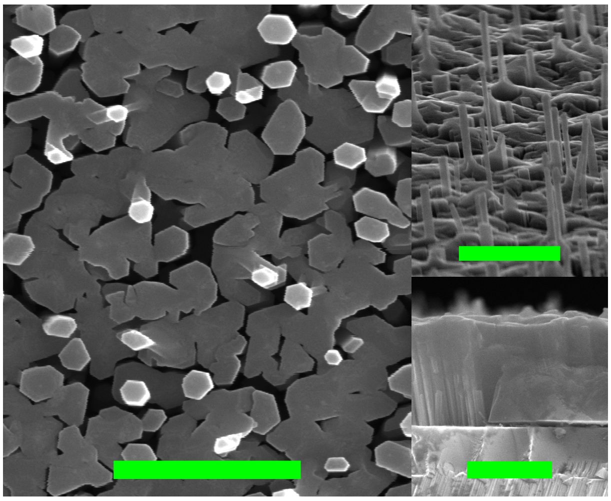

Figure 4.2: Plan-view FESEM image of sample A2 showing the nanorods emerging out of base matrix layer. Right-top inset shows a 75° tilted-view image and right-bottom inset shows a cross-sectional view of the sample. The scale bar corresponds to 500 nm.

calculate the residual strain. The sample is found to have c-oriented wurtzite structure, as expected for growth on c-sapphire. $2\theta - \omega$ scans were carried out in symmetric and skew symmetric geometry to determine the c and a lattice parameters. Figure 4.3 shows the $2\theta - \omega$ scans for 002 and 101 reflection. The symmetric 002 peak could be fitted with a single Gaussian peak, however the 101 peak profile is not symmetric, and required two Gaussian functions for an acceptable fit. The calculated c lattice parameter for the sample is 5.188 $\AA$ and the a lattice parameters corresponding to the centre of the two fitted Gaussian peaks are 3.185 $\AA$ and 3.069 $\AA$. Assuming relaxed GaN lattice parameters to be 3.1891 $\AA$ and 5.1855 $\AA$ we estimated the out-of-plane strain to be $+4.82 \times 10^{-4}$ and in-plane strains to be -1.25×10^{-3} and -3.76×10^{-2}[26] using eqn. (2) and (3) of the introductory chapter. The strain in c-plane is thus compressive and strain perpendicular to c-plane is tensile. The compressive nature of the in-plane residual strain is expected due to mismatch between the sapphire substrate and overlayer lattice parameters.

In figure 4.3, the positions corresponding to the relaxed lattice parameters have been marked with an arrow as a visual guide. The out-of-plane strain of the sample is small whereas the in-plane strain is comparatively higher. The bimodality of the microstructure is found to manifest as peak splitting for the asymmetric XRD scan here. It is apparent that different regions of the sample have different magnitudes of strain. Broadly speaking, the sample consists of two types of structures, the thin nanorods and

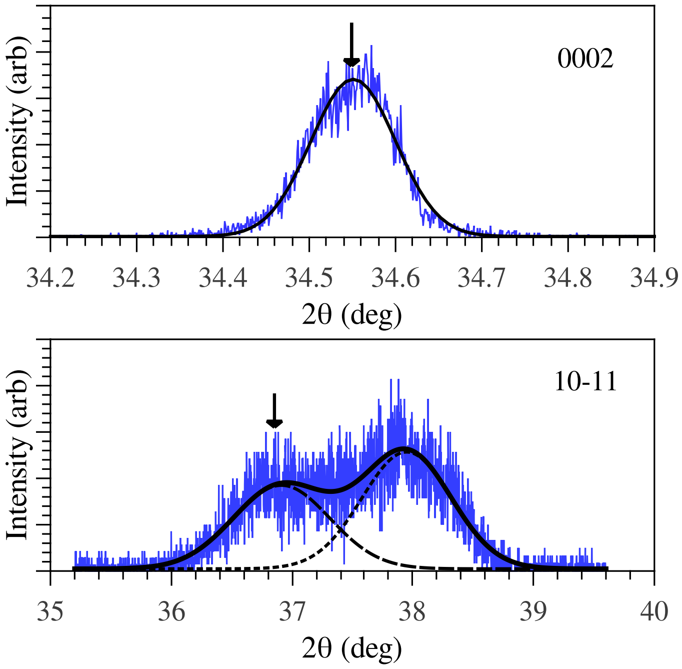

Figure 4.3: HRXRD $2\theta-\omega$ scans of sample A2. (Top) 002 reflection and (bottom) 101 reflection. 2θ positions corresponding to relaxed GaN lattice parameters are marked with arrows.

the wide and short coalesced nanorods which make up the matrix layer. Owing to the free top surface, both the thin longer nanorods and the shorter coalesced nanorods are free to relax the out-of-plane stress elastically. Although the longer nanorods have free side surface enabling them to elastically relax the in-plane stress also, the coalesced shorter nanorods do not have that provision. Based on this, it is fair to assume that in the 101 reflection, the sub-peak at lower angle (with lattice parameter closer to ideal) originates from the longer nanorods, whereas the sub-peak at higher angle (higher strain), originates from the matrix layer. The breadth of the peak is related to the non-uniformity of the strain.

To independently measure the level of residual stress, we carry out Raman spectroscopy of sample A2. We observe a peak corresponding to sapphire at 418 cm^{-1} and the GaN E_2^H peak at 568.4 cm^{-1}, shown in Figure 4.4. There is a blue shift of the E_2^H peak with respect to the stress-free value for heteroepitaxially grown GaN at 567.6 cm^{-1}[100]. The blue shift indicates a compressive stress in the c-plane, which is generally accompanied by a tensile stress perpendicular to c-plane due to Poisson effect.

The in-plane biaxial strain and stress are related as:

$$\sigma = M\epsilon_{xx}^{bi} \tag{4.1}$$

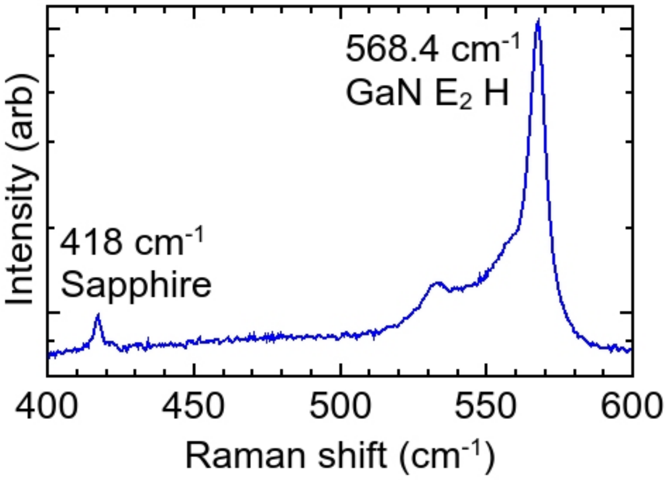

Figure 4.4: Raman spectra of sample A2 showing sapphire substrate peak and GaN $E_2{}^H$ peak.

With

$$M = c_{11} + c_{12} - 2\frac{c_{13}^2}{c_{33}} \tag{4.2}$$

Taking widely accepted literature values for the elastic constants for GaN, we get a value of M = 478.5 GPa[29]. In addition, the stress-shift rate for GaN $E_2{}^H$ peak is taken to be 2.9 cm^{-1}GPa^{-1} from the literature[100]. Combining these, the residual biaxial strain for sample A2 is estimated to be 5.76×10^{-4}, of compressive nature. Apart from the type of strain, the values do not closely match, however it is to be noted that this estimation of strain from Raman spectra only considers pure biaxial strain and ignores the hydrostatic strain, which can be significant.

As both HRXRD and Raman spectroscopy provide results from a comparatively large area of the sample which is averaged out, we carry out transmission electron microscopy study to investigate the sample microscopically. For this study, scratched-off material from the sample was ultrasonicated in organic solvent and drop-casted onto a TEM grid. Figure 4.5 shows the low magnification image of a representative region of the sample. It contains both the thin long nanorod portion (marked as A) and matrix layer portion composed of shorter nanorods (marked as B). Figure 4.5 insets show the electron diffraction pattern (DP) from the two regions marked A and B. The DP of region A corresponds to 10-10 zone axis whereas that of B corresponds to 11-20 zone axis. This indicates that there is an exact 30° in-plane rotation between the longer rods and the shorter ones. This particular observation of 30° rotation has been verified from other scratched-off sample portions placed on the grid.

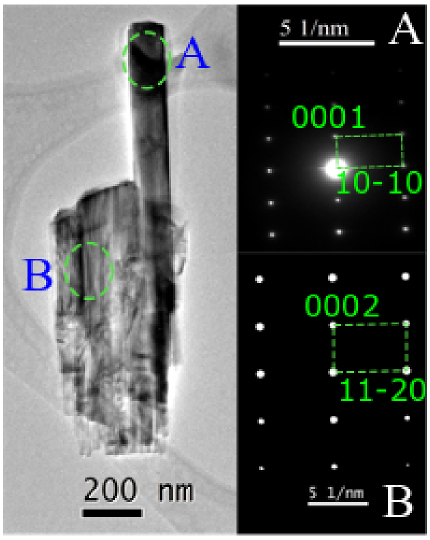
A
B
200 nm
5 1/nm
A
0001
10-10
0002
11-20
5 1/nm
B

Figure 4.5: (Left) low resolution TEM image of a nanorod and matrix layer from sample A2. (Right) electron diffraction patterns corresponding to regions marked as A and B in the micrograph.

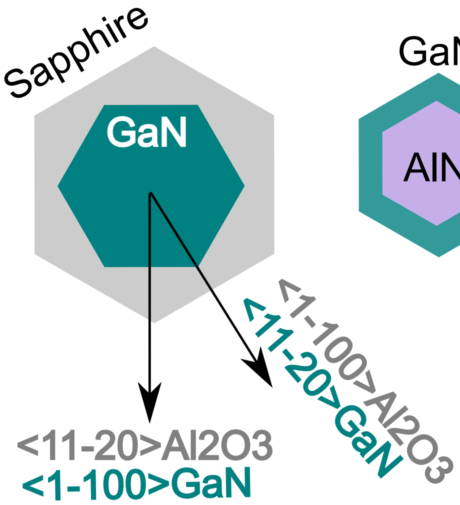
Sapphire
GaN
GaN
AlN
<11-20>Al2O3
<1-100>GaN
<1-100>Al2O3
<11-20>GaN

Figure 4.6: Schematic diagram showing in-plane epitaxial relationship between GaN grown directly on c-sapphire and GaN grown on AlN.

We correlate the 30° in-plane rotation among the bimodal nanorods with the rotation of GaN unit cell for strain minimisation. GaN when grown on c-sapphire, rotates its unit cell by 30° to reduce the in-plane mismatch from -33% to +16%. However, when GaN is grown on AlN, the mismatch is small, 2.3% and GaN unit cell does not rotate. These in-plane epitaxial relationships have been shown in the schematic diagram of Figure 4.6. Introduction of an AlN interlayer can change the polarity of GaN. Figure 4.7 defines the Ga- and N-polarity. For Ga-polar GaN, the Ga-N bond along c-direction goes from Ga to N atoms whereas it is from N to Ga atom for N-polar GaN.

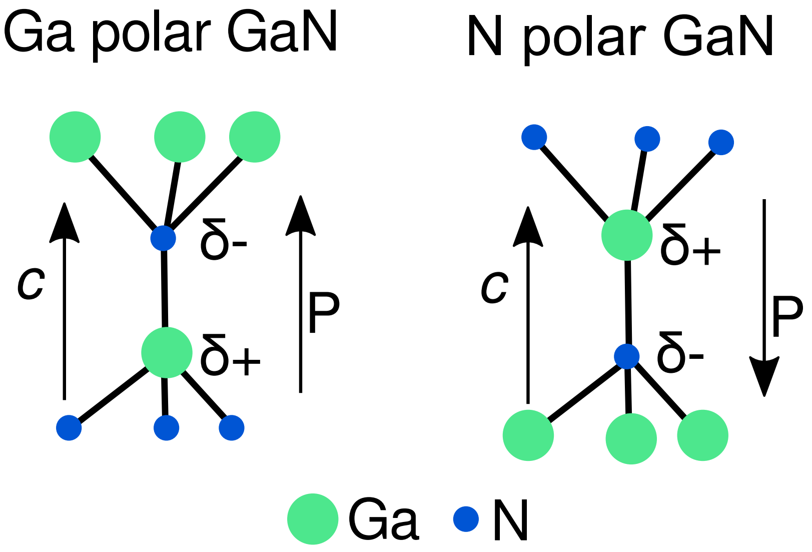

Figure 4.7: Schematic diagram demonstrating atomic geometry of Ga-polar and N-polar GaN. Accumulation of induced charges and direction of polarisation vector P are also shown.

In this work, any AlN intermediate layer was not deliberately grown, however before beginning growth, the substrate temperature was ramped down to growth temperature and stabilised, and simultaneously nitrogen plasma was allowed to stabilise. In absence of an isolation chamber for the active nitrogen plasma, the active nitrogen leaks into the growth chamber as indicated by the pressure reading of the ion gauges. It is known that for sapphire nitridation at low temperature and for long duration, a smooth 1-2 monolayer thick AlN film forms whereas for high temperature nitridation for a short duration creates rough patches of AlN[101].Apart from deposition of AlN buffer layer, sapphire nitridation has also been used to control the polarity of GaN overlayer[102]. Georgakilas observed formation of Ga-face

GaN for high nitridation temperature and N-face GaN for low nitridation temperature[103]. Similar observation was also reported by Mikroulis et al. who stated that significant sapphire nitridation only takes place at high substrate temperatures and leads to formation of Ga-face GaN overlayer[104]. While these reports dealt with sapphire nitridation using RF nitrogen plasma, Sonoda et al. used ammonia-MBE to study the effect of nitridation on GaN polarity and found that Ga-polar film is obtained following sapphire nitridation using ammonia gas and N-polar without nitridation[105]. For MOCVD growth, it was found that when substrate is at a high temperature, introduction of ammonia for a few seconds is enough to change polarity of the overgrown GaN film through an unintentional nitridation[102]. Specifically for growth of GaN nanorods on sapphire, mixed polarity nanorods have been observed for incomplete nitridation in contrast to pure N-polar nanorods for optimised nitridation[106].

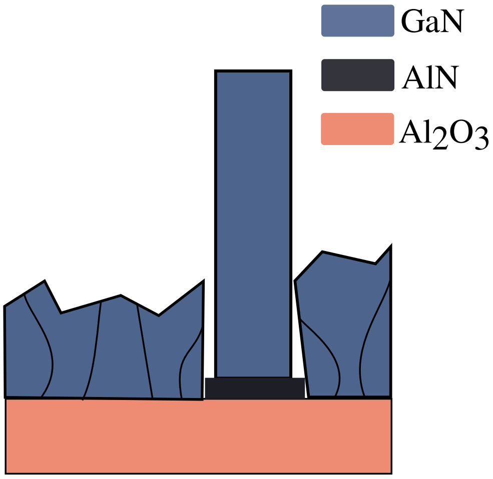

Figure 4.8: Schematic diagram of GaN nanorod and matrix layer grown on partially nitrided sapphire.

In case of (0001) sapphire, the crystal structure consists of two closely spaced aluminium layers and an oxygen layer. The nitridation of c-sapphire without supplying any aluminium involves the formation of bonds between the terminating aluminium layer and active nitrogen atoms. By changing the conditions of nitridation, a monolayer or a bilayer of AlN of desired smoothness can be formed. We propose that an unintentional nitridation which takes place prior to growth, leads to small AlN patches which work as nucleation centres for growth of GaN nanorods. The reduced incubation time for these initial nanorods allows them to grow longer compared to the nanorods which grow directly on bare sapphire, requiring longer incubation periods and are comparatively shorter. Thus a non-uniform initial growth condition (incomplete nitridation) leads to a bimodal morphology of the final sample. Figure 4.8 is a diagram illustrating the proposed scheme. As discussed previously, the coalesced shorter nanorods are significantly strained and thus may be undesirable for applications. An optimisation of growth conditions, including optimal nitridation is expected help minimise the growth of the matrix layer.

4.3 Residual strain in porous films

Porous materials have myriad applications owing to their unique and tunable properties[77][78]. One of the prototypical porous semiconductors - porous silicon has been used in diverse applications such as light emission, optical waveguide, gas sensing, battery technology, and microfluidics, to name a few. An important use for porous semiconductors is their use as a growth template for growth of subsequent layers for strain and defect engineering as the porous structure allows for strain relaxation and dislocation annihilation[107][108]. Thus, it is important to study the effect of microstructural parameters of a bottom up synthesised porous semiconductor on its structural properties. In this section we vary the growth conditions to grow a set of porous GaN samples using MBE and probe their strain related properties.

4.3.1 Experimental details

A set of three porous GaN samples were deposited on c-sapphire using PAMBE. Before deposition, the substrates were cleaned using organic solvents, rinsed in de-ionised water, dried and then thermally degassed inside MBE. Samples A3, B3 and C3 were grown for a duration of 4 hours by keeping substrate temperature constant at 630° and plasma power fixed at 375 W. The gallium flux and nitrogen flow were varied from sample to sample as noted in Table4.1. Although all three samples were grown in nitrogen rich condition, a progressively higher Ga flux was applied from sample A3 to C3. FESEM images were acquired in plan-view and cross-sectional-view. Open source ImageJ software was employed to quantify the samples' porosity through image analysis. Structural characterisation of the samples was performed using Bruker D8 discover high resolution XRD.

Sample	Ga flux BEP (Torr)	Nitrogen flow (sccm)	N/Ga Flux ratio
A3	1.65×10^{-7}	6.5	216
B3	2.80×10^{-7}	8	159
C3	5.50×10^{-7}	4.5	50

Table 4.1: Growth conditions of porous GaN samples

4.3.2 Results

Figure 5.5 shows the plan-view FESEM images of samples A3, B3, and C3. It is seen that a variation in N/Ga flux ratio during growth leads to a change in the samples' porosity. Through image analysis, the mean size of the pores and their average density were estimated and are given in Table 4.2 along with the sample thickness.

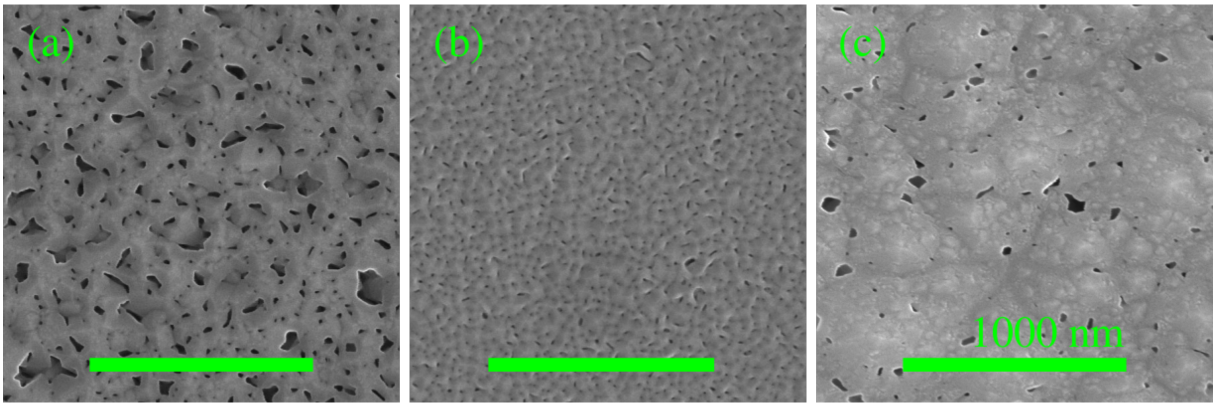

Figure 4.9: Plan-view FESEM images of sample (a)A3 (b)B3, and (c)C3. The scale bar corresponds to 1 μm.

A direct correlation is found between applied Ga flux and sample thickness as expected. A higher Ga metal flux leads to a higher vertical growth rate in Ga limited growth conditions. The pore size and density do not follow a simple trend. The pore size increases from sample B3 to C3 to A3 while density increases from C3 to A3 to B3. The relative area occupied by the pores (void fraction) however, decreases consistently from A3 to B3 to C3 as applied N/Ga ratio decreases.

To probe the sample strain, we measure the lattice parameters using XRD. It is known that the error in lattice parameter through Bragg's law depends on the particular 2θ angles. The following equation is obtained by taking logarithm of the Bragg's law and differentiating[109].

$$(\Delta d_{hkl})^2 = (\frac{cos\theta\lambda\Delta\theta}{2sin^2\theta})^2 + (\frac{\Delta\lambda}{2sin\theta})^2 \tag{4.3}$$

Sample	Mean pore size (nm)	Pore density (μm^{-2})	Thickness (μm)
A3	60	160	0.55
B3	13	330	0.68
C3	30	50	2.3

Table 4.2: Microstructural parameters of porous GaN samples

Here, Δd_{hkl} is the error in measuring d_{hkl}, $\Delta\lambda$ depends on particular optics used in the HRXRD system such as the type of monochromator, and $\Delta\theta$ depends on the optics as well as the step size. Based on this, high index reflections occurring at higher 2θ angles would yield lower errors. Practically though, these high index reflections have a lower intensity and signal-to-noise ratio, due to a corresponding lower number of atomic planes associated with them, and therefore a balance has to be found. We use 004 symmetric reflection instead of 002 and 006 to measure the c lattice parameter and 102 and 105 asymmetric reflections to calculate the a lattice parameter.

Sample	a($\AA$)	c($\AA$)	ϵ_a	ϵ_c
A3	3.201	5.189	$+3.73 \times 10^{-3}$	$+6.75 \times 10^{-4}$
B3	3.178	5.186	-3.48×10^{-3}	$+9.64 \times 10^{-5}$
C3	3.198	5.186	$+2.79 \times 10^{-3}$	$+9.64 \times 10^{-5}$

Table 4.3: Lattice parameters and strain of porous GaN samples

Table 4.3 tabulates the measured lattice parameters of the samples and the calculated strain values of the samples. It can be seen that the out-of-plane strain values ϵ_c are very small indicating a relaxation of the structure whereas the in-plane values are more significant. In case of a flat thin film of GaN epitaxially grown on c-sapphire, considering the mismatch of lattice parameters and thermal expansion coefficients, there should be a compressive stress on the GaN film. We see here that sample B3 has a compressive strain but the other two have tensile strain.

Keeping in mind the formation of porous films by coalescence of three-dimensional islands as discussed in the previous chapter, we can explain the observed tensile strain. If during growth, two neighbouring islands have a gap of the order of atomic dimensions, they coalesce to reduce energy by replacing the two solid-gas interface by a single solid-solid interface, leading to a tensile stress[110]. A complex interplay of growth and coalescence of the initial islands results in the final observed morphology whose strain is difficult to estimate a priori. But as porous samples have been used as a template for growth of secondary layers and structures, an optimisation of growth parameters can be used to tune the strain as desired[111][108].

4.4 Microstructural properties of NwN

The complex structure of GaN nanowall network which is highly porous and randomly oriented in-plane is an interesting problem for study. A kinetic control of the atomistic growth processes allows one to tune to morphology and microstructural properties which are interlinked with the structural properties. As mentioned previously, the porous structure can be used to tune the strain in a heteroepitaxial growth and reduce dislocation density. Based on this GaN NwN can be used as a template to grow superior quality thin films and nanostructures. Indeed in a previous study, we have observed a huge enhancement of electrical transport properties in InN nanostructures growth on GaN nanowall network[112]. Additionally, the residual strain can modify the band structure which influences its optical and transport properties. Thus it is important to study the morphology dependent structural properties of GaN nanowall network.

4.4.1 Experimental details

A set of three GaN NwN samples were deposited on c-sapphire using PAMBE. The routine cleaning and thermal degassing procedures were followed prior to deposition. Samples A4,B4,C4 were grown by keeping the plasma forward power constant at 375 watt and a fixed Ga flux with beam equivalent pressure of 5×10^{-7} Torr. Nitrogen flow and growth temperature were varied. The growth parameters and cross-sectional thickness of samples A4,B4, and C4 are listed in Table 4.4.

Sample	Nitrogen flow	$T_{\text{Substrate}}$ (°)	Duration	Thickness (μm)
A4	2.5	630	2 hour	0.8
B4	4.5	630	4 hour	1.5
C4	4.5	645	4 hour	1.5

Table 4.4: Growth conditions of GaN samples

FESEM was used to study the sample morphology. A cathodoluminescence set-up attached with FESEM was used for mapping. For HRXRD measurements, Bruker D8 Discover was used with 4 bounce Ge (220) crystal monochromator and scintillation counter as detector. Raman spectroscopy has been carried out in backscattering geometry using a Horiba Jovin Yvon system with an Argon laser of wavelength 514 nm.

4.4.2 Results

The sample morphologies studied using FESEM are shown in Figure 4.10, which also shows the sample thickness which have been tabulated in Table 4.4. All the samples have NwN morphology, though they differ in microstructural parameters such as porosity and average nanowall length and width. The plan-view images were analysed using open source ImageJ software. Figure 4.10 right panel shows the distribution of individual nanowall widths and the mean value calculated by fitting a Gaussian distribution to the data. Samples A4, B4 and C4 were found to have mean nanowall widths of 62, 106, and 135 nm.

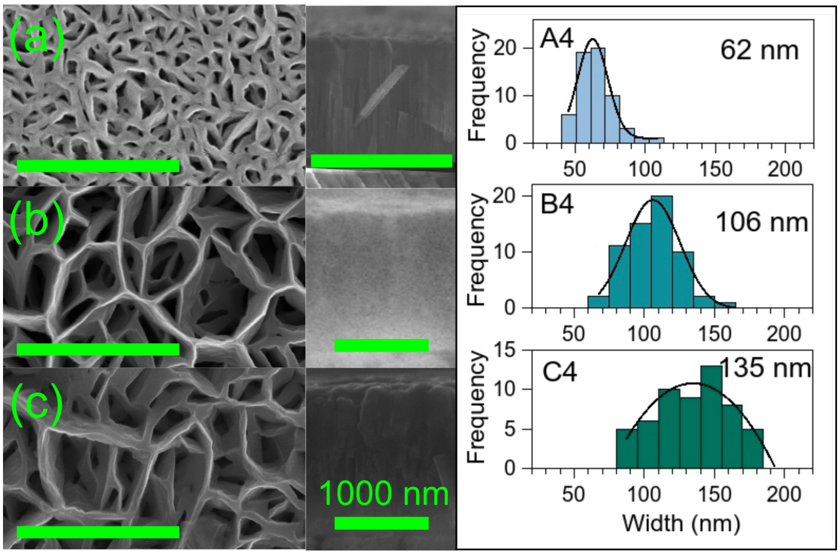

Figure 4.10: Left column: plan view FESEM images of the samples (a) A4, (b) B4, and (c) C4. Middle column: cross-sectional view of the samples. The scale bars correspond to 1 μm. Right column: the average width of the nanowalls obtained from image analysis.

4.4.2.1 Epitaxial relationship

To study the crystallinity of the NwN samples we carry out long range symmetric HRXRD scans. Figure 4.11(a) shows that in the symmetric mode, only GaN 00l peaks and $\alpha - Al_2O_3$ 00l$'$ peaks are recorded. This indicates that the GaN growth is c-oriented with the epitaxial relationship $[0001]_{GaN}||[0001]_{Al_2O_3}$. Azimuthal ($\phi$) scans as shown in Figure 4.11(b) were carried out to ascertain in-plane epitaxial relationship. Phi scans of GaN 101 reflection showed 6 dominant peaks separated by 60°. Phi scans of sapphire 1010 showed 3 peaks which are separated from GaN peaks by 30°, confirming the expected epitaxial relationship $[10-10]_{GaN}||[11-20]_{Al_2O_3}$. Thus, the NwN samples are single phase and c-oriented.

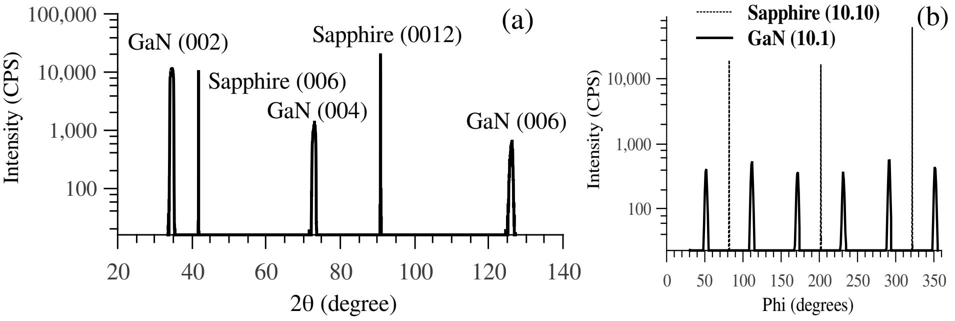

Figure 4.11: (a) Symmetric $2\theta-\omega$ scan and (b) azimuthal ϕ scans of GaN 101 and sapphire 1010 reflection.

4.4.2.2 Strain

For the lattice parameter determination, a set of 3 symmetric and 3 asymmetric reflections viz. GaN 002, 004, 006, 101, 105, and 204 were chosen. As per equation (3), as the error in measurement of d-spacing decreases with increasing 2θ angle, we used a weighted non-linear least square fit for determining the a and c values, with the following weight[113][114]

$$W_{jj}=(\frac{\theta_j}{\Delta\theta_j})^2 \tag{4.4}$$

The system of equations:

$$\frac{4}{3}(h^2+hk+k^2)\times\frac{1}{a^2}+l^2\times\frac{1}{c^2}=\frac{1}{d_{hkl}^2} \tag{4.5}$$

is cast in the matrix form **AU=D**
where:
A is coefficient matrix determined by hkl values.
$\mathbf{U}=(\frac{1}{a^2},\frac{1}{c^2})^T$ and
$\mathbf{D}=(1/d_{002},1/d_{004}...)^T$

A weighted minimization of $(1/d_{calc}^2-1/d_{meas}^2)$ yields the value of the lattice parameters. The following calculation was done using the open

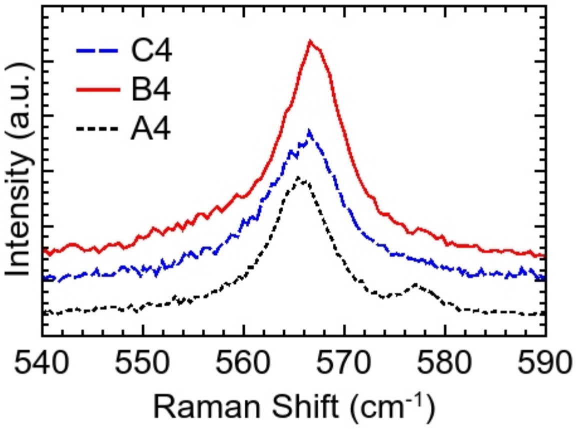

Figure 4.12: Raman spectra of samples A4, B4, and C4 showing the $E_2{}^H$ peak.

source Numpy-Python package.[115]

$$\sum_{j=1}^{n} [W]_{jj}(AU - D)_j^2 \rightarrow min \tag{4.6}$$

The calculated lattice parameters are tabulated in Table 4.5. The in-plane (ϵ_a) and out-of-plane (ϵ_c) strains are calculated assuming relaxed lattice parameters for heteroepitaxial GaN to be 3.1891 $\AA$ and 5.1855 $\AA$[26]. The in-plane strain appears to change from compressive to tensile. Keeping in mind that this value to strain includes both the pure biaxial strain due to mismatch in parameters between substrate and overlayer as well as hydrostatic strain due to point defects, we separate the pure biaxial and hydrostatic strain components following the procedure laid out in the introductory chapter and the results are shown in Table 4.5. We find that for all three NwN samples, the in-plane biaxial strain is of compressive nature whereas the out-of-plane strain is of tensile nature. Similar to the previous case of porous GaN samples, it can be seen that ϵ_c values are smaller than ϵ_a values for each sample owing to the free top surface for relaxation. The magnitude of strain however does not follow a trend and is morphology dependent.

Sample	a($\AA$)	c($\AA$)	$\epsilon_a(\times10^{-3})$	$\epsilon_c(\times10^{-3})$	$\epsilon_h(\times10^{-3})$	$\epsilon_a^{bi}(\times10^{-3})$	$\epsilon_c^{bi}(\times10^{-3}$
A4	3.179	5.187	-3.261	+0.3278	+0.7904	-2.343	+1.246
B4	3.190	5.191	+0.2822	+1.061	-0.9179	-0.5082	+0.2702
C4	3.185	5.191	-1.286	+1.061	+0.2462	-1.532	+0.8144

Table 4.5: Lattice parameters and strain of GaN NwN samples

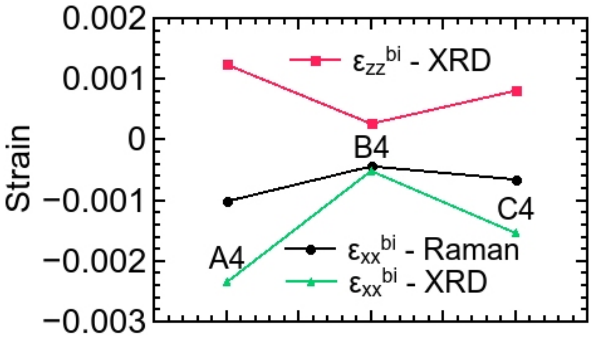

Figure 4.13: A comparison of out-of-plane biaxial strain calculated from XRD and in-plane biaxial strain calculated from XRD and Raman data for samples A4, B4, and C4.

For an independent estimation of the strain state of the NwN samples, we perform Raman spectroscopy of the samples in backscattering geometry. The position of the $E_2{}^H$ peak for each sample is shown in Figure 4.12. Using eqn. (1) and (2), we estimate that the in-plane biaxial strains for samples A4, B4, and C4 are: -1.01×10^{-3}, -4.32×10^{-4}, and -6.49×10^{-4} respectively, indicating compressive strain. Figure 4.13 shows the values of in-plane and out-of-plane strain for the samples measured through XRD and Raman spectroscopy. We see that overall, the magnitude of strain is least for sample B4 followed by C4 and A4. The strain values calculated from the Raman data follow the same trend as those from XRD data.

4.4.2.3 Line profile analysis

For GaN grown on sapphire, due to the high degree of mismatch between film and substrate lattice parameters, a high density of defects form, of which the most prominent are threading dislocations (TD). The dislocations can either be randomly positioned, with uniform density or these can create particular dislocation structures such as small-angle grain boundary (SAGB).[116],[117] The lattice distortion resulting from straight dislocations decay slowly (atomic displacement $u \sim \frac{1}{r}$), hence total lattice displacement at a point depends on contribution from the whole defect distribution. Unlike point defects, dislocations can broaden X-ray diffraction profile (XDP) even in low density[118]. Authors such as Kaganer[119], Holy[120] have developed methods for analysis of XDP to determine density and distribution of dislocations. Kaganer showed[119] that in case of dislocation related peak broadening, the low intensity tail region of the XDP follows a characteristic power law dependence:

$$I(q) \sim q^{-3}$$

Where, q is the deviation of the scattering vector from the reciprocal lattice vector.

$$\mathbf{q} = \mathbf{Q} \text{ - } \mathbf{Q_0} \tag{4.7}$$

Here scattering vector

$$\mathbf{Q} = \mathbf{K^o} \text{ - } \mathbf{K^i} \tag{4.8}$$

with K^i and K^o as the incident and scattered X-ray wave vectors. Equivalently

$$|\mathbf{Q}| = \frac{4\pi sin(\theta)}{\lambda} \tag{4.9}$$

It is to be noted that q^{-3} asymptotic behaviour is seen for a wide detector. We have used widely open slits in front of the detector for recording the pattern. If analyser crystal or narrow slit is used in the detector set-up for collimation of scattered beam, then the asymptote becomes $I(q) \sim q^{-4}$. As a wide detector accepts scattered beams from a significant angular distribution, that is akin to an integration in reciprocal space, changing from q^{-4} to q^{-3} behaviour. Apart from microstrain due to dislocations, size and misorientation effects, if present, will also broaden the XDP.

Here, we follow the formalism developed by Kaganer et al. in[119] and[121] to do a line profile analysis of our XDPs. The method consists of expressing the measured X-ray intensity as a Fourier transform of the pair correlation function

$$G(\mathbf{r_1},\mathbf{r_2}) = exp(i\mathbf{Q}.[\mathbf{U(r_1)}\text{-}\mathbf{U(r_2)}]) \tag{4.10}$$

where $\mathbf{U(r)}$ is the total displacement field at $\mathbf{r}$. After making certain assumptions such as ignoring size effect, misfit dislocations and considering only straight parallel threading dislocations, they finally arrived at the following expression:

$$I(\omega) = I_{bg} + I_0 \int_0^\infty exp(A_s x^2 log(1 + B_s/x) + A_e x^2 log(1 + B_e/x)) cos(\omega x) dx \tag{4.11}$$

Here, I_0 is $1/\pi\times$ area of XDP, I_{bg} is background intensity, the factors A and B are related to total dislocation density and dislocation correlation length respectively. The subscript s and e indicate screw and edge dislocation cases. The expressions for A and B are as follows:

$$A = f\rho b^2, B = gL/b$$

where, ρ is edge or screw dislocation density, b is the corresponding Burgers vector, L is the correlation length for the dislocation distribution and f and g are factors depending on X-ray diffraction geometry (e.g. symmetric or skew symmetric) whose calculations are non-trivial and their explicit expressions can be found in[121]. One way our calculation differs from[121] is that we have ignored the mixed dislocation as in any case this formalism is unable to distinguish between screw (edge) component of a mixed dislocation and pure screw (edge) dislocation. For large ω, the asymptotic behaviour of intensity in equation (11) is:

$$I(\omega) \propto \frac{A}{\omega^3} \tag{4.12}$$

We fit 002 and 101 XDPs with equation (11) using numerical integration and non-linear optimization. Figure 4.14 shows the fits for sample A4. The fit of data to equation (11) is nominally good, with a Gaussian peak shape in the central region and non-Gaussian tail region following the asymptotic $1/\omega^3$ trend. The latter trend indicates that strain due to threading dislocations is present. As mentioned, the threading dislocations present in a heteroepitaxially grown film can either be uncorrelated and randomly distributed, or correlated - having a particular distribution. We can extract the correlation parameter M from the preceding analysis to gain an understanding of the dislocation distribution as:

$$M = L\sqrt{\rho} \tag{4.13}$$

A value of M parameter of the order of unity indicates a correlated dislocation distribution whereas a value much greater than unity indicates an uncorrelated random distribution. From the fitting of equation (11) to symmetric and asymmetric $2\theta - \omega$ XDP of samples A4 to C4, we obtain values of A and B. Using relevant values of parameters f, g and b, we extract ρ and L values which yield the following values of M.

The values of M are found to be of the order of unity, suggesting that the threading dislocations in NwN are not uniformly and randomly distributed. Keeping in mind that the dislocations act as non-radiative recombination centres for charge carriers due to the strained lattice regions around them, a mapping of luminescence can provide some idea regarding dislocation distribution. We carry out panchromatic cathodoluminescence mapping of sample C4.

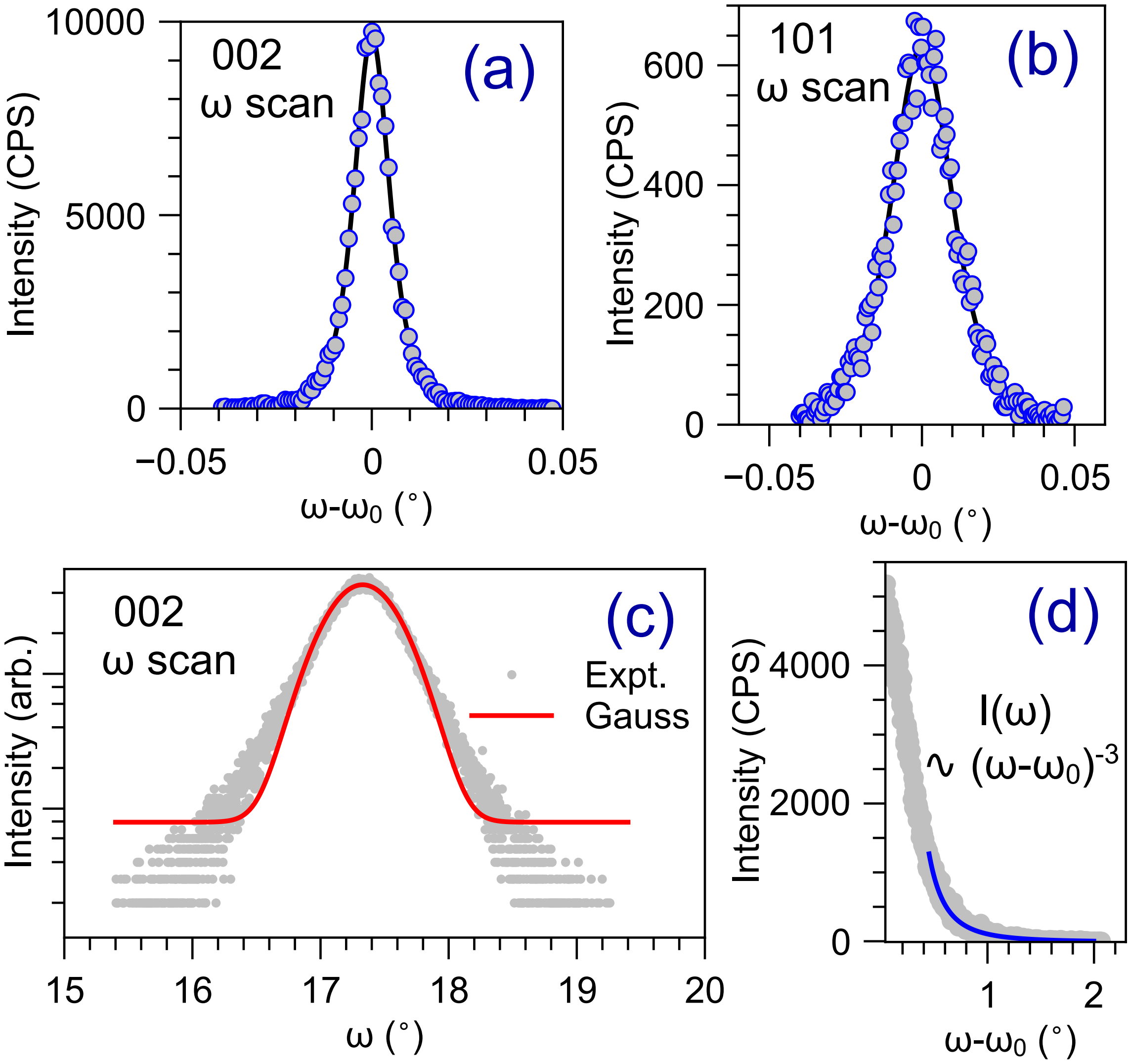

Figure 4.14: Sample A4 (a) 002 omega scan and (b) 101 omega scan, fitted by equation (11). (c) The central portion of the XDP of 002 omega scan fitted with Gaussian function. (d) The tail portion of 002 omega scan fitted with inverse cubic asymptotic function.

Sample	M
A4	3.0
B4	3.2
C4	2.4

Table 4.6: Dislocation correlation parameters for NwN samples.

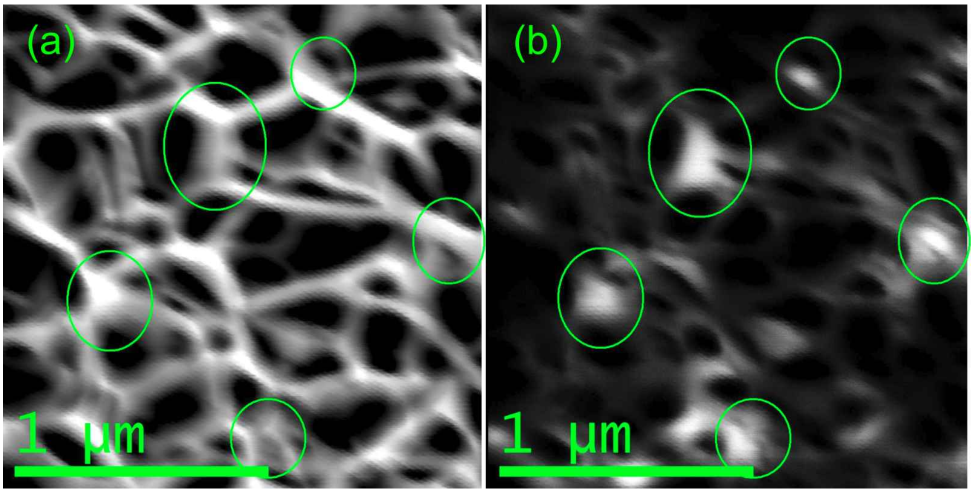

Figure 4.15: (a) Plan-view FESEM image of sample C4. (b) Panchromatic cathodoluminescence mapping of the same region of sample C4. Circled regions show high brightness in cathodoluminescence map compared to other regions. The scale bar corresponds to 1 μm.

Figure 4.15 shows the plan-view FESEM image of sample C4 and the cathodoluminescence mapping of the same region side-by-side. The cathodoluminescence mapping has a non-uniform contrast. The circled regions in the FESEM image represents the junction regions where the individual nanowalls join. These regions appear to have a comparatively higher brightness relative to the straight nanowall regions indicating that a higher density of threading dislocations exist in the individual nanowalls compared to the junction areas. This is consistent with the growth mechanism which describes nanowall network growth by joining of elongated island edges if we consider the ‘junction’ regions to be the initial islands. Additional experiments are required to study this further.

4.4.2.4 Mosaic model

The bunching of threading dislocations in nanowall network allows us to analyse its properties with the help of the ‘mosaic model’. This model is widely employed for heteroepitaxial films with a large degree of mismatch. Here, the sample is assumed to consist of crystallites called mosaic blocks which have a finite mean lateral and vertical size, called the lateral and vertical coherence lengths (L_{lat} and L_{vert}). The mosaic blocks typically have some misorientation among themselves. The out-of-plane misorientation with respect to the surface normal is called tilt and the in-plane misorientation is called twist. The tilt and twist are estimated from width of the omega scans of a symmetric and high inclination angle asymmetric reflection, respectively. Gay et al. showed that there exists a correlation between dislocation density and FWHM of the omega scan[122]. For a completely random distribution of dislocations the following formulae are well known:

$$\rho_{screw} = \frac{(tilt)^2}{4.35 b_{screw}^2}, \rho_{edge} = \frac{(twist)^2}{4.35 b_{edge}^2} \tag{4.14}$$

These formulae were given by Dunn and Koch[123]. A similar expression was given by Kurt who used the numerical factor 9 instead of 4.35 in the denominator[124]. For a mosaic structure, the dislocation density is found to be linearly dependent on the misorientation magnitude[125].

$$\rho_{edge} = \frac{(twist)}{2.1 b_{edge} L_{lat}} \tag{4.15}$$

For a flat and compact film, the tilt and twist are caused by the screw and edge threading dislocations and the above analysis is valid. For nanostructures such as nanorods and nanowalls, however there exists a geometric component to the tilt and twist. For example, a portion of the measured tilt of a nanorod array can be due to misorientations of individual nanorods as a whole rather than due to presence of screw dislocations.

To begin with, we perform omega scans of 002 reflection for the samples. The width of the scans are found to be 31, 35 and 42 arcmin for A4, B4, and C4 respectively. These values are significant and are due to a combination of the contributing factors such as threading dislocation density, geometric misorientation and minor factors such as instrumental broadening and small size of portions of the nanowall network. To analyse whether the omega scan width is predominantly due to dislocation related microstrain, we carry out the following analysis.

The broadening of a reciprocal lattice point due to a non-uniform strain is proportional to the length of the scattering vector while broadening due to finite sample size is independent of it. As scattering vectors for 004

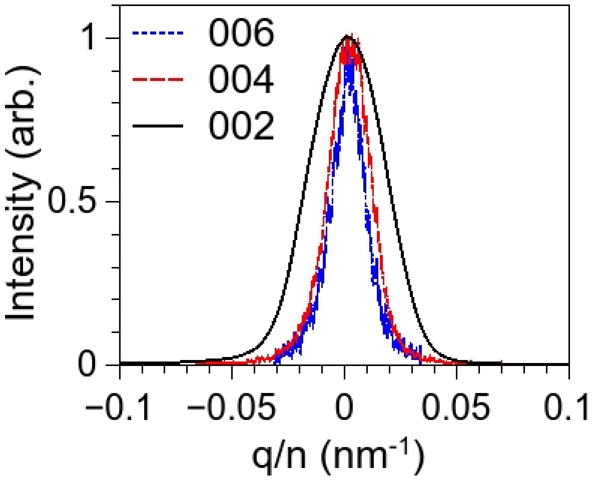

Figure 4.16: Normalized 002, 004 and 006 $2\theta-\omega$ scans of sample A4. X axis is the deviation of scattering vector from Bragg position, divided by reflection order.

and 006 reflection are twice and thrice the length of that of 002, ($Q_0^{002} = \frac{1}{2}Q_0^{004} = \frac{1}{3}Q_0^{006}$), if micro-strain is predominantly responsible for the peak broadening, then the peak widths should be proportional to the order of diffraction and therefore peak widths should be same when scaled down by the diffraction order[126].

Figure 4.16 hows the $2\theta-\omega$ scans for sample A4, where x-axis is q vector scaled by 1/n for reflection 00n. For a pure strain related broadening, we expect the peaks to overlap. The fact that the peaks in the figure are clearly non-overlapping, suggests that size and/or misorientation related effects are at play. Indeed, in a previous TEM study of nanowall network, we have verified geometric tilts among the individual nanowalls[127].

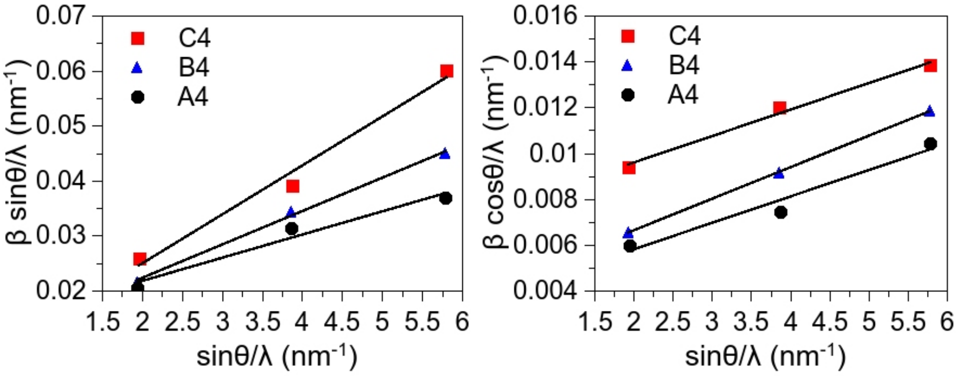

Figure 4.17: Williamson-Hall plot of samples A4, B4, and C4. The extracted parameters are given in Table 4.7.

We continue our analysis to determine the mosaicity parameters using a modified Williamson-Hall (WH) method and a widely used method by Lee et al. The Williamson-Hall method[128] is used to separate the strain and size contribution to peak broadening. By taking the peak width of symmetric $\omega - 2\theta$ scans and ω scans and plotting with respect to $Q = \frac{4\pi sin(\theta)}{\lambda}$ we can get the values of coherence lengths, tilt, and micro-strain. Plotting peak width (β_ω) times $sin(\theta)/\lambda$ versus $sin(\theta)/\lambda$ yields a slope equal to the tilt value and y intercept equal to 1/(2*L_{lat}). Here β_ω is the integral breadth of the ω scan and not its FWHM. The integral breadth is calculated by dividing the peak area by the peak height. Next, plotting peak width ($\beta_{\omega-2\theta}$) times $cos(\theta)/\lambda$ versus $sin(\theta)/\lambda$ yields a slope equal to 4 times the micro-strain value and y intercept equal to 1/(2*L_{vert}). The resulting graphs are shown in Figure 4.17 and parameter values are tabled in Table 4.7.

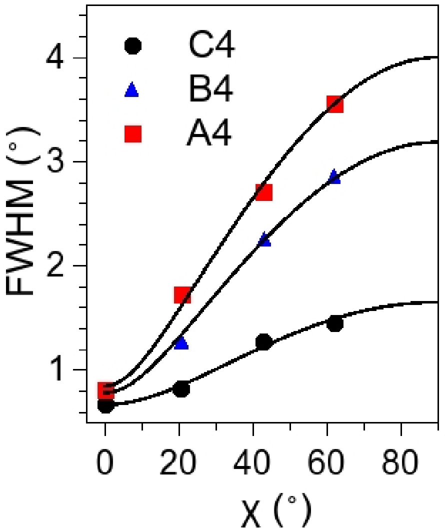

Figure 4.18: The FWHM of omega scans of symmetric and asymmetric reflections 105, 204 and 101 of samples A4, B4, and C4 as a function of the inclination angle of the reflections. The solid line is a fit using equation (16). The extracted parameters are given in Table 4.7.

Sample	tilt$_{(\text{Lee})}$	twist$_{(\text{Lee})}$	tilt$_{(\text{WH})}$	ϵ_{micro} ($\times 10^{-4}$)	L_{lat}	L_{vert}
A4	0.673	1.65	0.241	2.88	37.2	142
B4	0.786	3.19	0.348	3.44	48.6	128
C4	0.851	4.00	0.510	2.89	68.7	68.5

Table 4.7: Parameters extracted from Williamson-Hall plots

The second method we use is given by Lee et al.[129] The authors assumed a Gaussian peak shape and gave the following expression for peak width:

$$\beta_{hkl}^2 = ((tilt)cos(\chi))^2 + ((twist)sin(\chi))^2 \tag{4.16}$$

Here, the inclination angle χ is the angle between surface normal and normal to the diffracting hkl planes under consideration. Figure 4.18 shows the FWHM of one symmetric and three asymmetric reflections (105, 204 and 101) of the three samples as the function of the inclination angle of the particular reflection. The experimental data is fitted with eqn. (16) to extract the values of tilt and twist which are tabulated in Table 4.7.

Now let us compare the results obtained for samples A4, B4, and C4. The values of L_{lat} for samples decreases from sample A4 to C4. These values show same trend as nanowall width, though values are not similar, indicating that each individual nanowall does not diffract X-ray coherently. The values of tilt obtained from the W-H method and Lee method differ significantly though they follow the same trend. The underlying reason for the discrepancy is the a priori assumption of the peak shape. Williamson-Hall method assumes a Lorentzian peak shape of the XDP and Lee's method assumes a Gaussian one. In reality neither function describes XDP accurately, as we also saw in previous section. People have used other functions such as pseudo-Voigt (which is a weighted sum of Gaussian and Lorentzian functions) in W-H analysis to improve the accuracy, but that approach is quite ad hoc[130]. We believe the true values of tilt lies in between the values from the two methods. Similar to tilt, the mosaic twist increases monotonically from sample A4 to C4. The tilt and twist values are comparable to the values commonly observed for a nanorod array.

We ascribe these tilt and twist values partly to dislocation induced misorientation and partly to geometric effects. The values presented in Table 4.7 are therefore an upper limit and actual values may be significantly lower. Proportional to the misorientation values, the dislocation density would increase from A4 to C4. Since the nanowall width increases from A4 to C4, we theorize that the regions where the nanowalls coalesce are the major sources of strain and dislocation. The individual nanowalls grow with a random in-plane direction and their out-of-plane orientations lie in a small ($< 1°$) distribution. When they coalesce with one another, a dislocation array is is formed to accommodate the relative misorientation. For example, edge dislocations would need to be formed to accommodate the in-plane directional mismatch. It has been shown theoretically and experimentally in case of GaN nanowires that boundary dislocations form at the coalescence joints[131]. Apart from that, the elastic strain release mechanism in nanostructures needs free surface. A high aspect ratio GaN nanowire is nearly strain free as it is able to relax sideways and axially. This free surface area is partly lost when the nanowalls coalesce. Jenichen et al. showed for GaN nanowires on Silicon[132] that for the sample with a higher degree of coalescence, the microstrain is more. In view of this, it is proposed that the growth conditions for nanowall should be optimized for a very low lateral growth rate and high axial growth rate, which would result in small wall widths and increased height, in order to reduce the residual strain and dislocation density.

4.5 Conclusion

To summarise, in this chapter we studied the structural properties of MBE grown GaN nanorods, porous films and nanowall network. The morphology of nanorod array was found to depend on the choice of substrate. In case of growth on sapphire, a basal matrix layer forms along with the nanorods which is absent for growth on silicon. For the nanorod sample grown on sapphire, the matrix layer was seen to be composed of coalesced shorter nanorods. The residual strain was found to be tensile in out-of-plane direction and compressive in-plane through XRD and Raman measurements. The strain was comparatively less in out-of-plane direction and had two values for in-plane direction indicating non-uniformity. From TEM studies, a 30° in-plane rotation was observed between thinner-longer nanorods and shorter nanorods which make up the matrix layer. Based on many literature reports of effect of sapphire nitridation on GaN overlayer polarity and considering the present growth condition, it was proposed that conditions prior to GaN growth lead to an incomplete nitridation of the sapphire substrate in form of thin sub-monolayer AlN patches which act as nucleation centres for nanorods which finally become the longer and thinner nanorods whereas the nanorods forced to grow on bare sapphire take longer incubation time and thereby have a reduced growth period. They lead to shorter and wider nanorods which coalesce to form the matrix layer.

By varying the growth parameters in MBE, a set of porous GaN samples were deposited with different microstructural parameters. Contrary to the expected compressive in-plane and tensile out-of-plane strain for GaN grown on sapphire, the actual residual strain magnitude and type was found to be morphology dependent, explained on the basis of interplay of lattice mismatch, thermal expansion coefficient mismatch and tensile stress due to island coalescence during film growth.

To probe the structural properties of GaN nanowall network in detail, a set of three nanowall network samples were grown by varying the deposition parameters. The samples had different thickness and average nanowall lengths and widths. Epitaxial relationships between sapphire substrate and GaN nanowall network were determined from XRD $2\theta - \omega$ and ϕ scans and nanowall network was found to be c-oriented and single phase. Multiple symmetric and asymmetric reflections were used to accurately calculate the lattice parameters and strain values. The hydrostatic and biaxial strain components of the strain were separated through analysis and it was found that all three samples had a compressive in-plane strain and tensile out-of-plane strain which was again morphology dependent. Large density of threading dislocations are prevalent in heteroepitaxially grown GaN and their distribution can either be uniform and random or non-uniform and bunched. Detailed XDP analysis was done and correlation parameter ‘M’ was extracted for each sample. Low value (of the order of unity) of M indicated a non-uniform distribution of threading dislocations bunched in particular places. This was confirmed through pan-chromatic cathodoluminescence mapping as highly dislocated regions tend to be darker. This non-uniform dislocation structure and peculiar morphology of nanowall network allowed us to employ the mosaic model to describe the structural properties of nanowall network. The parameters of the mosaic model - the lateral and vertical coherence lengths and the in-plane and out-of-plane misorientations were extracted using Williamson-Hall and Lee’s methods. The misorientation angles of the samples were found to scale with the average width of the nanowalls of that sample. This was explained on the basis of island coalescence model of growth of nanowall network in which larger initial width of the coalescing islands leads to a higher degree of misorientation which then needs the formation of a higher density of boundary dislocations to accommodate the dislocations. Thus this provides a recipe to tune the residual strain and dislocation density of the nanowall network which is important for a number of applications.

Chapter 5

Study of optical properties

This chapter describes the optical properties of molecular beam epitaxy grown GaN nanostructures. The effect of shape, size, defects and carrier concentration on the optical properties are studied using absorption spectroscopy and temperature and excitation power dependent photoluminescence spectroscopy coupled coupled with additional characterisation techniques such as electron microscopy, Raman spectroscopy, and Hall measurement system for a comparative study.

5.1 Introduction

The optical properties of semiconductor materials are directly related to the energy band structure and are influenced by factors such as size, shape, presence of bulk and surface defects and carrier concentration. For nanostructures, the size effect can manifest in several different ways - by confining the electron-hole pairs through quantum confinement, increasing boundary collisions of carriers, or through the enhanced effects of surface states[133]. In this chapter, we are concerned with photoluminescence properties of GaN nanostructures, the basic mechanism of which entails formation of electron-hole pairs and their radiative recombination. For GaN, the binding energy of excitons is reported to be about 20-25 meV but depends significantly on material size and carrier concentration, among other factors[134]. For atomically thin GaN, it may increase up to a few hundred meV, whereas an increase in carrier concentration reduces it significantly[135].

The luminescence properties of GaN nanostructures are dependent on presence of defects - both extended and atomic. Atomic point defects introduce energy levels in the bandgap leading to new optical transitions. Defects that act as non-radiative recombination centres reduce the overall luminescence efficiency of the material. Extended defects such as dislocations and stacking faults can modify the residual strain and thereby the band structure, and they can also be decorated by point defects[43],[136].

A complex interplay of the nature and concentration of defects, carrier concentration and morphology related effects determine the overall optical property of nanostructured semiconductors, and in this chapter, we investigate these using MBE grown GaN nanostructures.

5.2 Luminescence properties of nanorods: effect of size

The size and shape of materials play crucial roles in their optical properties. In the case of large aspect ratio one-dimensional nanostructures, the band-structure is influenced by quantum confinement effects and strain relaxation, which in turn affects their optical properties. Due to the large surface-to-volume ratio, surface electronic states have a significant density and can affect the optical properties by providing donor or acceptor type energy levels. Additionally, a change in growth-parameters to form nanostructures of different dimensionality and sizes can also influence the type and concentration of native point defects affecting the defect-related luminescence properties. In this section, we study the size-dependent luminescence properties of a set of GaN nanorods grown on silicon with varying growth duration.

Experiment

A set of 4 GaN samples were deposited on Si(111) by varying the growth duration. A Ga flux BEP of 2×10^{-7} Torr is applied by keeping the K-cell temperature around $1020 - 1025$°C and a nitrogen flow of 4 sccm and substrate temperature of 630°C were used. A1, B1, C1 and D1 were deposited with growth durations of 30, 50, 90, and 300 minutes respectively. Here the growth duration is measured from the time Ga and N shutters are opened and includes the incubation period during which stable GaN clusters are formed. The incubation period depends on the substrate, growth temperature and source fluxes. For the present growths, the incubation period is found to be a few minutes, inferred from observation of RHEED patterns. The formation of GaN islands was confirmed by high-resolution FESEM of a sample grown for a total of 10 minutes. Thus the incubation period can be practically neglected for the samples. Prior to growth, the substrates were thoroughly cleaned by RCA-1, HF dip, and RCA-2 procedure and blow-dried with nitrogen before their transfer into MBE. PL spectra of

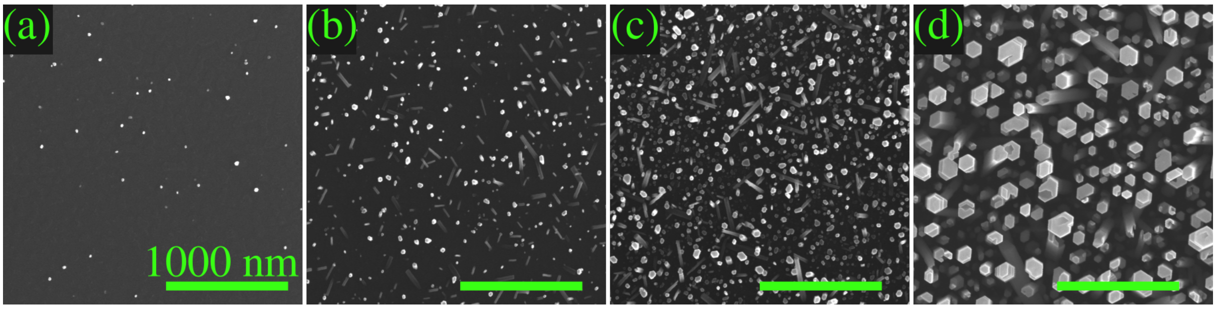

Figure 5.1: Plan-view FESEM images of samples (a) A1 (b) B1 (c) C1 and (d) D1. the scale bar corresponds to 1000 nm.

the as-grown samples were recorded at room temperature using a 325 nm He-Cd laser source and visible PMT detector.

Results

Figure 5.1 shows the plan-view FESEM micrographs of the samples. With an increase in growth duration, the sample morphology changes from being sparsely occupied by NRs to a crowded NR array although remaining un-coalesced nevertheless. The NR height, diameter and density increase monotonically with time. The mean NR diameter for samples A1 to D1 are 19, 25, 34 and 130 nm, respectively.

Next, we study the luminescence properties of these NRs by exciting with a supra-bandgap laser source. Figure 5.2 shows the room temperature PL spectra of the samples. The spectra has two portions - a near band-edge (NBE) emission and defect-related spectra at lower energies involving deep levels in the bandgap. Figure 5.3 shows only the NBE emission portion with the actual intensity indicating the sample's band edge peak increases in intensity with an increase in size as expected, due to a larger volume of material contributing. The position of the NBE peak for samples A1, B1, C1, and D1 are measured to be 3.45, 3.44, 3.43, and 3.42 eV, respectively, showing a monotonic red shift of the NBE peak with NR size. If we take the room temperature bandgap of GaN to be 3.42 eV, most NBE peaks exhibit a blue shift. This effect of material size on emission energy is well known and can be explained by the carrier confinement effect.

The spectra have been acquired at identical conditions to allow for comparison. The left panel figure presents the samples' PL with the NBE peak normalised. The defect emission to NBE emission intensity ratio (I_D/I_{NBE}) varies from sample to sample. There is no significant difference in I_D/I_{NBE} from A1 to B1; then, it attains a maximum for C1 before re-

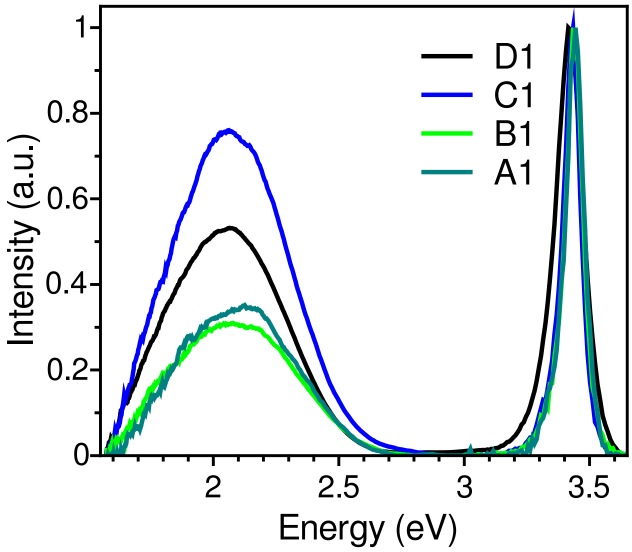

Figure 5.2: Normalized room temperature PL spectra of samples A1 to D1 showing near band-edge emission and defect related luminescence.

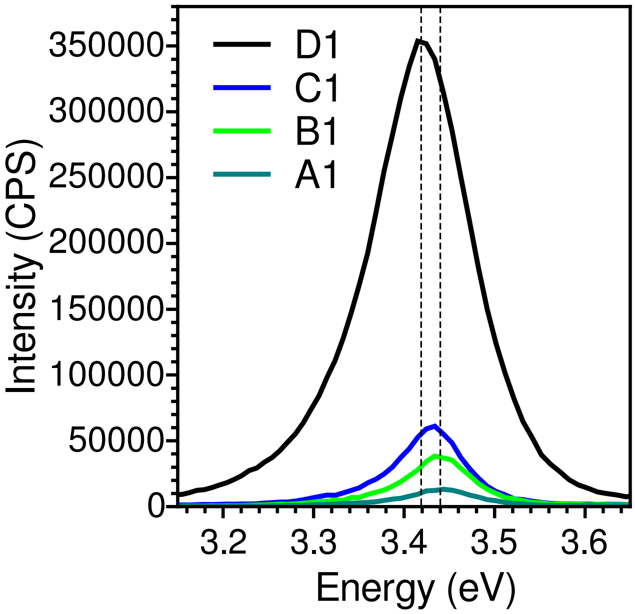

Figure 5.3: Room temperature PL spectra of samples A1 to D1 showing the near band-edge emission.

ducing for D1. At a glance, the deep level emissions appear similar; thus, we carry out a further analysis by fitting the defect intensity with multiple Gaussian peaks. Undoped GaN has a number of well-known luminescence bands which appear in samples growth in different conditions or even with different techniques. This indicates those bands originate from point defects that have a high incorporation probability. Oxygen, hydrogen, carbon are some of the most common impurities for samples grown with MOCVD, HVPE and MBE growth in addition to the native point defects which may occur. Some of the most common luminescence features for undoped GaN are UV luminescence (UVL) around 3.27 eV, green luminescence (GL) at 2.3-2.4 eV, yellow luminescence (YL) around 2.1-2.2 eV, and red luminescence (RL) at about 1.8 eV. Additionally, doping with Zn or Mg may give rise to additional features such as blue luminescence around 2.9-3.0 eV[43].

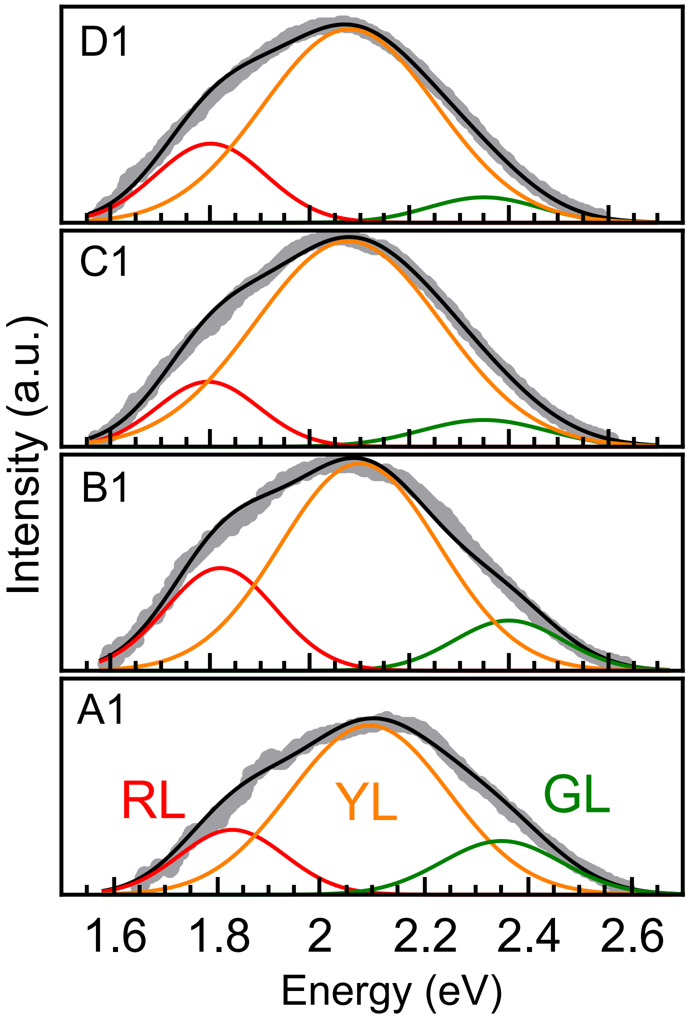

Figure 5.4: Room temperature PL spectra for samples A1 to D1 showing defect related luminescence. The spectra has been fitted with Gaussian peaks corresponding to red, yellow and green luminescence with peaks at 1.8, 2.1 and 2.35 eV.

We have been able to fit the wide defect-related spectra in the range 1.6 to 2.7 eV with three Gaussian peaks centred at 1.8, 2.1 and 2.35 eV corresponding to RL, YL and GL. This is shown in Figure 5.4. It can be seen that the relative contribution of each luminescence peak varies from sample to sample. The percentage contribution to total emission intensity (determined by taking area ratio) for RL is 17%, 23%,14%, and 19% for samples A1 to D1. For YL it is 67%, 66%, 79%, and 75% and for GL it is 16%, 11%, 7%, and 6% respectively. Thus as the NRs grow, the GL luminescence becomes weaker, whereas the YL becomes strong.

The formation energy of defects is in general lower on the surface compared to bulk. If a change in morphology leads to a change in surface-to-volume ratio, this can lead to a change in concentration and type of native or impurity point defects incorporated, resulting in a change in the defect-related luminescence. Since the samples have been deposited in exactly identical growth conditions, with the exception of growth duration, it is unlikely that different types of defects incorporate inside the NR arrays. The only possible explanation for sample-to-sample variation in relative intensity of different luminescence bands is a difference in defect concentration due to the different specific surface areas. In literature, the effect of size on the defect emissions have been reported for materials such as GaN nanopowder and ZnO NR arrays and have evidenced the influence of the surface-to-volume ratio[137 138].

Conclusions

In this section, we have studied the effect of size on the NBE and defect-related luminescence spectra of GaN nanorods. The NBE peak position showed a red shift with increasing nanorod diameter which can be understood as due to confinement effects and the NBE peak intensity increased with increasing material volume contributing to luminescence. The defect-related spectra was deconvoluted into red, yellow, and green luminescence and it was found that as the nanorods grew in height and diameter, the relative intensity of green luminescence decreased in favour of red and yellow luminescence. A change in active surface area can change the defect formation energies leading to a modification of the deep level defect luminescence spectra.

5.3 Luminescence properties of porous samples

Porous semiconductor materials are very interesting from both fundamental and application points of view. A number of optical applications of porous materials are made possible by the ability to tune the dielectric constant by modifying the pore size and density which can be used to enhance the electric field distribution and increase of light extraction efficiency by reducing total internal reflection loss. For LED applications, porosification thus improves the overall efficiency[139 140]. Porous semiconductors also have other applications such as distributed Bragg reflectors[141], photodetectors[142], and optical detection of chemical and biological entities[143],[144]. The interest in optical properties of porous semiconductors was spurned by observation of red luminescence from the prototypical porous silicon, which has an indirect bandgap[145]. This luminescence can be tuned by varying the porosity and attributed to defect-related emission. In this section, we carry out a comparative study of luminescence properties of MBE grown porous GaN material.

Experiment

A set of three GaN samples A2, B2, and C2, were deposited on c-sapphire by varying the source flux ratio of MBE. Following the usual cleaning procedures of the substrate and pre-growth treatment, GaN samples were grown for 4 hours at 630 °C substrate temperature. The Ga flux BEP was varied as 5.5×10^{-7}, 2.4×10^{-7}, and 2.8×10^{-7} Torr and N_2 flow was varied as 4.5, 6.5 and 8 sccm for A2, B2, and C2, respectively. The N/Ga ratio thus changed as 50, 150 and 160 for A2, B2, and C2. The PL spectra of the as-grown samples were recorded at a low temperature of 12 K using 325 nm He-Cd laser source and visible PMT detector.

Results

Figure 5.5 shows the FESEM images of the samples. All samples are meso /macroporous according to IUPAC classification criteria. The low temperature PL spectra of the samples is shown in Figure 5.6. All three samples show NBE emission, UVL involving shallow defects and deep defect related emission. The NBE peak appears at 3.47, 3.45 and 3.44 eV for A2, B2, and C2 whereas at room temperature they appear at 3.42, 3.39, and 3.39 eV. The low temperature PL spectra is dominated by the defect related

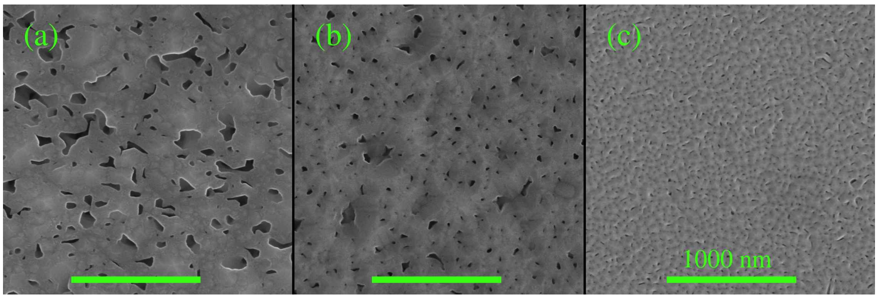

Figure 5.5: Plan-view FESEM images of samples A2, B2, and C2. The scale bar corresponds to 1 μm.

spectra in all cases. In case of A2, the deep defect related emission peaks around 2 eV, whereas it is 2.2 eV and 1.8 eV for B2 and C2.

The relative contribution of NBE emission and defect related emission to total intensity is often used as a gauge of sample quality and concentration of point defects, although additional factors such as Fermi level position determining occupancy of dopants play a role in this. The area under NBE peak was found to be 1.6%, 3.8%, and 0.28% of total intensity for A2, B2 and C2.

The conditions of growth of the three samples involved only the change of N/Ga flux ratio from 50 to 160, keeping everything else the same. All samples have been grown in general in highly nitrogen rich ambient to promote the growth of porous structure. A relatively moderate change in growth parameters is found to have an extreme effect on the luminescence properties of the porous samples. We believe there to be two reasons behind this. First, a change in N/Ga flux can change the concentration of defects such as the nitrogen and gallium vacancies, two of the most common native defects in undoped GaN. The former is a donor and the latter is an acceptor. Secondly, the incorporation of impurities from the ambient into the sample depends on the growth parameters. For MBE growth of GaN, oxygen and carbon are important impurity defects; the former is a shallow donor and the latter amphoteric. A reduction in substrate temperature and nitrogen rich growth conditions are known in literature to promote the incorporation of impurity defects[146],[147].

Conclusion

In summary, by moderately varying the N/Ga source flux ratio, a set of porous GaN films were deposited which exhibited a significantly different luminescence spectra. At low temperature, the overall defect-related

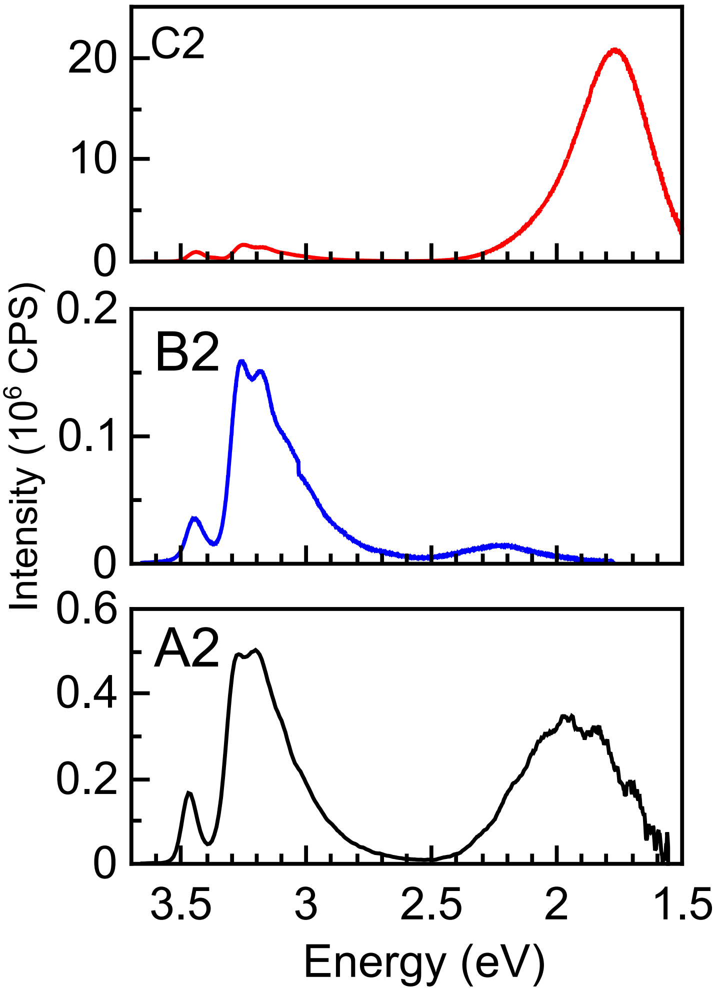

Figure 5.6: PL spectra of samples A2, B2, and C2 taken at 11 K temperature.

luminescence intensity highly surpassed that of NBE emission. A UV luminescence band was common to all samples and in addition, deep defect related red, yellow and green luminescence was present. Similar to the case of nanorods, a simple change in growth conditions is seen to lead to a significantly different distribution of defects.

5.4 Luminescence properties of nanowalls

The GaN nanowall network has a highly porous morphology consisting of connected tapered nanowalls with tips which may be of the order of excitonic Bohr radius of GaN making carrier confinement related effects possible. The enhancement of electric field in porous dielectric materials leading to modification of optical properties are applicable for this material as is enhancement of light extraction efficiency through sidewall scattering. Like previously discussed nanorods and porous GaN, a change in growth parameters can lead to a change in type and concentration of incorporated point defects which we study in this section. Finally, the as grown GaN nanowall network is unintentionally highly n-doped and it is interesting the effect of the carrier concentration on the band edge and defect related optical properties.

5.4.1 Experiment

Ga k-cell temperature and N_2 flow were changed to grow a set of five samples A3 to E3 on c-sapphire substrate. The N/Ga flux ratio was increased from sample A3 to E3, as given in Table 5.1. For all samples, the substrate temperature was fixed at 630°C. PL spectra were recorded using a PL system (Edinburgh,UK) employing Xe arc lamp and a 325 nm CW He-Cd laser as source, NIR PMT as detector and closed cycle He cooled cryostat as sample holder. The PL spectra was taken under identical conditions for all samples. Field emission scanning electron microscopy (FEI Quanta 3D SEM) was used to study the sample morphology. For acquiring Raman spectra a 532 nm Nd:YAG laser was used with Jobin Yvon LabRam HR spectrometer. Optical transmission spectra were acquired using Perkin Elmer UV-vis spectrometer. Electron concentration was estimated using a tabletop Hall measurement set-up (Ecopia HMS 3000).

5.4.2 Results

The FESEM images of the samples are shown in Figure 5.7 and the samples consist of a random network of tapered nanowalls. The bulk electron concentration (n) of these unintentionally doped GaN samples calculated from Hall measurement are given in Table 5.1. The value of n increases from 3.84×10^{19} cm^{-3} for sample A3 to 1.38×10^{20} cm^{-3} for sample E3. These values exceed the Mott limit for GaN ($\approx 1.2\times10^{18}$ cm^{-3}) and therefore all five NwN samples are unintentionally degenerately n-doped.

Table 5.1: Sample growth parameters and results of Hall measurement, and Raman spectroscopy: carrier concentration n and the E_2^H peak position

Sample	Ga flux BEP	N_2 flow (sccm)	n (cm^{-3})	E_2^H (cm^{-1})
A3	5.5×e-7	2.5	3.84×10^{19}	565.9
B3	5.0×e-7	2.5	5.82×10^{19}	565.6
C3	5.0×e-7	4.5	8.39×10^{19}	567.1
D3	4.8×e-7	4.5	1.05×10^{20}	566.1
E3	4.8×e-7	8.0	1.38×10^{20}	565.7

Figure 5.8 shows the PL spectra of the samples acquired at 11 K (LT) and 300 K (RT). The spectra of samples C3,D3 and E3 which have higher carrier concentration, possess a wide NBE peak at both low and room temperatures. Samples A3 and B3, which have comparatively lower carrier concentration, exhibit a wide luminescence peak around 2 eV and a UV luminescence band at 3.27 eV in addition to the NBE peak. The UVL spectra for both A3 and B3 persist upto 190 K. For sample A3, at 300 K, only a portion of the low energy defect peak at 1.8 eV survives, showing that the deep level defect luminescence has multiple components with distinct origins. Figure 5.9 shows the LT PL spectrum for sample A3 deconvoluted into multiple components. Gaussian functions have been used for fitting the defect peaks. Fixing a peak at 1.8 eV corresponding to the RL requires another peak at 2.1 eV corresponding to YL for a satisfactory fit. The UVL is known to occur at low temperatures by a transition from a shallow donor to a shallow acceptor and with increasing temperature changes to a transition from CB to a shallow acceptor. In GaN, the UVL peak often has phonon replicas involving LO phonons of energy 92 meV. In Figure 5.9, the deconvolution of the UV region of PL spectrum was done by Gaussian functions centred at 3.27, 3.18 and 3.11 eV, with 0.09 eV difference.

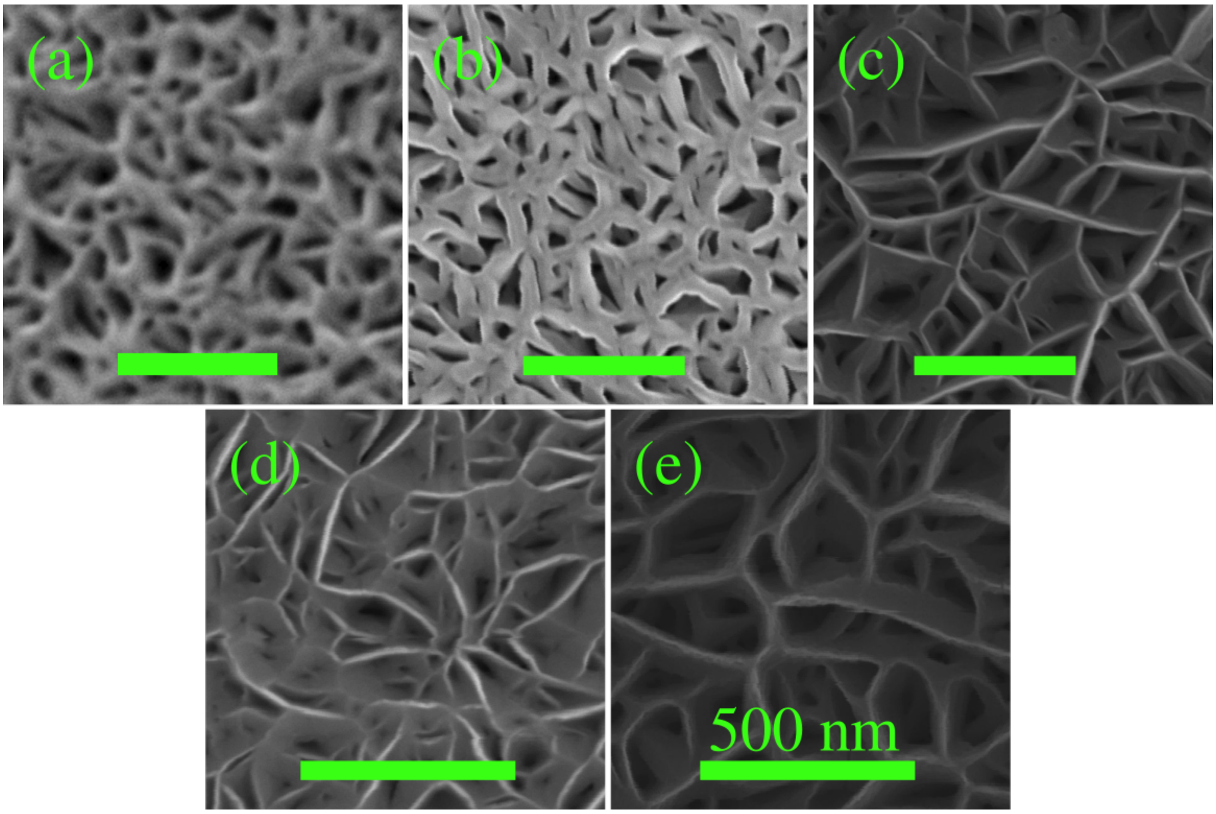

Figure 5.7: Plan-view FESEM images of NwN samples (a)A3, (b)B3, (c)C3, (d)D3, and (e)E3. The scale bar corresponds to 500 nm.

Considering that samples A3 and E3 have the highest difference in carrier concentration and show a qualitative difference in the LT PL spectra, their study can reveal the underlying mechanisms. Figure 5.10 shows the integrated intensity of NBE peak and UVL peak of sample A3 and intensity of NBE peak of sample E3 as a function of excitation power density, acquired with the help of a variable neutral density filter coupled with CW He-Cd laser. The integrated intensity has been fitted with a power law as $I(P) \sim P^{\mathrm{k}}$. Here the value of k is found to be 1.04 ± 0.036 and 0.996 ± 0.016 for NBE peaks of sample A3 and B3 respectively, and 0.901 ± 0.034 for the UV luminescence peak of sample A3. For peaks related to bound excitons, the scaling of intensity with power is superlinear ($\mathrm{k} > 1$), for free electron-hole (band-to-band) or free excitonic recombination, the exponent k is approximately linear, whereas for recombinations involving a localized defect, such as (D-h) (e-A) or DAP transitions, the scaling is sublinear ($0.5 < \mathrm{k} < 1$). The near linear scaling indicates free electron-hole (band-to-band) recombination underlying the NBE emission and the sublinear scaling of UVL suggests involvement of localized defects[148]. This is consistent with the donor-acceptor pair (DAP) mechanism underlying the UV

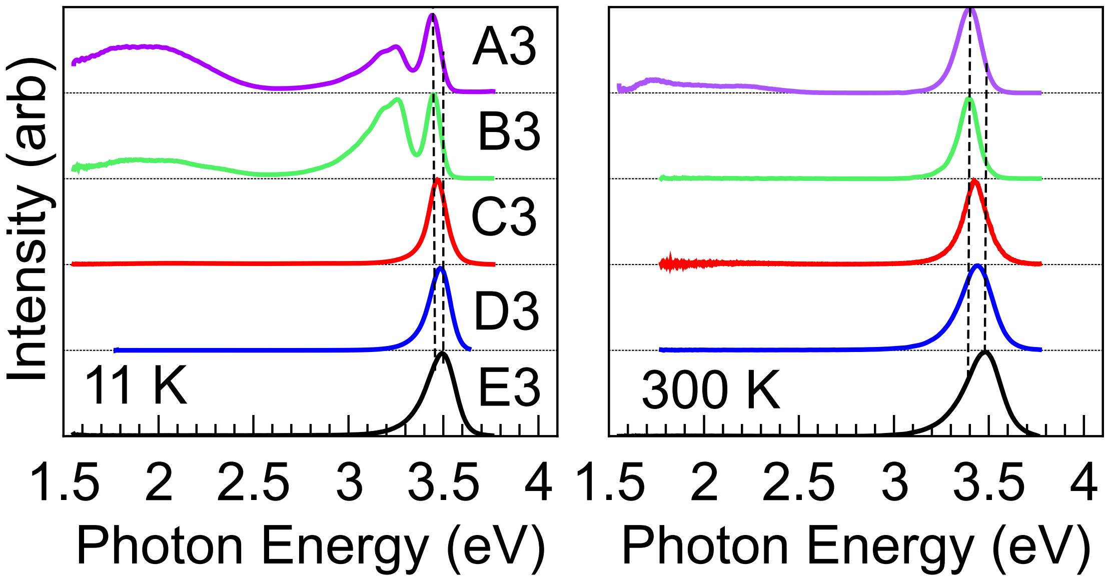

Figure 5.8: PL spectra of samples A3, B3, C3, D3, and E3 taken at (left) 11 K and (right) 300 K.

peak.

The energy of the zero phonon line of the DAP transition is determined by:

$$\hbar\omega = E_G - E_D - E_A + \frac{e^2}{\epsilon R} \tag{5.1}$$

where E_G, E_D, and E_A are the band-gap, activation energy of the donors and acceptors, respectively, and the last term represents the Coulomb interaction of ionized donor and ionized acceptor, a distance R apart in a medium with static dielectric constant ϵ.

In Figure 5.11 we present the integrated intensity of NBE and UVL peaks of samples A3 and B3 as a function of inverse temperature. The intensities have been normalized and suitably displaced for visual clarity. It can be seen that for sample A3, as temperature increases from 11 K upto ≈ 17 K (about 60 K^{-1} in inverse temperature scale) the PL intensity is comparatively lower, and jumps to a higher value, thereafter attaining a more or less constant value upto ≈ 100 K. This trend is true for both NBE and UVL. The normalized intensities have been fitted with an Arrhenius type decay equation given in eqn(5.2)[149].

$$I = \frac{I_0}{1 + A_1 exp(-E_1/K_BT) + A_2 exp(-E_2/K_BT)} \tag{5.2}$$

Fitting equation(5.2) to I_{UVL} vs 1000/T yields E_1 and E_2 = 25 meV

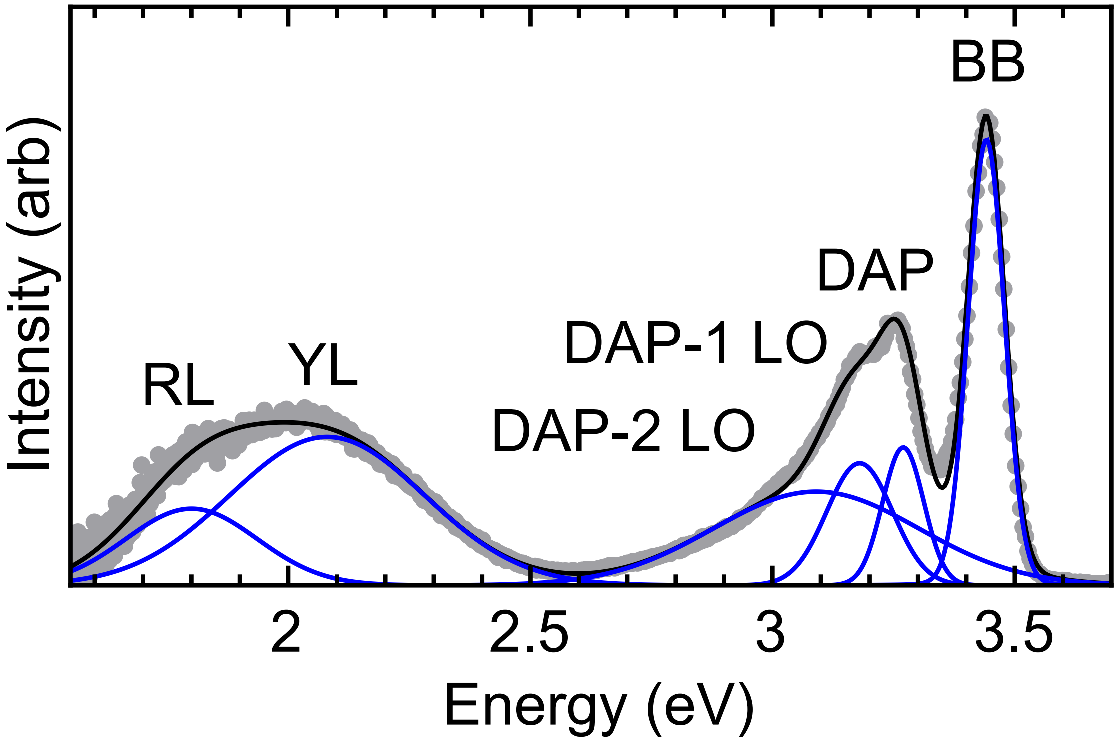

Figure 5.9: PL spectra of sample A3 taken at 11 K showing the deconvoluted defect related peaks.

and 164 meV, respectively for sample A3 and 50 meV and 131 meV, respectively, for sample B3. We also calculate the energy difference between band edge and zero phonon line of DAP line, which corresponds to $E_A + E_D - \frac{e^2}{\epsilon R}$. The Coulomb term is estimated to have value around 15 meV[43] and, thus the energy difference is mostly constituted by B.E. of acceptor. The energy difference was calculated to be approximately 190 meV for both samples A3 and B3 and based on this, we assign the larger of the activation energies, viz. 164 meV for sample A3 and 131 meV for sample B3 to acceptor binding energies. Literature reports have given values ranging from 150 to more than 200 meV for the shallow acceptor responsible for DAP line in GaN[43].

O_N and Si_{Ga} impurities and native V_N defects are possible shallow donors of GaN. Due to usage of high purity sources and UHV conditions, V_N is the likely donor defect. Literature reports regarding the identity of the shallow acceptor in undoped GaN, have suggested contamination related defects such as Si_N, C_N and Mg_{Ga} to be possible candidates, though there has been no consensus till date[43]. Korotkov et al. from their tran-

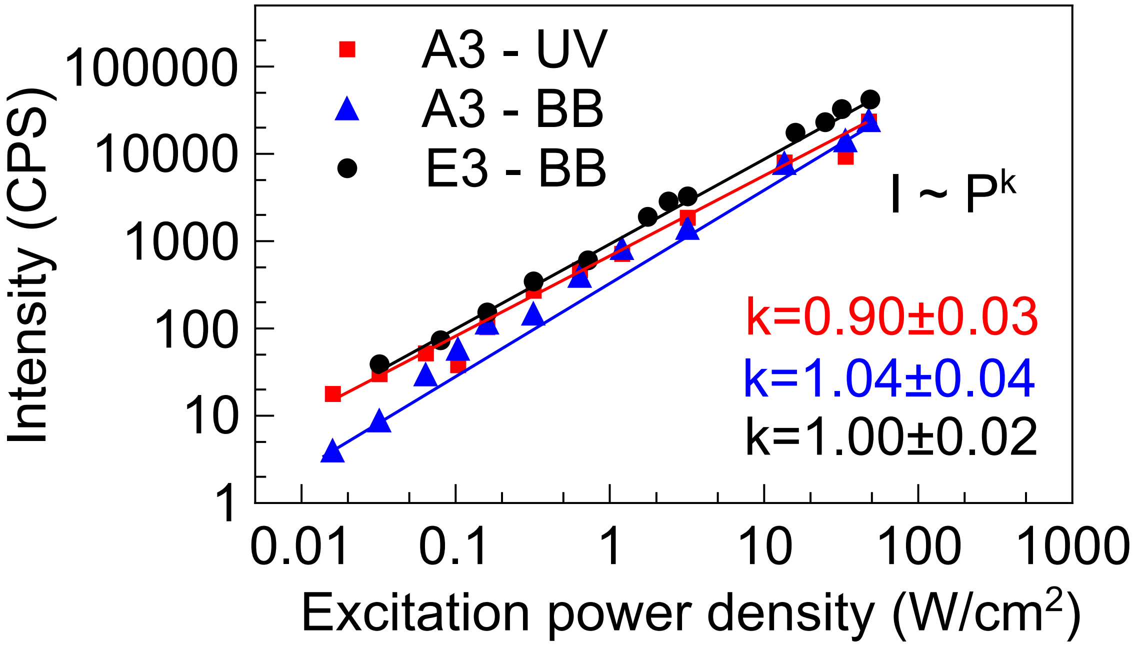

Figure 5.10: PL intensity as a function of excitation power density for samples A3 and E3. The solid line fit corresponds to a power law fit with the extracted exponent depicted.

sient PL studies of undoped GaN, suggest that a defect complex containing V_{Ga} and a donor defect such as O_N or hydrogen are probable candidates for shallow acceptors[150]. They surmised that transition between a particular shallow donor and different shallow or deep acceptor gives rise to UV, blue and yellow luminescence. Xie et al. carried out a comprehensive hybrid QM-MM embedded cluster calculations of native defects of GaN and their electronic and optical properties[41] and concluded that V_N is the major compensating centre for acceptor impurities in GaN. In view of this, we propose that depending on the growth conditions the concentration of V_N in the samples vary. Samples A3 and B3, have comparatively less V_N concentrations whereas samples C3,D3 and E3 have higher values. This is consistent with the carrier concentration trend found from Hall measurement. V_N acts as compensation centres for the shallow and deep acceptors in GaN and thereby suppresses the UV and yellow luminescence.

Temperature dependence of band gap

The temperature dependence of the band gap is mainly determined by two factors - electron-phonon interaction and temperature induced change in lattice dimensions, out of which the former is the dominant factor. Thus a study of the band gap of NwN as a function of temperature can provide valuable insight into the nature of the electron-phonon interaction. We have already attributed the NBE PL peak to the band-to-band transition after discounting excitonic nature, and the position of the NBE emission peak is plotted as a function of temperature for all NwN samples in Figure 5.12. The temperature induced band-gap shrinkage (BGS), which we define here, as change in band gap from 15 K to 290 K, ranges from 22 to 40 meV for the samples, which is lower than typical literature values. For a GaN epilayer grown on sapphire, Teisseyre et. al. reported a change of 74 meV in the same temperature range[1]. The comparatively lower value of BGS for the NwN samples can be due to screening of the electron-phonon interaction[151]. The widely used empirical Varshni equation given below describes the band-gap shrinkage in a number of semiconductors including group III-V semiconductors. However, deviations from it are not uncommon, especially for wide band gap semiconductors, which sometimes yields a negative value of β, which is supposed to correspond to Debye temperature, and can not be negative.

$$E_g(T) = E_g(0) + \frac{\alpha T^2}{\beta + T} \tag{5.3}$$

Here we use a more analytical approach by Passler, who gave the following equation:

$$E_g(T) = E_g(0) + \frac{\alpha\theta}{2}[\sqrt[p]{1 + (\frac{2T}{\theta})^p} - 1] \tag{5.4}$$

Here, θ is comparable to average phonon temperature, α is high temperature limit of dE_g/dT. The exponent p is related to the phonon dispersion for the material. If the average energy of the phonons spectra contributing to BGS is $\bar{\epsilon}$ and the effective width of that spectra is $\Delta\epsilon$, then the phonon dispersion coefficient is given by $\delta_{ph} \approx \frac{\Delta\epsilon}{\bar{\epsilon}}$. Finally we have $\delta_{ph} \approx \frac{1}{\sqrt{p^2 - 1}}$. The solid lines shown in Figure 5.12 are fits to equation(5.4), and the best fit values of p are: 4.88, 3.49, 3.27, 3.21 and 4.04 respectively for samples A3 to E3. The calculated values of δ_{ph} are then 0.209, 0.299, 0.321, 0.328 and 0.256 respectively. The regimes of large and small phonon dispersion are characterized by $p < 2$ and $p \geq 3.3$ respectively, and thus for the NwN samples, we are in weak dispersion regime, which means the contribution of low energy phonons towards BGS is very less compared to that of high energy phonons.

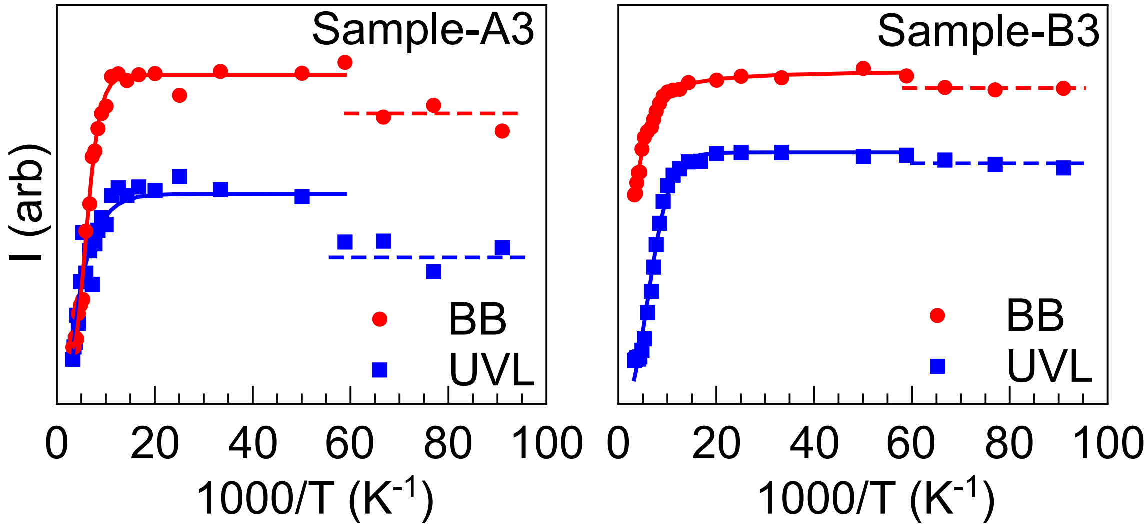

Figure 5.11: Intensity of NBE and UV luminescence peaks as a function of inverse temperature for samples (left) A3 and (right) B3.

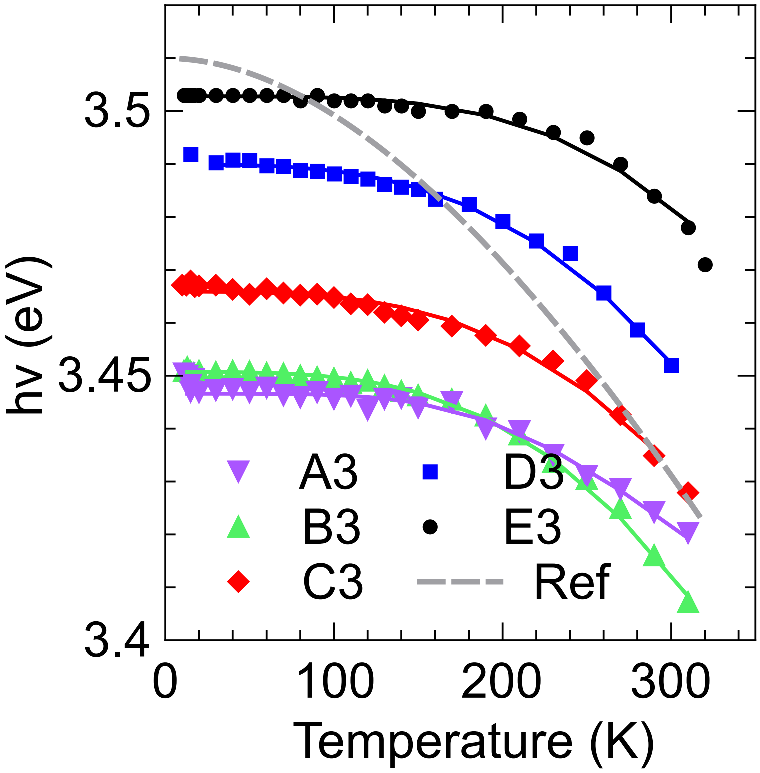

Figure 5.12: Positions of band edge for samples A3, B3, C3, D3, and E3 as a function of temperature. Also shown is data from ref[1].

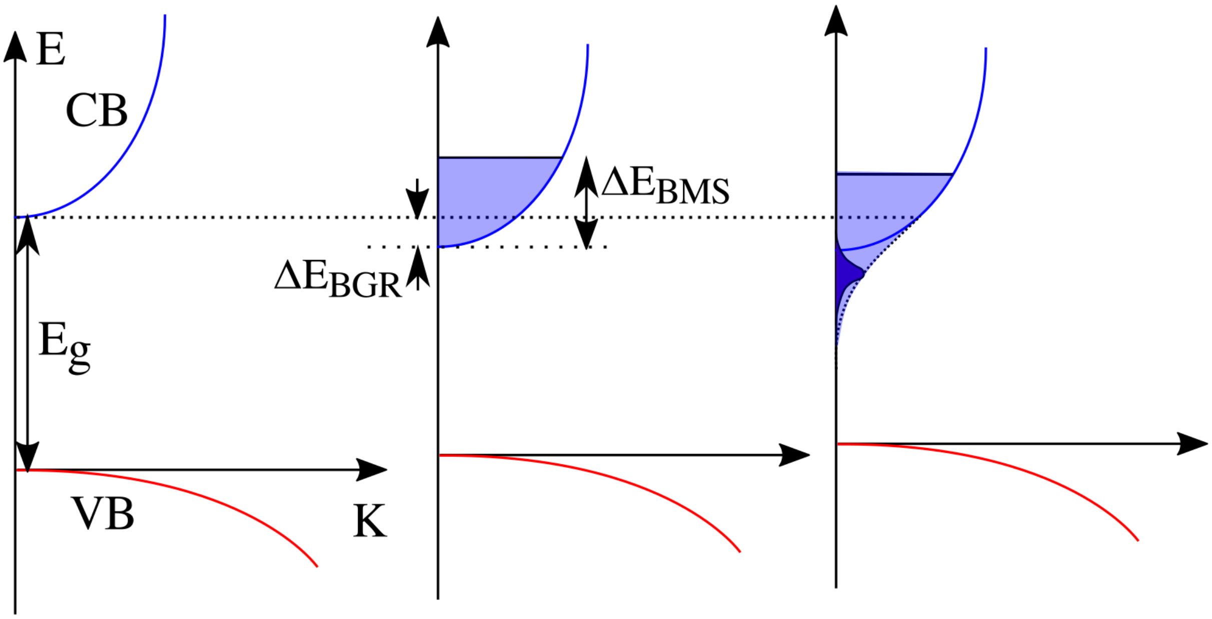

Figure 5.13: Schematic diagram of band structure showing band gap renormalisation (BGR) and Burstein-Moss shift (BMS). Right panel shows donor band overlapping with conduction band tail.

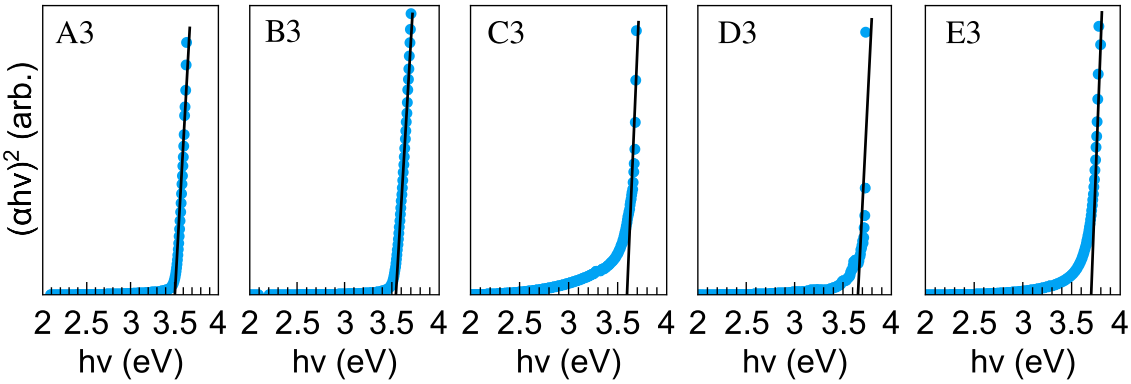

Figure 5.14: Square of absorption coefficient versus energy plot for samples A3, B3, C3, D3 and E3.

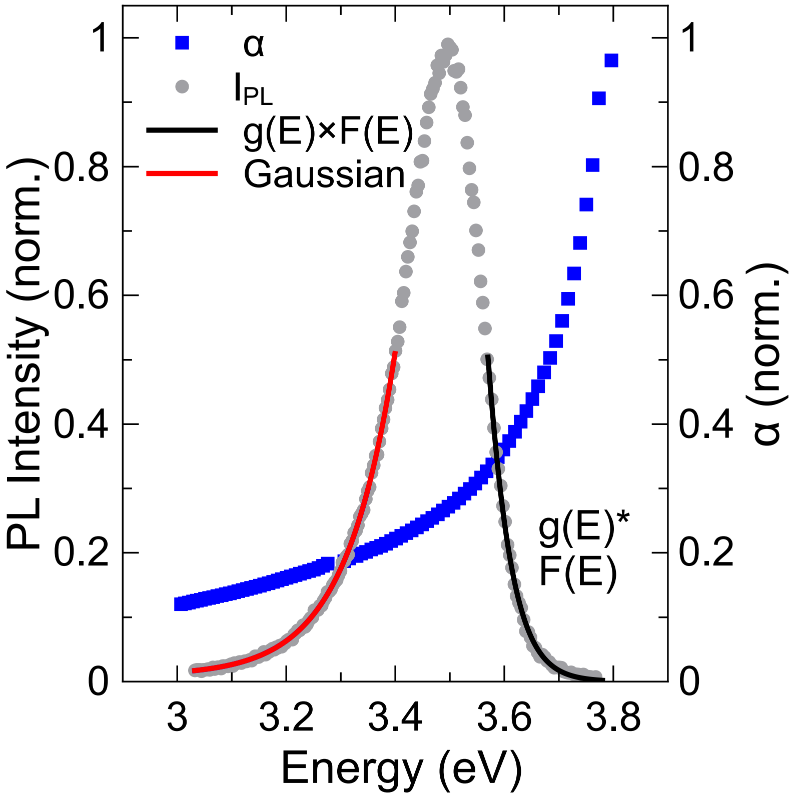

Figure 5.15: PL spectrum and absorption coefficient for sample E3. Lower energy tail of PL peak fitted with Gaussian function and higher energy tail fitted with density of occupied states.

The large carrier concentration modifies the band-gap through band-gap renormalization (BGR) and Burstein-Moss shift (BMS), which we calculate here to estimate the modified band-gap. These effects are schematically shown in Figure 5.13. The BGR has two components due to electron-electron interaction and electron-ion interaction given as follows:

$$\Delta E_{e-e} = \frac{e^2 k_F}{2\pi^2 \epsilon_0 \epsilon_s} + \frac{e^2 k_{TF}}{8\pi \epsilon_0 \epsilon_s}[1 - \frac{4}{\pi} tan^{-1}(\frac{k_F}{k_{TF}})] \tag{5.5}$$

and

$$\Delta E_{e-i} = \frac{e^2 n}{\epsilon_0 \epsilon_s a_B k_{TF}^3} \tag{5.6}$$

Here, Fermi wavevector is $k_{\mathrm{F}} = (3\pi^2 n)^{\frac{1}{3}}$, Thomas-Fermi screening length is given as $k_{\mathrm{TF}} = 2\sqrt{k_{\mathrm{F}}/\pi a_B}$, in which $\mathrm{a_B}$ is Bohr radius and ϵ_s is static dielectric constant of GaN. Net BGR is $\Delta E_{BGR} = \Delta E_{e-e} + \Delta E_{e-i}$

The Burstein-Moss shift for a parabolic conduction band is given as:

$$\Delta E_{BMS} = \frac{\hbar^2}{2m^*}(3\pi^2 n)^{\frac{2}{3}} \tag{5.7}$$

Residual strain of the samples is known to modify the fundamental band-gap, a compressive strain enhances the band-gap and tensile strain reduces it. We have estimated the biaxial strain of the samples from the shift of the E_H^2 Raman mode, which is tabulated in Table 5.1. $\Delta E_{strain} = a_{PL}\Delta\epsilon$ and $\Delta\epsilon = \Delta\omega/a_R$. Here, ΔE_{strain} is PL shift due to strain, $\Delta\epsilon$ is the strain calculated from shift $\Delta\omega$ of E_2^H peak. Also, a_R is the deformation potential taken to be 911 cm^{-1} and a_{PL} as -7.1 eV[152].The calculated values of ΔE_{BGR}, ΔE_{BMS} and ΔE_{strain} is given in Table 5.2 along with room temperature positions of PL NBE peak and experimental absorption edge calculated from UV-visible transmittance spectroscopy. Figure 5.14 shows the plot of square of absorption coefficient versus energy for nanowall samples for calculation of absorption edge. The modified band-gap is then given by $E_g^* = E_g - \Delta E_{BGR} + \Delta E_{strain}$ and the absorption edge is given as $E_{abs}^* = E_g + \Delta E_{BMS} - \Delta E_{BGR} + \Delta E_{strain}$, where E_g is the original band-gap of GaN.

From Table 5.2 we can see that there is good agreement between calculated values of absorption edge and the experimentally observed values, which attests to the applicability of our analysis. Next, we focus on the width of the NBE peak at room temperature, which for samples A3 to E3 are 145, 120, 148, 196 and 221 meV, respectively. The width of the NBE

Sample	ΔE_{BGR}	ΔE_{BMS}	ΔE_{strain}	E_g^*	E_{PL}	E_{abs}^*	E_{abs}
A3	0.138	0.207	0.013	3.292	3.42	3.499	3.50
B3	0.161	0.273	0.016	3.269	3.42	3.542	3.55
C3	0.184	0.348	0.004	3.245	3.43	3.594	3.60
D3	0.201	0.404	0.012	3.229	3.46	3.633	3.65
E3	0.223	0.485	0.015	3.207	3.49	3.692	3.70

Table 5.2: Summary of calculated energy shifts and characteristic energies.ΔE_{BGR}, ΔE_{BMS} and ΔE_{strain} are shifts due to band-gap renormalization, Burstein-Moss effect and strain, respectively. E_g^* and E_{abs}^* are calculated values of modified band-gap and absorption edge. E_{PL} and E_{abs} experimentally observed positions of PL NBE peak and absorption edge. All energies are in eV.

peak is affected by a number of factors such as: natural linewidth of the optical transition, thermal broadening, stress related broadening, broadening due to band filling and due to band tailing. The natural line-width is very small, less than a meV, and thermal broadening is of the order $\frac{3}{2}\mathrm{K_B T}$, which is about 40 meV. The broadening due to non-uniform strain can be assumed to be of the same order as the resulting peak blue shift, as given in Table 5.2[152].

If BM band-filling effect is the dominant broadening mechanism, in that case, the lower energy tail of the PL NBE peak should follow a $\sim (E-E_g)^{\frac{1}{2}}$ shape, i.e. the DOS of CB, and the resulting peak width should be roughly $\frac{3}{4}(E_F - E_C)$[153]. Taking the calculated modified values of E_F and E_C, the resulting width due to BM effect are found to be 155, 205, 261, 303 and 364 meV for samples A3 to E3, which do not match with the experimental values. Further we see that the low energy tail of NBE peak does not follow $(E - E_g)^{\frac{1}{2}}$, but rather has a Gaussian shape. Thus we can say that BM band-filling effect is not the dominant broadening factor.

Figure 5.15 shows the normalized PL peak of sample E3, and its absorption coefficient where the Stokes portion of PL peak has been fit by a Gaussian lineshape and the anti-Stokes portion has been fit by the density of occupied states (DOOS), which is a product of DOS for CB and Fermi-Dirac function. We have used a simple Kane type parabolic DOS: $g(E) = \dfrac{(2m^*e)^{3/2}}{2\pi^2\hbar^3} * (E - E_C)^{1/2}$? . The good fit indicates that the high energy part of PL comes from occupied states in CB and low energy part from the band-tail states, which usually originate from potential fluctuations around defect atomic sites and follow a Gaussian profile. It is to be noted that in degenerately doped semiconductors, both k-conserving (direct) and non k-conserving (indirect) transitions may be possible, with electron-electron scattering and electron-ion scattering contributing to the momentum change. However, if the indirect transitions dominates, the lower energy tail of PL must follow the shape given by CB DOS, as mentioned above. Thus, we can say that even if indirect transitions are present in our samples, it must be dominated by direct transitions from CB as well as CB tails to the valence band. The width of PL peak, is thus an indication of the extent of tailing, apart from other factors listed above. A significant concentration of donors in nanowall network material is expected to form a delocalised donor band rather than a sharp donor level which may merge with the CB tail. This would have the effect of absence of carrier freeze out at low temperatures which is known to occur in nanowall samples and will be discussed in next chapter. This existence of donor band is shown in right panel of Figure 5.13.

Conclusions

In conclusion, a set of nanowall network samples with different carrier concentrations was deposited to investigate the resultant optical properties. While defect related spectra was not seen at any temperatures for samples with higher carrier concentrations, for samples with lower carrier concentration, it was seen at cryogenic temperatures. BY deconvolution using Gaussian peak fitting the PL spectrum was fitted with UV luminescence peak and its phonon replicas, and red and yellow luminescence peaks. An excitation power dependent PL study showed that the UV luminescence band involved transition between shallow donors and shallow acceptors and the NBE peak due to band-to-band recombination of free electron-hole pairs rather than excitons. A temperature dependent PL spectroscopic study enabled us to estimate the binding energies of the shallow dopants involved in the UV luminescence. The temperature dependent bandgap shrinkage was investigated to glean insight into the electron-phonon interaction in nanowall network. It was found that the electron-phonon coupling is weak, possibly due to screening effect of the carriers. Also, we found contribution of low energy phonons in band shrinkage is small compared to that of high energy phonons. The blue shift of the NBE peak of nanowall network was quantitatively explained by considering the carrier related bandgap renormalisation, band filling and strain effect. The low energy tail of PL peak and tail of absorption spectra are explained on the basis of tailing effect of conduction band due to potential fluctuation of incorporated dopants.

5.5 Conclusion

In summary, we have investigated the morphology dependent optical properties of MBE grown nanorods, porous films and nanowall network. It was seen that size related confinement effects determine the NBE peak position. A change in growth conditions affecting the material morphology was found to have a significant effect in deep defect related luminescence. A high carrier concentration in GaN nanowall network can reduce the electron-phonon interaction and can suppress the defect-related luminescence by filling acceptor levels. The carrier related bandgap renormalisation and bandgap filling determines the overall NBE peak position, peak width and absorption edge position. Potential fluctuations around atomic defects lead to band tail which further widens the NBE peak. Overall, by tuning the morphology and carrier concentration, the optical properties of MBE grown GaN nanostructures can be engineered.

Chapter 6

Study of electronic, electrical transport and magnetic properties

This chapter describes the electronic band structure properties of MBE grown GaN nanowall network studied through X-ray photoelectron spectroscopy, capacitance measurements and by means of electrochemical studies such as cyclic voltammetry and impedance spectroscopy. The magneto-transport properties are investigated by temperature and magnetic field dependent resistivity and Hall measurements. Analysis of the data is carried out to understand the quantum mechanical effects involved in the transport. Temperature and magnetic field dependent magnetisation measurements and magnetic force microscopy studies are performed to investigate unusual magnetic properties of nanowall network of typically non-magnetic GaN material.

6.1 Introduction

In the preceding chapters, we have discussed the effect of different types of defects and low-dimensionality on the growth, structural and optical properties of the MBE grown GaN nanostructured materials. Both nanostructuring and the presence of defects influence the electronic structure of the material, which affects the majority of its properties. In this chapter, we study the electronic, electrical transport and magnetic properties of the GaN nanowall network and how the defects and the low-dimensionality influence them. Accordingly, this chapter has been divided into three sections. The first section deals with the study of the electronic band structure properties of the nanowall network studied through X-ray photoelectron spectroscopy and separately with electrochemical studies accompanied with luminescence spectroscopy. The second part of the chapter deals with the electrical transport properties of the nanowall network as a function of temperature and magnetic field to investigate the nature of the carrier transport and the underlying quantum mechanical effects. The last portion of the chapter pertains to the magnetic properties of the nanowall network studied through temperature and field-dependent SQUID magnetisation measurements and magnetic force microscopy.

6.2 Electronic properties

The electronic structure of a semiconductor determines the majority of its application-specific properties such as luminescence, photovoltaic property, catalysis and transport, to name a few. The electronic band structure varies from bulk to surface and is influenced by the presence of defects - native, impurities or adsorbates. GaN being an established material, its band structure has been studied extensively both experimentally and using theoretical calculations. The as-grown GaN is n-type with an upward band bending. States present on the surface, whether from dangling bonds, vacancies or impurities, can pin the Fermi level. The amount of band bending influences the carrier distribution and separation of photogenerated carriers. The gap states on the surface can trap the charge carriers and can reduce the radiative recombination efficiency through Shockley-Reed-Hall trap assisted non-radiative recombination. The large surface area of the GaN nanowall network makes surface states more influential in determining the overall properties of the nanowall network. From a fundamental as well as application point of view, it is crucial to investigate the surface electronic structure of the GaN nanowall network.

6.2.1 Photoelectron spectroscopy study

X-ray photoelectron spectroscopy (XPS) is used to study the electronic structure and surface chemical composition of thin films and nanostructures. The electronic band structure and composition of the material may differ from bulk to surface, and XPS provides valuable information on the surface properties. Thermodynamic energy considerations determine the surface atomic structure of the nanomaterial and hence the orientation of the bounding surface becomes important. The atomic structure of the surface and the presence of adsorbates determine the nature of the surface electronic structure. We combine XPS with luminescence spectroscopy to investigate stoichiometric composition, surface electronic structure and defect-related states of the MBE grown GaN samples.

6.2.1.1 Experimental details

A set of three GaN samples A1, B1, and C1 were grown using PAMBE system. C-plane sapphire was used as the substrate, which was degreased by ultrasonicating in organic solvents and rinsed in de-ionised water before being inserted in the preparation chamber of MBE. Here, it was thermally cleaned by degassing at 600 °C for 1 hour. The substrate was then transferred to the main growth chamber, where it was again degassed at 850 °C for 30 minutes. The samples A1 to C1 were grown in nitrogen-rich conditions, wherein the substrate was held at 630 °C. Ga k-cell temperatures of 1050, 1020, and 1100 °C, and nitrogen flow rates of 4.5, 6, and 4.5 sccm were used for depositing samples A1, B1 and C1, respectively. All samples were grown for 4 hours with the RF plasma forward power of 375 W. The sample D1 is a commercially obtained 2 μm thick MOCVD grown GaN flat epilayer which is used for comparative studies of morphology dependence of properties. The morphology of the samples was observed by FESEM, which is also fitted with a cathodoluminescence (CL) detector. Electrical properties were determined by Hall measurements at room temperature, and the surface chemistry was studied by X-ray photoelectron spectroscopy (XPS). The as-deposited samples were directly inserted in the XPS chamber, without any surface treatment, to determine their native properties. Both non-monochromatic Al K-α and Mg K-α were used as X-ray sources. After the initial studies, 0.8 KeV energy Ar^+ ion sputtering was employed for varying periods to remove the surface contaminants, followed by XPS core level and valence band analysis.

6.2.1.2 Results

Figure 6.1 shows the plan view FESEM images of samples A1 to D1, which are in the order of reducing surface roughness and porosity. A1 is a highly porous nanowall network, B1 is a meso/macroporous film, sample C1 consists of coalesced flat-topped islands, and D1 is the flat GaN epilayer. The surface roughness of the samples was quantified by atomic force microscopy (AFM). The RMS roughness of the samples from A1 to D1 was found to be 57.4, 19.9, 7.8, and 0.4 nm, respectively.

We cut the samples into smaller pieces ($\approx 1 \times 1$ cm^2) and made indium

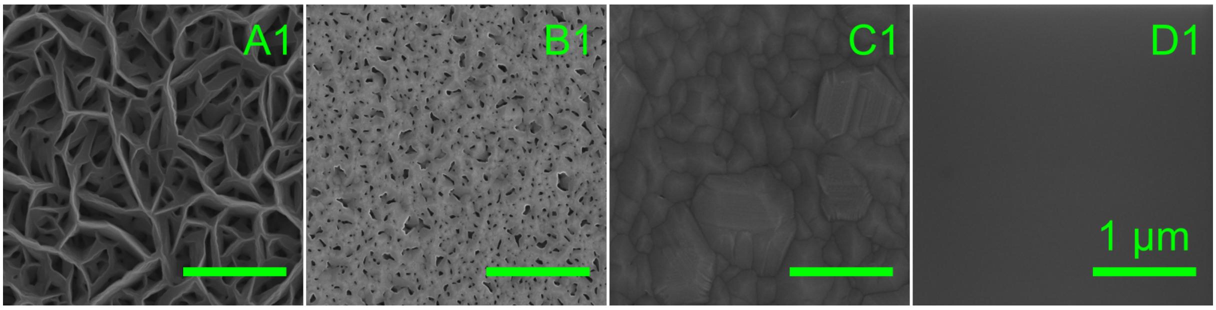

Figure 6.1: FESEM images of samples A1, B1, C1, and D1. The scale bar corresponds to 1 μm.

metal contacts on one set of samples to study the electrical properties. Four probe Hall measurements in van der Pauw geometry was carried out. We found the MBE grown samples to be unintentionally highly n-doped, with bulk carrier concentrations of (244, 122, 9.7)$\times$ 10^{18} cm^{-3} for A1, B1, and C1. MOCVD grown sample D1 had a carrier concentration of 2.0$\times$ 10^{17} cm^{-3}. The resistivities of samples A1 and B1 are $\sim 10^{-3}$ Ω cm, and those of C1 and D1 are $\sim 10^{-1}$ Ω cm.

We carried out XPS studies of the samples by acquiring survey and core-level spectra, without any surface treatment, to study the native surface. We found that the GaN samples have oxygen and carbon contaminants on the surface due to handling, storage, and atmospheric exposure. The adventitious carbon is generally unreactive and does not form chemical bonds with gallium. The oxygen species can form stoichiometric (Ga_2O_3) or non-stoichiometric (GaO_x) gallium oxides or even gallium oxynitrides. For the analysis of XPS data, the adventitious carbon was assumed to have a hydrocarbon nature, and its binding energy (B.E.) was taken to be 284.8 eV[154]. For the analysis of core-level spectra, a Shirley background correction was employed followed by deconvolution of the peak. The peak shape was taken to be Voigt, with a Gaussian contribution of 80% and Lorentzian of 20%. Figure 6.2 shows the deconvoluted Ga 3d core-level spectra of samples A1 to D1. The peak at 18.1 is due to the Ga-Ga metallic bond[155]. While the peak at (19.3 $\pm$ 0.2) eV and the one at (20.4 $\pm$ 0.1) eV have been attributed to the Ga-N bond and Ga-O bond, respectively[156]. Prabhakaran et al. found the native oxide on GaN to be predominantly monoclinic β-Ga_2O_3, although the formation of oxynitrides could not be ruled out[157].

The spectra in all cases predominantly show the Ga-N component, with the Ga-O component occurring at a higher B.E. value and the Ga-Ga component occurring at a low B.E. value. It can be observed in Figure 6.2

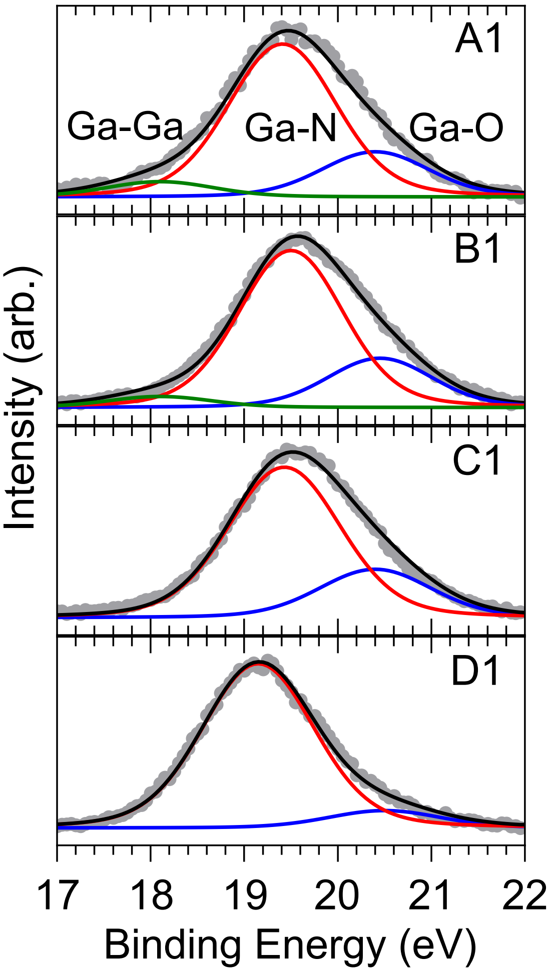

Figure 6.2: Deconvoluted XPS Ga 3d core level peak of samples A1, B1, C1, and D1.

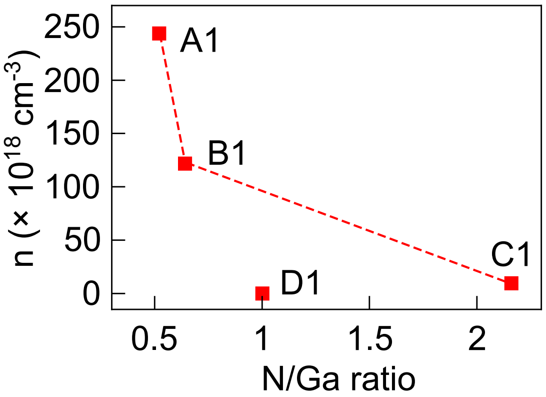

Figure 6.3: Plot of bulk carrier concentration n versus the calculated stoichiometry of the sample surface.

that samples A1 and B1 contain Ga-Ga metallic bonds, which is absent in samples C1 and D1.

To get the absolute surface composition of a sample from XPS, a completely clean surface is required. Several methods can be employed to achieve completely clean surfaces, for example ion sputtering[158], HCl cleaning[159], atomic hydrogen cleaning[160], and in situ annealing[161]. Each of these techniques has its own particular effect on the surface. The surface chemistry changes significantly after prolonged Ar^+ sputtering; without sputtering, the adsorbates mask the true composition. The GaN epilayer sample D1 has been assumed to be stoichiometric GaN, and relative compositions for sample A1-C1 have been estimated. A light 5 minutes sputtering (0.8 KeV, 50 μA) was performed on all the samples to remove some of the adsorbed contaminants. After that, the peak intensities were measured; and the elemental concentrations for Ga, N, O and C were estimated with appropriate atomic sensitivity factors (ASF), using the following relation:

$$X_i = \frac{I_i/S_i}{\Sigma_i I_i/S_i} \tag{6.1}$$

Where X_i, I_i and S_i are the concentration, intensity and ASF of the i-th element. Among the surface elements, we focus on the relative concentration of gallium and nitrogen elements and find that samples A1 and B1 are gallium rich, whereas C1 is gallium deficient. Figure 6.3 shows a plot of N/Ga stoichiometry of sample surface versus the measured carrier concentration. This graph is in line with the concept that a significant concentration of nitrogen-vacancy (leading to a Ga rich surface) is responsible for the unintentional n-doping of MBE grown GaN.

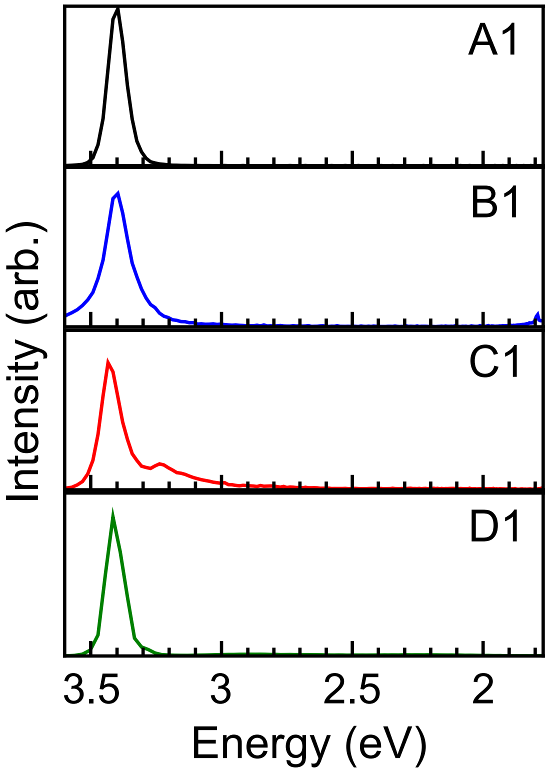

Figure 6.4: Cathodoluminescence spectra of samples A1, B1, C1, and D1 showing the NBE emission.

We employ CL spectroscopy to obtain information on the bandgap. Figure 6.4 shows the CL spectra of the samples taken at room temperature with an acceleration voltage of 20 kV and beam current of 4 nA. The spectra primarily consist of the NBE emission except for sample C1 which shows an additional UV luminescence peak. In the previous chapter, we have attributed the NBE peak as due to band-to-band recombination of free electrons and holes; thus, the position of the NBE peak equals the bandgap. All the samples are found to have the NBE peak at 3.40 ± 0.03 eV as expected.

To understand the band structure and the degree of band bending of these n-GaN samples, we need to find the relative positions of band edges and Fermi level. We use simple free-electron theory calculations to estimate the position of Fermi level on the sample surface with respect to the valence band edge position[162]. For degenerate semiconductors, the energy difference between Fermi level $\mathrm{E_F}$ and bandgap midpoint $\mathrm{E_i}$ is given as:

$$(E_F - E_i) = K_B T ln(\frac{n}{n_i}) \tag{6.2}$$

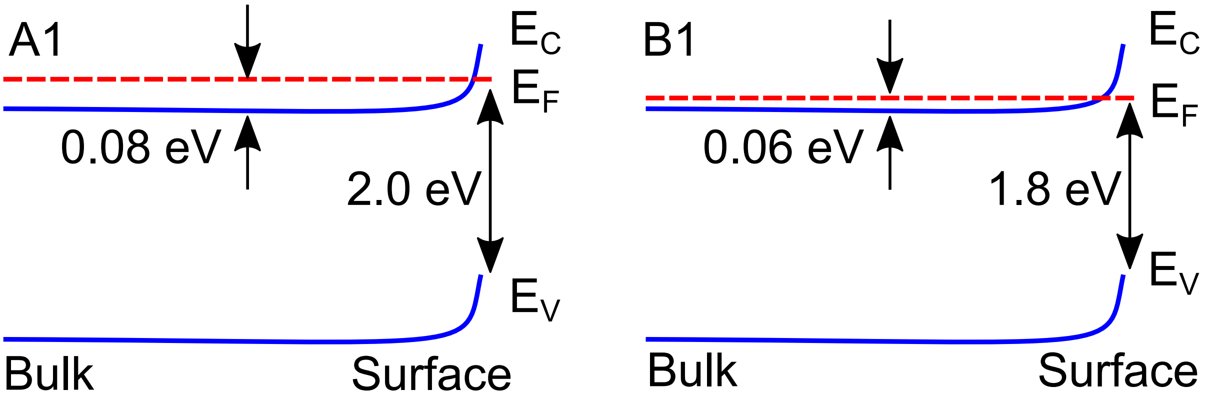

Figure 6.5: Schematic representation of band structure of samples A1 and B1 showing the degree of band bending and position of Fermi level.

Where n is the carrier concentration of the sample and n_i is the intrinsic carrier concentration of the material. Using value of n_i as 3.8×10^{-10} cm^{-3} and experimentally determined values of n, we find that at room temperature (E_F-E_i) equals 1.78, 1.76, 1.70, and 1.60 eV for samples A1, B1, C1, and D1. Taking $E_G = 3.40$ eV as determined from CL spectra, the Fermi levels of samples A1 and B1 are found to be above CBM.

To locate the position of Fermi level on the sample surface, a straight line was fitted to the leading edge of the valence band spectra, whose intersection with the background gives the position of E_V, with respect to $E_F = 0$ eV binding energy. (E_F-E_V) values so found, are: 2.0, 1.8, 1.6, and 1.7 eV, respectively, for samples A1, B1, C1, and D1. These values are also confirmed by measuring the separation between VBM and Ga 3d core level, which is independent of band bending. Using the (E_V - $E_{Ga\ 3d}$) value of 17.76 eV, given by Waldrop and Grant, and the experimentally determined Ga 3d core level position, the value of (E_F-E_V) are found to be 2 eV, 1.7 eV, 1.7 eV and 1.3 eV, for A1, B1, C1, and D1 respectively, which agree with the first method, at least for the porous samples[163]. The resulting schematic band diagrams for A1 and B1 are shown in Figure 6.5.

Thus, the results show that the Fermi level gets pinned at (1.8 ± 0.2) eV above VBM, for samples A1 and B1. Earlier, the experimental work of Kocan et. al.[164] showed that for GaN samples covered with a thin Ga adlayer, the Fermi level gets pinned 1.65 eV above VBM, and Van de Walle et. al. showed by DFT calculations[165] that for a metallic bilayer consisting of the terminating Ga atom and a Ga adatom, the Fermi level gets pinned at 1.8 eV above VBM for both polar and non-polar GaN surfaces. Comparison of these literature values and our data suggests that a Ga adlayer

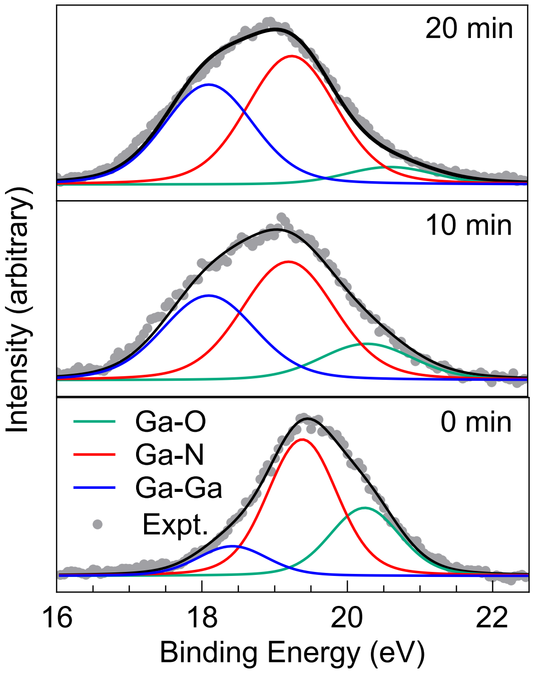

Figure 6.6: Deconvoluted XPS Ga 3d core level spectrum of sample A1 for different sputtering durations of 0, 10, and 20 minutes.

exists at the surface of samples A1 and B1.

As mentioned previously, Ar^+ sputtering, commonly used for cleaning purpose can lead to a change in surface chemical composition as the sputter yield, (average number of target atoms sputtered per incident Ar^+ ion) is not the same for all elements. The rate of nitrogen sputtering is more than that of gallium leading to a change in the surface chemistry for prolonged sputtering. Figure 6.6 shows the core level Ga 3d spectra of A1 deconvoluted into Voigt components, for the unsputtered sample and after 10 and 20 minutes of sputtering. As it can be expected, with sputtering, the gallium oxide component reduces, while the contribution of metallic Ga-Ga bond increases. The calculated Ga/N absolute concentration ratio for unsputtered A1 sample and after 10 and 20 minutes of sputtering, are 0.3, 0.9 and 1.2, respectively, indicating that the surface becomes more metal rich with increasing Ar^+ sputtering. Such surface metallisation with ion sputtering has been reported in the literature previously[166].

Figure 6.7 shows the normalized VB spectra of sample A1 at different sputtering times. Defects at semiconductor surfaces lead to a change in the DOS[167]. As VB spectra reflects the total DOS of the semiconductor, information regarding the type and abundance of point defects can often be estimated from VB spectra. A few observations can be made from

Figure 6.7. The unsputtered VB spectra has two prominent features, one around 3-4 eV (P_A) and another around 8-9 eV (P_B). The low binding energy peak originates from the hybridization of Ga 4p and N 2 orbitals and is referred to as ‘p-like’. The higher binding energy peak is ‘s-like’ and is attributed to hybridization of Ga 4s and N 2p orbitals. The feature appearing in between these two peaks is attributed to adsorbates or mixed hybridized orbitals[168],[169]. Experimentally, it has been found that there is a direct correlation between relative intensities of (P_A and (P_B and the polarity of the sample. Skuridina et. al.[170] showed that if the intensity of P_A is higher than P_B, the material is cation polar, whereas if the reverse occurs, it is N polar. So, from the Figure 6.7, it appears that A1 is N polar. After this initial visual analysis, the VB spectra was fitted by 4 Voigt peaks each, in the way described earlier. The peaks at 5.4 eV and 9.1 eV are assigned to Ga 4s - N 2p hybridized orbitals. The peak at 3.8 eV is assigned to Ga 4s - N 2p hybridized orbitals[171]. The peak P3, as mentioned before, is generally attributed to be either adsorbate related or due to mixed hybrid orbitals. Since this peak intensity did not change with sputtering, we discount the role of adsorbates, and attribute it to mixed hybrid orbitals. A prominent observation that can be made from Figure 6.7 is that a significant intensity can be seen gradually building up near the Fermi level position with sputtering, which is a characteristic of surface metallisation as also seen in the Ga 3d core level changes in Figure 6.6.

6.2.1.3 Conclusions

In summary, XPS and CL spectroscopy were used to study electronic band structure and surface composition of GaN nanowall network in comparison to GaN samples with different morphology. It was found that the GaN sample surface is comparatively Ga rich. Presence of Ga-Ga metallic bonds was found in case of nanowall network and porous GaN but not in the compact or flat GaN samples. The MBE grown compact GaN sample had a Ga deficient surface and lower carrier concentration, bolstering the correlation between nitrogen vacancies and unintentional high electron concentration. The CL spectra showed only NBE emission for the porous samples and allowed estimation of their bandgap. The position of the Fermi level on the surface of the porous samples was estimated by analysis of VB XPS spectra. Combining these two information, the degree of upward band bending was calculated. For nanowall network and porous GaN film, the Fermi level was found to be pinned 1.8±0.2 eV above VBM which

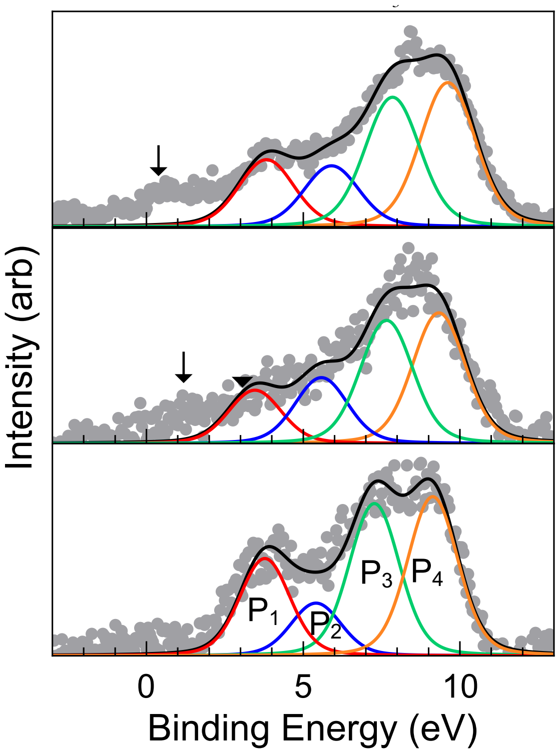

Figure 6.7: Deconvoluted XPS valence band spectra of sample A1 for different sputtering durations of 0, 10, and 20 minutes. The arrow marks the position of surface Fermi level at zero binding energy where a build-up of intensity indicates metallisation.

indicated to the presence of Ga adlayer on top of a Ga terminated surface according to computational studies on thermodynamics of GaN surfaces in the literature. The VB XPS spectra was also studied as a function of Ar^+ sputtering duration, and the analysis provided insight on the origin of the photoelectron peaks comprising the VB of GaN nanowall network.

6.2.2 Electrochemical studies

The majority of literature reports on electronic structure of GaN focus on material grown in either moderate or high Ga/N ratio conditions. Additionally, the first principle DFT calculations mostly pertain to polar (+c,-c) and non-polar (m,a) GaN surfaces[172]. From these, only a limited inference can be obtained regarding GaN nanowall network which are grown in highly N rich growth ambient and their wedge shaped morphology is bounded by semi-polar surfaces. The Ga/N flux ratio has a direct effect on the position of Fermi level, which, in turn determines the nature and concentration of native or impurity defects the grown material can incorporate. The growth parameters also determine the nature of interface between film and substrate which can often become highly defective with a degenerate local carrier concentration. The surface of the nanostructured film, based on the type and density of surface and adsorbate states can become comparatively electron rich or deficient with respect to the bulk. The surface concentration of electrons plays an important role in optical and transport properties.

Capacitance based methods are often used to characterise carrier distribution and presence of trap states. Formation of Schottky electrical contacts allows one to measure capacitance of the material. Whether a particular metal-semiconductor combination would act as Ohmic contact or as a Schottky diode depends firstly on the difference of work functions and importantly also on the nature of the interface and carrier concentration of the semiconductor material. Formation of an ideal Schottky junction, in absence of any surface states, leads to the formation of a depletion region with measurable capacitance. Presence of adsorbates and surface states can modify the height of the Schottky barrier and a high carrier concentration can make the width of the barrier small enough for carrier tunnelling. Presence of defects such as traps on the metal-semiconductor interface or the semiconductor-substrate interface modifies the capacitance of the system thereby providing a means of probing the density of such de-

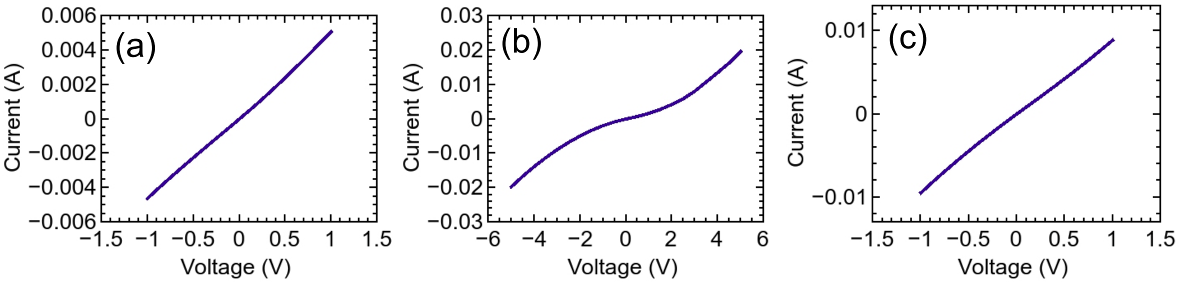

Figure 6.8: Current-voltage characteristics of different metal/GaN nanowall network contacts. (a) Al/GaN (b) Au/GaN, and (c) Pt/GaN.

fects.

Table 6.1: Typical metal contacts to n-GaN

Metal	ϕ_m(eV)	ϕ_m - χ_{GaN}(eV)	Expected contact type
Al	4.28	0.18	Ohmic
Au	5.10	1.0	Schottky
Pt	5.65	1.55	Schottky

Table 6.1 lists three common metals often used for making electrical contacts with n-GaN. Among these, Al is expected to make an ohmic contact due to the small work function difference and Au and Pt are expected to form Schottky contacts. Figure 6.8 shows the I-V characteristics of of GaN nanowall network samples with (a) Al contact, (b) Au contact, and (c) Pt contact.

The electrical conduction for Al contact is ohmic as expected but the Au and Pt contacts do not have the expected rectifying nature. Au-GaN contact shows some non-linearity which Pt-GaN contact does not. This can be attributed to degenerate nature of GaN nanowall network as the carriers can tunnel through the barrier.

A second method to measure capacitance is to use a metal-insulator-semiconductor (MIS) structure. Figure 6.9 shows a schematic diagram of the MIS structure in which the insulator partially covers the semiconductor sample and metallic contacts are deposited on both the exposed and covered semiconductor. An applied voltage is expected to modify the space charge region of the semiconductor and thereby yield valuable information. In an experiment we used GaN nanowall network as the semiconductor, polymethyl methacrylate (PMMA) as the insulator and Al as the metal. The PMMA was deposited on half of the sample using a solution and the metal was deposited using PVD. Capacitance measurements were then carried out with a Keithley 4200 system.

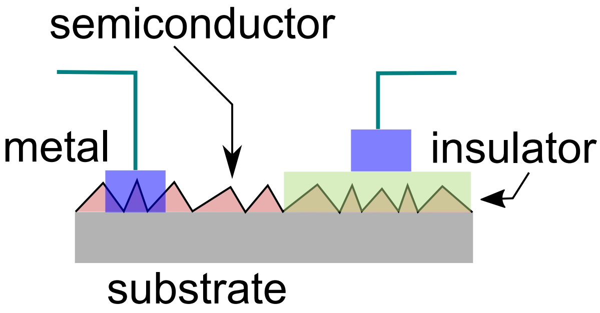

Figure 6.9: Schematic diagram of a metal-insulator-semiconductor (MIS) device.

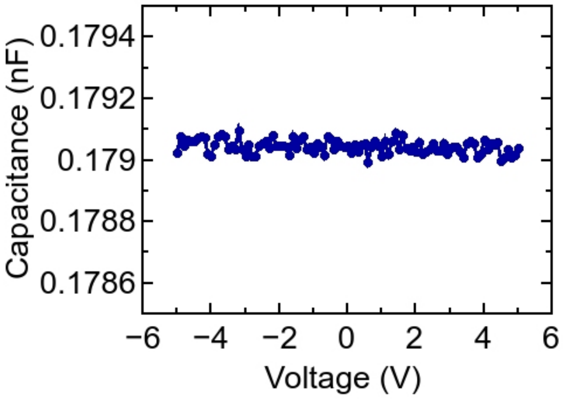

Figure 6.10: Capacitance-voltage characteristics of an MIS device with polymethyl methacrylate (PMMA) insulating layer and Al metal contact.

Figure 6.10 shows the results of the capacitance-voltage measurements. As we can see, the capacitance is bias independent and attributed to the constant capacitance of the insulator rather than that of semiconductor space charge layer.

A significant limitation of these experiments is immediately apparent in this case - the non-conformal nature of the electrical contact onto the nanowall surface. We choose to overcome this problem by using electrochemical rather than solid metals to ensure proper contact with the nanowall network.

We therefore study the charge transfer across the interface of the nanowall network and an aqueous electrolyte using cyclic voltammetry (CV) and impedance spectroscopy and compare with results from a MOCVD grown flat GaN epilayer to gain understanding about the electronic structure of nanowall network. The surface electronic structure is instrumental is determining in the charge transfer across the interface with another material. Since radiative transition leading to luminescence involve band edges and defect levels, we use photoluminescence to extract additional insight into the material.

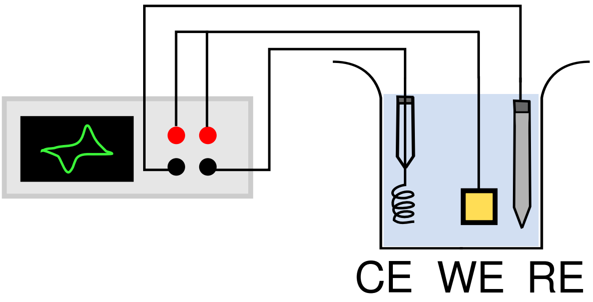

Figure 6.11: Schematic diagram of electrochemical measurement set-up with a three electrode configuration.

6.2.2.1 Experimental details

The GaN nanowall network samples were grown using plasma assisted molecular beam epitaxy directly on c-sapphire substrate. We provided gallium from a standard effusion cell and nitrogen from RF plasma source, both with a purity 7N. For sample A2 and B2 the Ga flux beam equivalent pressure was 4.4×10^{-7} Torr and 5.0×10^{-7}. The nitrogen flow was kept at 4.5 sccm and 2.5 sccm for samples A2 and B2. The substrate temperature and plasma power were kept fixed at 630 °C and 375 W for both samples. Sample C2 is an MOCVD grown GaN epilayer commercially obtained from Suzhou Nanowin and used as a reference.

The morphology of the samples was studied by FESEM. Cross-sectional FESEM images were used to estimate sample thickness. Room temperature Hall measurement was used for estimation of carrier concentration. For electrochemical characterisation, samples were cut into small pieces and cleaned using acetone and propanol and de-ionised water and dried. Indium metal was deposited to form ohmic contacts for measurements. For CV measurements Keithley 2450 source measure unit was used and for impedance spectroscopy CH instruments 760E electrochemical workstation was used. For both CV and impedance measurements, an usual three-electrode configuration was used with a saturated calomel electrode (SCE) as reference and a long platinum wire coil as counter electrode. Aqueous electrolytes were prepared from deionised water and 100 mM Na_2SO_4 which was purchased from Alfa Aesar and used as-is. All the CV were obtained at a scan rate of 50 mV/s. A 250 W Xe arc lamp (Oriel Newport) is used in conjunction with UV band pass filer to study photoresponse study. Impedance spectra were obtained by varying the frequency in the range of 10 Hz to 1 MHz at different DC biases (from -2 V to +2 V versus SCE) with AC modulation amplitude set to 5 mV.

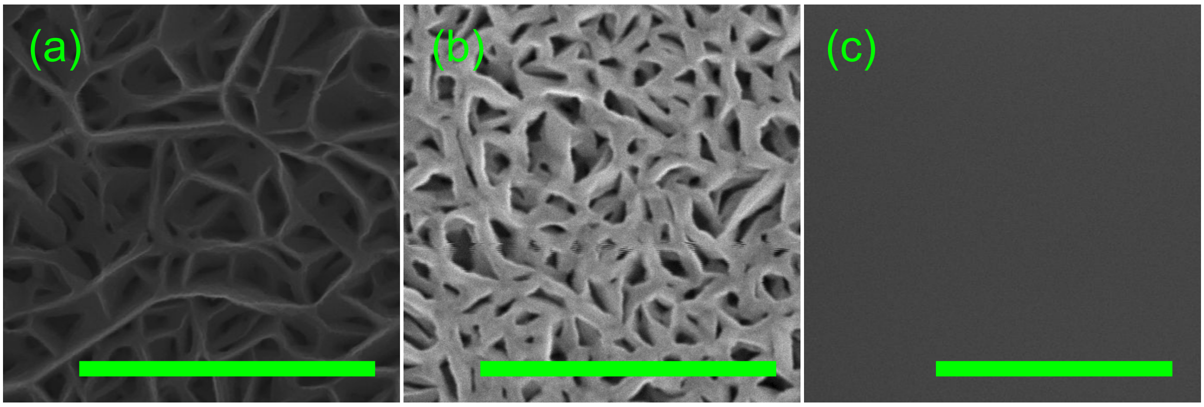

Figure 6.12: FESEM images of samples A2, B2, and C2. The scale bar corresponds to 1 μm.

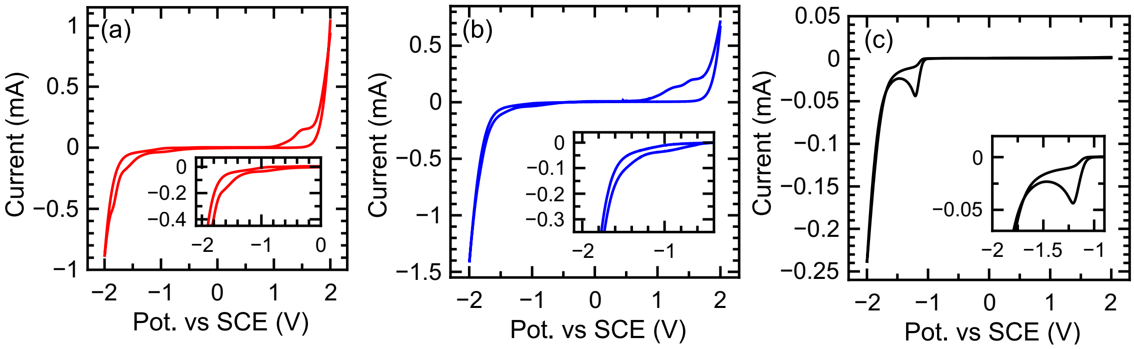

Figure 6.13: Cyclic voltammogram data for samples (a) A2, (b) B2, and (c) C2. The insets show a close-up view of the cathodic current.

6.2.2.2 Results

Figure 6.12 shows the plan-view FESEM images of the samples. Both A2 and B2 are highly porous nanowall network samples and sample C2 is flat. The pore sizes for A2 and B2 range from few tens of nanometres to several hundreds of nanometres, and thus we can categorise the nanowall network samples as meso/macroporous according to IUPAC norms[173]. The peculiar morphology, including the 'pore within a pore' nature make the estimation of true surface extremely complicated, though it is understood to be much greater than the geometrical surface area visible in the plan-view images. Porosity, defined as the fractional volume occupied by the voids is greater for sample A2 than B2.

The GaN nanowall network samples are n-type and their bulk carrier concentrations were estimated using Hall measurement and found to be 1.41×10^{20} cm^{-3}, 5.98×10^{19} cm^{-3} and 5.23×10^{17} cm^{-3} for samples A2, B2, and C2 respectively. Taking the density of states of wurtzite GaN at the conduction band minimum at room temperature to be 2.23×10^{18} cm^{-3}, it is

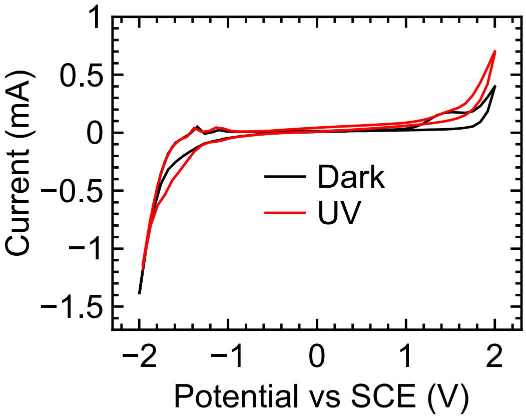

Figure 6.14: Cyclic voltammogram of sample B2 with and without illumination.

clear that the nanowall network samples are degenerately n-type whereas the epilayer is non-degenerate.

To investigate the surface electronic structure of the GaN nanowall network, we initially study the charge transfer between the sample and the aqueous electrolyte without any illumination. The current across the GaN/electrolyte interface is recorded as a function of the potential difference applied between the sample and the SCE reference electrode. Figure 6.13 depicts the cyclic voltammograms for samples A2, B2, and C2 for potentials in the window +2 V to -2 V. This range includes the potential window for water dissociation by GaN. Sample C2 shows no Faradaic currents for positive potentials whereas the nanowall network samples do. In the negative side cathodic currents are observed for all three samples. The cathodic current is attributed to hydrogen evolution (HER) which involves the following reaction:

$$2H_2O(l) + 2e^- \rightarrow H_2(g) + 2OH^- \tag{6.3}$$

The anodic current can be due to two possible electrochemical reactions - both involving holes (h^+) which are the minority carriers in our samples: oxidation of water to release oxygen or oxidation of GaN material itself[174]. The former reaction is:

$$4OH^- + 4h^+ \rightarrow O_2(g) + 2H_2O(l) \tag{6.4}$$

Whereas the latter reaction involves

$$GaN + 6OH^- + 3h^+ \rightarrow GaO_3^{3-} + 3H_2O(l) + \frac{1}{2}N_2(g) \tag{6.5}$$

The onset of cathodic current occurs around -0.5 V for samples A2 and B2 and around -1 V for sample C2. In case of the nanowall network samples, the cathodic current increases slowly after onset over a comparatively wide region and then rapidly increases with potential around -2 V. In contrast, for sample C2, we observe a sharper increase of the cathodic current and a local maximum at -1.2 V before the sharp tail associated with HER.

In an ideal case involving charge transfer only from the GaN band edges, the onset of cathodic current should occur at potentials more negative than flat band potential (V_{FB}) which is around -1 V for n-type GaN according to literature reports[175]. The n-type semiconductor is in a state of accumulation for potentials more negative than V_{FB} and in a state of depletion with a space charge region for potentials more positive than V_{FB}. These wide potential regions of non-zero cathodic current indicate non-ideality and possible explanation include charge transfer through surface states or electron tunnelling through SCR[176]. The moderately doped sample C2 is estimated to have several tens of nanometres thick SCR making electron tunnelling improbable and thus involvement of surface states in the charge transfer is the likely explanation.

The anodic current observed in case of nanowall network samples has onset at about 1 V for sample A2 and 0.7 V for sample B2. For both types of anodic reactions considered here, the necessary holes may be either be present in the bulk valence band, or be photogenerated, or generated by tunnelling of electrons from valence band to conduction band under conditions of deep depletion. All samples being highly n-type, existence of sufficient holes in the valence band is not possible. These CV experiments having been performed in the dark, exclude photogeneration, leaving only the final factor in play. Simple calculations show that for nanowall network samples the thickness of the SCR is only a few nanometres making it possible for electrons to tunnel from valence to conduction band generating holes. We believe that both reactions eqn(6.5) and eqn(6.4) take place for the nanowall network samples as has been reported previously[177][178]. Subtle changes to the CV have been observed after several dozen cycles indicating a modification of the surface taking place, possibly due to oxidation of GaN. For the sample C2, a larger depletion region thickness of several tens of nanometres precludes the tunnelling associated hole generation and no anodic current is expected.

We now turn to the photoresponse of the samples by carrying out cyclic

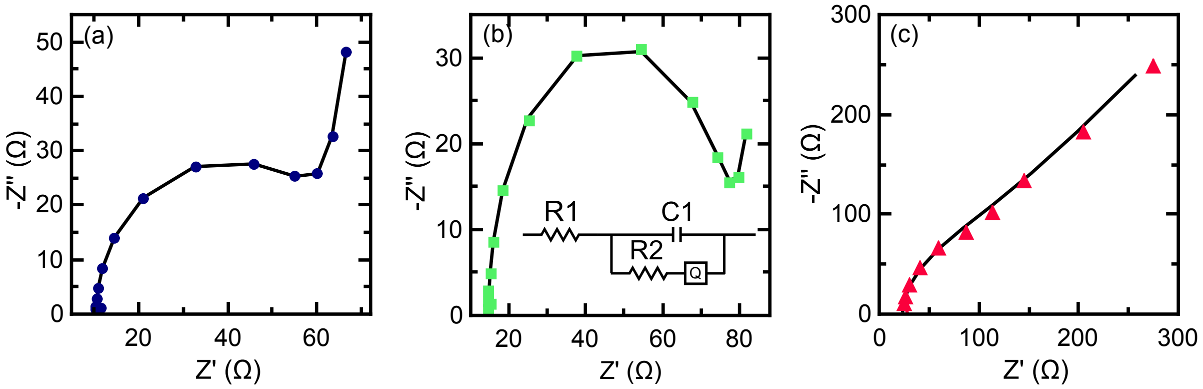

Figure 6.15: Representative frequency dependent impedance spectra of samples (a) A2, (b) B2, and (c) C2 plotted in Nyquist form. The solid lines are a fit to experimental data using an equivalent circuit shown in inset of (b).

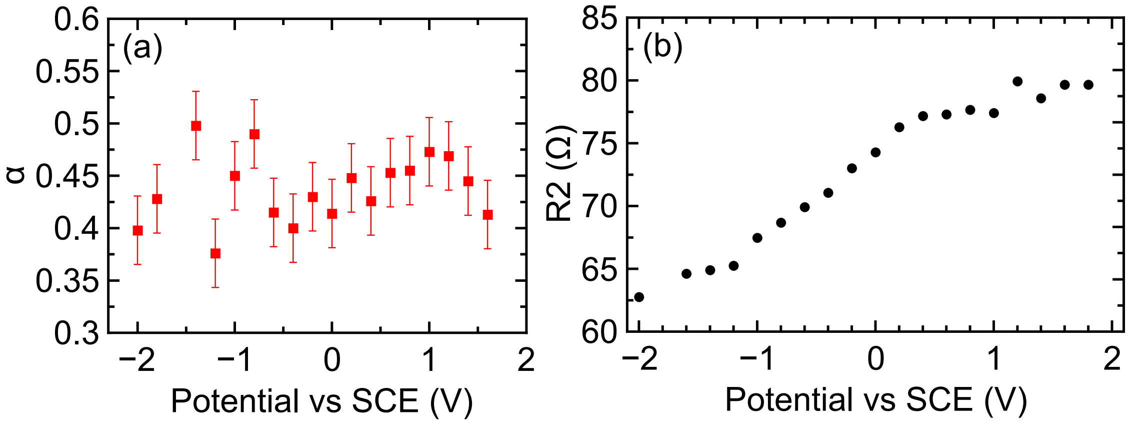

Figure 6.16: Bias dependent parameter values extracted from equivalent circuit fitting. (a) Exponent of constant phase element α and (b) charge transfer resistance R_2.

voltammetry with supra-bandgap UV light incident on the samples. All nanowall network samples which we studied in multiple experiments had a minor photoresponse and Figure 6.14 shows the results for sample B2. We see that upon illumination, the basic features of the CV remains same, with only a small increase of the cathodic and anodic currents. For example, the maximum anodic current increases from 0.39 mA to 0.68 mA in presence of UV light. The smallness of the photo-induced current suggests that the population of the photogenerated carriers are smaller than the carrier population already present in the degenerate nanowall network sample.

To gain further understanding of the nature of the sample/electrolyte interface, we study the impedance of the system as functions of frequency and applied bias. The same three-electrode cell was used to record the impedance for frequency from 10^2 to 10^5 Hz for different biases. Figure 6.15 shows representative impedance spectra of the three samples in

Nyquist plot. For both sample A2 and B2, we have a linear region in low frequency followed by semicircle for higher frequency. The low frequency linear behaviour is generally characteristic of diffusion related impedance and is represented by a Warburg element. For sample C2, the linear region extends for the majority of the frequency range ending in a small curved portion. To analyse the impedance spectra, an equivalent circuit model was used to fit the experimental data. We could fit the impedance spectra of all three samples using a modified Randles circuit and extract the values of parameters for further investigation. The equivalent circuit used here is shown in Figure 6.15(b) inset.

The Randles circuit is one of the most widely used equivalent circuit models in electrochemistry[179]. At its simplest form, it consists of a resistance representing the electrolytic solution (R1) in series with a parallel combination of a capacitance representing the double layer (C1) and a Faradaic impedance made of a charge transfer resistance (R2) in series with a Warburg element accounting for the diffusion process. The Warburg element is a type of constant phase element (CPE) used to take into account the diffusion related Faradaic processes. The basic Warburg element has complex impedance of the following form:

$$Z_W = (1-j)\frac{W_R}{\omega} \tag{6.6}$$

The theoretical model of the simple Warburg element assumes unrestricted semi-infinite diffusion to a large planar electrode. We found a good fit to the experimental data using a finite diffusion length Warburg element describing limited thickness of the diffusion layer near electrode. The impedance of this element varies with frequency as:

$$Z_W = W_R \frac{coth((j\omega W_T)^{\alpha})}{(j\omega W_T)^{\alpha}} \tag{6.7}$$

W_T is related to the diffusion coefficient of the active species and the diffusion layer thickness[180]. Although for Warburg element, the exponent α should have a value of 0.5, corresponding to a 45 ° phase angle, we encounter deviations from this ideal behaviour. The linear low frequency region of the Nyquist plot was found to have slopes different from 45°. Figure 6.16 shows the values of the extracted charge transfer resistance and Warburg exponent for sample A2. The value of exponent α varies from 0.38 to 0.49 without any clear trend. The mean value of the exponent

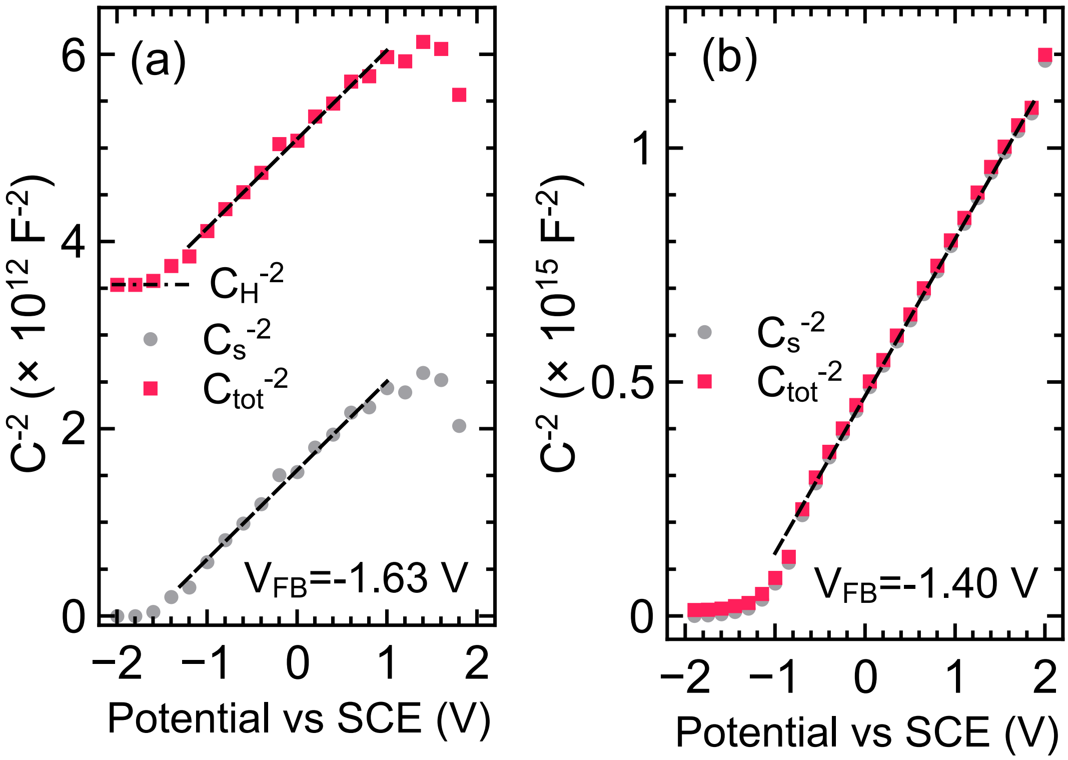

Figure 6.17: Capacitance of the electrochemical system of sample (a) A2 and (b) C2 depicted in Mott-Schottky plot. The solid squares represent the total capacitance and the solid circles represent the capacitance after removal of the Helmholtz layer contribution. The linear fits are according to Mott-Schottky equation.

α averaged over potentials for sample A2 is 0.44 and is 0.45 and 0.26 for samples B2 and C2. The deviation of the data from finite diffusion length Warburg element behaviour is attributed to the non-ideality of the rough porous electrode surface in contrast to the flat electrode assumed theoretically. We therefore classify this element as a CPE (represented by Q) of which the Warburg element is a special case.

Figure 6.16(b) shows the trend of the charge transfer resistance R2. As the potential becomes more negative, the value of charge transfer resistance decreases. This can be explained on the basis of a gradual charging of the surface states as the Fermi level is pushed upward towards the conduction band. A similar behaviour has been observed in case of n-type SiC in an aqueous electrolyte[181].

The capacitance element in our model represents the combined effect of semiconductor SCR, the contribution from surface states and contribution from the Helmholtz layer. Generally the Helmholtz capacitance is taken to be bias independent and the other two vary with the bias[182]. We have extracted the capacitance value by fitting the frequency dependent impedance with equivalent circuit for a number of biases. Figure 6.17 shows the Mott-Schottky plot of the extracted capacitance as a function of applied potential for sample A2 and sample C2. In Figure 6.17(a), the top graph (solid rectangles) represents the total capacitance. We can see the expected linear behaviour for an intermediate potential around -1 V to +1 V and deviations for potentials beyond that range. The epilayer shows the deviation only for the negative part. This is consistent with the CV data as such the linear Mott-Schottky trends comes in the non-Faradaic region of intermediate potentials and for charge transfer leading to oxidation and reduction reactions, we have a deviation. One can distinguish between the Faradaic and non-Faradaic potential regimes using chronoamperometry technique where the basal current values following voltage spikes remain similar for non-Faradaic process and show a staircase like increase in value for Faradaic charge transfer.

In typical cases where the Helmholtz layer capacitance is much larger than SCR capacitance, the Mott-Schottky equation is written as:

$$\frac{1}{C^2} = \frac{2}{e\epsilon_0\epsilon_r N_D A^2}(V - V_{FB} - \frac{K_B T}{e}) \tag{6.8}$$

In case the capacitances are comparable, or the latter is larger than the former, the Mott-Schottky equation is modified as:

$$\frac{1}{C^2} = \frac{1}{C_H^2} + \frac{2}{e\epsilon_0\epsilon_r N_D A^2}(V - V_{FB} - \frac{K_B T}{e}) \tag{6.9}$$

The filled rectangles depicting original data has a bias independent capacitance at the lower end of the potential in both cases. We attribute to the Helmholtz layer capacitance and separate it from the total capacitance value which is represented by filled circles. A significant difference is seen for the nanowall network sample but not for the epilayer sample for which the two curves nearly overlap. Using the x-intercept of the Mott-Schottky plot one calculates the flat band potential $\mathrm{V_{FB}}$ for a semiconductor/electrolyte system. In case of epilayer, $\mathrm{V_{FB}}$ is found to be -1.40 V which is a typical value for n-GaN according to literature reports[176],[175]. In case of nanowall network, the x-intercept for the original data is -5.5 V and for the corrected data is -1.63 V. Only the latter value is meaningful. This effect of Helmholtz layer capacitance in overestimating the flat band potential has been observed previously[182]. The corrected value of $\mathrm{V_{FB}}$ for nanowall network is more than that of epilayer.

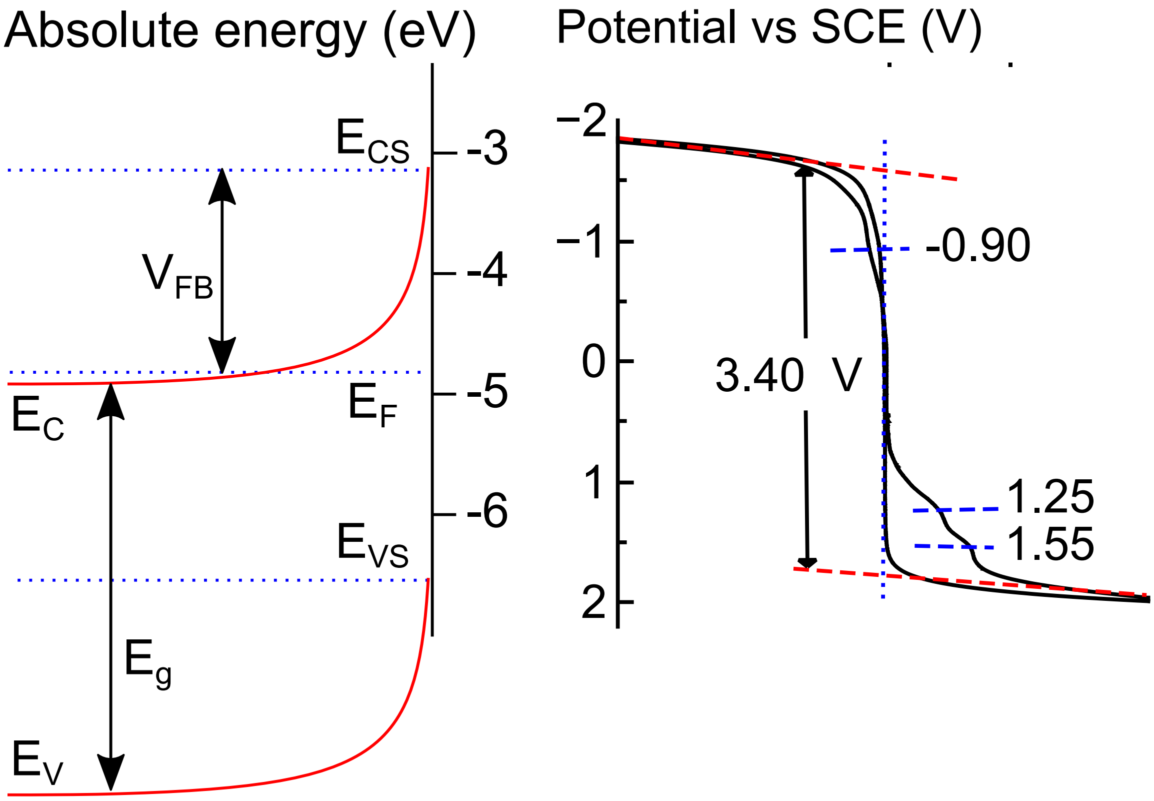

Figure 6.18: (Left) schematic band structure depicted alongside (right) cyclic voltammogram for sample A2. The positions of conduction and valence band edges are determined by a linear fit of the rising cathodic and anodic currents beyond the onset potential. The degree of band bending is determined from value of flat band potential.

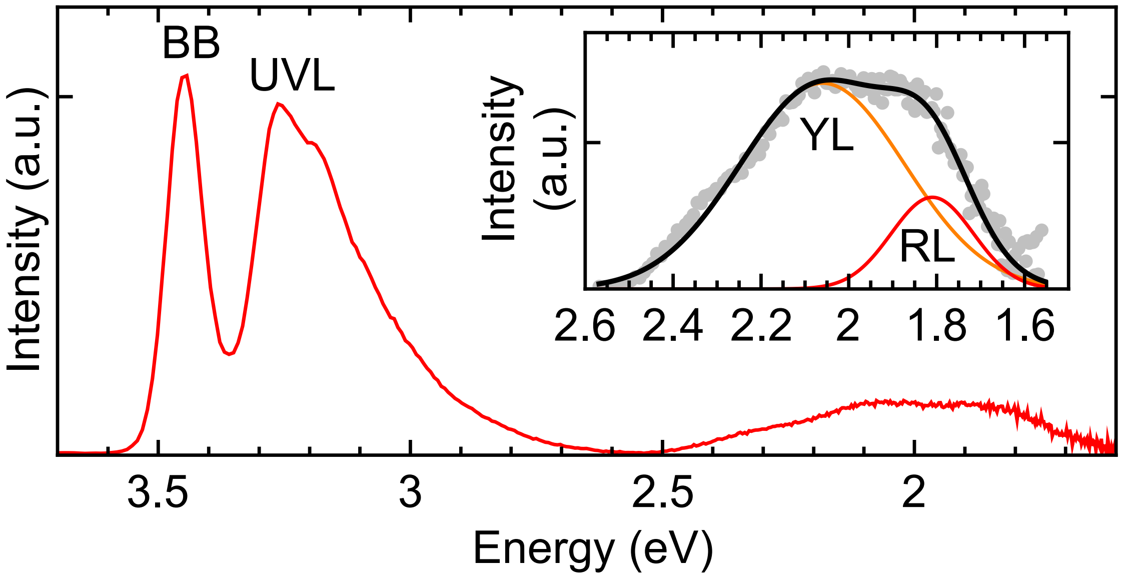

Figure 6.19: Low temperature photoluminescence spectrum of sample A2 at 12 K showing NBE and defect related peaks. The inset shows the defect related peak deconvoluted into red and yellow luminescence bands.

To investigate the electronic structure further, we obtain photoluminescence spectra of sample B2 at 11 K, which is shown in Figure 6.19. The spectra is acquired at low temperatures to better identify the defect related emissions. A number of features are seen in Figure 6.19, with the highest intensity peak being the near band edge (NBE) emission attributed to band-to-band transition. The position of the NBE peak is at 3.45 eV which shifts to 3.40 eV at room temperature (not shown). The second highest intensity peaks are categorised as UV luminescence with a peak at 3.26 eV. Next, we have a broad defect related luminescence, whose shape necessitated fitting by two Gaussian peaks. The deconvoluted Gaussian peaks are centred at 2.1 and 1.83 eV corresponding to yellow (YL) and red luminescence (RL). These features are well known for both doped and undoped n-GaN although their attribution to specific defects are still a matter of debate.

To infer more about the energy levels which are involved in the radiative transitions giving rise to features in the PL spectra of sample B2, we consider its CV again, in some detail. The band edge positions are determined by linear extrapolation of the rapidly rising (or falling) current to the baseline. The underlying concept being that the large density of states of the band edges provide carriers leading to high current values. For sample B2, we find that the CBM and VBM correspond to potential of

-1.65 V and +1.75 V with respect to SCE. Similar procedure to extract the HOMO and LUMO levels of molecules are well established. Next, we focus on the regions below the band edges where significant current flows (see Figure 6.13). We notice that small local maxima (minimum for cathodic current) exist in the current values. For surface state mediated Faradaic charge transfer, a peak in the DOS of a particular defect energy level translates to a peak in the current values. Similar procedures to evaluate the energetic positions of deep levels have been performed for semiconductor nanowire arrays[183] and nanocrystals[184]. We have located the local current extrema at E_1= -0.90 V, E_2= +1.25 V and E_3= +1.55 V, which correspond to energy level 0.75 eV below CBM, 0.5 eV above VBM and 0.2 eV above VBM respectively. These results have been depicted in Figure 6.18.

For GaN epilayer we observe a sharp extremum of cathodic current at 0.5 eV below the CBM. According to DFT studies, for polar GaN surface, there is a significant DOS originating from Ga dangling bonds (DB) which appears 0.5-0.7 eV below CBM[172]. This particular Ga DB energy level exists for both polar and non-polar surfaces and for both moderate or high Ga/N growth conditions. Although one needs to perform similar calculations for particular semi-polar GaN surfaces which bound nanowall network, it is possible that the E_1 level 0.75 eV below CBM may also arise from the Ga DB states.

The attribution of different observed luminescence bands in doped and undoped GaN to specific defects remains an open question. For example, V_{Ga} or its complex e.g. $V_{Ga}O_N$ were considered the most probable candidates for explaining the widely observed YL band in n-GaN. However, modern calculations predict that C_N or C_NO_N are more likely to provide the acceptor level required for YL transition[147]. The UV luminescence band appearing at about 0.2 eV below the NBE emission is attributed to a shallow donor-shallow acceptor transition at low temperatures and CB to shallow acceptor transition at higher temperatures. The shallow donor involved in the UV luminescence could be O_N which has an ionisation energy of only 0.03 eV and can be readily incorporated in GaN[43]. The carbon is an amphoteric impurity defect and has two thermodynamic levels: 0/- at $\sim$ 0.8-1.0 eV above VBM and +/0 at 0.3±0.1 eV above VBM[185] which have been detected experimentally. A transition from CBM to C_N -/0 state may produce YL. Although we do not observe any states near E_V+1 eV involved in electrochemical charge transfer, but We do observe energy level E_2 consistent with C_N 0/+ level. This defect level at E_3 could be responsible for the observed UVL. Carbon is a known impurity for MBE grown GaN along with oxygen. Especially under low growth temperatures and nitrogen rich conditions, significant concentrations of carbon (up to 8×10^{19} cm^{-3}) can be incorporated in GaN[147],[186],[187]. The RL is caused by transition from a shallow donor level to a deep acceptor level, whose identity remains unknown at this point. Further theoretical calculations are required to identify the origin of the E_2 state. Figure 6.18 combines the cyclic voltammetry and impedance spectroscopy results for nanowall network to provide a schematic view of the band structure.

6.2.2.3 Conclusions

In summary, we have carried out CV and impedance spectroscopy studies of GaN nanowall network along with photoluminescence spectroscopy to investigate the electronic structure. In contrast to flat epilayer, nanowall network showed anodic current explained on the basis on electron tunnelling from VB to CB providing holes to the surface. A non-ideal charge transfer from GaN to electrolyte was attributed to presence of surface states. A photoresponse study of nanowall network indicated population of photogenerated carriers to be smaller than the existing population resulting in a meagre change of current. Impedance spectra were fit using a modified Randles circuit. The deviation of the value of exponent of CPE from expected value was explained by non-ideal morphology of the highly porous electrode. Mott-Schottky plots were produced from capacitance extracted from the fit model. The contribution of Helmholtz layer capacitance was separated and the flat band potential from the corrected data was -1.63 V for nanowall network and -1.40 V for epilayer. Detailed analysis of local extrema of anodic and cathodic current for nanowall network indicated the presence of energy levels at E_C-0.75, E_V+0.5 and E_V+0.2. The first level was attributed to Ga dB and the last one to C_N defect acceptor level. The presence of C_N can explain the UV and yellow luminescence observed in low temperature PL spectra of nanowall network. Theoretical calculations taking into account specific morphology and growth conditions of nanowall network are required to further elucidate the observed energy levels.

6.3 Electrical transport properties

The electronic band structure, through its effect on carrier effective mass and thereby mobility influences the electrical transport property of semiconductor materials. Electrically active point and extended defects provide charge carriers and also determine the sample conductivity through carrier scattering. Measurement of resistivity and Hall coefficient as a function of temperature and magnetic field contains significant amount of information regarding carrier type, density, and predominant scattering mechanism. In this section, we perform magnetotransport measurements to gain insight into the underlying electrical transport mechanism of the GaN nanowall network.

6.3.1 Experimental details

A set of five samples, A3, B3, C3, D3, and E3, was grown using PAMBE for the study described in this section. The base pressure of the MBE system was 3×10^{-11} Torr. C-plane sapphire was used as the substrate, which was thoroughly cleaned before deposition by degreasing with organic solvents - acetone and propanol, rinsed with de-ionised water and then blow-dried. Thermal degassing of the substrate was done inside the MBE preparation chamber at 850 °C for 30 minutes. The substrate temperature was fixed at 630 °C for all samples. Ga flux and nitrogen flow were varied to deposit samples A3-E3, whose details can be found in Table 6.2. In situ RHEED was used to confirm atomic cleanliness of substrate through observation of sharp Kikuchi patterns and to monitor growth. After deposition, several ex-situ characterisation techniques were employed to study the samples as follows. FESEM was used to study the morphology and measure film thickness. HRXRD was used to determine structural properties and confirm the epitaxial nature of growth. Temperature and magnetic field dependent Hall and resistivity measurement were carried out for electrical characterisation.

Table 6.2: Growth parameters and carrier concentration n

Sample	Ga flux BEP ($\times10^{-7}$ Torr)	N_2 flow (sccm)	n ($\times10^{18}$ cm^{-3})
A3	4.8	4.5	295
B3	4.5	4.5	214
C3	2.5	4.5	138
D3	3.6	3.0	78
E3	5.5	2.5	1.91

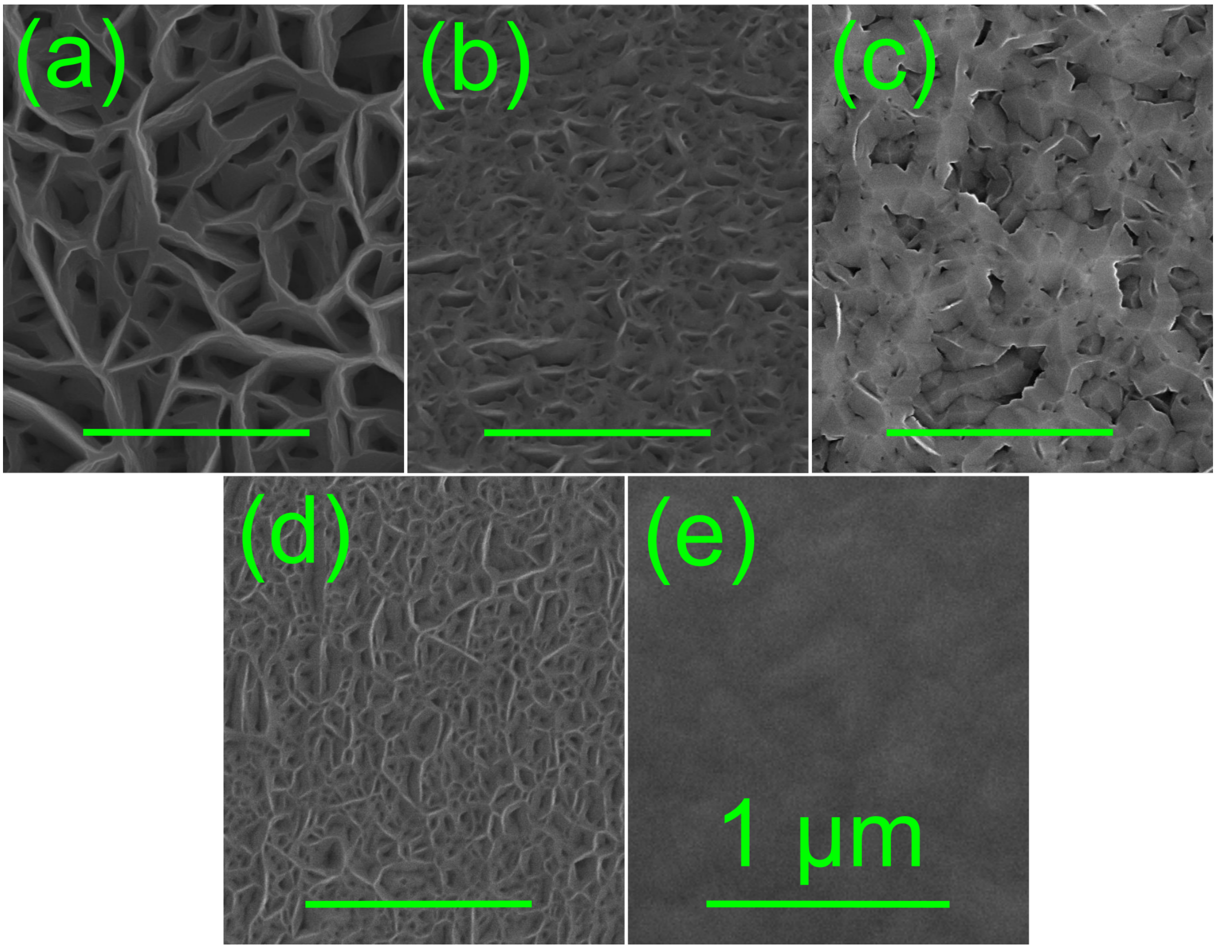

Figure 6.20: FESEM images of samples (a) A3, (b) B3, (c) C3, (d) D3, and (e) E3. The scale bar corresponds to 1 μm.

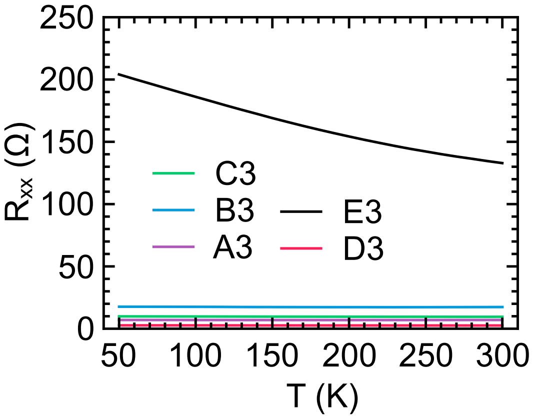

Figure 6.21: Temperature variation of longitudinal resistance for samples A3, B3, C3, D3, and E3.

6.3.2 Results

The variation in Ga and N fluxes led to a slight variation in sample morphology, as seen in Figure 6.20. The morphology of sample A3 consists of a network of tapered nanowalls whose in-plane orientations are random and the lateral thickness of the individual walls ranges from few tens of nanometres to 100 nm, which we term as nanowall network. Samples B3, C3, and D3 are also considered to be nanowall networks, albeit with less porosity and sample E3 has a compact surface.

The room temperature Hall measurements of Table 6.2 show approximately two orders of decrease in carrier density from samples A3 to E3. The corresponding temperature dependence of resistivities of the samples is shown in Figure 6.21. It is clearly seen that samples A3, B3, C3 and D3 have resistances that are nearly independent of temperature, whereas sample E3 exhibits a typical semiconductor behaviour. Temperature independence of resistivity is a signature of degenerate semiconductors. For wurtzite GaN, the density of states at conduction band minimum is reported to be about $2.23 \times 10^{18} cm^{-3}$, therefore based on the Hall measurement data, samples A3 to D3 are expected to be degenerate. However it is known that with an increase in doping concentration, the formation of compensation centres increases, which reduces the mobility by increasing scattering, ultimately limiting the conductivity[188].

To have a closer look at the temperature dependence of resistivities of the samples, we plotted the resistivity-temperature curve separately (Figure 6.22). Samples A3, B3 and C3, show a minimum of resistivity as temperature is varied, though the relative change is small. It is also seen

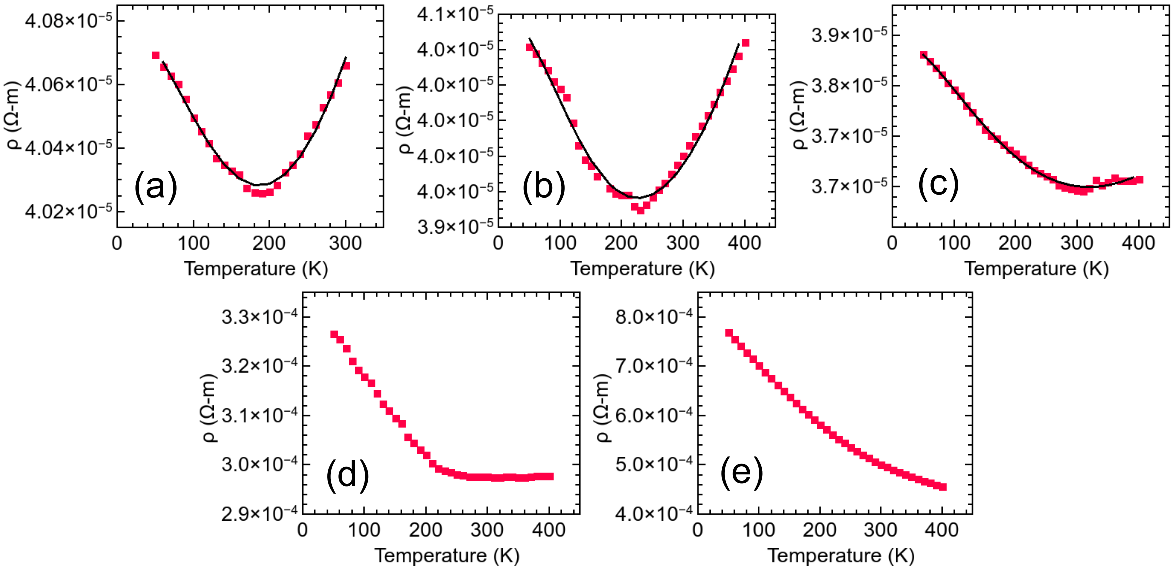

Figure 6.22: Temperature variation of resistivity for samples (a)A3, (b)B3, (c)C3, (d)D3, and (e)E3. The solid line fits to the experimental data are according to equation (6.12).

that the position of minimum for sample A3, B3 and C3 shifts from 190 K to 230 K to 310 K, respectively. A look at Table 6.2 indicates that as the carrier concentration reduces, the position of the minimum (T_{min}) shifts to higher temperatures. The change in the sign of temperature coefficient of resistance (TCR) with temperature, similar to the present case, has been observed in several material systems such as doped and undoped semiconductors[189],[190], dilute magnetic semiconductors[191], metal and metal alloys[192], among others. Additionally, in several other reports involving doped ZnO,[193],[194],[195], it was reported that the resistivity-temperature curve shows a minimum which was explained by an interplay of carrier scattering, hopping conduction and thermal activation of electrons into conduction band. A change in transport mechanism from hopping to band conduction led to a change in sign of TCR in these systems. Das et al. in their study of Al: ZnO also found that the temperature corresponding to the resistivity minimum, T_{min} decreases with the increase in level of Al doping[193]. Such shift in T_{min} was attributed to the decreased donor activation energy due to the enhanced electron concentration. The electrical transport dominated by carrier activation is gradually replaced by metal like carrier scattering, pushing the cross-over temperature T_{min} to a lower value. In these last cases the nature of the carrier transport changes with temperature.

Since A3, B3, and C3, do not exhibit any significant change in resis-

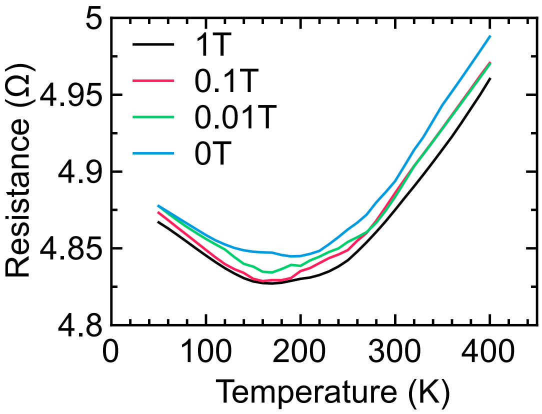

Figure 6.23: Temperature variation of longitudinal resistance for sample A3 with different magnetic fields of magnitude 0, 0.01, 0.1, and 1 T.

tivity over the entire experimental range of 50 K to 400 K, thus any major contribution of thermal activation of carriers and change in behaviour from semiconductor-like to metal-like is improbable. Nevertheless, various carrier scattering effects are expected to take part in defining overall transport property. A disordered metallic system is characterised by carrier localisation effects due to scattering from the defects causing disorder in the lattice and enhanced electron-electron interaction effects. Usually, stronger the disorder, stronger is the carrier localisation and more is the enhancement of resistivity. These effects are often clubbed under an umbrella term quantum correction to conductivity (QCC)[196]. A weak localisation (WL) often manifests as a minimum in the resistivity-temperature graph and also by the appearance of a cusp in the magnetoresistance of the sample. To analyse our data, we use the following expression of resistivity which includes contributions due to lattice (phonon) scattering, weak localisation, electron-electron coulomb interaction effects, and several temperature independent factors clubbed under a constant term.

$$\rho = \frac{1}{\sigma_0 + a1T^{p/2} + a2T^{1/2}} + bT^2 \tag{6.10}$$

Here, σ_0 encompasses the temperature independent terms, $a1T^{p/2}$ and $a2T^{1/2}$ are related to the weak localisation and electron-electron interaction effects and bT^2 is related to high temperature scattering[197]. In general, the QCC terms are small such that $a1T^{p/2} + a2T^{1/2} << \sigma_0$.

The fitting of the conductance data with eqn(6.10) as shown in Figure 6.22 showed that the WL term dominates the QCC and a very similar goodness of fit was achieved by omitting the electron-electron interaction effects term altogether.

The parameter p in the equation(6.10) is very important, as it contains information regarding the underlying interactions. With an increase in temperature, the self-interference of electronic wavefunction, which leads to WL, is diminished and eventually destroyed by inelastic scattering. The inelastic scattering time τ_{in} has two major components:

$$\frac{1}{\tau_{in}} = \frac{1}{\tau_{e-e}} + \frac{1}{\tau_{e-ph}} \tag{6.11}$$

which correspond to electron-electron and electron-phonon interactions and has the following temperature dependence:

$$\frac{1}{\tau_{in}} \sim T^p$$

The parameter p generally takes values from 2 to 4. When the dominant inelastic scattering is due to electron-electron interaction, p takes value around 2, whereas it takes a value 3-4 for electron-phonon inelastic scattering. The values of p corresponding to the best fit of eqn. 6.10 to the data of sample A3, B3 and C3 are 3.99, 3.98 and 3.57 respectively. Authors such as Saha et al. and Nistor et al. reported a value of approximately 3 for their ZnO samples under study[189],[197]. Sett et al. following an analysis of low temperature conductivity data of Ge nanowires by WL theory, reported a p value around 4[198]. They attributed the de-phasing process of the electrons to electron-phonon interactions. Based on this, the electron-phonon interaction can be assumed to play the dominant role in the inelastic scattering of electrons. It is to be noted that samples A3 and B3 have a similar value of p and close placed T_{min} values whereas C3 has a higher value of T_{min} and shows a more semiconductor like behaviour unlike A3 and B3. The p value of C3 is closer to the more commonly reported values of p in semiconductors. Here we note that a seemingly slight change of carrier concentration is able to change the electron scattering mechanisms. That and the somewhat unusually high value of p in samples A3 and B3 are worthy of further investigation.

To check the validity of our analysis of the resistivity-temperature data, we carry out magnetoresistance measurements of samples A3, B3 and C3 at 50 K temperature. Magnetic field related de-phasing of electron wavefunction can weaken and eliminate the weak localisation effect. Thus, with an increase in magnetic field, the extra contribution to resistivity from localisation should decrease and we should observe a negative magnetoresistance (NMR). Negative and positive magnetoresistance are known in literature to be signatures of weak localisation and weak anti-localisation effects respectively[199],[200]. Figure 6.23 shows the longitudinal value of resistance R_{xx} as a function of magnetic field at 50 K temperature for sample A3. The negative magnetoresistance clearly seen here for sample A3 is also exhibited by samples B3 and C3 (not shown here).

Formation of 2D electron gas

In our previous investigations of electrical transport properties of the GaN nanowall network, we have observed a number of properties which are exciting from both theoretical and application point of view. The GaN nanowall network exhibits a very high mobility of the order of 10^4 cm^2/Vs, despite its high carrier concentration, high coherence length and even an induction of superconductivity in the nanowall when it is in contact with a traditional superconductor[201][37]. Formation of a two-dimensional electron gas (2DEG) was revealed from experimental and computational studies which is expected to significantly influence the carrier transport[2]. The 2DEG is formed by carrier repulsion from polarisation induced charges of the bounding surfaces of the nanowall network. Solution of coupled Schroedinger-Poisson equations for the wedge shaped GaN materials shows the concentration of carriers near the central plane of the nanowall which is shown in Figure 6.24 reproduced from reference[2]. This 2DEG provides a fast conducting channel for the carrier electrons while encountering reduced scattering akin to traditional high mobility electronic devices made from semiconductor heterostructures. In case of nanowall network, this is achieved without the complex fabrication steps.

We have performed a study of magnetotransport properties of GaN nanowall network in high magnetic field up to 15 T. In this study, we have confirmed the presence of weak localisation[202]. Figure 6.23 shows the resistance as a function of temperature for different magnetic fields of 0, 0.01, 0.1 and 1 T, and shows that resistance decreases with an increase in magnetic field. Since the dephasing nature of magnetic field destroys the interference underlying the weak localisation, it is interesting to note that this weak quantum mechanical behaviour is found to survive at significant magnetic field. Secondly, the majority of the literature reports of observation of weak localisation occur at cryogenic temperatures. However, here

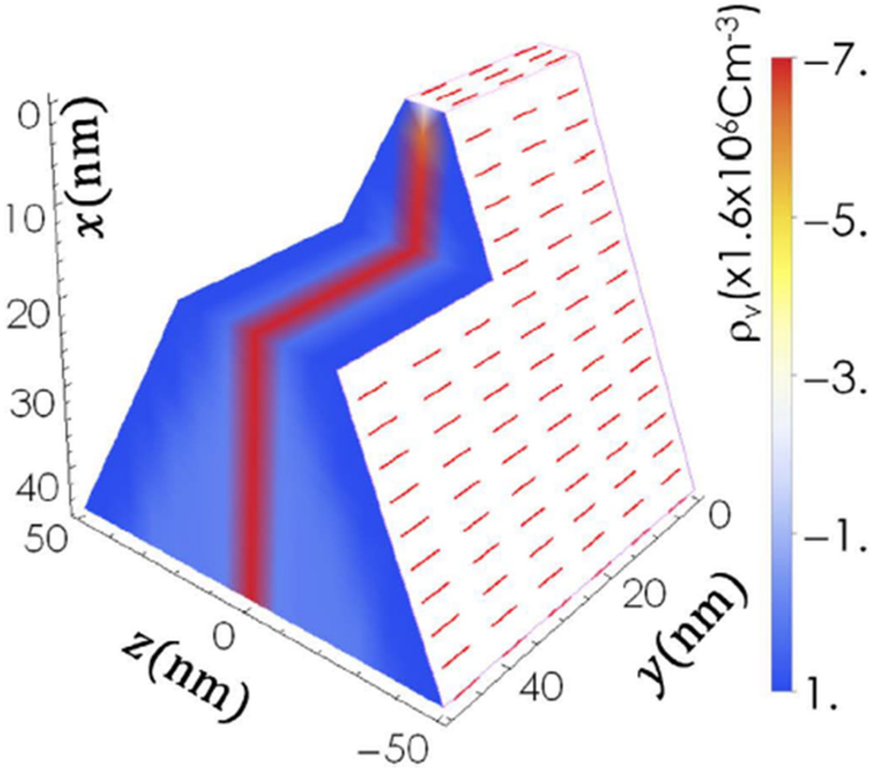

Figure 6.24: Calculated charge density distribution inside wedge shaped nanowall network depicting formation of 2DEG inside the nanowall[2]. Reprinted with permission.

we can observe the negative magnetoresistance at high temperatures also, as seen in Figure 6.23.

The persistence of the weak localisation at high temperatures can be attributed to the peculiar morphology of the nanowall network. The in-plane random orientation of the nanowalls ensures that whether the magnetic field is applied parallel or perpendicular or at any intermediate angle to the sample substrate, it can never be perpendicular to all the nanowalls. This is shown in Figure 6.25. Thus on average, only a fraction of the magnetic field is effectively applied to the carrier electrons concentrated near the central plane of the nanowalls, ensuring the persistence of WL at high magnetic fields. The high temperature persistence of WL needs further investigation.

Sample	$l_\phi(nm)at50K$	$l_\phi(nm)at300K$
A3	19.9	18.3
B3	57.5	45.1
C3	63.3	59.2

Table 6.3: Phase coherence length of samples at 50 K and 300 K calculated using eqn. 6.12

The phase coherence length, which is the distance over which the elec-

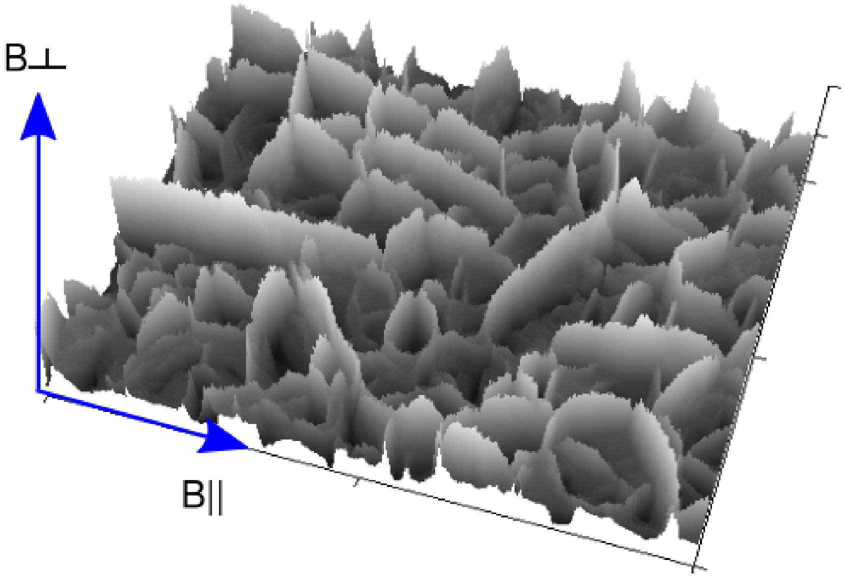

Figure 6.25: AFM image topographic data plotted in 3D to depict the orientation of applied magnetic field with respect to individual nanowalls.

tron maintains its phase information essential for quantum mechanical interference has been calculated for samples A3, B3, and C3 by fitting the well-known Hikami-Larkin-Nagaoka (HLN) equation (6.12) to the magnetic field dependent conductance. The Figure 6.26 shows a representative conductance data for sample A3. The solid fit to the experimental data is using the HLN equation.

$$\Delta G = AN_{ch}[\psi(0.5 + \frac{\hbar}{4eBl_{\phi}^{2}}) - ln(\frac{\hbar}{4eBl_{\phi}^{2}})] \tag{6.12}$$

Table 6.3 shows the extracted values of the phase coherence length for the chosen samples. The two observations readily apparent from this table is that the coherence length reduces with temperature as per expectation and that the coherence length increases with a decrease in carrier concentration from A3 to C3. This provides an avenue to tune the coherence length. Previously, our group has reported coherence lengths as large as several tens of microns for GaN nanowall network which is sufficient for practical spintronic device applications[2].

6.3.3 Conclusions

In summary, GaN nanowall network samples were grown by PAMBE by optimizing the growth parameters. The grown samples had an electron

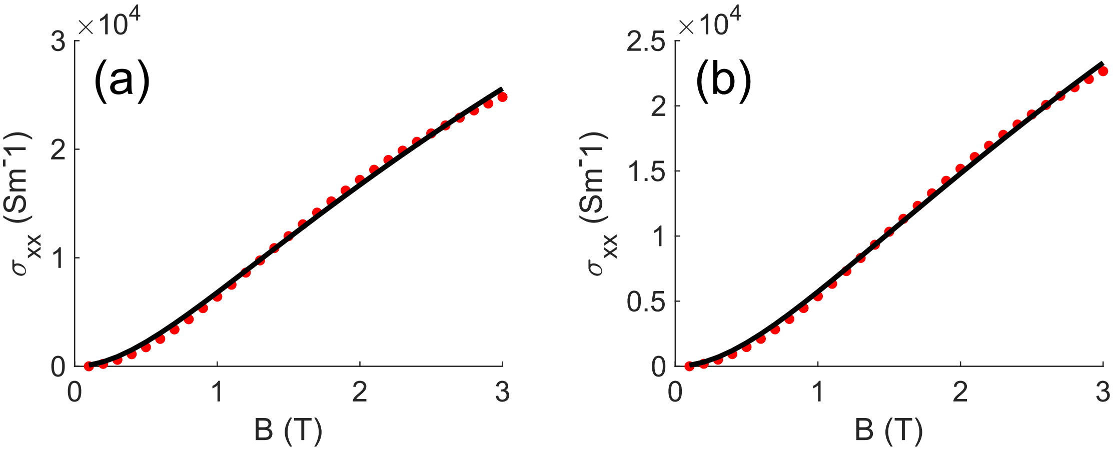

Figure 6.26: The longitudinal conductivity of sample A3 at (a) 50 K and (b) 300 K. The solid line represents a fit of equation (6.12) to the experimental data.

density ranging from 3.0×10^{20} cm^{-3} to 1.9×10^{18} cm^{-3} for compact reference sample. The nanowall network samples showed nearly temperature independent resistivities indicative of a degenerate semiconductor whereas the compact sample showed typical semiconductor behaviour. The high electron density nanowall network samples show a shallow minimum in the resistivity-temperature graph although the relative change is small, also the position of the minimum is found to vary with the electron density. The resistivity data was fitted by taking into account the phonon related scattering, weak localisation and other factors and weak localisation was found to be the dominant factor of the quantum correction to conductivity. From the analysis, the de-phasing mechanism of the electrons was found to be dominated by electron-phonon scattering. Magnetoresistance data showed a negative magnetoresistance in line with the presence of weak localisation in the system. The weak localisation phenomenon was found to persist even at room temperatures and at significant magnetic field and the latter was explained on the basis of the particular morphology of the nanowall network which prevents magnetic field to be applied perpendicularly to all the individual nanowalls. The phase coherence length extracted from the field-dependent conductance data shows that it increases with reducing carrier concentration.

6.4 Magnetic properties

Numerous experimental reports of observation of magnetic order in typically non-magnetic semiconductors often have two things in common, defects and reduced dimensions. Although conventional magnetism is associated with unpaired d and f electrons with highly localised magnetic moments, it has been found from theoretical calculations that 2p electrons of second-row elements such as nitrogen and oxygen are also fairly localised, and unpaired electrons in acceptor states can give rise to local magnetic moments. An interesting duality, in this case, is more extended tails of the 2p electronic wavefunction than 3d and 4f electrons making long-range magnetic coupling possible if the concentration of such acceptor defects is sufficient[203]. Experimentally, Ga vacancy induced ferromagnetism has been observed in PAMBE grown GaN thin films on sapphire that were found to be Ga deficient based on XPS measurements[204]. Nitrogen vacancies can also generate local magnetic moment in nitride nanostructures and the same has been reported for PVD grown AlN whiskers[205]. Reduced dimensions play a significant role in this case, as the formation energy of both Ga and N vacancies are less on the surface compared to the bulk; thus, nanostructures with a high surface-to-volume ratio can have a larger concentration of such native defects[206]. Additionally density functional theory calculations show that quantum confinement related size effects can enhance the spin polarisation in nanostructures[48].

The experimental studies so far show that the nanowall network has a degenerate carrier concentration which has high mobility and quantum mechanical effects influencing the carrier transport. The presence of localised defects, delocalised carriers, low-dimensionality of the material and observable effects of magnetic field on the carrier transport makes the nanowall network an interesting case study for d^0 magnetism often found in thin films and nanostructures in otherwise non-magnetic semiconductors. In this section, we perform several experiments to investigate the magnetic properties of the GaN nanowall network and its origin.

6.4.1 Experimental details

GaN samples of different morphologies were studied to investigate the morphology dependence of magnetisation. Sample A4 is a commercially obtained MOCVD grown 3 μm thick GaN film on c-sapphire. Sample B4 and C4 were grown in PAMBE using c-sapphire as substrate. A characteristic RHEED pattern with Kikuchi lines indicated that the substrates were atomically clean. Sample B4 was grown with Ga flux $2.34\times10^{14}cm^2s^{-1}$ and N2 flow of 4.5 sccm. Sample C4 was grown with Ga flux $4.46\times10^{14}cm^2s^{-1}$

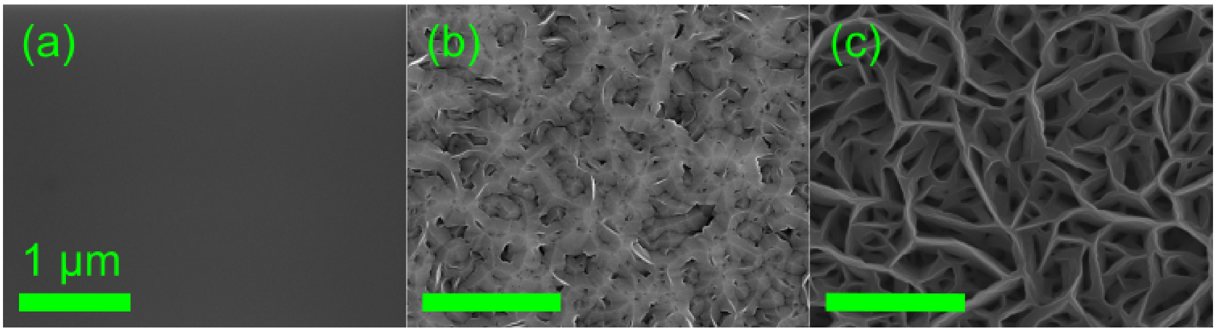

Figure 6.27: FESEM images of samples (a)A4, (b)B4, and (c)C4. The scale bar corresponds to 1 μm.

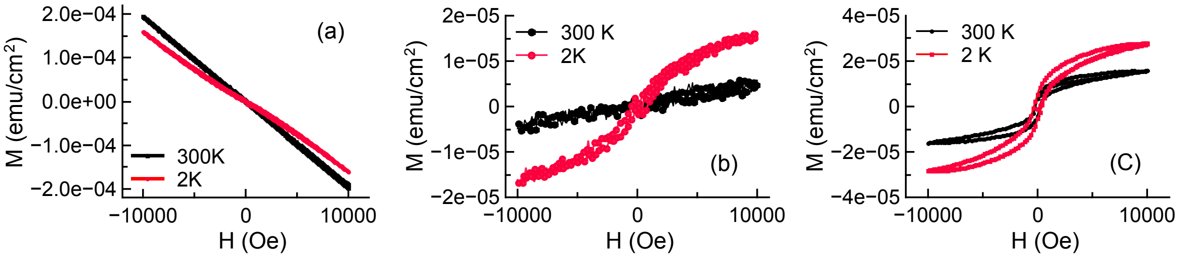

Figure 6.28: Field dependence of magnetisation for samples (a)A4, (b)B4, and (c)C4 at 2 K and 300 K temperature.

and N_2 flow of 8 sccm.

To study the morphology of the samples, FESEM and AFM were performed supplemented by HRTEM for high-resolution imaging. Magnetic force microscopy was used to observe the distribution of the magnetic moment in the sample. For magnetic and transport measurements, superconducting quantum interference device (SQUID) and a physical property measurement system (PPMS) were used. Utmost care has been taken during sample handling, including the use of only non-metallic tweezers, to rule out contamination as those may lead to false-positive signals.

6.4.2 Results

The plan-view FESEM images of the samples are shown in Figure 6.27. Sample A4 is highly flat, B4 has intermediate roughness and C4 is the highly porous nanowall network sample. The thickness of A4 is about 3 μm and that of B4 and C4 are about 1 μm.

The SQUID measurements of magnetisations of the samples as a function of the magnetic field have been performed. Since the sapphire substrate is diamagnetic and due to its larger thickness dominates over the GaN signal, M-H data of bare sapphire substrates have been acquired sep-

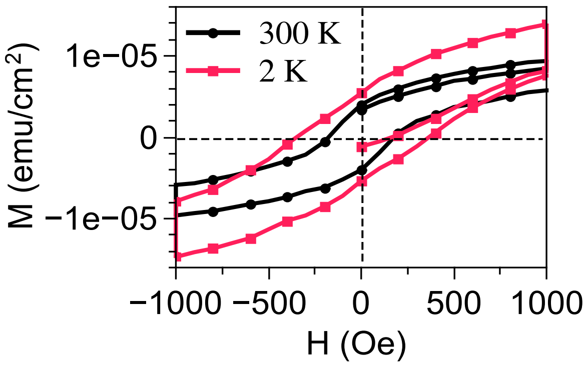

Figure 6.29: Field dependence of magnetisation for samples A4 in low magnetic field regime showing the magnitude of remanent magnetisation and coercivity at 2 K and 300 K.

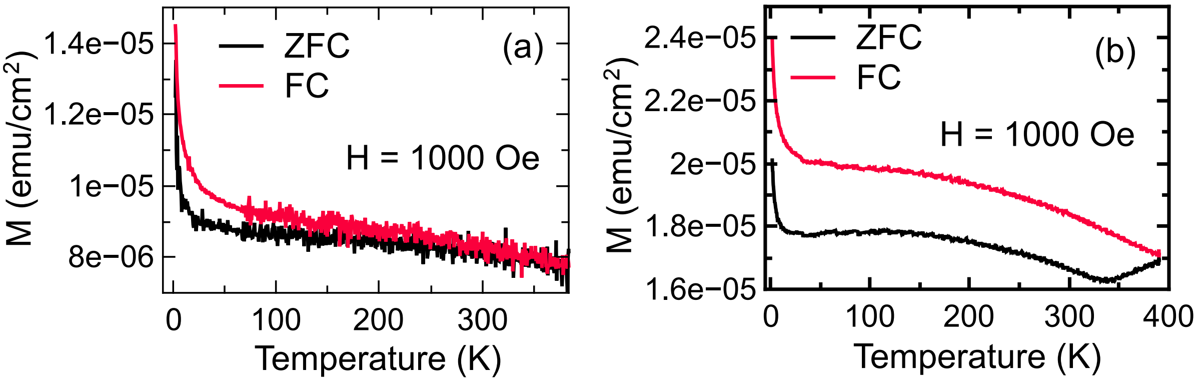

Figure 6.30: Temperature dependence of field cooled (FC) and zero field cooled (ZFC) magnetisation for samples (a)B4 and (b)C4. Applied magnetic field for FC measurements is 1000 Oe.

arately and its contribution has been subtracted from all 3 samples. Figure 6.28 shows the resultant M-H data taken at 2 K and 300 K.

The data for sample A4 is trivial and shows diamagnetism as expected from bulk GaN. Sample B4 interestingly shows a paramagnetic behaviour at room temperature, while at 2 K the M-H curve is 'S' shaped, and the hysteresis nature can be seen. The curve is non-saturating, indicating the presence of paramagnetism as was also seen at room temperature. Sample C4 shows an unmistakable hysteresis loop at both low (2 K) and room temperature (300 K). The Figure 6.29 shows a close-view near the zero field region. The coercivity has been roughly estimated as being 175 Oe at 300 K and 365 Oe at 2 K. As samples B4 and C4 showed ferromagnetic behaviour, we carried out further studies on these samples.

Figure 6.30 shows the temperature dependence of magnetisation for samples B4 and C4. The clear separation between the top curve corresponding to field cooled (FC) measurement and the bottom one corre-

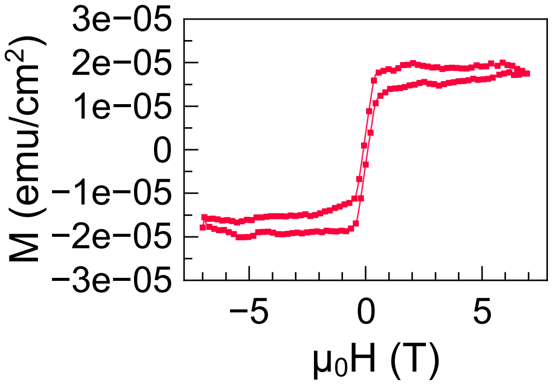

Figure 6.31: Field dependence of magnetisation for sample C4 at 370 K temperature.

sponding to zero field cooled (ZFC) measurement, is indicative of a remanent magnetisation. For B4, the two curves are non-coincident at lower temperatures, and explains why the B4 hysteresis behaviour was only seen at low temperature and not at 300 K. Interestingly for C4, the two curves branch out right from the maximum operating temperature of the SQUID instrument ($\sim$ 390 K). For both samples the magnetisation blows up near the low temperature limit.

To finally establish whether the Curie temperature (T_C) for the nanowall network is higher than room temperature, as would be required for any potential practical applications, we carry out M-H measurement for C4 at 370 K. Figure 6.31 shows the M-H data. As we can see in Figure 6.31, although the data is highly noisy as expected from a sample with small moment at high temperatures near the machine limit, nevertheless some hysteresis behaviour is present, although not as well behaved as seen in Figure 6.28 for room temperature. This shows that the Curie temperature for nanowall network is higher than 370 K which makes it a candidate for practical device applications.

Since field and temperature-dependent magnetisation data indicate that the nanowall network sample is ferromagnetic at room temperature, we carry out microscopy studies to understand the distribution of magnetic moment with respect to the morphology of the film. Figure 6.32(A) shows the AFM image of the nanowall network sample taken in a (2μm$\times 2\mu$m) region depicting its highly porous nature. Figure 6.32(B) shows the high resolution TEM image in cross sectional view. This figure shows that the tip region of the nanowall is very sharp, close to 5-10 nm at the apex. This value is comparable to the excitonic Bohr radius of GaN (3 nm) and sample is expected to show quantum mechanical size quantisation effects. The inset of Figure 6.32(B) shows the atomic scale image and provides additional clear evidence supporting the single crystalline nature of nanowall.

Figure 6.32(C) show the MFM image of the nanowall network sample. The topographical contributions to the tip deflection have been appropriately taken care of and the image only depicts the magnetic interactions between the tip and the sample. The MFM phase image is shown here rather than the amplitude as it is known to improve signal/noise ratio. It can be seen from MFM image that the magnetic moments are concentrated near the tip region of the nanowalls. To get a rough idea about the spatial extent, we zoom in on a wall portion marked in Figure 6.32(C) and perform a line profile along the marked line. The profile is presented in inset of Figure 6.32(D). It can be estimated that most of the moment is concentrated in width of about 30 nm. Thus, looking at the TEM and MFM data, we infer that the magnetism of the nanowall network is contributed mostly by the apex regions of the nanowall and might have a quantum mechanical origin.

The observed non-uniformity of the distribution of the magnetic moment led us to investigate whether the magnetic properties of GaN nanowall network are isotropic. To investigate this, we apply magnetic field in two different orientations with respect to the sample and carry out MFM study. Figure 6.33 shows the room temperature magnetisation data as a function of magnetic field in two different geometries - parallel and perpendicular to film substrate. It is seen that saturation magnetisation is higher, when applied field is parallel to growth direction, thus suggesting that c axis is the easy axis of magnetisation. This observed anisotropy also serves to finally rule out any sample contamination with magnetic impurities as those are expected to result in an isotropic response.

Summarising the observations made so far, the GaN nanowall network shows an high $\mathrm{T_C}$ ferromagnetic behaviour that is concentrated near the central part of the wall. It is anisotropic and morphology dependent. The sample B4 which can be thought of as a network of blunt tip walls and with material in the voids, exhibits a lower $\mathrm{T_C}$ and lower $\mathrm{M_S}$. In[207] the authors have shown through theoretical calculations that both the electron concentration and the mobility of the 2D channel decreases as the semi-vertical angle of the wedge increases. In our case, the observation that magnetic moments are concentrated in the region where the 2DEG exists, and also the fact that the saturation magnetisation is higher when magnetic field is applied along c direction, ie. parallel to the 2DEG, leads us to

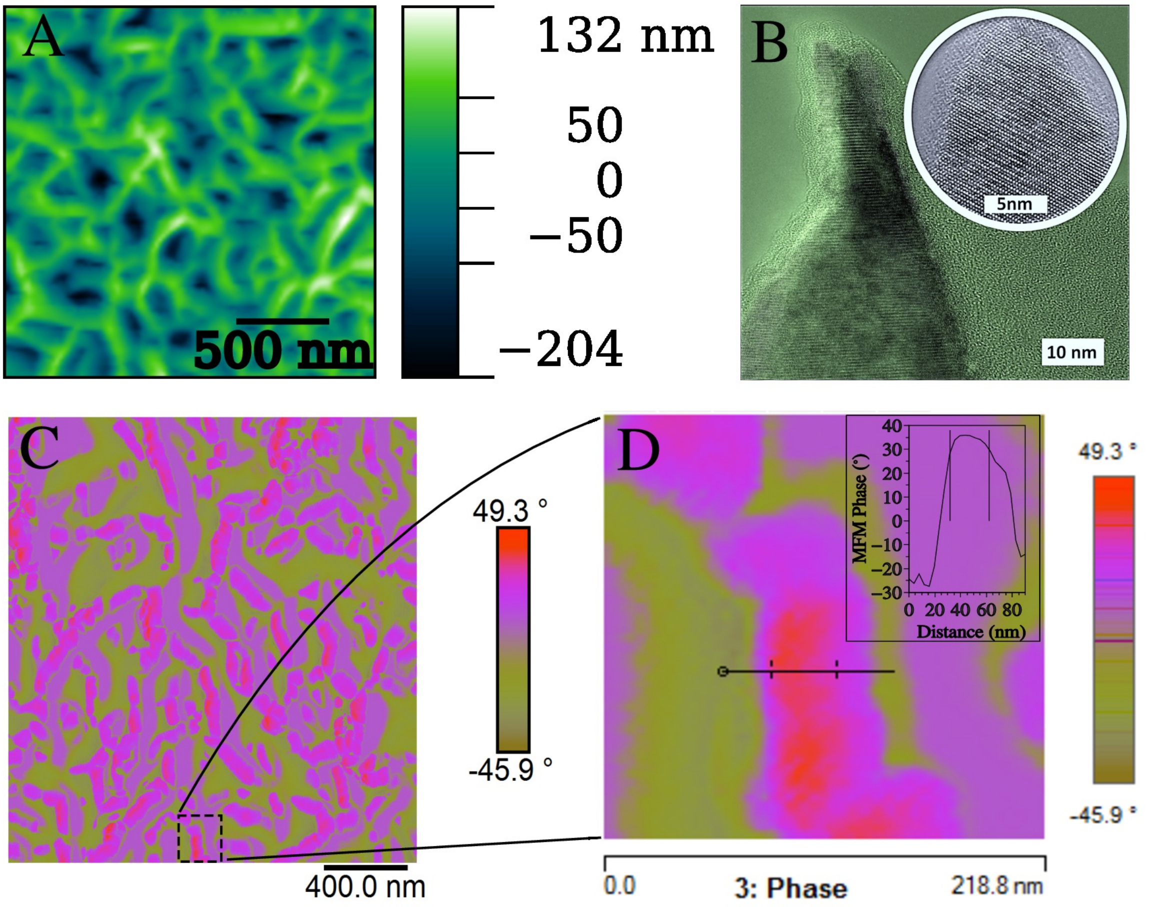
A
500 nm
132 nm
50
0
−50
−204
B
5nm
10 nm
C
400.0 nm
49.3 °
-45.9 °
D
MFM Phase (°)
40
30
20
10
0
−10
−20
−30
0 20 40 60 80
Distance (nm)
49.3 °
-45.9 °
0.0
3: Phase
218.8 nm

Figure 6.32: (A) Atomic force microscopy image of sample C4 showing the topography. (B) Cross-sectional transmission electron microscopy image of an individual nanowall showing the tapered geometry of the wall. The inset shows the high resolution image of the tip region. (C) Magnetic force microscopy image of sample C4 showing the non-uniform strength of magnetisation in different parts of the nanowall network. (D) Zoomed view of magnetisation distribution for an individual nanowall with a line scan for estimating size of the region with comparatively high magnetisation.

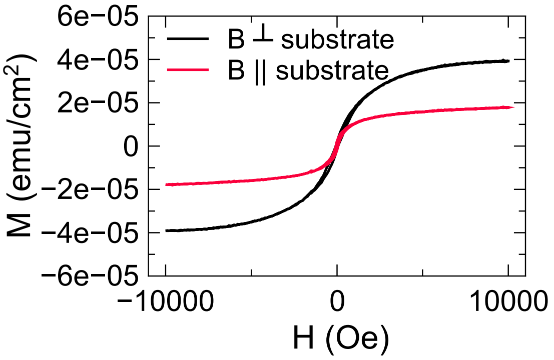

Figure 6.33: Field dependence of magnetisation with magnetic field applied parallel or perpendicular to the substrate.

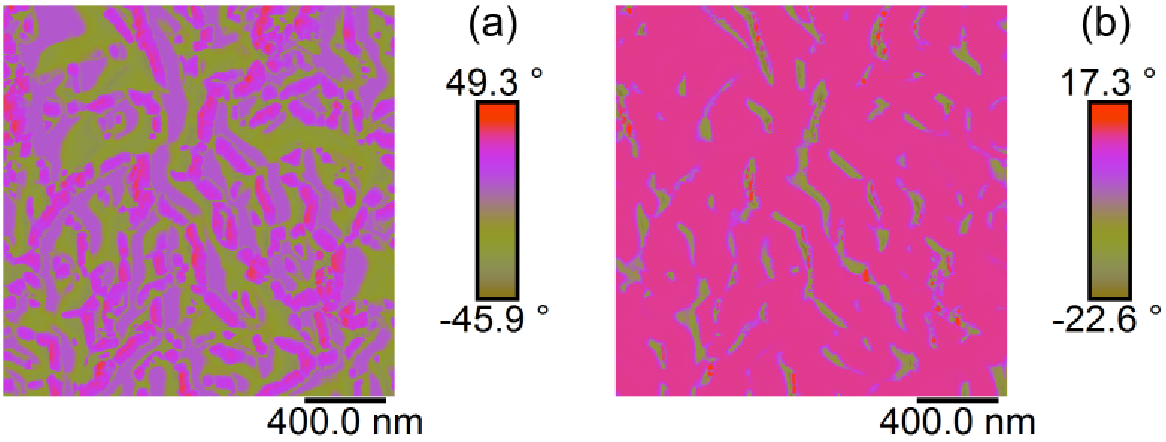

Figure 6.34: Magnetic force microscopy image of sample C4 with an external magnetic field applied perpendicular to the substrate with field direction (a) into and (b) coming out of the substrate plane.

believe that the 2DEG is responsible for the observed magnetism. There have been several literature reports of spontaneous spin polarization of 2DEG leading to ferromagnetism, though there can be different underlying causes for the spin splitting.

Han *et al.* worked on a system of Mg:ZnO/ZnO heterostructure which shows formation of 2DEG.[208] and an anisotropic room temperature ferromagnetism. The explanation put forward by them was formation of bound magnetic polarons (BMP) by a complex of cation vacancy defects and exchange interaction of 2DEG with the BMPs through overlap of wavefunctions causing the spin splitting of 2DEG and thereby the resulting high T_C ferromagnetism.

In contrast, the work by Yang *et al.*[209], who worked on a Gd doped GaN 2DEG systems and observed an anisotropic weak ferromagnetic effect in the doped as well as undoped GaN samples, ruling out any coupling between the ferromagnetic phase and the mobile 2DEG even though those regions were spatially overlapping. They observed an easy magnetisation axis along c axis and attributed it to exchange interaction among spins leading to their locking around c axis. The undoped sample's magnetism was again explained on the basis of direct exchange through defect wavefunction overlap.

Spin-orbit coupling (SOC) can lead to spin splitting and ferromagnetic behaviour. Though the typical Rashba type SOC is weak in GaN, (especially zinc blende GaN) owing to the light constituent elements, very strong spin splitting phenomena have indeed been observed[210] in wurtzite GaN heterostructures which can not be explained by considering only Rashba and Dresselhaus effects. Lo et al.[211] calculated theoretically that wurtzite structural inversion asymmetry and band folding effects, can lead to large spin splitting which is highly sensitive to electric field. It should be remembered that he spontaneous polarization fields in GaN are as large as 10^6 V/cm). Additionally, through Hartree-Fock method and Green's function calculation have shown that electron-electron interactions enhance the spin splitting further.[?] Factors like these combined with confinement effects, discussed earlier, strengthens the spin polarization. If cation vacancies are actually present, owing to the size effect near nanowall tip, a direct exchange among them and the 2DEG cannot be ruled out. In case of sample B4 which has wider angle nanowalls and presumably lower electron concentration near nanowall centre region and also reduced surface area, both the defect concentration and extent of 2DEG is supposed to be less compared to C4. This can explain the weaker magnetism of B4 compared to C4. Further quantum transport measurements are required to exactly ascertain the underlying cause.

6.4.3 Conclusions

We have performed transport and magnetic measurements of MBE grown GaN nanowall network. The nanowall network exhibits ferromagnetic behaviour with T_C more than 370 K. Magnetic force microscopy studies show that the magnetisation is concentrated near the narrow apex regions of the nanowall where a polarization induced can 2DEG exist. We believe that due to enhanced SOC, spontaneous spin polarization of 2DEG takes place, though contribution from cation vacancies strengthen by surface and quantum confinements cannot be ruled out. This leads to observation of high T_C anisotropic magnetism. This in addition to excellent transport properties of GaN nanowall network should open up new possibilities in the field of spintronics.

6.5 Conclusion

In this chapter we studied the electronic, electrical and magnetic properties of MBE grown GaN nanowall network. The XPS studies showed that that the surface is Ga rich with an additional Ga adlayer on top. Electrochemical studies showed that a significant density of surface states exist for nanowall network in contrast to flat GaN film. The energetic positions of these surface states were determined to be at 0.75 eV below CBM and 0.2 eV and 0.5 eV above VBM. The first of these states was attributed to Ga dangling bonds and the last one to the presence of carbon defects based on literature reports of density functional theory calculations. The presence of carbon defects also explains some of the observed defect related features in low temperatures luminescence spectra. Electrochemical impedance spectroscopy were fitted with a modified Randles circuit and the capacitance values were extracted. The resultant Mott-Schottky plot showed that the flat band potential of GaN nanowall to be -1.63 V which is more negative than flat GaN epilayer.

Temperature and magnetic field dependent Hall and four probe resistivity measurements were carried out for GaN nanowall network to study the electrical transport properties. The nanowall network samples with high carrier concentration showed a nearly temperature independent resistivity due to their degenerate nature with a shallow minimum which indicates that quantum mechanical corrections are to be taken into account. An analysis of the data showed that weak localisation is the dominant correction factor and the de-phasing mechanism was found to be electron-phonon scattering. The weak localisation was additionally confirmed by observation of negative magnetoresistance. The extracted phase coherence length was found to increase with a decrease in carrier concentration.

The GaN nanowall network was found to exhibit a weak ferromagnetic behaviour with a high Curie temperature of above 370 K. The magnetic properties are anisotropic and the magnetic moments are found to be concentrated near the tip of the nanowalls where a polarisation induced 2DEG exists. It is proposed that a spontaneous spin polarisation of the 2DEG, enhanced by the particular structure and morphology of the GaN nanowall network leads to the observed unusual magnetic properties.

Chapter 7

Summary and future directions

This chapter summarises the thesis, describing briefly the results obtained in the previous chapters. The limitations of the work contained in this thesis are mentioned and scope of further research work in continuation of present work are discussed. This work discussed in this thesis pertains to the MBE growth of several GaN nanostructures such as flat and porous thin films, nanorods, and nanowall network and their characterisation. It has been observed that by tuning the size shape and composition of the grown materials by varying the growth conditions, the resultant properties can be tuned as desired.

7.1 Summary of results

In chapter 3, growth of different GaN films and nanostructures have been carried out to investigate the effect of particular growth parameters on the resultant sample morphology. Focussing on the growth mechanism of nanorods, it was inferred that both the axial and radial growth of the nanorods involves step-flow growth. Changing Ga flux changes the kinetics of the growth and by this action alone, the shape of the nanorods, which is a crucial property application-wise, can be tuned from tapering to widening.

Both porous thin films and nanowall network can be grown in nitrogen rich conditions and the morphology can be tuned from former to latter by changing the N/Ga flux ratio. Several mechanisms have been proposed regarding the formation of such structures and have been discussed in this chapter, but the basic mechanism involves formation of 3D islands whose subsequent lateral growth leads to coalescence and formation of porous films and nanowall network.

In chapter 4 the structural properties of the above mentioned nanostructures have been studied using XRD, Raman and TEM. In was seen that the morphology and the strain state for GaN nanorods depends crucially on the choice of substrate. In case of GaN nanorods grown on sapphire, an additional basal matrix layer forms, but that is not the case for nanorods grown on silicon which results in well separated vertically aligned nanorods. It was determined that the matrix layer forms due to coalescence of shorter nanorods. The underlying cause of such a bimodal distribution has been found to be an incomplete and unintentional nitridation of the sapphire substrate when exposed to nitrogen plasma which forms AlN patches which act as favourable nucleation centres for some rods.

For both porous thin films and nanowall network, the residual stress is found to be dependent on morphology. For the epitaxial nanowall network, it was determined through analysis of HRXRD data that the distribution of threading dislocations is non-uniform and bunched which was corroborated through a pan-chromatic CL mapping. Using a mosaic model, the tilt and twist misorientations for several nanowall network samples were measured and it was found that the misorientations were found to scale with the mean nanowall width. This was explained on the basis of formation of boundary dislocations to accommodate individually misoriented 3D islands which coalesce to constitute the nanowall network. Thus to reduce the dislocation density and residual stress, it is better to grow thin nanowalls.

In chapter 5 we investigated the optical properties of the nanostructures. The size of the nanostructures play an important role in determining the NBE PL emission wavelength. The deep defect related emissions are found to be highly sensitive to the exact growth conditions and are explained on the basis of variation of defect formation energy with growth conditions and from surface to bulk, which leads to a change in concentration of optically active point defects with composition and surface to volume ratio.

The MBE grown GaN nanowall network shows a highly intense NBE PL emission compared to MBE or MOCVD grown thin films. A high carrier concentration of the nanowall network weakens the electron-phonon interaction which leads to a reduction in temperature dependent bandgap shrinkage. The high electron concentration can also suppress the defect related emissions by filling the acceptor levels. The bandgap renormalisation and band filing determine the NBE peak position, peak width and absorption edge. Thus by controlling the carrier concentration through growth parameter modification, the optical properties of the nanowall network can be engineered.

In chapter 6 we study the electronic and electrical transport properties of nanowall network. The electronic properties were studied separately using XPS and CL techniques and also with electrochemical voltammetry and impedance techniques. The XPS studies showed that the surface of GaN nanowall network and porous GaN film has a Ga rich composition. Calculation of band bending from XPS VB spectra and CL spectrum indicated that the Fermi level is pinned 1.8 eV above VBM suggesting that Ga adlayer is present on the surface. Cyclic voltammetry, impedance spectroscopy coupled with PL studies showed that a high density of surface states dominate the charge transfer process in contrast to flat GaN epilayer where the density of such states are less. Randles equivalent circuit was used to fit the impedance spectra and the analysis showed anomalous value of constant phase element parameter attributed to the porous surface of the nanowall network. Mott-Schottky plots were constructed for nanowall network and epilayer from the capacitance extracted from fitted circuits while accounting for the capacitance of the Helmholtz layer. The flat band potential was determined to be -1.63 V for nanowall network and -1.4 V for epilayer. From the analysis of the charge transfer data of nanowall network it was found that in addition to band edges, energy levels with significant density of states exist at 0.75 eV below CBM and 0.5 eV and 0.2 eV above VBM. Although additional experimental and theoretical studies and required to conclusively determine the origin of these energy levels, tentatively the energy level below CBM has been attributed to Ga dangling bonds and the energy level 0.2 eV above VBM has been attributed to C_N defects based on density functional theory calculation of their energy levels.

The electrical transport properties of GaN nanowall network show a number of exciting features such as observation of high mobility despite having a high carrier concentration of up to 10^{20} cm^{-3}, high coherence length and observation of proximity induced superconductivity, among others. We studied the electrical transport properties of a set of nanowall samples with varying carrier concentration to investigate its effect. For the samples with highest electron concentration, the resistivity was found to be mostly temperature independent due to the degenerate nature of the samples. Upon careful observation however, a shallow minimum was observed in the temperature-resistivity graph indicating some quantum corrections to the classically expected behaviour. An analysis of the data showed weak localisation as the underlying cause with electron-phonon inelastic scattering as the dephasing mechanism. The weak localisation effect was confirmed through the observation of negative magnetoresistance over a large temperature range.

Observation of quantum effects in the electrical transport and inspired by literature reports of magnetic order in nanostructures of d^0 semiconductors, we investigated the magnetic properties of GaN nanowall network. We studied a set of three samples with different morphology - a nanowall network, a flat epilayer and a sample with intermediate porous morphology. It was found that the flat GaN epilayer is diamagnetic as expected, while the porous film and nanowall network show ferromagnetic behaviour. The Curie temperature for the nanowall network was estimated to be above 370 K which is highly lucrative from an application point of view. The magnetic moment showed anisotropy - the magnetisation is higher when the magnetising field is applied perpendicular to the nanowall substrate compared to when applied parallel to it. Magnetic force microscopy showed that the magnetic moment is concentrated near the tip of the nanowalls and shows reversal when the magnetising field is reversed. A spontaneous polarisation of the 2DEG of the nanowall network is proposed to be underlying the anomalous magnetism.

7.2 Limitations and future directions

In this thesis we studied the growth of different dimensional nanostructures by investigating the final as grown samples without any significant real time observation of their growth except using in-situ RHEED which indicated that the growth of both one-dimensional nanorods and quasi-two-dimensional nanowall network begins by formation of three dimensional islands. A Monte-Carlo simulation in conjunction with microscopic studies of samples grown in appropriate conditions for a short duration of time will help gain a better understanding of growth of such nanostructures.

We showed via HRXRD and TEM studies that the often observed basal compact layer for GaN nanorod growth on sapphire originates from an unintentional incomplete nitridation of the substrate. It will be beneficial to conduct a cross-sectional HRTEM study for direct confirmation. Secondly, a study of different methods to control the nitridation to achieve a control over the polarity of the nanorods will be important for practical applications. In this thesis, we have studied the structural properties of nanowall network mainly through HRXRD, Raman spectroscopy. A detailed HRTEM and Raman mapping investigations are expected to provide further understanding of the exact formation mechanism and structural defect distribution of nanowall network. Similar studies on porous GaN films may also prove valuable as the residual strain of such materials influence a number of application related properties.

In our optical studies we gained insight into the energetic positions of the defect states which influence the luminescence properties of the nanostructures. Since first principles calculations often have widely disparate results regarding energy levels of particular defects or defect complexes, complementary studies such as positron annihilation spectroscopy and electron paramagnetic resonance are required to identify the defects.

Unlike thin films, electrical characterisation of one-dimensional nanorods is a non-trivial problem. To characterise individual nanorods complicated lithographic steps are required and forming metallic contacts on top of a nanorod array do not provide accurate results. In this scenario, electrochemical studies of a nanorod array can provide valuable information about the carrier concentration and charge transfer process. Conducting atomic force microscopy is another valuable tool to characterise nanostructures such as nanorods and nanowall network. In case of nanowall network, this technique can yield additional insight regarding the distribution of threading dislocations, as they can provide electrical leakage paths. Finally, theoretical and further experimental studies are required to fully explain the observed high Curie temperature anisotropic ferromagnetic properties of nanowall network.

Bibliography

[1] H. Teisseyre, P. Perlin, T. Suski, I. Grzegory, S. Porowski, J. Jun, A. Pietraszko, and T. D. Moustakas. Temperature dependence of the energy gap in GaN bulk single crystals and epitaxial layer. *Journal of Applied Physics*, 76(4):2429–2434, August 1994. ISSN 0021-8979, 1089-7550. doi: 10.1063/1.357592. URL `http://aip.scitation.org/doi/10.1063/1.357592`.

[2] S. Deb, H. P. Bhasker, Varun Thakur, S. M. Shivaprasad, and S. Dhar. Polarization induced two dimensional confinement of carriers in wedge shaped polar semiconductors. *Scientific Reports*, 6 (1):26429, May 2016. ISSN 2045-2322. doi: 10.1038/srep26429. URL `https://www.nature.com/articles/srep26429`.

[3] Hadis Morkoç. *Nitride Semiconductor Devices: Fundamentals and Applications.* John Wiley & Sons, April 2013. ISBN 978-3-527-64902-0.

[4] Farid Medjdoub. *Gallium Nitride (GaN): Physics, Devices, and Technology.* CRC Press, December 2017. ISBN 978-1-4822-2004-9.

[5] Timothy David Veal, Christopher F. McConville, and William J. Schaff. *Indium Nitride and Related Alloys.* CRC Press, June 2011. ISBN 978-1-4398-5961-2.

[6] W. C. Johnson, J. B. Parson, and M. C. Crew. Nitrogen Compounds of Gallium. III. *The Journal of Physical Chemistry*, 36(10):2651–2654, October 1932. ISSN 0092-7325. doi: 10.1021/j150340a015. URL `https://doi.org/10.1021/j150340a015`.

[7] Herbert Paul Maruska and Walden Clark Rhines. A modern perspective on the history of semiconductor nitride blue light sources. *Solid-State Electronics*, 111:32–41, September 2015. ISSN 0038-1101. doi: 10.1016/j.sse.2015.04.010. URL `http://www.sciencedirect.com/science/article/pii/S0038110115001318`.

[8] J. I. Pankove. Tunneling-Assisted Photon Emission in Gallium Arsenide $\textbackslashmathrm{pn}$ Junctions. *Physical Review Letters*, 9(7):283–285, October 1962. doi: 10.1103/PhysRevLett.9.283. URL `https://link.aps.org/doi/10.1103/PhysRevLett.9.283`.

[9] H. G. Grimmeiss and H. Scholz. Efficiency of recombination radiation in GaP. *Physics Letters*, 8 (4):233–235, February 1964. ISSN 0031-9163. doi: 10.1016/S0031-9163(64)90997-7. URL `http://www.sciencedirect.com/science/article/pii/S0031916364909977`.

[10] John A. Edmond, Hua-Shuang Kong, and Calvin H. Carter. Blue LEDs, UV photodiodes and high-temperature rectifiers in 6H–SiC. In Chris G. Van de Walle, editor, *Wide-Band-Gap Semiconductors*, pages 453–460. Elsevier, Amsterdam, January 1993. ISBN 978-0-444-81573-6. doi: 10.1016/B978-0-444-81573-6.50072-4. URL `http://www.sciencedirect.com/science/article/pii/B9780444815736500724`.

[11] J. I. Pankove, E. A. Miller, D. Richman, and J. E. Berkeyheiser. Electroluminescence in GaN. *Journal of Luminescence*, 4(1):63–66, July 1971. ISSN 0022-2313. doi: 10.1016/0022-2313(71)90009-3. URL `http://www.sciencedirect.com/science/article/pii/0022231371900093`.

[12] H. P. Maruska, W. C. Rhines, and D. A. Stevenson. Preparation of Mg-doped GaN diodes exhibiting violet electroluminescence. *Materials Research Bulletin*, 7(8):777–781, August 1972. ISSN 0025-5408. doi: 10.1016/0025-5408(72)90127-4. URL `http://www.sciencedirect.com/science/article/pii/0025540872901274`.

[13] Toshiharu Kawabata, Toshio Matsuda, and Susumu Koike. GaN blue light emitting diodes prepared by metalorganic chemical vapor deposition. *Journal of Applied Physics*, 56(8):2367–2368, October 1984. ISSN 0021-8979. doi: 10.1063/1.334277. URL `https://aip.scitation.org/doi/abs/10.1063/1.334277`.

[14] H. Amano, N. Sawaki, I. Akasaki, and Y. Toyoda. Metalorganic vapor phase epitaxial growth of a high quality GaN film using an AlN buffer layer. *Applied Physics Letters*, 48(5):353–355, February 1986. ISSN 0003-6951. doi: 10.1063/1.96549. URL `https://aip.scitation.org/doi/10.1063/1.96549`.

[15] Shuji Nakamura, Takashi Mukai, and Masayuki Senoh. High-Power GaN P-N Junction Blue-Light-Emitting Diodes. *Japanese Journal of Applied Physics*, 30(12A):L1998, December 1991. ISSN 1347-4065. doi: 10.1143/JJAP.30.L1998. URL `https://iopscience.iop.org/article/10.1143/JJAP.30.L1998/meta`.

[16] M. Asif Khan, J. M. Van Hove, J. N. Kuznia, and D. T. Olson. High electron mobility GaN/AlxGa1-xN heterostructures grown by low-pressure metalorganic chemical vapor deposition. *Applied Physics Letters*, 58(21):2408–2410, May 1991. ISSN 0003-6951. doi: 10.1063/1.104886. URL `https://aip.scitation.org/doi/abs/10.1063/1.104886`.

[17] M. Asif Khan, A. Bhattarai, J. N. Kuznia, and D. T. Olson. High electron mobility transistor based on a GaN-AlxGa1-xN heterojunction. *Applied Physics Letters*, 63(9):1214–1215, August 1993. ISSN 0003-6951. doi: 10.1063/1.109775. URL `https://aip.scitation.org/doi/10.1063/1.109775`.

[18] Fabio Bernardini, Vincenzo Fiorentini, and David Vanderbilt. Spontaneous polarization and piezoelectric constants of III-V nitrides. *Physical Review B*, 56(16):R10024–R10027, October 1997. doi: 10.1103/PhysRevB.56.R10024. URL `https://link.aps.org/doi/10.1103/PhysRevB.56.R10024`.

[19] O. Ambacher, J. Smart, J. R. Shealy, N. G. Weimann, K. Chu, M. Murphy, W. J. Schaff, L. F. Eastman, R. Dimitrov, L. Wittmer, M. Stutzmann, W. Rieger, and J. Hilsenbeck. Two-dimensional electron gases induced by spontaneous and piezoelectric polarization charges in N- and Ga-face AlGaN/GaN heterostructures. *Journal of Applied Physics*, 85(6):3222–3233, March 1999. ISSN 0021-8979. doi: 10.1063/1.369664. URL `https://aip.scitation.org/doi/abs/10.1063/1.369664`.

[20] S. T. Sheppard, K. Doverspike, W. L. Pribble, S. T. Allen, J. W. Palmour, L. T. Kehias, and T. J. Jenkins. High-power microwave GaN/AlGaN HEMTs on semi-insulating silicon carbide substrates. *IEEE Electron Device Letters*, 20(4):161–163, April 1999. ISSN 1558-0563. doi: 10.1109/55.753753.

[21] W. Saito, Y. Takada, M. Kuraguchi, K. Tsuda, and I. Omura. Recessed-gate structure approach toward normally off high-Voltage AlGaN/GaN HEMT for power electronics applications. *IEEE Transactions on Electron Devices*, 53(2):356–362, February 2006. ISSN 1557-9646. doi: 10.1109/TED.2005.862708.

[22] Y. Cai, Y. Zhou, K. M. Lau, and K. J. Chen. Control of Threshold Voltage of AlGaN/GaN HEMTs by Fluoride-Based Plasma Treatment: From Depletion Mode to Enhancement Mode. *IEEE Transactions on Electron Devices*, 53(9):2207–2215, September 2006. ISSN 1557-9646. doi: 10.1109/TED.2006.881054.

[23] S. Tripathy, Vivian K. X. Lin, S. B. Dolmanan, Joyce P. Y. Tan, R. S. Kajen, L. K. Bera, S. L. Teo, M. Krishna Kumar, S. Arulkumaran, G. I. Ng, S. Vicknesh, Shane Todd, W. Z. Wang, G. Q. Lo, H. Li, D. Lee, and S. Han. AlGaN/GaN two-dimensional-electron gas heterostructures on 200 mm diameter Si(111). *Applied Physics Letters*, 101(8):082110, August 2012. ISSN 0003-6951. doi: 10.1063/1.4746751. URL `https://aip.scitation.org/doi/full/10.1063/1.4746751`.

[24] H. Amano, Y. Baines, E. Beam, Matteo Borga, T. Bouchet, Paul R. Chalker, M. Charles, Kevin J. Chen, Nadim Chowdhury, Rongming Chu, Carlo De Santi, Maria Merlyne De Souza, Stefaan Decoutere, L. Di Cioccio, Bernd Eckardt, Takashi Egawa, P. Fay, Joseph J. Freedsman, L. Guido, Oliver Häberlen, Geoff Haynes, Thomas Heckel, Dilini Hemakumara, Peter Houston, Jie Hu, Mengyuan Hua, Qingyun Huang, Alex Huang, Sheng Jiang, H Kawai, Dan

Kinzer, Martin Kuball, Ashwani Kumar, Kean Boon Lee, Xu Li, Denis Marcon, Martin März, R McCarthy, Gaudenzio Meneghesso, Matteo Meneghini, E. Morvan, A. Nakajima, E. M. S. Narayanan, Stephen Oliver, Tomás Palacios, Daniel Piedra, M. Plissonnier, R. Reddy, Min Sun, Iain Thayne, A. Torres, Nicola Trivellin, V. Unni, Michael J. Uren, Marleen Van Hove, David J. Wallis, J. Wang, J. Xie, S. Yagi, Shu Yang, C Youtsey, Ruiyang Yu, Enrico Zanoni, Stefan Zeltner, and Yuhao Zhang. The 2018 GaN power electronics roadmap. *Journal of Physics D: Applied Physics*, 51(16):163001, 2018. ISSN 0022-3727. doi: 10.1088/1361-6463/aaaf9d. URL `http://stacks.iop.org/0022-3727/51/i=16/a=163001`.

[25] Patrick Fay, Debdeep Jena, and Paul Maki. Introduction and Overview. In Patrick Fay, Debdeep Jena, and Paul Maki, editors, *High-Frequency GaN Electronic Devices*, pages 1–3. Springer International Publishing, Cham, 2020. ISBN 978-3-030-20208-8. doi: 10.1007/978-3-030-20208-8_1. URL `https://doi.org/10.1007/978-3-030-20208-8_1`.

[26] M. A. Moram and M. E. Vickers. X-ray diffraction of III-nitrides. *Reports on Progress in Physics*, 72(3):036502, February 2009. ISSN 0034-4885. doi: 10.1088/0034-4885/72/3/036502. URL `https://doi.org/10.1088%2F0034-4885%2F72%2F3%2F036502`.

[27] S. J. Pearton, F. Ren, Erin Patrick, M. E. Law, and Alexander Y. Polyakov. Review—Ionizing Radiation Damage Effects on GaN Devices. *ECS Journal of Solid State Science and Technology*, 5 (2):Q35, November 2015. ISSN 2162-8777. doi: 10.1149/2.0251602jss. URL `https://iopscience.iop.org/article/10.1149/2.0251602jss/meta`.

[28] S A Kukushkin, A V Osipov, V N Bessolov, B K Medvedev, V K Nevolin, and K A Tcarik. SUBSTRATES FOR EPITAXY OF GALLIUM NITRIDE: NEW MATERIALS AND TECHNIQUES. *REVIEW ON ADVANCED MATERIALS SCIENCE*, page 32, 2008.

[29] V. S. Harutyunyan, A. P. Aivazyan, E. R. Weber, Y. Kim, Y. Park, and S. G. Subramanya. High-resolution x-ray diffraction strain-stress analysis of GaN/sapphire heterostructures. *Journal of Physics D: Applied Physics*, 34(10A):A35–A39, May 2001. ISSN 0022-3727. doi: 10.1088/0022-3727/34/10A/308. URL `https://doi.org/10.1088%2F0022-3727%2F34%2F10a%2F308`.

[30] J. W. Matthews, D. C. Jackson, and A. Chambers. Effect of coherency strain and misfit dislocations on the mode of growth of thin films. *Thin Solid Films*, 26(1):129–134, March 1975. ISSN 0040-6090. doi: 10.1016/0040-6090(75)90172-8. URL `http://www.sciencedirect.com/science/article/pii/0040609075901728`.

[31] Chinkyo Kim, I. K. Robinson, Jaemin Myoung, Kyuhwan Shim, Myung-Cheol Yoo, and Kyekyoon Kim. Critical thickness of GaN thin films on sapphire (0001). *Applied Physics Letters*, 69(16):2358–2360, October 1996. ISSN 0003-6951. doi: 10.1063/1.117524. URL `https://aip.scitation.org/doi/abs/10.1063/1.117524`.

[32] Md Ashfaque Hossain Khan and Mulpuri V. Rao. Gallium Nitride (GaN) Nanostructures and Their Gas Sensing Properties: A Review. *Sensors*, 20(14):3889, January 2020. doi: 10.3390/s20143889. URL `https://www.mdpi.com/1424-8220/20/14/3889`.

[33] Chao Zhao, Tien Khee Ng, Rami T. ElAfandy, Aditya Prabaswara, Giuseppe Bernardo Consiglio, Idris A. Ajia, Iman S. Roqan, Bilal Janjua, Chao Shen, Jessica Eid, Ahmed Y. Alyamani, Munir M. El-Desouki, and Boon S. Ooi. Droop-Free, Reliable, and High-Power InGaN/GaN Nanowire Light-Emitting Diodes for Monolithic Metal-Optoelectronics. *Nano Letters*, 16(7):4616–4623, July 2016. ISSN 1530-6984. doi: 10.1021/acs.nanolett.6b01945. URL `https://doi.org/10.1021/acs.nanolett.6b01945`.

[34] V. Consonni. Self-induced growth of GaN nanowires by molecular beam epitaxy: A critical review of the formation mechanisms. *physica status solidi (RRL) – Rapid Research Letters*, 7(10):699–712, 2013. ISSN 1862-6270. doi: 10.1002/pssr.201307237. URL `https://onlinelibrary.wiley.com/doi/abs/10.1002/pssr.201307237`.

[35] Kris A. Bertness, Norman A. Sanford, and Albert V. Davydov. GaN Nanowires Grown by Molecular Beam Epitaxy. *IEEE Journal of Selected Topics in Quantum Electronics*, 17(4):847–858, July 2011. ISSN 1558-4542. doi: 10.1109/JSTQE.2010.2082504.

[36] Manoj Kesaria, Satish Shetty, and S. M. Shivaprasad. Evidence for Dislocation Induced Spontaneous Formation of GaN Nanowalls and Nanocolumns on Bare C-Plane Sapphire. *Crystal Growth & Design*, 11(11):4900–4903, November 2011. ISSN 1528-7483. doi: 10.1021/cg200749w. URL `https://doi.org/10.1021/cg200749w`.

[37] Abhijit Chatterjee, Shashidhara Acharya, and S.M. Shivaprasad. Morphology-Related Functionality in Nanoarchitectured GaN. *Annual Review of Materials Research*, 50(1), July 2020. ISSN 1531-7331, 1545-4118. doi: 10.1146/annurev-matsci-081919-014810. URL `https://www.annualreviews.org/doi/10.1146/annurev-matsci-081919-014810`.

[38] D. Q. Fang and R. Q. Zhang. Size effects on formation energies and electronic structures of oxygen and zinc vacancies in ZnO nanowires: A first-principles study. *Journal of Applied Physics*, 109 (4):044306–044306–5, February 2011. ISSN 0021-8979. doi: 10.1063/1.3549131. URL `https://aip.scitation.org/doi/full/10.1063/1.3549131`.

[39] M. G. Ganchenkova and R. M. Nieminen. Nitrogen Vacancies as Major Point Defects in Gallium Nitride. *Physical Review Letters*, 96(19):196402, May 2006. doi: 10.1103/PhysRevLett.96.196402. URL `https://link.aps.org/doi/10.1103/PhysRevLett.96.196402`.

[40] Giacomo Miceli and Alfredo Pasquarello. Energetics of native point defects in GaN: A density-functional study. *Microelectronic Engineering*, 147:51–54, November 2015. ISSN 0167-9317. doi: 10.1016/j.mee.2015.04.015. URL `https://www.sciencedirect.com/science/article/pii/S016793171500221X`.

[41] Zijuan Xie, Yu Sui, John Buckeridge, C Richard A Catlow, Thomas W Keal, Paul Sherwood, Aron Walsh, Matthew R Farrow, David O Scanlon, Scott M Woodley, and Alexey A Sokol. Donor and acceptor characteristics of native point defects in GaN. *Journal of Physics D: Applied Physics*, 52(33):335104, August 2019. ISSN 0022-3727, 1361-6463. doi: 10.1088/1361-6463/ab2033. URL `https://iopscience.iop.org/article/10.1088/1361-6463/ab2033`.

[42] Jörg Neugebauer and Chris G. Van de Walle. Native defects and impurities in GaN. In Reinhard Helbig, editor, *Advances in Solid State Physics 35*, Advances in Solid State Physics, pages 25–44. Springer, Berlin, Heidelberg, 1995. ISBN 978-3-540-75334-6. doi: 10.1007/BFb0107538. URL `https://doi.org/10.1007/BFb0107538`.

[43] Michael A. Reshchikov and Hadis Morkoç. Luminescence properties of defects in GaN. *Journal of Applied Physics*, 97(6):061301, March 2005. ISSN 0021-8979. doi: 10.1063/1.1868059. URL `http://aip.scitation.org/doi/abs/10.1063/1.1868059`.

[44] Rocío Félix, Marco Peres, Sergio Magalhães, Maria Rosario Correia, Armando Lourenço, Teresa Monteiro, Rafael García, and Francisco M. Morales. The Role of Edge Dislocations on the Red Luminescence of ZnO Films Deposited by RF-Sputtering, 2015. URL `https://www.hindawi.com/journals/jnm/2015/970545/`.

[45] D. G. Zhao, D. S. Jiang, Hui Yang, J. J. Zhu, Z. S. Liu, S. M. Zhang, J. W. Liang, X. Li, X. Y. Li, and H. M. Gong. Role of edge dislocations in enhancing the yellow luminescence of n-type GaN. *Applied Physics Letters*, 88(24):241917, June 2006. ISSN 0003-6951. doi: 10.1063/1.2213509. URL `https://aip.scitation.org/doi/full/10.1063/1.2213509`.

[46] Jonas Lähnemann, Uwe Jahn, Oliver Brandt, Timur Flissikowski, Pinar Dogan, and Holger T. Grahn. Luminescence associated with stacking faults in GaN. *Journal of Physics D: Applied Physics*, 47(42):423001, October 2014. ISSN 0022-3727. doi: 10.1088/0022-3727/47/42/423001. URL `https://doi.org/10.1088/0022-3727/47/42/423001`.

[47] Ranber Singh. Unexpected magnetism in nanomaterials. *Journal of Magnetism and Magnetic Materials*, 346:58–73, November 2013. ISSN 0304-8853. doi: 10.1016/j.jmmm.2013.07.005. URL `https://www.sciencedirect.com/science/article/pii/S0304885313004812`.

[48] Pratibha Dev, Hao Zeng, and Peihong Zhang. Defect-induced magnetism in nitride and oxide nanowires: Surface effects and quantum confinement. *Physical Review B*, 82(16):165319, October 2010. doi: 10.1103/PhysRevB.82.165319. URL `https://link.aps.org/doi/10.1103/PhysRevB.82.165319`.

[49] C. Madhu, A. Sundaresan, and C. N. R. Rao. Room-temperature ferromagnetism in undoped $\textbackslashmathrm{GaN}$ and $\textbackslashmathrm{CdS}$ semiconductor nanoparticles. *Physical Review B*, 77(20):201306, May 2008. doi: 10.1103/PhysRevB.77.201306. URL `https://link.aps.org/doi/10.1103/PhysRevB.77.201306`.

[50] E. Iliopoulos, A. Adikimenakis, E. Dimakis, K. Tsagaraki, G. Konstantinidis, and A. Georgakilas. Active nitrogen species dependence on radiofrequency plasma source operating parameters and their role in GaN growth. *Journal of Crystal Growth*, 278(1):426–430, May 2005. ISSN 0022-0248. doi: 10.1016/j.jcrysgro.2005.01.013. URL `https://www.sciencedirect.com/science/article/pii/S0022024805000151`.

[51] Y. C. Chen, S. H. Li, P. K. Bhattacharya, J. Singh, and J. M. Hinckley. Direct measurement of the Hall factor for holes in relaxed Si1-xGex. *Applied Physics Letters*, 64(23):3110–3111, June 1994. ISSN 0003-6951. doi: 10.1063/1.111363. URL `https://aip.scitation.org/doi/abs/10.1063/1.111363`.

[52] Kenji Harafuji, Taku Tsuchiya, and Katsuyuki Kawamura. Molecular dynamics simulation for evaluating melting point of wurtzite-type GaN crystal. *Journal of Applied Physics*, 96(5):2501–2512, September 2004. ISSN 0021-8979. doi: 10.1063/1.1772878. URL `https://aip.scitation.org/doi/full/10.1063/1.1772878`.

[53] Peter Capper, Stuart Irvine, and Tim Joyce. Epitaxial Crystal Growth: Methods and Materials. In Safa Kasap and Peter Capper, editors, *Springer Handbook of Electronic and Photonic Materials*, Springer Handbooks, pages 1–1. Springer International Publishing, Cham, 2017. ISBN 978-3-319-48933-9. doi: 10.1007/978-3-319-48933-9_14. URL `https://doi.org/10.1007/978-3-319-48933-9_14`.

[54] Gerald B. Stringfellow. *Organometallic Vapor-Phase Epitaxy: Theory and Practice*. Elsevier, December 2012. ISBN 978-0-323-13917-5.

[55] Marian A. Herman and Helmut Sitter. *Molecular Beam Epitaxy: Fundamentals and Current Status*. Springer Science & Business Media, December 2012. ISBN 978-3-642-80060-3.

[56] Toma Stoica, Eli Sutter, Ralph J. Meijers, Ratan K. Debnath, Raffaella Calarco, Hans Lüth, and Detlev Grützmacher. Interface and Wetting Layer Effect on the Catalyst-Free Nucleation and Growth of GaN Nanowires. *Small*, 4(6):751–754, 2008. ISSN 1613-6829. doi: https://doi.org/10.1002/smll.200700936. URL `https://onlinelibrary.wiley.com/doi/abs/10.1002/smll.200700936`.

[57] K. Oura, M. Katayama, A. V. Zotov, V. G. Lifshits, and A. A. Saranin. Growth of Thin Films. *Surface Science*, pages 357–387, 2003. doi: 10.1007/978-3-662-05179-5_14. URL `https://link.springer.com/chapter/10.1007/978-3-662-05179-5_14`.

[58] H. Brune. Growth Modes, 2001. URL `http://infoscience.epfl.ch/record/135795`.

[59] Hans J Scheel. Historical aspects of crystal growth technology. *Journal of Crystal Growth*, 211(1):1–12, April 2000. ISSN 0022-0248. doi: 10.1016/S0022-0248(99)00780-0. URL `http://www.sciencedirect.com/science/article/pii/S0022024899007800`.

[60] Grazyna Antczak and Gert Ehrlich. Jump processes in surface diffusion. *Surface Science Reports*, 62(2):39–61, February 2007. ISSN 0167-5729. doi: 10.1016/j.surfrep.2006.12.001. URL `http://www.sciencedirect.com/science/article/pii/S016757290600121X`.

[61] D. D. Koleske, A. E. Wickenden, R. L. Henry, W. J. DeSisto, and R. J. Gorman. Growth model for GaN with comparison to structural, optical, and electrical properties. *Journal of Applied Physics*, 84(4):1998–2010, August 1998. ISSN 0021-8979. doi: 10.1063/1.368353. URL `https://aip.scitation.org/doi/abs/10.1063/1.368353`.

[62] Aaron Joseph Ptak. *Growth kinetics and doping of gallium nitride grown by rf-plasma assisted molecular beam epitaxy*. PhD, West Virginia University Libraries, May 2001. URL `https://researchrepository.wvu.edu/etd/1351`.

[63] D. F. Storm, T. McConkie, D. S. Katzer, B. P. Downey, M. T. Hardy, D. J. Meyer, and David J. Smith. Effect of interfacial oxygen on the microstructure of MBE-grown homoepitaxial N-polar GaN. *Journal of Crystal Growth*, 409:14–17, January 2015. ISSN 0022-0248. doi: 10.1016/j.jcrysgro.2014.09.042. URL `https://www.sciencedirect.com/science/article/pii/S002202481400668X`.

[64] V. Consonni, M. Knelangen, L. Geelhaar, A. Trampert, and H. Riechert. Nucleation mechanisms of epitaxial GaN nanowires: Origin of their self-induced formation and initial radius. *Physical Review B*, 81(8):085310, February 2010. doi: 10.1103/PhysRevB.81.085310. URL `https://link.aps.org/doi/10.1103/PhysRevB.81.085310`.

[65] E Galopin, L Largeau, G Patriarche, L Travers, F Glas, and J C Harmand. Morphology of self-catalyzed GaN nanowires and chronology of their formation by molecular beam epitaxy. *Nanotechnology*, 22(24):245606, June 2011. ISSN 0957-4484, 1361-6528. doi: 10.1088/0957-4484/22/24/245606. URL `http://stacks.iop.org/0957-4484/22/i=24/a=245606?key=crossref.bb0f46fb8ee8343e20f5f8bb076c18cb`.

[66] Hao Tang, Jack C. Chang, Yueyue Shan, D. D. D. Ma, Tsz-Yan Lui, Juan A. Zapien, Chun-Sing Lee, and Shuit-Tong Lee. Growth mechanism of ZnO nanowires via direct Zn evaporation. *Journal of Materials Science*, 44(2):563–571, January 2009. ISSN 1573-4803. doi: 10.1007/s10853-008-3071-6. URL `https://doi.org/10.1007/s10853-008-3071-6`.

[67] Vladimir G. Dubrovskii, Vincent Consonni, Lutz Geelhaar, Achim Trampert, and Henning Riechert. Scaling growth kinetics of self-induced GaN nanowires. *Applied Physics Letters*, 100(15):153101, April 2012. ISSN 0003-6951, 1077-3118. doi: 10.1063/1.3701591. URL `http://aip.scitation.org/doi/10.1063/1.3701591`.

[68] Liverios Lymperakis and Jörg Neugebauer. Large anisotropic adatom kinetics on nonpolar GaN surfaces: Consequences for surface morphologies and nanowire growth. *Physical Review B*, 79(24):241308, June 2009. doi: 10.1103/PhysRevB.79.241308. URL `https://link.aps.org/doi/10.1103/PhysRevB.79.241308`.

[69] Marta Sawicka, Henryk Turski, Marcin Siekacz, Julita Smalc Koziorowska, Marcin Krysko, Igor Dziecielewski, Izabella Grzegory, and Czesław Skierbiszewski. Step-flow anisotropy of the m -plane GaN (1 -1 00) grown under nitrogen-rich conditions by plasma-assisted molecular beam epitaxy. *Physical Review B*, 83(24), June 2011. ISSN 1098-0121, 1550-235X. doi: 10.1103/PhysRevB.83.245434. URL `https://link.aps.org/doi/10.1103/PhysRevB.83.245434`.

[70] Song Jin, Matthew J. Bierman, and Stephen A. Morin. A New Twist on Nanowire Formation: Screw-Dislocation-Driven Growth of Nanowires and Nanotubes. *The Journal of Physical Chemistry Letters*, 1(9):1472–1480, May 2010. doi: 10.1021/jz100288z. URL `https://doi.org/10.1021/jz100288z`.

[71] Fei Meng, Stephen A. Morin, Audrey Forticaux, and Song Jin. Screw Dislocation Driven Growth of Nanomaterials. *Accounts of Chemical Research*, 46(7):1616–1626, July 2013. ISSN 0001-4842. doi: 10.1021/ar400003q. URL `https://doi.org/10.1021/ar400003q`.

[72] Satish Shetty, Manoj Kesaria, Jay Ghatak, and S. M. Shivaprasad. The Origin of Shape, Orientation, and Structure of Spontaneously Formed Wurtzite GaN Nanorods on Cubic Si(001) Surface. *Crystal Growth & Design*, 13(6):2407–2412, June 2013. ISSN 1528-7483. doi: 10.1021/cg4000928. URL `https://doi.org/10.1021/cg4000928`.

[73] D. Cherns, L. Meshi, I. Griffiths, S. Khongphetsak, S. V. Novikov, N. R. S. Farley, R. P. Campion, and C. T. Foxon. Defect-controlled growth of GaN nanorods on (0001)sapphire by molecular beam epitaxy. *Applied Physics Letters*, 93(11):111911, September 2008. ISSN 0003-6951, 1077-3118. doi: 10.1063/1.2987423. URL `http://aip.scitation.org/doi/10.1063/1.2987423`.

[74] T. Auzelle, G. Calabrese, and S. Fernández-Garrido. Tuning the orientation of the top-facets of GaN nanowires in molecular beam epitaxy by thermal decomposition. *Physical Review Materials*, 3(1), January 2019. ISSN 2475-9953. doi: 10.1103/PhysRevMaterials.3.013402. URL `https://link.aps.org/doi/10.1103/PhysRevMaterials.3.013402`.

[75] Xin Yin and Xudong Wang. Kinetics-Driven Crystal Facets Evolution at the Tip of Nanowires: A New Implementation of the Ostwald-Lussac Law. *Nano Letters*, 16(11):7078–7084, November 2016. ISSN 1530-6984. doi: 10.1021/acs.nanolett.6b03317. URL `https://doi.org/10.1021/acs.nanolett.6b03317`.

[76] Vladimir Kochergin and Helmut Föll. *Porous Semiconductors: Optical Properties and Applications*. Springer Science & Business Media, August 2009. ISBN 978-1-84882-578-9.

[77] Eduard Monaico, Ion Tiginyanu, and Veaceslav Ursaki. Porous semiconductor compounds. *Semiconductor Science and Technology*, 35(10):103001, September 2020. ISSN 0268-1242. doi: 10.1088/1361-6641/ab9477. URL `https://doi.org/10.1088/1361-6641/ab9477`.

[78] P. H. Griffin and R. A. Oliver. Porous nitride semiconductors reviewed. *Journal of Physics D: Applied Physics*, 53(38):383002, July 2020. ISSN 0022-3727. doi: 10.1088/1361-6463/ab9570. URL `https://doi.org/10.1088/1361-6463/ab9570`.

[79] J. N. Chazalviel, R. B. Wehrspohn, and F. Ozanam. Electrochemical preparation of porous semiconductors: from phenomenology to understanding. *Materials Science and Engineering: B*, 69-70:1–10, January 2000. ISSN 0921-5107. doi: 10.1016/S0921-5107(99)00285-8. URL `https://www.sciencedirect.com/science/article/pii/S0921510799002858`.

[80] Hao Wang, Inkyung Sung, Xiaodong Li, and Dongpyo Kim. Fabrication of Porous SiC Ceramics with Special Morphologies by Sacrificing Template Method. *Journal of Porous Materials*, 11(4): 265–271, October 2004. ISSN 1573-4854. doi: 10.1023/B:JOPO.0000046353.24308.86. URL `https://doi.org/10.1023/B:JOPO.0000046353.24308.86`.

[81] Caterina Ducati. Porosity in a single crystal. *Nature*, 495(7440):180–181, March 2013. ISSN 1476-4687. doi: 10.1038/nature11961. URL `https://www.nature.com/articles/nature11961`.

[82] Angel Barranco, Ana Borras, Agustin R. Gonzalez-Elipe, and Alberto Palmero. Perspectives on oblique angle deposition of thin films: From fundamentals to devices. *Progress in Materials Science*, 76:59–153, March 2016. ISSN 0079-6425. doi: 10.1016/j.pmatsci.2015.06.003. URL `https://www.sciencedirect.com/science/article/pii/S0079642515000705`.

[83] Matthew M. Hawkeye and Michael J. Brett. Glancing angle deposition: Fabrication, properties, and applications of micro- and nanostructured thin films. *Journal of Vacuum Science & Technology A*, 25(5):1317–1335, July 2007. ISSN 0734-2101. doi: 10.1116/1.2764082. URL `https://avs.scitation.org/doi/10.1116/1.2764082`.

[84] C. M. Zhou and D. Gall. Development of two-level porosity during glancing angle deposition. *Journal of Applied Physics*, 103(1):014307, January 2008. ISSN 0021-8979. doi: 10.1063/1.2828174. URL `https://aip.scitation.org/doi/full/10.1063/1.2828174`.

[85] J. Rouquerol, D. Avnir, C. W. Fairbridge, D. H. Everett, J. M. Haynes, N. Pernicone, J. D. F. Ramsay, K. S. W. Sing, and K. K. Unger. Recommendations for the characterization of porous solids (Technical Report). *Pure and Applied Chemistry*, 66(8):1739–1758, January 1994. ISSN 1365-3075. doi: 10.1351/pac199466081739. URL `https://www.degruyter.com/document/doi/10.1351/pac199466081739/html`.

[86] D. Cherns, W. T. Young, J. W. Steeds, F. A. Ponce, and S. Nakamura. Observation of coreless dislocations in alpha-GaN. *Journal of Crystal Growth*, 178(1):201–206, June 1997. ISSN 0022-0248. doi: 10.1016/S0022-0248(97)00081-X. URL `https://www.sciencedirect.com/science/article/pii/S002202489700081X`.

[87] Shigeyoshi Usami, Atsushi Tanaka, Hayata Fukushima, Yuto Ando, Manato Deki, Shugo Nitta, Yoshio Honda, and Hiroshi Amano. Correlation between nanopipes formed from screw dislocations during homoepitaxial growth by metal-organic vapor-phase epitaxy and reverse leakage current in vertical p–n diodes on a free-standing GaN substrates. *Japanese Journal of Applied Physics*, 58 (SC):SCCB24, May 2019. ISSN 1347-4065. doi: 10.7567/1347-4065/ab1250. URL `https://doi.org/10.7567/1347-4065/ab1250`.

[88] F. C. Frank. Capillary equilibria of dislocated crystals. *Acta Crystallographica*, 4(6):497–501, November 1951. ISSN 0365-110X. doi: 10.1107/S0365110X51001690. URL `//scripts.iucr.org/cgi-bin/paper?a00514`.

[89] E. Valcheva, T. Paskova, P. O. Å Persson, and B. Monemar. Nanopipes in Thick GaN Films Grown at High Growth Rate. *physica status solidi (a)*, 194(2):532–535, 2002. ISSN 1521-396X. doi: https://doi.org/10.1002/1521-396X(200212)194:2⟨532::AID-PSSA532⟩3.0.CO;2-R. URL `https://onlinelibrary.wiley.com/doi/abs/10.1002/1521-396X%28200212%29194%3A2%3C532%3A%3AAID-PSSA532%3E3.0.CO%3B2-R`.

[90] W. Qian, M. Skowronski, M. De Graef, K. Doverspike, L. B. Rowland, and D. K. Gaskill. Microstructural characterization of alpha-GaN films grown on sapphire by organometallic vapor phase epitaxy. *Applied Physics Letters*, 66(10):1252–1254, March 1995. ISSN 0003-6951. doi: 10.1063/1.113253. URL `https://aip.scitation.org/doi/10.1063/1.113253`.

[91] W. K. Burton, N. Cabrera, F. C. Frank, and Nevill Francis Mott. The growth of crystals and the equilibrium structure of their surfaces. *Philosophical Transactions of the Royal Society of London. Series A, Mathematical and Physical Sciences*, 243(866):299–358, June 1951. doi: 10.1098/rsta.1951.0006. URL `https://royalsocietypublishing.org/doi/abs/10.1098/rsta.1951.0006`.

[92] Aihua Zhong and Kazuhiro Hane. Growth of GaN nanowall network on Si (111) substrate by molecular beam epitaxy. *Nanoscale Research Letters*, 7(1):686, December 2012. ISSN 1556-276X. doi: 10.1186/1556-276X-7-686. URL `https://doi.org/10.1186/1556-276X-7-686`.

[93] David Poppitz, Andriy Lotnyk, Jürgen W. Gerlach, and Bernd Rauschenbach. Microstructure of porous gallium nitride nanowall networks. *Acta Materialia*, 65:98–105, February 2014. ISSN 1359-6454. doi: 10.1016/j.actamat.2013.11.041. URL `http://www.sciencedirect.com/science/article/pii/S1359645413008999`.

[94] Aihua Zhong, Ping Fan, Yuanting Zhong, Dongping Zhang, Fu Li, Jingting Luo, Yizhu Xie, and Kazuhiro Hane. Structure Shift of GaN Among Nanowall Network, Nanocolumn, and Compact Film Grown on Si (111) by MBE. *Nanoscale Research Letters*, 13(1):51, February 2018. ISSN 1556-276X. doi: 10.1186/s11671-018-2461-1. URL `https://doi.org/10.1186/s11671-018-2461-1`.

[95] Sanjay Nayak, Rajendra Kumar, and S. M. Shivaprasad. Edge enhanced growth induced shape transition in the formation of GaN nanowall network. *Journal of Applied Physics*, 123(1):014302, January 2018. ISSN 0021-8979. doi: 10.1063/1.5004496. URL `https://aip.scitation.org/doi/abs/10.1063/1.5004496`.

[96] H. W. Seo, Q. Y. Chen, M. N. Iliev, L. W. Tu, C. L. Hsiao, James K. Mean, and Wei-Kan Chu. Epitaxial GaN nanorods free from strain and luminescent defects. *Applied Physics Letters*, 88(15):153124, April 2006. ISSN 0003-6951. doi: 10.1063/1.2190269. URL `https://aip.scitation.org/doi/10.1063/1.2190269`.

[97] D Cherns, L Meshi, I Griffiths, S Khongphetsak, S V Novikov, R P Campion, C T Foxon, C Liu, P Shields, and W N Wang. GaN devices based on nanorods. *Journal of Physics: Conference Series*, 209:012001, February 2010. ISSN 1742-6596. doi: 10.1088/1742-6596/209/1/012001. URL `https://iopscience.iop.org/article/10.1088/1742-6596/209/1/012001`.

[98] W. L. Johnson, S. A. Kim, R. Geiss, C. M. Flannery, K. A. Bertness, and P. R. Heyliger. Vibrational modes of GaN nanowires in the gigahertz range. *Nanotechnology*, 23(49):495709, November 2012. ISSN 0957-4484. doi: 10.1088/0957-4484/23/49/495709. URL `https://doi.org/10.1088/0957-4484/23/49/495709`.

[99] L. Liu and J. H. Edgar. Substrates for gallium nitride epitaxy. *Materials Science and Engineering: R: Reports*, 37(3):61–127, April 2002. ISSN 0927-796X. doi: 10.1016/S0927-796X(02)00008-6. URL `http://www.sciencedirect.com/science/article/pii/S0927796X02000086`.

[100] Hiroshi Harima. Properties of GaN and related compounds studied by means of Raman scattering. *Journal of Physics: Condensed Matter*, 14(38):R967–R993, September 2002. ISSN 0953-8984. doi: 10.1088/0953-8984/14/38/201. URL `https://doi.org/10.1088%2F0953-8984%2F14%2F38%2F201`.

[101] Maria Losurdo, Pio Capezzuto, Giovanni Bruno, Gon Namkoong, W. Alan Doolittle, and April S. Brown. Role of sapphire nitridation temperature on GaN growth by plasma assisted molecular beam epitaxy: Part II. Interplay between chemistry and structure of layers. *Journal of Applied Physics*, 91(4):2508–2518, January 2002. ISSN 0021-8979. doi: 10.1063/1.1435835. URL `https://aip.scitation.org/doi/abs/10.1063/1.1435835`.

[102] M. Sumiya and S. Fuke. Review of polarity determination and control of GaN. *MRS Internet Journal of Nitride Semiconductor Research*, 9(1):1, June 2014. ISSN 1092-5783. doi: 10.1557/S1092578300000363. URL `https://doi.org/10.1557/S1092578300000363`.

[103] A. Georgakilas, S. Mikroulis, V. Cimalla, M. Zervos, A. Kostopoulos, Ph Komninou, Th Kehagias, and Th Karakostas. Effects of the Sapphire Nitridation on the Polarity and Structural Properties of GaN Layers Grown by Plasma-Assisted MBE. *physica status solidi (a)*, 188(2):567–570, 2001. ISSN 1521-396X. doi: https://doi.org/10.1002/1521-396X(200112)188:2⟨567::AID-PSSA567⟩3.0.CO;2-W. URL `https://onlinelibrary.wiley.com/doi/abs/10.1002/1521-396X%28200112%29188%3A2%3C567%3A%3AAID-PSSA567%3E3.0.CO%3B2-W`.

[104] S. Mikroulis, A. Georgakilas, A. Kostopoulos, V. Cimalla, E. Dimakis, and Ph. Komninou. Control of the polarity of molecular-beam-epitaxy-grown GaN thin films by the surface nitridation of Al2O3 (0001) substrates. *Applied Physics Letters*, 80(16):2886–2888, April 2002. ISSN 0003-6951. doi: 10.1063/1.1472481. URL `https://aip.scitation.org/doi/abs/10.1063/1.1472481`.

[105] Saki Sonoda, Saburo Shimizu, Xu-Qiang Shen, Shiro Hara, and Hajime Okumura. Characterization of Polarity of Wurtzite GaN Film Grown by Molecular Beam Epitaxy Using NH3. *Japanese Journal of Applied Physics*, 39(3A):L202, March 2000. ISSN 1347-4065. doi: 10.1143/JJAP.39.L202. URL `https://iopscience.iop.org/article/10.1143/JJAP.39.L202/meta`.

[106] B. Zhao, M. N. Lockrey, P. Caroff, N. Wang, L. Li, J. Wong-Leung, H. H. Tan, and C. Jagadish. The effect of nitridation on the polarity and optical properties of GaN self-assembled nanorods. *Nanoscale*, 10(23):11205–11210, June 2018. ISSN 2040-3372. doi: 10.1039/C8NR00737C. URL `https://pubs.rsc.org/en/content/articlelanding/2018/nr/c8nr00737c`.

[107] H. Hartono, C. B. Soh, S. J. Chua, and E. A. Fitzgerald. Fabrication and characterization of nano-porous GaN template for strain relaxed GaN growth. *physica status solidi (b)*, 244(6):1793–1796, 2007. ISSN 1521-3951. doi: https://doi.org/10.1002/pssb.200674705. URL `https://onlinelibrary.wiley.com/doi/abs/10.1002/pssb.200674705`.

[108] C. B. Soh, H. Hartono, S. Y. Chow, S. J. Chua, and E. A. Fitzgerald. Dislocation annihilation in regrown GaN on nanoporous GaN template with optimization of buffer layer growth. *Applied Physics Letters*, 90(5):053112, January 2007. ISSN 0003-6951. doi: 10.1063/1.2437056. URL `https://aip.scitation.org/doi/full/10.1063/1.2437056`.

[109] V. Darakchieva, B. Monemar, and A. Usui. On the lattice parameters of GaN. *Applied Physics Letters*, 91(3):031911, July 2007. ISSN 0003-6951. doi: 10.1063/1.2753122. URL `https://aip.scitation.org/doi/10.1063/1.2753122`.

[110] Srinivasan Raghavan, Jeremy Acord, and Joan M. Redwing. In situ observation of coalescence-related tensile stresses during metalorganic chemical vapor deposition of GaN on sapphire. *Applied Physics Letters*, 86(26):261907, June 2005. ISSN 0003-6951. doi: 10.1063/1.1968436. URL `https://aip.scitation.org/doi/10.1063/1.1968436`.

[111] M. G. Mynbaeva, K. D. Mynbaev, A. Sarua, and M. Kuball. Porous GaN/SiC templates for homoepitaxial growth: effect of the built-in stress on the formation of porous structures. *Semiconductor Science and Technology*, 20(1):50–55, December 2004. ISSN 0268-1242. doi: 10.1088/0268-1242/20/1/008. URL `https://doi.org/10.1088/0268-1242/20/1/008`.

[112] Malleswararao Tangi, Arpan De, Jay Ghatak, and S. M. Shivaprasad. Electron mobility of self-assembled and dislocation free InN nanorods grown on GaN nano wall network template. *Journal of Applied Physics*, 119(20):205701, May 2016. ISSN 0021-8979. doi: 10.1063/1.4952380. URL `https://aip.scitation.org/doi/full/10.1063/1.4952380`.

[113] Martin Frentrup, Nirupam Hatui, Tim Wernicke, Joachim Stellmach, Arnab Bhattacharya, and Michael Kneissl. Determination of lattice parameters, strain state and composition in semipolar III-nitrides using high resolution X-ray diffraction. *Journal of Applied Physics*, 114(21):213509, December 2013. ISSN 0021-8979. doi: 10.1063/1.4834521. URL `https://aip.scitation.org/doi/abs/10.1063/1.4834521`.

[114] C. Roder, S. Einfeldt, S. Figge, T. Paskova, D. Hommel, P. P. Paskov, B. Monemar, U. Behn, B. A. Haskell, P. T. Fini, and S. Nakamura. Stress and wafer bending of a-plane GaN layers on r-plane sapphire substrates. *Journal of Applied Physics*, 100(10):103511, November 2006. ISSN 0021-8979, 1089-7550. doi: 10.1063/1.2386940. URL `http://aip.scitation.org/doi/10.1063/1.2386940`.

[115] Travis E Oliphant. *Guide to NumPy*. 2015. ISBN 978-1-5173-0007-4.

[116] Mikhail A. Krivoglaz. *X-Ray and Neutron Diffraction in Nonideal Crystals*. Springer-Verlag, Berlin Heidelberg, 1996. ISBN 978-3-642-74293-4. URL `https://www.springer.com/in/book/9783642742934`.

[117] Saka Hiroyasu. *Classical Theory Of Crystal Dislocations: From Iron To Gallium Nitride*. World Scientific, September 2017. ISBN 978-981-4749-18-3.

[118] Rozaliya I. Barabash and Gene E. Ice. Diffraction Analysis of Defects: State of the Art. In *Strain and Dislocation Gradients from Diffraction*, pages 1–52. IMPERIAL COLLEGE PRESS, February 2013. ISBN 978-1-908979-62-9. doi: 10.1142/9781908979636_0001. URL `https://www.worldscientific.com/doi/abs/10.1142/9781908979636_0001`.

[119] V. M. Kaganer, O. Brandt, A. Trampert, and K. H. Ploog. X-ray diffraction peak profiles from threading dislocations in GaN epitaxial films. *Physical Review B*, 72(4), July 2005. ISSN 1098-0121, 1550-235X. doi: 10.1103/PhysRevB.72.045423. URL `https://link.aps.org/doi/10.1103/PhysRevB.72.045423`.

[120] Ullrich Pietsch, Vaclav Holy, and Tilo Baumbach. *High-Resolution X-Ray Scattering: From Thin Films to Lateral Nanostructures*. Advanced Texts in Physics. Springer-Verlag, New York, 2 edition, 2004. ISBN 978-0-387-40092-1. URL `https://www.springer.com/gp/book/9780387400921`.

[121] Viktor S. Kopp, Vladimir M. Kaganer, Marina V. Baidakova, Wsevolod V. Lundin, Andrey E. Nikolaev, Elena V. Verkhovtceva, Maria A. Yagovkina, and Nikolay Cherkashin. X-ray determination of threading dislocation densities in GaN/Al2O3(0001) films grown by metalorganic vapor phase epitaxy. *Journal of Applied Physics*, 115(7):073507, February 2014. ISSN 0021-8979. doi: 10.1063/1.4865502. URL `https://aip.scitation.org/doi/full/10.1063/1.4865502`.

[122] P Gay, P. B Hirsch, and A Kelly. The estimation of dislocation densities in metals from X-ray data. *Acta Metallurgica*, 1(3):315–319, May 1953. ISSN 0001-6160. doi: 10.1016/0001-6160(53)90106-0. URL `https://www.sciencedirect.com/science/article/pii/0001616053901060`.

[123] C. G Dunn and E. F Kogh. Comparison of dislocation densities of primary and secondary recrystallization grains of Si-Fe. *Acta Metallurgica*, 5(10):548–554, October 1957. ISSN 0001-6160. doi: 10.1016/0001-6160(57)90122-0. URL `https://www.sciencedirect.com/science/article/pii/0001616057901220`.

[124] A. D. Kurtz, S. A. Kulin, and B. L. Averbach. Effect of Dislocations on the Minority Carrier Lifetime in Semiconductors. *Physical Review*, 101(4):1285–1291, February 1956. doi: 10.1103/PhysRev.101.1285. URL `https://link.aps.org/doi/10.1103/PhysRev.101.1285`.

[125] T. Metzger, R. Höpler, E. Born, O. Ambacher, M. Stutzmann, R. Stömmer, M. Schuster, H. Göbel, S. Christiansen, M. Albrecht, and H. P. Strunk. Defect structure of epitaxial GaN films determined by transmission electron microscopy and triple-axis X-ray diffractometry. *Philosophical Magazine A*, 77(4):1013–1025, April 1998. ISSN 0141-8610. doi: 10.1080/01418619808221225. URL `https://doi.org/10.1080/01418619808221225`.

[126] V. M. Kaganer, M. Wölz, O. Brandt, L. Geelhaar, and H. Riechert. X-ray diffraction profiles from axial nanowire heterostructures. *Physical Review B*, 83(24):245321, June 2011. doi: 10.1103/PhysRevB.83.245321. URL `https://link.aps.org/doi/10.1103/PhysRevB.83.245321`.

[127] Sanjay Kumar Nayak, Danish Shamoon, Jay Ghatak, and Sonnada Math Shivaprasad. Nanostructuring GaN thin film for enhanced light emission and extraction: Nanostructuring GaN thin film for enhanced light emission and extraction. *physica status solidi (a)*, 214(1):1600300, January 2017. ISSN 18626300. doi: 10.1002/pssa.201600300. URL `http://doi.wiley.com/10.1002/pssa.201600300`.

[128] M. K. Öztürk, Yu Hongbo, B. Sarıkavak, S. Korçak, S. Özçelik, and E. Özbay. Structural analysis of an InGaN/GaN based light emitting diode by X-ray diffraction. *Journal of Materials Science: Materials in Electronics*, 21(2):185–191, February 2010. ISSN 0957-4522, 1573-482X. doi: 10.1007/s10854-009-9891-6. URL `http://link.springer.com/10.1007/s10854-009-9891-6`.

[129] S. R. Lee, A. M. West, A. A. Allerman, K. E. Waldrip, D. M. Follstaedt, P. P. Provencio, D. D. Koleske, and C. R. Abernathy. Effect of threading dislocations on the Bragg peakwidths of GaN, AlGaN, and AlN heterolayers. *Applied Physics Letters*, 86(24):241904, June 2005. ISSN 0003-6951. doi: 10.1063/1.1947367. URL `https://aip.scitation.org/doi/abs/10.1063/1.1947367`.

[130] Jian-Qi Liu, Yong-Xin Qiu, Jian-Feng Wang, Ke Xu, and Hui Yang. Analysis of Modified Williamson-Hall Plots on GaN Layers. *Chinese Physics Letters*, 28(1):016101, January 2011. ISSN 0256-307X. doi: 10.1088/0256-307X/28/1/016101. URL `https://doi.org/10.1088%2F0256-307x%2F28%2F1%2F016101`.

[131] Vladimir M. Kaganer, Bernd Jenichen, and Oliver Brandt. Elastic versus Plastic Strain Relaxation in Coalesced GaN Nanowires: An X-Ray Diffraction Study. *Physical Review Applied*, 6(6), December 2016. ISSN 2331-7019. doi: 10.1103/PhysRevApplied.6.064023. URL `https://link.aps.org/doi/10.1103/PhysRevApplied.6.064023`.

[132] B Jenichen, O Brandt, C Pfüller, P Dogan, M Knelangen, and A Trampert. Macro- and microstrain in GaN nanowires on Si(111). *Nanotechnology*, 22(29):295714, July 2011. ISSN 0957-4484, 1361-6528. doi: 10.1088/0957-4484/22/29/295714. URL `http://stacks.iop.org/0957-4484/22/i=29/a=295714?key=crossref.4ac367a808ed35b878e828ba1209760d`.

[133] Marcin L. Sadowski, Marek Potemski, and Marian Grynberg. *Optical Properties of Semiconductor Nanostructures.* Springer Science & Business Media, June 2000. ISBN 978-0-7923-6316-3.

[134] W. Shan, B. D. Little, A. J. Fischer, J. J. Song, B. Goldenberg, W. G. Perry, M. D. Bremser, and R. F. Davis. Binding energy for the intrinsic excitons in wurtzite GaN. *Physical Review B*, 54(23):16369–16372, December 1996. doi: 10.1103/PhysRevB.54.16369. URL `https://link.aps.org/doi/10.1103/PhysRevB.54.16369`.

[135] Dylan Bayerl and Emmanouil Kioupakis. Room-temperature stability of excitons and transverse-electric polarized deep-ultraviolet luminescence in atomically thin GaN quantum wells. *Applied Physics Letters*, 115(13):131101, September 2019. ISSN 0003-6951. doi: 10.1063/1.5111546. URL `https://aip.scitation.org/doi/full/10.1063/1.5111546`.

[136] Michael A. Reshchikov. Measurement and analysis of photoluminescence in GaN. *Journal of Applied Physics*, 129(12):121101, March 2021. ISSN 0021-8979. doi: 10.1063/5.0041608. URL `https://aip.scitation.org/doi/10.1063/5.0041608`.

[137] R. Kudrawiec, M. Nyk, M. Syperek, A. Podhorodecki, J. Misiewicz, and W. Strek. Photoluminescence from GaN nanopowder: The size effect associated with the surface-to-volume ratio. *Applied Physics Letters*, 88(18):181916, May 2006. ISSN 0003-6951. doi: 10.1063/1.2199489. URL `https://aip.scitation.org/doi/10.1063/1.2199489`.

[138] Andres Galdámez-Martinez, Guillermo Santana, Frank Güell, Paulina R. Martínez-Alanis, and Ateet Dutt. Photoluminescence of ZnO Nanowires: A Review. *Nanomaterials*, 10(5):857, May 2020. doi: 10.3390/nano10050857. URL `https://www.mdpi.com/2079-4991/10/5/857`.

[139] Day-Shan Liu, Tan-Wei Lin, Bing-Wen Huang, Fuh-Shyang Juang, Po-Hsun Lei, and Chen-Ze Hu. Light-extraction enhancement in GaN-based light-emitting diodes using grade-refractive-index amorphous titanium oxide films with porous structures. *Applied Physics Letters*, 94(14):143502, April 2009. ISSN 0003-6951. doi: 10.1063/1.3116613. URL `https://aip.scitation.org/doi/full/10.1063/1.3116613`.

[140] XingXing Fu, Bei Zhang, XiangNing Kang, JunJing Deng, Chang Xiong, Tao Dai, XianZhe Jiang, TongJun Yu, ZhiZhong Chen, and Guo Yi Zhang. GaN-based light-emitting diodes with photonic crystals structures fabricated by porous anodic alumina template. *Optics Express*, 19(S5):A1104, September 2011. ISSN 1094-4087. doi: 10.1364/OE.19.0A1104. URL `https://www.osapublishing.org/oe/abstract.cfm?uri=oe-19-S5-A1104`.

[141] J R Pugh, E G H Harbord, A Sarua, P S Fletcher, Y Tian, T Wang, and M J Cryan. A Tamm plasmon-porous GaN distributed Bragg reflector cavity. *Journal of Optics*, 23(3):035003, March 2021. ISSN 2040-8978, 2040-8986. doi: 10.1088/2040-8986/abdccb. URL `https://iopscience.iop.org/article/10.1088/2040-8986/abdccb`.

[142] Mingxiang Zhang, Youqing Wang, Feng Teng, Lulu Chen, Jian Li, Jinyuan Zhou, Xiaojun Pan, and Erqing Xie. A photoelectrochemical type self-powered ultraviolet photodetector based on GaN porous films. *Materials Letters*, 162:117–120, January 2016. ISSN 0167-577X. doi: 10.1016/j.matlet.2015.10.001. URL `https://www.sciencedirect.com/science/article/pii/S0167577X15306522`.

[143] Nurul Huda Mohd Noor, Zainuriah Hassan, and Fong Kwong Yam. Porous GaN for Gas Sensing Application. *Advanced Materials Research*, 1043:50–56, 2014. ISSN 1662-8985. doi: 10.4028/www.scientific.net/AMR.1043.50. URL `https://www.scientific.net/AMR.1043.50`.

[144] Jialing Zhou, Hui Huang, Shunji Chen, Mengyuan Wang, Danna Zhao, Jun Yu, Senlin Jin, Yuan Zhong, Xiaoming Chen, Xiaocai Yu, Pengbo Liu, and Jian Zhao. A high sensitive chemiresistive-biosensor based on self-assembly grown GaN porous layer. *Sensors and Actuators B: Chemical*, 345:130360, October 2021. ISSN 0925-4005. doi: 10.1016/j.snb.2021.130360. URL `https://www.sciencedirect.com/science/article/pii/S092540052100928X`.

[145] M. J. Sailor, J. L. Heinrich, and J. M. Lauerhaas. Luminescent porous silicon: Synthesis, chemistry, and applications. In Prashant V. Kamat and Dan Meisel, editors, *Studies in Surface Science and Catalysis*, volume 103 of *Semiconductor Nanoclusters - Physical, Chemical, and Catalytic Aspects*, pages 209–235. Elsevier, January 1997. doi: 10.1016/S0167-2991(97)81104-4. URL `https://www.sciencedirect.com/science/article/pii/S0167299197811044`.

[146] Felix Schubert, Steffen Wirth, Friederike Zimmermann, Johannes Heitmann, Thomas Mikolajick, and Stefan Schmult. Growth condition dependence of unintentional oxygen incorporation in epitaxial GaN. *Science and Technology of Advanced Materials*, 17(1):239–243, January 2016. ISSN

1468-6996. doi: 10.1080/14686996.2016.1178565. URL `https://doi.org/10.1080/14686996.2016.1178565`.

[147] Michael A. Reshchikov. Chapter Nine - Point Defects in GaN. In Lucia Romano, Vittorio Privitera, and Chennupati Jagadish, editors, *Semiconductors and Semimetals*, volume 91 of *Defects in Semiconductors*, pages 315–367. Elsevier, January 2015. doi: 10.1016/bs.semsem.2014.11.003. URL `http://www.sciencedirect.com/science/article/pii/S0080878414000040`.

[148] Conrad Spindler, Thomas Galvani, Ludger Wirtz, Germain Rey, and Susanne Siebentritt. Excitation-intensity dependence of shallow and deep-level photoluminescence transitions in semiconductors. *Journal of Applied Physics*, 126(17):175703, November 2019. ISSN 0021-8979. doi: 10.1063/1.5095235. URL `https://aip.scitation.org/doi/10.1063/1.5095235`.

[149] M. Leroux, N. Grandjean, B. Beaumont, G. Nataf, F. Semond, J. Massies, and P. Gibart. Temperature quenching of photoluminescence intensities in undoped and doped GaN. *Journal of Applied Physics*, 86(7):3721–3728, September 1999. ISSN 0021-8979. doi: 10.1063/1.371242. URL `https://aip.scitation.org/doi/10.1063/1.371242`.

[150] R.Y Korotkov, M.A Reshchikov, and B.W Wessels. Acceptors in undoped GaN studied by transient photoluminescence. *Physica B: Condensed Matter*, 325:1–7, January 2003. ISSN 09214526. doi: 10.1016/S0921-4526(02)01209-7. URL `https://linkinghub.elsevier.com/retrieve/pii/S0921452602012097`.

[151] Niladri Sarkar and Subhasis Ghosh. Temperature dependent band gap shrinkage in GaN: Role of electron–phonon interaction. *Solid State Communications*, 149(31):1288–1291, August 2009. ISSN 0038-1098. doi: 10.1016/j.ssc.2009.05.008. URL `http://www.sciencedirect.com/science/article/pii/S0038109809002683`.

[152] Vladimir M. Kaganer, Bernd Jenichen, Manfred Ramsteiner, Uwe Jahn, Christian Hauswald, Frank Grosse, Sergio Fernández-Garrido, and Oliver Brandt. Quantitative evaluation of the broadening of x-ray diffraction, Raman, and photoluminescence lines by dislocation-induced strain in heteroepitaxial GaN films. *Journal of Physics D: Applied Physics*, 48(38):385105, September 2015. ISSN 0022-3727. doi: 10.1088/0022-3727/48/38/385105. URL `https://doi.org/10.1088%2F0022-3727%2F48%2F38%2F385105`.

[153] E. Iliopoulos, D. Doppalapudi, H. M. Ng, and T. D. Moustakas. Broadening of near-band-gap photoluminescence in n-GaN films. *Applied Physics Letters*, 73(3):375–377, July 1998. ISSN 0003-6951. doi: 10.1063/1.121839. URL `https://aip.scitation.org/doi/10.1063/1.121839`.

[154] Shin-ichi Kan, Shu Takemoto, Kentaro Kaneko, Isao Takahashi, Masahiro Sugimoto, Takashi Shinohe, and Shizuo Fujita. Electrical properties of α-Ir2O3/α-Ga2O3 pn heterojunction diode and band alignment of the heterostructure. *Applied Physics Letters*, 113(21):212104, November 2018. ISSN 0003-6951. doi: 10.1063/1.5054054. URL `https://aip.scitation.org/doi/10.1063/1.5054054`.

[155] Nanako Shiozaki, Taketomo Sato, and Tamotsu Hashizume. Formation of Thin Native Oxide Layer on n-GaN by Electrochemical Process in Mixed Solution with Glycol and Water. *Japanese Journal of Applied Physics*, 46(4R):1471, April 2007. ISSN 1347-4065. doi: 10.1143/JJAP.46.1471. URL `https://iopscience.iop.org/article/10.1143/JJAP.46.1471/meta`.

[156] K. Idczak, P. Mazur, S. Zuber, L. Markowski, M. Skiścim, and S. Bilińska. Growth of thin zirconium and zirconium oxides films on the n-GaN(0001) surface studied by XPS and LEED. *Applied Surface Science*, 304:29–34, June 2014. ISSN 0169-4332. doi: 10.1016/j.apsusc.2014.01.102. URL `https://www.sciencedirect.com/science/article/pii/S0169433214001421`.

[157] K. Prabhakaran, T. G. Andersson, and K. Nozawa. Nature of native oxide on GaN surface and its reaction with Al. *Applied Physics Letters*, 69(21):3212–3214, November 1996. ISSN 0003-6951. doi: 10.1063/1.117964. URL `https://aip.scitation.org/doi/abs/10.1063/1.117964`.

[158] J. Kovač and A. Zalar. Surface composition changes in GaN induced by argon ion bombardment. *Surface and Interface Analysis*, 34(1):253–256, 2002. ISSN 1096-9918. doi: 10.1002/sia.1294. URL `https://analyticalsciencejournals.onlinelibrary.wiley.com/doi/abs/10.1002/sia.1294`.

[159] S. W. King, J. P. Barnak, M. D. Bremser, K. M. Tracy, C. Ronning, R. F. Davis, and R. J. Nemanich. Cleaning of AlN and GaN surfaces. *Journal of Applied Physics*, 84(9):5248–5260, November 1998. ISSN 0021-8979. doi: 10.1063/1.368814. URL `https://aip.scitation.org/doi/10.1063/1.368814`.

[160] L. F. J. Piper, T. D. Veal, M. Walker, I. Mahboob, C. F. McConville, Hai Lu, and W. J. Schaff. Clean wurtzite InN surfaces prepared with atomic hydrogen. *Journal of Vacuum Science & Technology A*, 23(4):617–620, July 2005. ISSN 0734-2101. doi: 10.1116/1.1927108. URL `https://avs.scitation.org/doi/abs/10.1116/1.1927108`.

[161] Azusa N. Hattori, Katsuyoshi Endo, Ken Hattori, and Hiroshi Daimon. Surface treatments toward obtaining clean GaN(0001) from commercial hydride vapor phase epitaxy and metal-organic chemical vapor deposition substrates in ultrahigh vacuum. *Applied Surface Science*, 256(14):4745–4756, May 2010. ISSN 0169-4332. doi: 10.1016/j.apsusc.2010.03.001. URL `https://www.sciencedirect.com/science/article/pii/S0169433210002862`.

[162] Simon M. Sze and Kwok K. Ng. *Physics of Semiconductor Devices*. John Wiley & Sons, December 2006. ISBN 978-0-470-06830-4.

[163] J. R. Waldrop and R. W. Grant. Measurement of AlN/GaN (0001) heterojunction band offsets by x-ray photoemission spectroscopy. *Applied Physics Letters*, 68(20):2879–2881, May 1996. ISSN 0003-6951. doi: 10.1063/1.116355. URL `https://aip.scitation.org/doi/abs/10.1063/1.116355`.

[164] M. Kočan, A. Rizzi, H. Lüth, S. Keller, and U. K. Mishra. Surface Potential at as-Grown GaN(0001) MBE Layers. *physica status solidi (b)*, 234(3):773–777, 2002. ISSN 1521-3951. doi: 10.1002/1521-3951(200212)234:3⟨773::AID-PSSB773⟩3.0.CO;2-0. URL `https://onlinelibrary.wiley.com/doi/abs/10.1002/1521-3951%28200212%29234%3A3%3C773%3A%3AAID-PSSB773%3E3.0.CO%3B2-0`.

[165] D. Segev and C. G. Van de Walle. Origins of Fermi-level pinning on GaN and InN polar and nonpolar surfaces. *EPL (Europhysics Letters)*, 76(2):305, September 2006. ISSN 0295-5075. doi: 10.1209/epl/i2006-10250-2. URL `https://iopscience.iop.org/article/10.1209/epl/i2006-10250-2/meta`.

[166] Matthew S. Makowski, Dmitry Y. Zemlyanov, and Albena Ivanisevic. Olefin metathesis reaction on GaN (0001) surfaces. *Applied Surface Science*, 257(10):4625–4632, March 2011. ISSN 0169-4332. doi: 10.1016/j.apsusc.2010.12.100. URL `https://www.sciencedirect.com/science/article/pii/S0169433210018295`.

[167] Lili Cai and Cuiju Feng. Effect of Vacancy Defects on the Electronic Structure and Optical Properties of GaN. *Journal of Nanotechnology*, 2017:e6987430, February 2017. ISSN 1687-9503. doi: 10.1155/2017/6987430. URL `https://www.hindawi.com/journals/jnt/2017/6987430/`.

[168] Monu Mishra, Shibin Krishna T. C, Neha Aggarwal, Mandeep Kaur, Sandeep Singh, and Govind Gupta. Pit assisted oxygen chemisorption on GaN surfaces. *Physical Chemistry Chemical Physics*, 17(23):15201–15208, 2015. doi: 10.1039/C5CP00540J. URL `http://pubs.rsc.org/en/Content/ArticleLanding/2015/CP/C5CP00540J`.

[169] Monu Mishra, T. C. Shibin Krishna, Neha Aggarwal, and Govind Gupta. Surface chemistry and electronic structure of nonpolar and polar GaN films. *Applied Surface Science*, 345(Supplement C):440–447, August 2015. ISSN 0169-4332. doi: 10.1016/j.apsusc.2015.03.166. URL `http://www.sciencedirect.com/science/article/pii/S0169433215007825`.

[170] D. Skuridina, D. V. Dinh, B. Lacroix, P. Ruterana, M. Hoffmann, Z. Sitar, M. Pristovsek, M. Kneissl, and P. Vogt. Polarity determination of polar and semipolar (1122) InN and GaN layers by valence band photoemission spectroscopy. *Journal of Applied Physics*, 114(17):173503, November 2013. ISSN 0021-8979. doi: 10.1063/1.4828487. URL `https://aip.scitation.org/doi/full/10.1063/1.4828487`.

[171] Martin Magnuson, Maurizio Mattesini, Carina Höglund, Jens Birch, and Lars Hultman. Electronic structure of GaN and Ga investigated by soft x-ray spectroscopy and first-principles methods. *Physical Review B*, 81(8):085125, February 2010. doi: 10.1103/PhysRevB.81.085125. URL `https://link.aps.org/doi/10.1103/PhysRevB.81.085125`.

[172] Chris G. Van de Walle and David Segev. Microscopic origins of surface states on nitride surfaces. *Journal of Applied Physics*, 101(8):081704, April 2007. ISSN 0021-8979. doi: 10.1063/1.2722731. URL `https://aip.scitation.org/doi/full/10.1063/1.2722731`.

[173] Kenneth S. W. Sing. Characterization Of Porous Solids: An Introductory Survey. In F. Rodriguez-Reinoso, J. Rouquerol, K. S. W. Sing, and K. K. Unger, editors, *Studies in Surface Science and Catalysis*, volume 62 of *Characterization of Porous Solids II*, pages 1–9. Elsevier, January 1991. doi: 10.1016/S0167-2991(08)61303-8. URL `https://www.sciencedirect.com/science/article/pii/S0167299108613038`.

[174] Susanne Schafer, Amelie H. R. Koch, Alda Cavallini, Martin Stutzmann, and Ian D. Sharp. Charge Transfer across the n-Type GaN–Electrolyte Interface. *The Journal of Physical Chemistry C*, 116 (42):22281–22286, October 2012. ISSN 1932-7447, 1932-7455. doi: 10.1021/jp302000x. URL `http://pubs.acs.org/doi/10.1021/jp302000x`.

[175] Shyam S. Kocha, Mark W. Peterson, Douglas J. Arent, Joan M. Redwing, Michael A. Tischler, and John A. Turner. Electrochemical Investigation of the Gallium Nitride-Aqueous Electrolyte Interface. *Journal of The Electrochemical Society*, 142(12):L238–L240, December 1995. ISSN 0013-4651, 1945-7111. doi: 10.1149/1.2048511. URL `http://jes.ecsdl.org/content/142/12/L238`.

[176] Andrea Winnerl, Jose A. Garrido, and Martin Stutzmann. Electrochemical characterization of GaN surface states. *Journal of Applied Physics*, 122(4):045302, July 2017. ISSN 0021-8979. doi: 10.1063/1.4995429. URL `https://aip.scitation.org/doi/abs/10.1063/1.4995429`.

[177] G. Nowak, X. H. Xia, J. J. Kelly, J. L. Weyher, and S. Porowski. Electrochemical etching of highly conductive GaN single crystals. *Journal of Crystal Growth*, 222(4):735–740, February 2001. ISSN 0022-0248. doi: 10.1016/S0022-0248(00)00988-X. URL `https://www.sciencedirect.com/science/article/pii/S002202480000988X`.

[178] Katsushi Fujii, Takeshi Karasawa, and Kazuhiro Ohkawa. Hydrogen Gas Generation by Splitting Aqueous Water Using n-Type GaN Photoelectrode with Anodic Oxidation. *Japanese Journal of Applied Physics*, 44(No. 18):L543–L545, April 2005. ISSN 0021-4922. doi: 10.1143/JJAP.44.L543. URL `https://iopscience.iop.org/article/10.1143/JJAP.44.L543`.

[179] Mark E. Orazem and Bernard Tribollet. *Electrochemical Impedance Spectroscopy.* John Wiley & Sons, October 2011. ISBN 978-1-118-20994-3.

[180] Tien Quang Nguyen and Cornelia Breitkopf. Determination of Diffusion Coefficients Using Impedance Spectroscopy Data. *Journal of The Electrochemical Society*, 165(14):E826, November 2018. ISSN 1945-7111. doi: 10.1149/2.1151814jes. URL `https://iopscience.iop.org/article/10.1149/2.1151814jes/meta`.

[181] Matthias Sachsenhauser, Ian D. Sharp, Martin Stutzmann, and Jose A. Garrido. Surface State Mediated Electron Transfer Across the N-Type SiC/Electrolyte Interface. *The Journal of Physical Chemistry C*, 120(12):6524–6533, March 2016. ISSN 1932-7447. doi: 10.1021/acs.jpcc.5b11569. URL `https://doi.org/10.1021/acs.jpcc.5b11569`.

[182] Anna Hankin, Franky E. Bedoya-Lora, John C. Alexander, Anna Regoutz, and Geoff H. Kelsall. Flat band potential determination: avoiding the pitfalls. *Journal of Materials Chemistry A*, 7 (45):26162–26176, November 2019. ISSN 2050-7496. doi: 10.1039/C9TA09569A. URL `https://pubs.rsc.org/en/content/articlelanding/2019/ta/c9ta09569a`.

[183] Abdurrahman Shougee, Foivia Konstantinou, Tim Albrecht, and Kristel Fobelets. Cyclic Voltammetry Peaks Due to Deep Level Traps in Si Nanowire Array Electrodes. *IEEE Transactions on Nanotechnology*, 17(1):154–160, January 2018. ISSN 1941-0085. doi: 10.1109/TNANO.2017.2754581.

[184] Erol Kucur, Wendelin Bücking, Ralf Giernoth, and Thomas Nann. Determination of Defect States in Semiconductor Nanocrystals by Cyclic Voltammetry. *The Journal of Physical Chemistry B*, 109(43):20355–20360, November 2005. ISSN 1520-6106. doi: 10.1021/jp053891b. URL `https://doi.org/10.1021/jp053891b`.

[185] M. A. Reshchikov, R. M. Sayeed, U. Ozgur, D. O. Demchenko, J. D. McNamara, V. Prozheeva, F. Tuomisto, H. Helava, A. Usikov, and Yu. Makarov. Unusual properties of the RY3 center in GaN. *Physical Review B*, 100(4), July 2019. ISSN 2469-9950, 2469-9969. doi: 10.1103/PhysRevB.100.045204. URL `https://link.aps.org/doi/10.1103/PhysRevB.100.045204`.

[186] A. Bell, I. Harrison, T. S. Cheng, D. Korakakis, C. T. Foxon, S. Novikov, B. Ya Ber, and Y. A. Kudriavtsev. An investigation into the origin of the 3.424 eV peak in the low-temperature photoluminescence of GaN grown by molecular beam epitaxy. *Semiconductor Science and Technology*, 15(8):789–793, June 2000. ISSN 0268-1242. doi: 10.1088/0268-1242/15/8/301. URL `https://doi.org/10.1088/0268-1242/15/8/301`.

[187] H. Tang, S. M. Sadaf, X. Wu, and W. Jiang. Highly efficient p-type doping of GaN under nitrogen-rich and low-temperature conditions by plasma-assisted molecular beam epitaxy. *AIP Advances*, 9 (5):055008, May 2019. ISSN 2158-3226. doi: 10.1063/1.5089658. URL `http://aip.scitation.org/doi/10.1063/1.5089658`.

[188] Kohei Ueno, Fudetani Taiga, Atsushi Kobayashi, and Hiroshi Fujioka. Optical characteristics of highly conductive n-type GaN prepared by pulsed sputtering deposition. *Scientific Reports*, 9(1): 1–5, December 2019. ISSN 2045-2322. doi: 10.1038/s41598-019-56306-0. URL `https://www.nature.com/articles/s41598-019-56306-0`.

[189] D. Saha, Amit. K. Das, R. S. Ajimsha, P. Misra, and L. M. Kukreja. Effect of disorder on carrier transport in ZnO thin films grown by atomic layer deposition at different temperatures. *Journal of Applied Physics*, 114(4):043703, July 2013. ISSN 0021-8979, 1089-7550. doi: 10.1063/1.4815941. URL `http://aip.scitation.org/doi/10.1063/1.4815941`.

[190] I. Naik. Weak localization and electron–electron interaction induce resistance minimum in 2H-Ga0.20NbSe2. *Materials Research Express*, 3(12):126506, December 2016. ISSN 2053-1591. doi: 10.1088/2053-1591/3/12/126506. URL `https://doi.org/10.1088%2F2053-1591%2F3%2F12%2F126506`.

[191] Jun Kondo. Resistance Minimum in Dilute Magnetic Alloys. *Progress of Theoretical Physics*, 32 (1):37–49, July 1964. ISSN 0033-068X. doi: 10.1143/PTP.32.37. URL `https://academic.oup.com/ptp/article/32/1/37/1834632`.

[192] A. Gerber, I. Kishon, D. Bartov, and M. Karpovski. Resistivity minimum in granular composites and thin metallic films. *Physical Review B*, 94(9):094202, September 2016. doi: 10.1103/PhysRevB.94.094202. URL `https://link.aps.org/doi/10.1103/PhysRevB.94.094202`.

[193] Amit K. Das, P. Misra, R. S. Ajimsha, A. Bose, S. C. Joshi, D. M. Phase, and L. M. Kukreja. Studies on temperature dependent semiconductor to metal transitions in ZnO thin films sparsely doped with Al. *Journal of Applied Physics*, 112(10):103706, November 2012. ISSN 0021-8979. doi: 10.1063/1.4765733. URL `https://aip.scitation.org/doi/10.1063/1.4765733`.

[194] R. V. Muniswami Naidu, A. Subrahmanyam, A. Verger, M. K. Jain, S. V. N. Bhaskara Rao, S. N. Jha, and D. M. Phase. Electron-electron interactions based metal-insulator transition in Ga doped ZnO thin films. *Electronic Materials Letters*, 8(4):457–462, August 2012. ISSN 1738-8090, 2093-6788. doi: 10.1007/s13391-012-1086-2. URL `http://link.springer.com/10.1007/s13391-012-1086-2`.

[195] V. Bhosle, A. Tiwari, and J. Narayan. Metallic conductivity and metal-semiconductor transition in Ga-doped ZnO. *Applied Physics Letters*, 88(3):032106, January 2006. ISSN 0003-6951, 1077-3118. doi: 10.1063/1.2165281. URL `http://aip.scitation.org/doi/10.1063/1.2165281`.

[196] Patrick A. Lee and T. V. Ramakrishnan. Disordered electronic systems. *Reviews of Modern Physics*, 57(2):287–337, April 1985. ISSN 0034-6861. doi: 10.1103/RevModPhys.57.287. URL `https://link.aps.org/doi/10.1103/RevModPhys.57.287`.

[197] M. Nistor, F. Gherendi, N. B. Mandache, C. Hebert, J. Perrière, and W. Seiler. Metal-semiconductor transition in epitaxial ZnO thin films. *Journal of Applied Physics*, 106(10):103710, November 2009. ISSN 0021-8979. doi: 10.1063/1.3259412. URL `https://aip.scitation.org/doi/full/10.1063/1.3259412`.

[198] Shaili Sett, K Das, and A K Raychaudhuri. Weak localization and the approach to metal–insulator transition in single crystalline germanium nanowires. *Journal of Physics: Condensed Matter*, 29(11):115301, March 2017. ISSN 0953-8984, 1361-648X. doi: 10.1088/1361-648X/aa58fe. URL `http://stacks.iop.org/0953-8984/29/i=11/a=115301?key=crossref.b7dc6e80ee1b032d4d6efa7e0d391a5b`.

[199] R Akiyama, K Fujisawa, R Sakurai, and S Kuroda. Weak antilocalization in (111) thin films of a topological crystalline insulator SnTe. *Journal of Physics: Conference Series*, 568(5):052001, December 2014. ISSN 1742-6588, 1742-6596. doi: 10.1088/1742-6596/568/5/052001. URL `http://stacks.iop.org/1742-6596/568/i=5/a=052001?key=crossref.ab2866570236e8d41935e7b7e1e93bfa`.

[200] Huichao Wang, Haiwen Liu, Cui-Zu Chang, Huakun Zuo, Yanfei Zhao, Yi Sun, Zhengcai Xia, Ke He, Xucun Ma, X. C. Xie, Qi-Kun Xue, and Jian Wang. Crossover between Weak Antilocalization and Weak Localization of Bulk States in Ultrathin Bi 2 Se 3 Films. *Scientific Reports*, 4(1):1–6, July 2014. ISSN 2045-2322. doi: 10.1038/srep05817. URL `https://www.nature.com/articles/srep05817`.

[201] Himadri Chakraborti, Swarup Deb, Rüdiger Schott, Varun Thakur, Abhijit Chatterjee, Santosh Yadav, Rajendra K. Saroj, Andreas Wieck, S. M. Shivaprasad, K. Das Gupta, and S. Dhar. Coherent transmission of superconducting carriers through a ∼2 μ m polar semiconductor. *Superconductor Science and Technology*, 31(8):085007, 2018. ISSN 0953-2048. doi: 10.1088/1361-6668/aacd89. URL `http://stacks.iop.org/0953-2048/31/i=8/a=085007`.

[202] E. P. Amaladass, Abhijit Chatterjee, Shilpam Sharma, Awadhesh Mani, and S. M. Shivaprasad. Weak localization and electron–electron interaction in GaN nanowalls. *Materials Research Express*, 4(9):095014, 2017. ISSN 2053-1591. doi: 10.1088/2053-1591/aa89b0. URL `http://stacks.iop.org/2053-1591/4/i=9/a=095014`.

[203] Pratibha Dev and Peihong Zhang. Unconventional magnetism in semiconductors: Role of localized acceptor states. *Physical Review B*, 81(8), February 2010. ISSN 1098-0121, 1550-235X. doi: 10.1103/PhysRevB.81.085207. URL `https://link.aps.org/doi/10.1103/PhysRevB.81.085207`.

[204] Basanta Roul, Mohana K. Rajpalke, Thirumaleshwara N. Bhat, Mahesh Kumar, A. T. Kalghatgi, S. B. Krupanidhi, Nitesh Kumar, and A. Sundaresan. Experimental evidence of Ga-vacancy induced room temperature ferromagnetic behavior in GaN films. *Applied Physics Letters*, 99(16):162512, October 2011. ISSN 0003-6951. doi: 10.1063/1.3654151. URL `https://aip.scitation.org/doi/10.1063/1.3654151`.

[205] Yu Liu, Liangbao Jiang, Gang Wang, Sibin Zuo, Wenjun Wang, and Xiaolong Chen. Adjustable nitrogen-vacancy induced magnetism in AlN. *Applied Physics Letters*, 100(12):122401, March 2012. ISSN 0003-6951. doi: 10.1063/1.3696023. URL `https://aip.scitation.org/doi/10.1063/1.3696023`.

[206] Sanjay Nayak, Mit H. Naik, Manish Jain, Umesh V. Waghmare, and Sonnada M. Shivaprasad. First-principles theoretical analysis and electron energy loss spectroscopy of vacancy defects in bulk and nonpolar (10 1 0) surface of GaN. *Journal of Vacuum Science & Technology A*, 38(6): 063205, December 2020. ISSN 0734-2101. doi: 10.1116/6.0000402. URL `https://avs.scitation.org/doi/full/10.1116/6.0000402`.

[207] Swarup Deb and Subhabrata Dhar. Wedge-Shaped GaN Nanowalls: A Potential Candidate for Two-Dimensional Electronics and Spintronics. *SPIN*, 08(01):1840003, March 2018. ISSN 2010-3247. doi: 10.1142/S2010324718400039. URL `https://www.worldscientific.com/doi/abs/10.1142/S2010324718400039`.

[208] K. Han, N. Tang, J. D. Ye, J. X. Duan, Y. C. Liu, K. L. Teo, and B. Shen. Spin-polarized two-dimensional electron gas in undoped Mg $_{\text{x}}$ Zn $_{\text{1-x}}$ O/ZnO heterostructures. *Applied Physics Letters*, 100(19):192105, May 2012. ISSN 0003-6951, 1077-3118. doi: 10.1063/1.4711775. URL `http://aip.scitation.org/doi/10.1063/1.4711775`.

[209] Zihao Yang, Thomas F. Kent, Jing Yang, Hyungyu Jin, Joseph P. Heremans, and Roberto C. Myers. Anisotropic defect-induced ferromagnetism and transport in Gd-doped GaN two-dimensional electron gasses. *Physical Review B*, 92(22), December 2015. ISSN 1098-0121, 1550-235X. doi: 10.1103/PhysRevB.92.224416. URL `https://link.aps.org/doi/10.1103/PhysRevB.92.224416`.

[210] S. Schmult, M. J. Manfra, A. Punnoose, A. M. Sergent, K. W. Baldwin, and R. J. Molnar. Large Bychkov-Rashba spin-orbit coupling in high-mobility Ga N / Al x Ga 1 - x N heterostructures. *Physical Review B*, 74(3), July 2006. ISSN 1098-0121, 1550-235X. doi: 10.1103/PhysRevB.74.033302. URL `https://link.aps.org/doi/10.1103/PhysRevB.74.033302`.

[211] Ikai Lo, W. T. Wang, M. H. Gau, S. F. Tsay, and J. C. Chiang. Wurtzite structure effects on spin splitting in GaN / AlN quantum wells. *Physical Review B*, 72(24), December 2005. ISSN 1098-0121, 1550-235X. doi: 10.1103/PhysRevB.72.245329. URL `https://link.aps.org/doi/10.1103/PhysRevB.72.245329`.